Performance and Lifetime Limiting Effects in Li-ion Batteries

Scipioni, Roberto

Publication date:
2016

Document Version
Publisher's PDF, also known as Version of record

Performance and Lifetime Limiting Effects in Li-ion Batteries

RISØ, DENMARK 2013-2016

ROBERTO SCIPIONI
Department of Energy Conversion and Storage
Technical University of Denmark

SUPERVISORS

SENIOR SCIENTIST SØREN HØJGAARD JENSEN
SENIOR SCIENTIST JOHAN HJELM
SENIOR SCIENTIST POUL NORBY

2016
TECHNICAL UNIVERSITY OF DENMARK

Submitted in candidacy for the degree Doctor of Philosophy

Preface

This thesis is submitted in candidacy for the PhD degree in Electrochemistry from the Technical University of Denmark (DTU) and the work was carried out at the Department of Energy Conversion and Storage in the period of June 2013 to June 2016. The project was mainly supervised by Senior Scientist Søren Højgaard Jensen and co-supervised by Senior Scientists Johan Hjelm and Poul Norby. The work was funded through the ALPBES project (contract no. 0603-00589B), by the Danish Council for Strategic Research. Four months of the work were carried out through an external stay at Northwestern University, Evanston, IL (USA) at the Scott A. Barnett Research Group, Department of Materials Science and Engineering. This work included one of the main authoring papers and was made possible through the financial support from the Office of Naval Research Grant #N00014-12-1-0713.

Acknowledgements

Firstly, I would like to express my sincere gratitude to my main supervisor Senior Scientist *Søren Højgaard Jensen* for the continuous support and guidance during these three years. Thank you for giving me all the necessary help and support, motivating in my research and giving me a lot of useful tips and ideas. You have been a great teacher. Thank you for being my mentor and being a great person.

Thank you Senior Scientist *Johan Hjelm* for the inspiration, discussions and guidance during these years. Thanks a lot for introducing me to Python and to Impedance Spectroscopy. I always found your door open to discuss about my research. Thank you Senior Scientist *Poul Norby* for the guidance and discussions about x-ray diffraction and for the help and the inspiring meetings about the development of micro-capillary batteries. Thank you Prof. *Tejs Vegge* for the inspiration and discussions during the "interface" meetings.

I would also like to gratefully thank Researcher *Peter Stanley Jørgensen* and Researcher *Søren Bredmose Simonsen* for their guidance and help in microscopic analysis, and Laboratory Technician *Ebtisam Abdellahi* for her help in sample preparations. She is able to do miracles.

A big thanks to Prof. *Anke Hagen* and all the AEC section for the nice three years spent together, the social events and the inspiring section meeting.

Thanks a lot *Heidi* for assisting me in all the bureaucracy during these years, and especially for all the coffee breaks with cookies. I don't really know what I would do without you.

I would also like to thank Prof. *Scott A. Barnett* and his entire research group in Northwestern University for the very productive collaboration during my external stay. A big thank also to Scott's family (*Joann*, *Casey*, *Charlie* and *Piper*) for the very warm welcome. I felt part of your family.

Thanks *Kristian* for being an awesome officemate. It has been three years of great discussions, coffee breaks and desserts. You have been a great colleague, but first a great buddy. I want to thanks also *Filippo*, the new entry in kontor S-23. You are an awesome officemate too and a big friend.

Thank you *Ane, Mie, Reza, Duc-The, Jonathan, Andreas, Mathias* and all people from the battery group for being great colleagues and always ready to give a helping hand or discuss work and issues over a cup of coffee.

Thanks to all my friends here at DTU and all the people from the PhD group (*Jean-Claude*, *Salvo*, *Kosova* and *Simone* in particular). And thank you *Stefano* and *Fabrizio* for all the nice discussions in front of a cup of coffee over these years. You cheered me up

many times. Thanks to you also *Spandi* for supporting me the last month with coffee breaks and spandauer.

A big thank to all my old friends, especially *Giuseppe, Enrico, Carmelo, Antonio*, for being always close to me, although the big distance.

Finally I want to thank my parents and family because they let me do what I want and always support me, and thank you my little sister *Silvia*, and *Gianluca* of course, for being always close to me in every moment of my life.

Abstract

Lithium-ion batteries (LIBs) find widespread use for electricity storage, from portable devices such as smart phones to electric vehicles (EV), because of their high energy density and design flexibility. However, limited lifetime is still a challenge for several LIB materials. Specifically, the detailed coupling between degradation mechanisms and battery usage is not fully understood, which impede lifetime improvements. To understand the degradation mechanisms and increase the performance of these materials, the development of improved characterization methods is crucial. This PhD thesis focuses on the thorough analysis of degradation mechanism in LIBs, trying to relate morphological and structural changes in Lithium-ion battery electrodes to performance degradation observed during electrode cycling.

Degradation mechanisms in laboratory scale LFP cathodes were correlated with the degradation mechanisms observed in commercial LIBs. The structural and morphological changes in cycled laboratory LFP cathodes were studied by low-kV FIB/SEM Tomography and TEM analysis and related to the electrode performance using Electrochemical Impedance Spectroscopy (EIS). The two main degradation processes observed by microscopy analysis in the aged electrode were cracking of LFP particles and agglomeration of carbon black (CB) additive. The increased heterogeneity of the CB network reduces the electron percolation throughout the porous electrode, thereby decreasing the amount of electrochemically active LFP particles. The electron resistivity was quantified with the EIS analysis using a Transmission Line Model (TLM) developed for porous LFP electrodes.

Similar TLM models were applied for the analysis of the polarization processes in a commercial LFP and graphite electrodes. The microscopy analysis of the electrodes showed the presence of carbonaceous agglomerates on the electrode/electrolyte interfaces. The agglomerates are expected to increase the ionic resistance and be related to of loss of lithium inventory (LLI).

Resumé

På grund af deres høje energitæthed og design fleksibilitet anvendes Lithium-ion-batterier (LIB) til mange forskellige former for ellagring, lige fra bærbare enheder mobiltelefoner til elbiler (EV). Desværre er begrænset levetid stadig problematisk for de anvendte LIB materialer. Mere specifikt er den detaljerede kobling mellem degraderingsmekanismer og brug af batteriet ikke forstået til fulde, hvilket vanskeliggør udviklingen af effektive levetidsforbedringer. For at forbedre forståelsen af koblingen mellem degraderingsmekanismerne og batteriernes anvendelse er det vigtigt at udvikle forbedrede degraderingsmekanismekarakteriseringsmetoder. Denne ph.d.-afhandling er koncentreret om en grundig analyse af degraderingsmekanismerne i LIB, og forsøger at relatere morfologiske og strukturelle ændringer i LIB elektroder, til den gradvise forringelse af elektrodernes ydeevne under cykling af elektroderne.

I PhD projektet er degraderingsmekanismer observeret i laboratorieskala LFP katoder sammenlignet med degraderingsmekanismer observeret i kommercielle LFP katoder. De strukturelle og morfologiske ændringer i cyklede laboratorie LFP katoder blev undersøgt vha. lav-kV FIB / SEM Tomografi og TEM-analyse og relateret til elektrodens ydeevne bla. vha. elektrokemisk impedans spektroskopi (EIS). De to vigtigste degraderingsprocesser observeret ifbm. mikroskopianalyserne er revnedannelse i LFP partiklerne og agglomerering af carbon black (CB) additiv. Den øgede heterogenitet i CB-netværket reducerer elektronledningsevnen i den porøse elektrode, hvilket reducerer mængden af elektrokemisk aktive LFP-partikler. Elektronledningsevnen blev beregnet vha. EIS-analysen med en ækvivalentkredsløbsmodel udviklet til porøse LFP elektroder.

Lignende ækvivalentkredsløbsmodeller blev efterfølgende anvendt til analyse af polariseringsprocesser i kommercielle LFP og grafit elektroder. Mikroskopianalyse af elektroderne viste tilstedeværelsen af karbonholdige agglomerater på elektrode / elektrolyt interfacene. Agglomeraterne antages at øge den joniske modstand i batteriet og være relateret til tab af lithium (LLI).

List of Publications

This thesis is based on the following papers, which are referred to in the text by Roman numerals.

Paper I: R. Scipioni, P.S. Jørgensen, D.-T. Ngo, S.B. Simonsen, Z. Liu, K. J. Yakal-Kremski, H. Wang, J. Hjelm, P. Norby, S.A. Barnett, S.H. Jensen. "Electron microscopy investigations of changes in morphology and conductivity of $LiFePO_4$/C electrodes." *J. Power Sources* **307**, 259–269 (2016).

Paper II: R. Scipioni, P.S. Jørgensen, D.-T. Ngo, S.B. Simonsen, J. Hjelm, P. Norby, S.H. Jensen. "Low-voltage FIB/SEM Tomography for 3D Microstructure Evolution of $LiFePO_4$/C Electrode." *ECS Trans.* **69**(18), 71-80 (2015).

Paper III: D.-T. Ngo, R. Scipioni, S.B. Simonsen, P.S. Jørgensen, and S.H. Jensen. "A TEM study of morphological and structural degradation phenomena in $LiFePO_4$-CB cathodes." *Int. J. Energy Res.* (2016)

Paper IV: R. Younesi, A.S. Christiansen, R. Scipioni, D.-T. Ngo, S.B. Simonsen, K. Edström, J. Hjelm, P. Norby. "Analysis of the Interphase on Carbon Black Formed in High Voltage Batteries." *J. Electrochem. Soc.* **162**, A1289-A1296 (2015).

Paper V: R. Scipioni, P.S. Jørgensen, J. Hjelm, S. H. Jensen. "A transmission line model for a full $LiFePO_4$/C 26650 cylindrical cell derived by combined single-electrode Impedance and FIB/SEM-tomography analysis." *In manuscript.*

Paper VI: R. Scipioni, P.S. Jørgensen, D. I. Stroe, J. Hjelm, S. H. Jensen. "Analysis of Aging Mechanisms in a Commercial $LiFePO_4$/Graphite 26650 Cylindrical Cell by Low – kV FIB/SEM Tomography." *In manuscript.*

Comments on my contribution to the appended papers

Paper I: In this work I prepared two laboratory $LiFePO_4$/C electrodes, performed the electrochemical testing in three-electrode setup and then prepared the samples for microscopy analysis. I executed the low-voltage FIB/SEM analysis of the sample at Risø DTU, performed segmentation and 3D reconstruction in collaboration with Prof. S.A. Barnett's group and finally wrote most of the above mentioned article.

Paper II: I prepared two laboratory $LiFePO_4$/C electrodes, performed the electrochemical testing in three-electrode setup (galvanostatic cycling and impedance spectroscopy) and the modelling of the impedance spectra. I executed the low-voltage FIB/SEM analysis, performed segmentation and 3D reconstruction and finally wrote most of the above mentioned article.

Paper III: I prepared two laboratory $LiFePO_4$/C electrodes, performed the electrochemical testing in three-electrode setup (galvanostatic cycling and impedance spectroscopy) and then prepared the samples for microscopy analysis. I performed the low-voltage FIB/SEM analysis of the sample and finally wrote the paragraphs on "charge-discharge cycling" and "impedance analysis".

Paper IV: In this work I performed the electrochemical testing of the samples in three-electrode setup (galvanostatic cycling and impedance spectroscopy). I performed the modelling of the impedance spectra and finally wrote part of the "experimental" and "results and discussion" sections.

Paper V: I tested and disassembled commercial $LiFePO_4$/C cylindrical cells. I developed an equivalent circuit model for EIS analysis and performed FIB/SEM tomography, data analysis and 3D reconstruction, and finally wrote most of the above mentioned article.

Paper VI: In this work I tested and disassembled fresh and aged commercial $LiFePO_4$/C cylindrical cells, performed FIB/SEM tomography, data analysis and 3D reconstruction to study degradation mechanisms, and finally wrote most of the above mentioned article.

Contents

1. Scope of the thesis **1**

2. Introduction **2**
2.1. The energy storage problem 2
2.2. Li-ion batteries 4
2.3. Cathode materials 6
2.3.1. $LiFePO_4$ 7
2.3.2. Carbon additives 7
2.3.3. Aging mechanisms in $LiFePO_4$/C cathodes 8
2.4. Anode materials 8
2.4.1. Graphite 9
2.4.2. Aging mechanisms in graphite anodes 10

3. Characterization Techniques **12**
3.1. Galvanostatic Cycling with Potential Limitation (GCPL) 14
3.2. Electrochemical Impedance Spectroscopy (EIS) 14
3.2.1. EIS Modelling 16
3.2.2. The Transmission Line Model (TLM) – Generalized 18
3.2.3. The Transmission Line Model (TLM) – Simplified 20
3.3. Focused Ion Beam/Scanning Electron Microscopy (FIB/SEM) 21
3.3.1. The Scanning Electron Microscope (SEM) 22
3.3.2. Interaction of the electrons with the specimen 22
3.3.3. Low – Voltage Scanning 23
3.4. Transmission Electron Microscopy (TEM) 24
3.4.1. Scanning Transmission Electron Microscopy (STEM) 25

4. Cell Designs and Battery Assembly **26**
4.1. EL – CELL (Three-electrode setup) 26
4.2. Pouch Cell (Two-electrode setup) 27
4.3. Commercial 26650 Cylindrical Cell (Two-electrode setup) 28

5. Summary of Results and Discussion **29**
5.1. Laboratory Scale Li-ion batteries 29
5.1.1. Low-kV FIB/SEM analysis for changes in morphology and conductivity of $LiFePO_4$/C electrodes 29
5.1.2. A transmission line model (TLM) for laboratory $LiFePO_4$/C electrodes 35
5.1.3. A TEM study of morphological and structural degradation phenomena in $LiFePO_4$-CB cathodes 37

5.1.4. Analysis of the Interphase on Carbon Black Formed in High Voltage Batteries 41
5.2. Commercial $LiFePO_4$/C 26650 cylindrical cells 47
5.2.1. A transmission line model for a full $LiFePO_4$/C 26650 cylindrical cell derived by combined single-electrode Impedance and FIB/SEM tomography analysis 47
5.2.2. Analysis of Aging Mechanisms in a Commercial $LiFePO_4$/ Graphite 26650 Cylindrical Cell by Low – kV FIB/SEM Tomography 59

6. Concluding Remarks and Future Outlook 66
6.1. Outlook 67

Bibliography 68

7. Appendix 77

Paper I 79

Paper II 93

Paper III 105

Paper IV 119

Paper V 129

Paper VI 165

Scope of the Thesis 1

Limited lifetime is still a challenge for most Lithium-ion battery materials. Specifically, the detailed coupling between degradation mechanisms and battery usage is not fully understood, which impede lifetime improvements. This PhD thesis focuses on the said coupling by relating morphological and structural changes in Lithium-ion battery electrodes, measured with a number of different characterization techniques, to performance degradation observed during electrode cycling. It consists of six chapters as described below.

Chapters 1 and **2** furnish the motivation and a general introduction about the importance of the energy storage and the role played by lithium-ion batteries (LIBs) in our society. A thorough analysis of the state-of-the-art of LIB technology is presented, together with a full description of all solid-state components: cathode and anode materials, and carbon additive. Degradation mechanisms that affect the above mentioned materials are also listed but, as said before, a detailed correlation between these mechanisms and loss in performance is not fully understood yet. These chapters give a general idea of all the challenges encountered in the development and commercialization of LIBs materials, providing the context of this PhD thesis.

Chapter 3 is a collection of all the characterization techniques applied to the electrode materials and used to study degradation mechanisms in LIBs.

Chapter 4 describes the experimental setup used in this work, from cell design assembly, drying procedures and sample preparation for microscopy analysis.

Chapter 5 presents and discusses all the results obtained and published during this PhD project. It is divided in two sections which are focused on the characterization of laboratory and commercial LIBs. First section includes the analysis of degradation mechanisms which occur in a laboratory $LiFePO_4$/C cathode by different characterization techniques (**paper I – III**), and in a carbon black additive for high voltage batteries (**paper IV**). Second section is instead focused on the buildup of a combined Transmission Line Model (TLM) for Electrochemical Impedance Spectroscopy (EIS) characterization of commercial $LiFePO_4$/C 26650 cylindrical cells (**paper V**), and the analysis of aging mechanisms by low – voltage FIB/SEM tomography (**paper VI**).

Chapter 6 gives a conclusion and an outlook based on the presented results.

Introduction 2

2.1. The energy storage problem

Electricity is one of the dominant forms of energy used worldwide and the demand for it is increasing at a faster rate than the overall energy consumption. Approximately 68% of the today's electrical energy is supplied from fossil fuel, while the remaining part is supplied by nuclear (14%), hydro (15%) and renewable energies technologies (3%) [1]. However the environmental concerns over the use of fossil fuel, combined with their diminishing production expected in the next few decades, made the development and use of renewable energies rapidly grow in the last few years [1], [2]. Solar and wind power are among the most abundant and readily available renewable sources [1], [3] however the intermittent and unpredictable character of these sources (Fig. 2.1), in addition to the fluctuations in the supply of energy and load needed, creates imbalances within the system making grid integration challenging [1]–[4].

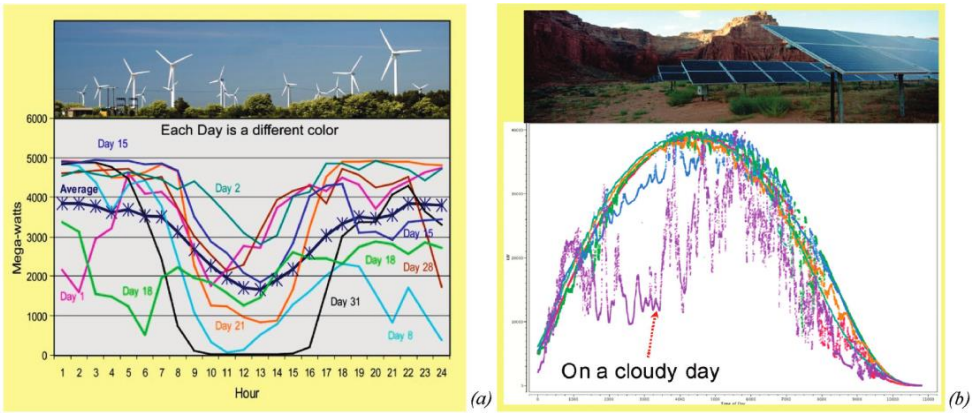

Figure 2.1. (a) Daily profiles of wind power projected by 7X output in April 2005 for the year 2011 in Tehachapi, California (Courtesy of ISO California). (b) 5 MW PV power over a span of 6 days in Spain (Courtesy of AES). Adapted with permission from [1]. Copyright © 2011 American Chemical Society.

The integration of Electrical Energy Storage (EES), generally using lead batteries, in an electric grid is often presented as a solution to the problem of intermittent renewables [2]. However lead batteries cannot stand high cycling rates or store large amounts of energy in a small volume so the development and implementation of new types of storage technologies become a crucial element in the management of energy from renewable sources [1], [5]. EES can be achieved converting electricity in another form of storable energy, and

transforming it back when needed, and many possible techniques have been explored: thermal, mechanical, chemical and electrochemical storage [2], [6]. For the large-scale system the energy is preferred to be stored as gravitational energy (hydropower), thermal energy, compressed air or chemical energy (flow batteries). In the small-scale systems the energy is instead stored as kinetic energy (flywheel), hydrogen (fuel cells) or batteries and supercapacitors [2], [6].

Fig. 2.2 shows a wide range of EES technologies and most of them are actually based on batteries: lead-acid, nickel-cadmium, nickel-metal hydride, nickel-iron, metal-air, sodium-sulphur, lithium-ion, etc. Batteries are portable devices, capable to deliver the stored chemical energy as electrical energy, often used in portable systems and could represent an excellent EES technology for the integration of renewable resources, because of many features: pollution-free operations, high round-trip efficiency, compact size, flexible power and energy characteristics [6]. Furthermore they represent a valid alternative to combustion engines because of their application in electric motors for sustainable vehicles, such as hybrid vehicles (HEVs) and full electric vehicles (EVs) [7]. On the other hand the main inconveniency is the high cost and their relatively low durability for large-amplitude cycling (from few hundreds to few thousands of cycles). The modularity and scalability of different battery systems provide the promise of a drop in costs in the coming years, making them more suitable for permanent applications [2], [6]. However reliability, cycle life and other important factors regarding batteries for automotive and stationary energy storage are still an issue and need to be improved [2], [6], [7].

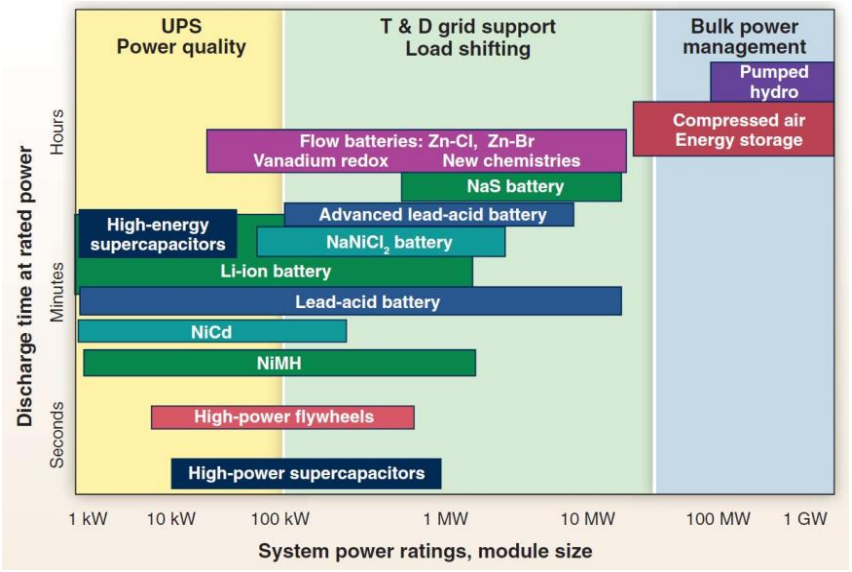

Figure 2.2. Comparison of discharge time and power rating for various EES technologies. The comparisons are of a general nature because several of the technologies have broader power ratings and longer discharge times than illustrated. [Courtesy of EPRI]. Reprinted with permission from [6]. Copyright © 2011 The American Association for the Advancement of Science.

2.2. Li-ion batteries

Rechargeable batteries plays an important role for various energy storage applications, and particularly appealing are the batteries with high specific energy, high rate capability, high safety and relative low cost [7]. Li-ion batteries (LIBs) are today the most promising candidates since they are light, compact and with a voltage of around 4 V. They also exceed by a factor of 2.5 most of the competing technology thanks to the high value of specific energy density (up to 200 W h kg^{-1}), as shown in Fig. 2.3 [6]–[9].

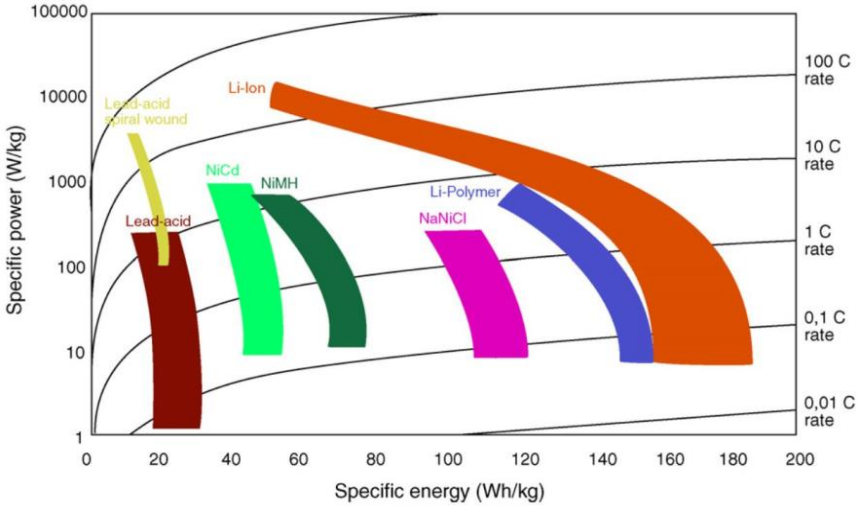

Figure 2.3. Ragone plot distribution of different electrochemical accumulators. Reprinted with permission from [9]. Copyright © 2006 Elsevier.

LIBs, in their most conventional structure, consist of a graphite anode (e.g. mesocarbon microbeads, MCMB), a lithium metal oxide cathode ($LiMO_2$, with M = Co, Ni) and a liquid electrolyte consisting of a solution of a lithium salt (e.g. $LiPF_6$) in a mixed organic solvent imbedded in a separator felt [8]. The two electrodes are Li-intercalation compounds, while the electrolyte in between the two electrodes allow Li ions to migrate from one electrode to the other (Fig. 2.4).

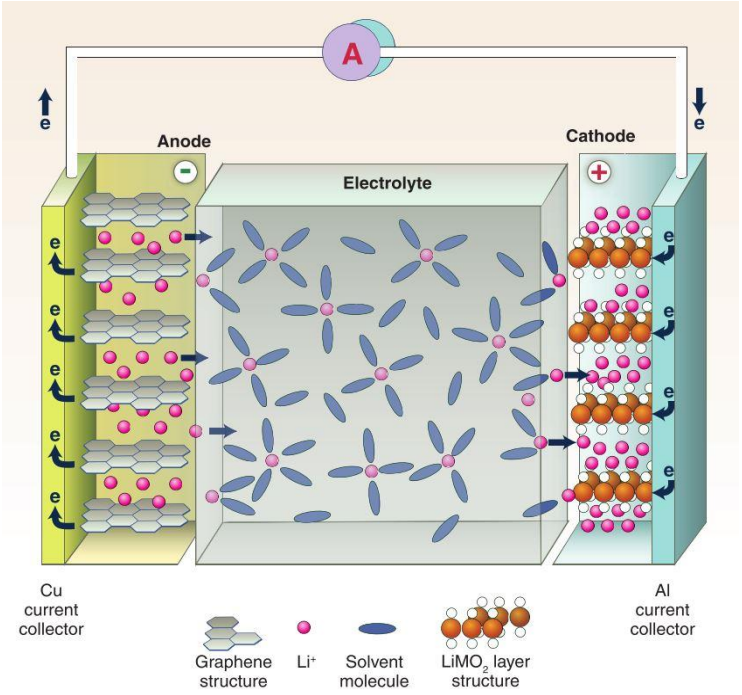

Figure 2.4. Schematic of a LIB. The negative electrode is a graphitic carbon that holds Li in its layers, whereas the positive electrode is a Li-intercalation compound – usually an oxide because of its higher potential – that often is characterized by a layered structure. Both electrodes are able to reversibly insert and remove Li ions from their respective structures. On charging, Li ions are removed or deintercalated from the layered oxide compound and intercalated into the graphite layers. The process is reversed on discharge. The electrodes are separated by a nonaqueous electrolyte that transports Li ions between the electrodes. Reprinted with permission from [6]. Copyright © 2011 The American Association for the Advancement of Science.

The LIBs technology was commercially introduced for the first time by Sony in the early 1990s [10]. This first battery contained a carbon negative electrode and a $LiCoO_2$ positive electrode and was assembled in the discharged state. The cell was then activated by charging, making the Lithium leaves the positive electrode material, raising its potential, and move to the carbon negative electrode, with its potential concurrently reduced. The cell can be represented as:

$$Li_xC_6 \text{ / organic solvent electrolyte / } Li_{1-x}CoO_2$$

And the two half – cell reactions as:

$$\textit{Anode:} \qquad 6C + xLi^+ + xe^- \leftrightarrow Li_xC_6 \tag{2.1}$$

$$\textit{Cathode:} \qquad LiCoO_2 \leftrightarrow Li_{1-x}CoO_2 + xLi^+ + xe^- \tag{2.2}$$

Which combined give the total cell reaction:

$$\textit{Cell reaction:}\quad LiCoO_2 + 6C \leftrightarrow Li_{1-x}CoO_2 + Li_xC_6 \qquad (2.3)$$

This Li-ion cell operates with 3.7 V at 25°C, has a capacity of about 150 A h kg^{-1} and a power over 200 W h kg^{-1} [1]. However this early Li-ion chemistries are relatively unsafe: the lithiated graphite electrode operates in fact at a potential close to that of metallic lithium, with a high risk of Li-dendrite growth and consequent electrical shorting. This, in presence of flammable organic electrolyte solvent could lead to heat generation and then fire. Furthermore, as mentioned in the previous paragraph, the production cost of these cells (acceptable for portable electronic applications) could be critical for scaled-up applications [1]. Extensive efforts have been made in the past decades to overcome barriers of various natures (safety, cycle life, cost, wide temperature operational range and materials availability) which still prevent this step. The main approach to improve safety is represented by the replacement of the organic carbonate liquid electrolyte with safer and more reliable solutions [8]. Replacement of graphite and lithium cobalt oxide electrodes is instead required in favor of alternative, higher capacity, higher power and lower cost anode and cathode materials [8].

2.3. Cathode materials

Lithium cobalt oxide, $LiCoO_2$ (theoretical specific capacity 140 mAh g^{-1}), is a layered oxide developed as cathode material for commercial LIBs but, because of the toxic and expensive cobalt, it has been mainly replaced today by manganese-based compounds and olivine lithium metal phosphates [8], [11].

Lithium manganese spinel $LiMn_2O_4$ seems to be a good candidate to substitute the high cost and partially toxic lithium cobalt oxide. The manganese oxide is in fact more available and environmental friendly. However its use is limited by some operational issues, such as manganese dissolution into the electrolyte at temperature higher than room temperature, that drastically reduce cycle life. This effect could be lowered by partial substitution of manganese ions with foreign ions [8], [12], [13] or surface modification by oxide coating [8], [14]. Two other promising materials in the manganese family are the spinel structure lithium nickel manganese oxide, $LiNi_{0.5}Mn_{1.5}O_4$, and the nickel manganese cobalt oxide (NMC), $LiNi_{1/3}Mn_{1/3}Co_{1/3}O_2$, that has a layered structure. Both materials arouse interest for high voltage battery applications since they are characterized by an operating voltage of 4.5 V and 3.8 V vs Li, and a theoretical specific capacity of 146 and 160-170 mAh g^{-1} [8], [11].

The olivine lithium metal phosphates ($LiMPO_4$, with M = Fe, Mn, Co), and in particular $LiFePO_4$ are considered as another highly interesting cathode materials for the new generation LIBs. Such an interest is motivated by a relative high specific capacity (170 mAh g^{-1}), good structural stability, lower cost than $LiCoO_2$ and higher safety because of the strong P – O bonds which reduce the risk of oxygen release with subsequent fire [8], [11], [15].

2.3.1. $LiFePO_4$

The phospho-olivine $LiFePO_4$ (LFP) was used as cathode material for LIBs for the first time in 1997 by J. B. Goodenough and thoroughly described by *Padhi et al* [16]. Since its discovery, LFP is considered as a promising choice for powering HEVs and EVs, since it is not expensive, non-toxic, environmental friendly and is characterized by a reversible lithium extraction/insertion at 3.5 V vs Li/Li^+ with a relative high theoretical capacity of 170 mAh g^{-1} [16]–[19].

$$LiFePO_4 \leftrightarrow Li_{1-x}FePO_4 + xLi^+ + xe^- \quad (2.4)$$

Eq. 2.4 shows the electrochemical reaction that describes the reversible extraction of Lithium from LFP. It occurs at a potential of 3.5 V, when cycled with very low current density, and the charge/discharge curve is characterized by a very flat plateau associated with the motion of a two-phase ($LiFePO_4/FePO_4$) interface on lithium extraction/insertion, as described by *Padhi et al* [16]. This (de)insertion process of lithium leads to a reversible phase transformation from triphylite ($LiFePO_4$) to heterosite ($FePO_4$), creating a disordered solid solution of $Li_{1-}xFePO_4$ proposed to follow different models, such as the "core-shell model" [16], or the "spinodal-decomposition model" [20] and the "domino cascade model" [21].

$LiFePO_4$, when cycled, has a practical capacity of 110 mAh g^{-1}, much lower than the theoretical capacity of 170 mAh g^{-1}, and *Padhi et al* [16] suggested that this difference comes from the poor lithium ion diffusion through the $LiFePO_4/FePO_4$ interface. A good way to circumvent this problem is reducing the particle size [22], since the smaller the particle size, the shorter the diffusion path of lithium ion in LFP, as well as making a porous structure to assure a larger specific surface area [23].

Another drawback of LFP is the low electronic conductivity but it could be improved by metal ions doping (such as Nb^{5+} 1 wt. % doping), coating the particles with carbon and addition of carbon particles [17].

2.3.2. Carbon additives

LiFePO4 is a poor electron conductor and the addition of an electronically conductive carbon additive is one of the most important aspects for the $LiFePO_4$ manufacturing in order to obtain satisfying electrode performance. These aspects explain why many different carbon additives are currently explored and optimized for improvements in LIBs performance. The most common carbon additives currently considered are carbon blacks (CBs), acetylene black, graphene, fibrous products and nanostructured carbon as carbon nanotubes (CNTs) and multi-walled carbon nanotubes (MWCNTs) [24]–[28].

Carbon black (CB) is considered member of an important family of carbon products, widely used as nano-material additive for LFP electrodes. They differ from diamond, graphite, cokes and charcoal for their composition, characterized by aggregates with complex, quasi-crystalline structure. These aggregates are usually composed by spheres (called primary "particles" or "nodules") fused together, which are the results of many graphene layers arranged concentrically [29].

2.3.3. Aging mechanisms in $LiFePO_4$/C cathodes

Cathodic materials such as composite $LiFePO_4$/C are known to be subjected to structural changes and mechanical stress upon cycling. The lithiation/delithiation process of the host structure leads to the molar volume change of the cathode material, creating changes in the crystal structure, and inducing mechanical stresses and strains, crack propagation and fractures, with consequent capacity loss [11], [30], [31]. Furthermore, olivine-type materials ($LiMPO_4$, with M = Fe, Mn, Co), in presence of HF, developed by liquid electrolyte decomposition, are subject to M dissolution [11], [32], [33]. Furthermore decomposition of electrolyte on the electrode surface can create passivating films with increased resistivity [34], [35].

These aging mechanisms can cause irreversible capacity fade because of loss of active materials, and could occur either during storage or cycling of the battery. In particular, during cycling, there are many factors that could accelerate degradation, such as utilization mode, temperature conditions, etc. [34].

The dispersion of the CB additive plays an important role for the improvement of the LFP/C electrode performance. Many numerical studies have been done in order to predict and optimize the LFP:CB ratio, and to obtain a more homogeneous distribution of CB network with less agglomeration of CB particles [36], [37], however not so many degradation studies have been performed that focuses on the CB network in a LFP/C battery.

2.4. Anode materials

Lithium metal would be an interesting LIBs anode material but, because of its predisposition to form dendrites, presents a high risk of short-circuit and it is not considered a safe material [11].

The first generation of commercial LIBs used in fact carbonaceous material as anode and in particular graphite (theoretical specific capacity 372 mAh g^{-1}), as already mentioned above, but also C-C composite, mesocarbon microbeads (MCMB), carbon nanotubes and carbon films [11], [38]–[41]. All these material intercalate/deintercalate lithium at a

potential very close to Li/Li^+ (less than 100 mV versus Li/Li^+ for graphite), still presenting risk of lithium depositing and short-circuit of the cell. They are also characterized by the formation of a solid electrolyte interphase (SEI) during the cycling of the cell, formed by electrolyte decomposition products at the electrode/electrolyte interface. Although this SEI layer would result in a loss of the cell voltage and reduction of active surface area of the anode, it will definitely improve the cycle life and the power rating of the battery because prevents graphite from further exfoliation, and electrolyte from further reduction and consumption of lithium [11], [38]–[41].

Another class of promising material for negative electrodes are lithium metal alloys, such as lithium-silicon (Li-Si) and lithium-tin (Li-Sn) alloys. They have a much higher specific capacity compared to graphite: 4000 mAh g^{-1} and 990 mAh g^{-1}, respectively. However their commercialization is still not feasible because of the large volume expansion-contraction during cycling, whose mechanical stress induce an accelerated degradation of the electrode with failure of the cell [8], [11], [39], [41].

With the research of new negatives electrode, new materials such as titanium oxide TiO_2 (TO) and lithium titanium oxide $Li_4Ti_5O_{12}$ (LTO) have been also explored. They have a specific capacity comparable (335 mAh g^{-1} for TO) or lower (170 mAh g^{-1} for LTO) than graphite, and a higher voltage level (1.5 V vs. Li), which will result in a lower specific energy. However interest toward TO and LTO is still motivated by many characteristics such as high cycling and thermal stability, no SEI formation and low risk of dendrites formation [8], [11], [39].

Carbonaceous materials, and graphite in particular, are however still the most used negative electrodes in commercial LIBs and degradation mechanisms that affect anode performance in commercial cells are studied in this manuscript.

2.4.1. Graphite

Graphite is one of the first used anodic materials for commercial LIBs, and it is still one of the most used [10]. It has a layered structure where the carbon atoms are sp^2 hybridized, arranged in a hexagonal pattern, forming graphene layers which are stacked in a staggered alternance, ABAB sequence, with a distance of 3.35 Å [10], [42], [43]. Graphite is anisotropic since it is a good thermal and electrical conductor within the layers, but poor perpendicular to the layers because they are linked by weak Van der Waals bonds [10], [42], [43].

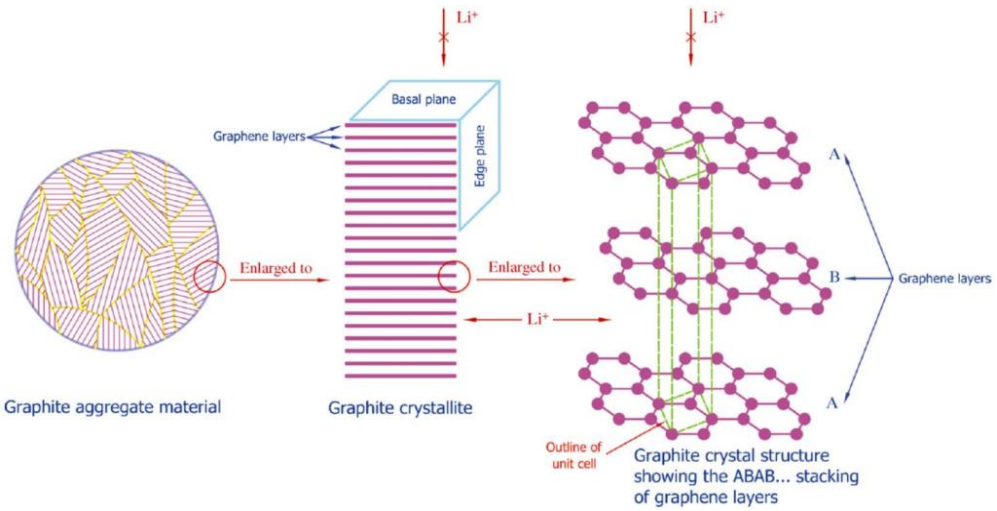

Figure 2.5. Relationship between a graphite aggregate material and its constituent graphite crystallites. Reprinted with permission from [43]. Copyright © 2010 Elsevier.

Lithium ions can intercalate between the graphene layers according to the electrochemical reaction:

$$6C + xLi^{+} + xe^{-} \leftrightarrow Li_xC_6 \tag{2.5}$$

With $0 < x < 1$ and a theoretical specific capacity of 372 mAh g^{-1}. The electrochemical intercalation of lithium into graphite occurs through different steps, each of them characterized by a different cell potential, as a function of the intercalation degree.

Graphite can also intercalate solvent molecules from the liquid electrolyte, together with lithium ions, causing large expansion along the c-axis and irreversible exfoliation into graphite flakes. This phenomena is generally avoided when the solvent decompose on the graphite surface, creating a solid electrolyte interphase (SEI), which prevent graphite from further intercalation of solvent molecules [43]–[45]. The solvent choice is then a crucial part for graphite usage as negative electrode, and ethylene carbonate (EC) – based electrolyte are always preferred to propylene carbonate (PC) – based ones because of their predisposition to form the SEI layer [43]–[45].

2.4.2. Aging mechanisms in graphite anodes

The first "degradation mechanisms" that occurs in a graphite anode is the formation of a SEI layer at the electrode/electrolyte interface, after decomposition of electrolyte. The SEI layer consumes in fact the active lithium, consequently reducing the surface area of active material and increasing impedance of the anode. It could form at both anode and cathode, but is more dominant on the anode side because of the lower potential (vs Li/Li^{+}) [11], [34].

The SEI layer, once formed in the initial cycle, limits the further reduction of electrolyte and prevents the anode surface from corrosion, being permeable to lithium ions. However, upon cycling, the SEI layer could grow, increasing the internal resistance and causing capacity fade [11], [34]. SEI layer dissolving is also a degradation mechanism that affect graphite electrode, since it causes also intercalation of solvent molecules in between graphene layers, with consequent exfoliation and loss of active material, and lithium plating on electrode surface, with loss of active lithium.

Characterization Techniques 3

In this chapter are listed all the routine techniques used to test and study the performance of LIBs. Furthermore, some advanced characterization methods to investigate the degradation processes that occur in the electrode materials are presented. They include mainly electrochemical and microscopic techniques. Before introducing the various techniques a brief overview of electrochemical cell electrode dynamics is presented.

An electrochemical cell usually consists of a working electrode (WE) and a counter, or auxiliary, electrode (CE) separated by an electrolyte (two-electrode configuration). The working electrode (WE) is usually an electrode where the reaction of interest is occurring (i.e. $LiFePO_4$ and carbon in this thesis project). The counter electrode (CE) is used to close the current circuit in the electrochemical cell and its surface area need to be similar to, or higher, than the area of the WE in order to not be the limiting factor in the kinetics of the investigated electrochemical processes. The cells are characterized by an open circuit voltage (OCV) which is the potential difference between WE and CE. The OCV depends on the used electrode materials. In studying the dynamics of the WE, a reference electrode (RE) helps separating the contribution of WE from CE (three-electrode configuration). The insertion of a RE permits to control either the current (or the potential) while measuring the single electrode potential (or current). An electrochemical cell can be divided in two half cells, where a redox reaction occurs (reaction 3.1), and the potential of each half cell, at the OCV condition, is governed by Nernst equation (Eq. 3.2).

$$ox + ne^- \leftrightarrows red \tag{3.1}$$

Where *ox* is the oxidized specie, *red* is the reduced specie, and *n* is the number of transferred electrons.

$$E = E^{0'} + \frac{R_g T}{nF} \ln\left(\frac{C_{ox}}{C_{red}}\right) \tag{3.2}$$

Where *E* is the potential, $E^{0'}$ is the formal potential, which includes adjustment for the activity coefficients of *ox* and *red*; R_g is the gas constant, *T* the temperature, *F* the Faraday constant and C_i is the bulk concentration of each specie.

Once the battery is subjected to charge/discharge cycling, its voltage ($E_{battery}$) will deviate from OCV because of overvoltages (η) due to ohmic resistances, electrochemical reactions and diffusion processes. The battery voltage during discharge (schematically represented in Fig. 3.1) could be expressed by Eq. 3.3 [46]:

$$E_{battery} = E_{OCV} - IR - \eta_{reaction} - \eta_{diffusion} \tag{3.3}$$

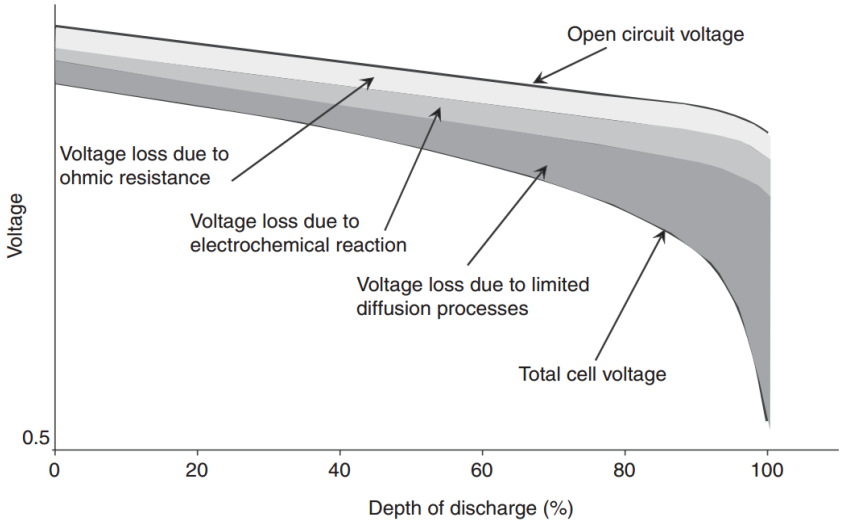

Fig. 3.1. Schematic of a discharge curve of a battery with different voltage losses starting from the oen-circuit voltage (OCV) and finally resulting in the total cell voltage. Reprinted with permission from [46]. Copyright © 2009 Elsevier.

The Ohmic voltage drop *IR* is caused by the ohmic resistances of all elements in the current path (poles, plate connectors, grids, electron conductivity in the active material and ionic conductivity in the electrolyte).

The reaction overvoltage $\eta_{reaction}$ is caused by the reaction charge-transfer resistance and it is described by the Butler-Volmer equation (Eq. 3.4) [46]:

$$I = j_0 A \left(\frac{C_{ox}}{C_{ox}^0} \cdot exp\left(\frac{\alpha \cdot n \cdot F \cdot \eta_{reaction}}{R \cdot T} \right) - \frac{C_{red}}{C_{red}^0} \cdot exp\left(\frac{-(1-\alpha) \cdot n \cdot F \cdot \eta_{reaction}}{R \cdot T} \right) \right) \tag{3.4}$$

where I is the battery current, j_0 the normalized reaction current, A the active inner electrode surface, α the symmetry coefficient for the reaction between charging and discharging, n the number of electrons involved in the reaction per molecule of the active material, F the Faraday constant, R the general gas constant, T the absolute temperature, $\eta_{reaction}$ the overvoltage caused by the electrode reaction, and C_{ox} and C_{red} are the concentration of the oxidizing and reducing ions from the electrolyte and $C_{ox}^{\ 0}$ and $C_{red}^{\ 0}$ the respective equilibrium concentrations of the ions in the electrolyte.

The diffusion overvoltage $\eta_{diffusion}$ occurs if concentration gradients in the electrolyte occur. It is proportional to the logarithm of the ratio between the actual ion concentration C and the equilibrium concentration C_0 (Eq. 3.5) [46].

$$\eta_{diffusion} = \frac{RT}{nF} \ln\left(\frac{C}{C_0} \right) \tag{3.5}$$

3.1. Galvanostatic Cycling with Potential Limitation (GCPL)

From the analysis of the charge/discharge curves, the total capacity of a battery (or the WE in a three-electrode setup measurement) could be calculated. The capacity is defined as the total amount of electric charge [Ah] delivered by the electrochemical cell under certain conditions. Many parameters could affect it, such as applied current rate (C-rate), temperature and upper and lower cutoff voltage. Furthermore, the analysis of the coulombic efficiency (η_{Ah}) gives useful information about the state-of-health (SOH) of the battery and it is defined as the ratio between discharge and charge capacity (Eq. 3.6).

$$\eta_{Ah} = \frac{discharge\ Ah}{charge\ Ah} \tag{3.6}$$

LIBs are often subjected to relative fast degradation (depending on the investigated material) which would first results in a capacity fade over a range of few hundreds or thousands of cycles. The study of changes in performance of a LIB has been then investigated by galvanostatic cycling with potential limitation (GCPL) under different conditions (different C-rate, and cutoff voltages) and in different configurations (two- and three-electrode setups).

GCPL measurements were performed using a Biologic VMP3 with Potentiostat/Galvanostat (Pstat/Gstat) boards.

3.2. Electrochemical Impedance Spectroscopy (EIS)

Electrochemical impedance spectroscopy (EIS) is one of the most interesting techniques to study an electrochemical system. It is a powerful and non-invasive tool to measure the dielectric and transport properties of materials, investigate interfaces and mechanisms o electrochemical reactions and explore the properties of porous electrodes. In an EIS measurement the response of a system, subjected to a small amplitude sinusoidal signal of either current or potential in a frequency range 100 kHz – 1 mHz, is studied. The amplitude of the applied signal is usually really small, about 10 mV in a potentiostatic EIS measurement (PEIS) or a small percentage of the d.c. current in a galvanostatic EIS measurement (GEIS), and a response in a.c. current or voltage is obtained from the system. If the applied perturbation is sufficiently small, will ensure a linear voltage-current relation and a sinusoidal response at the same measured frequency but shifted of a certain phase angle. The excitation voltage and the response current can be expressed by eq. 3.7 and 3.8.

$$E(t) = E_0 \cdot sin(\omega t) \tag{3.7}$$

$$I(t) = I_0 \cdot sin(\omega t + \varphi) \tag{3.8}$$

The impedance response Z is calculated according the generalized Ohm's law, eq. 3.9.

$$Z = \frac{E(t)}{I(t)} = \frac{E_0 \cdot sin(\omega t)}{I_0 \cdot sin(\omega t + \varphi)} \tag{3.9}$$

Where E_0 and I_0 are the peak amplitude of the a.c. potential and current, ω is the angular frequency, t is the time and φ is the phase shift, related to the frequency f through $\omega = 2\pi f$.

Since most of the electric components (i.e. capacitors or inductors) give a response which is not in phase with the stimulus, representing the impedance Z as a vector (eq. 3.10) in a complex plane is a good way to deal with the phase shift φ.

$$Z(\omega) = Z_{re} + (-jZ_{im}) \tag{3.10}$$

This complex plane, called Nyquist plot, shows the real part Z_{re} of the impedance in the abscissa and the imaginary part Z_{im} in the ordinate. By convention the imaginary part is represent with the opposite sign. The Bode plot is also a useful graphical representation, where the modulus of the impedance (or only real or imaginary part) and the phase angle are plotted as function of the logarithm of the frequency. Fig. 3.2 illustrates an example of Nyquist (Fig. 3.2a) and Bode plot (Fig. 3.2b).

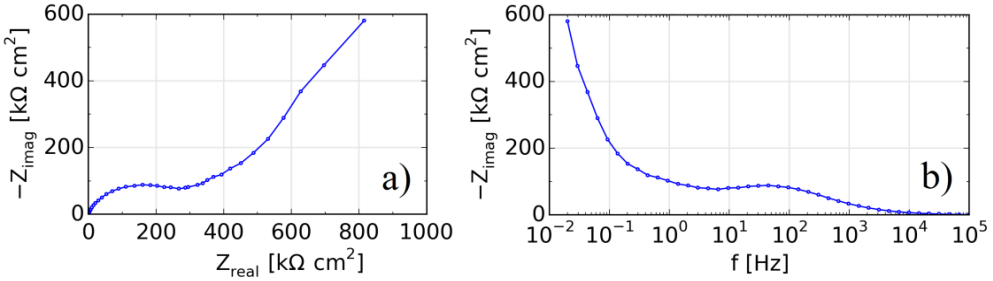

Figure 3.2. Example of a (a) Nyquist and (b) Bode plot.

The interpretation of the results of an EIS spectrum, or modelling, becomes important for the distinction of the different processes that occur in an electrochemical system. Many processes have in fact distinctive and characteristic impedance frequencies, so that an EIS spectrum could be modeled by an equivalent circuit model (ECM) in order to distinguish and calculate several parameters from adsorption processes, charge-transfer resistances, and mass transports.

EIS measurements were performed using a Biologic VMP3 with Pstat/Gstat boards.

3.2.1. EIS Modelling

As already mentioned above the modelling of an EIS spectrum assumes an important role for the thorough understanding of the polarization processes occurring in an electrochemical system and the subsequent parameters calculation. The goal of EIS modelling consists in the building of an ECM which accurately represents the investigated electrochemical system. Here below a number of elements usually used to build a full ECM are described (Table 3.1) and discussed.

Table 3.1. List of elements used to build an equivalent circuit model (ECM).

Element	Description	Impedance Z
R	Resistor	R
C	Capacitor	$\frac{1}{j\omega C}$
Q or CPE	Constant Phase Element	$\frac{1}{Q_0(j\omega)^n}$
RC	Resistor – Capacitor in parallel	$\frac{R}{1+R\cdot j\omega C}$
RQ	Resistor – CPE in parallel	$\frac{R}{1+R\cdot Q_0(j\omega)^n}$
W	Semi – infinite Warburg	$\left(\frac{2}{\omega}\right)^{1/2}\cdot A_w$
$W_{GFS,1D}$	1D General Finite Space Warburg Element [used in **papers II** and **V**]	$R_w\frac{\coth[(j\omega\tau_w)^{n_w}]}{(j\omega\tau_w)^{n_w}}$
$W_{GFS,2D}$	2D General Finite Space Warburg Element [used in **paper V**]	$R_w\frac{I_0[(j\omega\tau_w)^{n_w}]}{(j\omega\tau_w)^{n_w}\,I_1[(j\omega\tau_w)^{n_w}]}$
Randles circuit	($RW_{GFS,1D}$) – Q in parallel [used in **papers II** and **V**]	$\left\{\left[R_w\frac{\coth[(j\omega\tau_w)^{n_w}]}{(j\omega\tau_w)^{n_w}}+R\right]^{-1}+Q_0(j\omega)^n\right\}^{-1}$
Randles circuit	($RW_{GFS,2D}$) – Q in parallel [used in **papers V**]	$\left\{\left[R_w\frac{I_0[(j\omega\tau_w)^{n_w}]}{(j\omega\tau_w)^{n_w}\,I_1[(j\omega\tau_w)^{n_w}]}+R\right]^{-1}+Q_0(j\omega)^n\right\}^{-1}$
Generalized TLM	Transmission line model [used in **papers II** and **V**]	$\frac{R_{el}*R_{ion,L}}{R_{el}+R_{ion,L}}\left(L+\frac{2\lambda}{\sinh(L/\lambda)}\right)+$ $+\lambda_{TLM}\frac{R_{el}^2+R_{ion,L}^2}{R_{el}+R_{ion,L}}\coth(L/\lambda_{TLM})$
Simplified TLM	Transmission line model [used in **papers II, IV** and **V**]	$\lambda_{TLMs}\,R_{ion,L}\coth(L/\lambda_{TLMs})$

The ohmic resistor R is the simplest element, independent of frequency, and has no complex part, as shown in the formula to calculate Z in table 3.1. It is used to model series resistance and it coincides with the intercept in the abscissa in a Nyquist plot (Fig. 3.3a).

The impedance of an ideal capacitor C has no real part (Table 3.1) .It can be used to represent non-Faradaic processes such as charging of interfacial double-layers and in a Nyquist plot is represented by a vertical line (Fig. 3.3a).

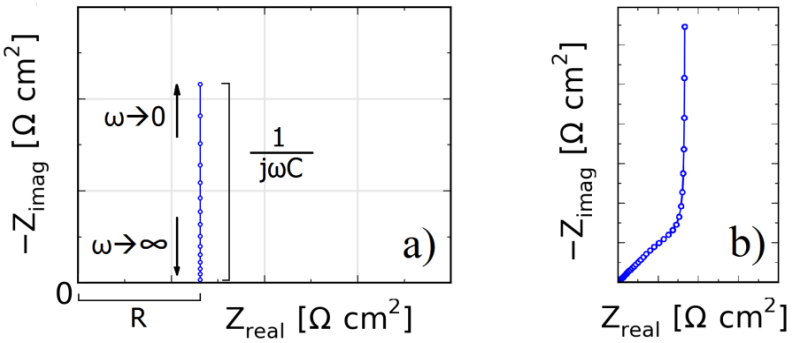

Figure 3.3. Impedance simulation of a (a) Capacitor and (b) Finite Space Warburg Element.

The Warburg element W is often used to model semi-infinite linear diffusion, when redox species diffuses to and from an electrode surface where charge-transfer may take place. In a Nyquist plot it is described by a 45° line. The general finite space Warburg W_{GFS} describes instead the diffusion in a situation where there is an impermeable boundary blocking for the diffusion species, like in a solid intercalation particle of a storage device (i.e. LIB), where there is a limited space for intercalating ions. It could use a 1D geometry and describe a diffusion process along a one-dimensional diffusion path $W_{GFS,1D}$ (like in $LiFePO_4$), or a 2D geometry which describes diffusion along radial axis, as usually occurs in the layered-structure electrode (e.g. graphite, $LiCoO_2$). In a Nyquist plot is represented by a 45° line, followed by a vertical tail (Fig. 3.3b).

The constant phase element Q has no direct electrical equivalent and its physical interpretation depends on the exponent n. For values n = 1, the Q element is equal to a capacitor, while for n = 0 it is a resistor. In general it is used to model processes (such as charging) that occur at a rough electrode surface.

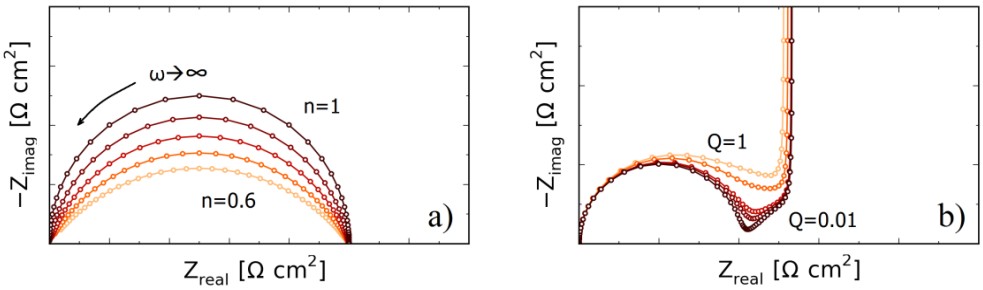

Figure 3.4. Impedance simulation of a (a) RQ element and (b) Randles circuit.

The RC (or RQ) element is a circuit in which a resistor and a capacitor (or constant phase element) are connected in parallel and it is usually used to model a double-layer capacitance which takes place at an interface, in parallel connection with a charge-transfer resistance correlated to a Faradaic reaction. It is represented by a semicircle (more or less depressed for a RQ element, depending on n values) in the Nyquist plot (Fig. 3.4a).

The Randles circuit consists of a resistor R and a Warburg element W (in series), connected in parallel with a constant phase element Q. It is usually used to model a double layer capacitance at an interface, connected in parallel with a charge-transfer resistance associated with a Faradaic reaction and then followed by (solid-state) diffusion. Fig. 3.4b shows a simulation of a Randles circuit in a Nyquist plot. Two different kind of Randles circuit have been used (one with $W_{GFS,1D}$ and one with $W_{GFS,2D}$) and implemented in a Transmission Line Model (TLM), as described in sections 3.2.2 and 3.2.3.

3.2.2. The Transmission Line Model (TLM) – Generalized

The state of the art of EIS, used as tool to study aging mechanisms in porous electrodes, started to include in the last decades the use of Transmission Line Model (TLM) to study the response of porous electrodes, usually infiltrated by liquid electrolyte [47]–[50]. The importance of these TLMs resides in the calculation of important parameters such as ionic resistance in the infiltrated pores $R_{ion,L}$ and the electronic resistance in the porous materials R_{el}. The model assumes cylindrical pores with length L filled with the electrolytic solution and oriented perpendicular to the current collector (Fig. 3.5a).

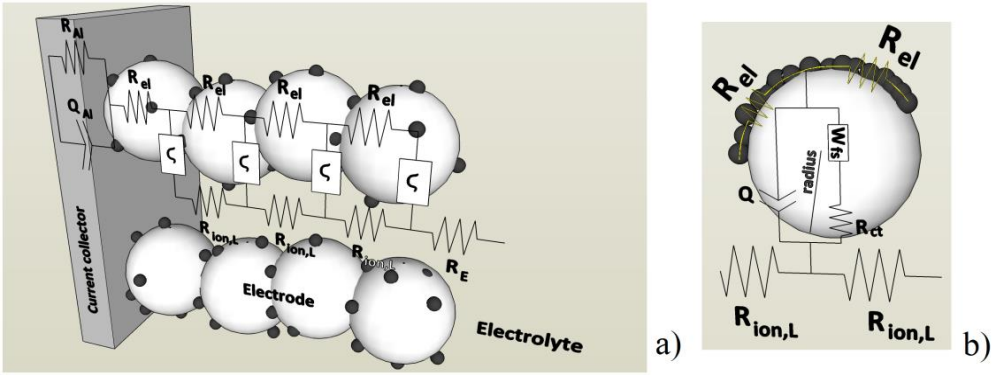

Figure 3.5. (a) Generalized Transmission Line Model, (b) Randles circuit used to model electrode/electrolyte interface with Li^+ diffusion (Warburg General Finite Space element, $W_{GFS,1D}$) within a particle with radius r. The Randles circuit resembles the element ς in (a). The yellow resistors in (b) model the resistivity along the electron pathway on the surface of the LFP particles. Adapted from **paper V**.

$R_{ion,L}$ is the resistance associated with Lithium ions traveling in the pores. In this project the TLM is applied to a carbon coated $LiFePO_4$ (LFP) electrode, then R_{el} is the resistance associated with electrons traveling in the surface coating. The equivalent circuit element ζ, usually referred to the surface impedance in the context of TLM, which models the impedance of the electrode/electrolyte interface, in this case include the diffusion of lithium ions inside the LFP particles. ζ consists of a charge transfer resistance R_{ct} in parallel with a constant phase element Q modeling the apparent double layer capacitance. Additionally R_{ct} is in series with a General Finite Space Warburg element $W_{GFS,1D}$ which models the impedance associated with lithium ion solid state diffusion (Fig. 3.5b). The electronic resistance is often assumed to be much lower than the ionic resistance of the solution (R_{el}<<$R_{ion,L}$) resulting in a simplified transmission line model where R_{el} is omitted [51], [52]. A generalized TLM [49], [53], [54] is often used in this work in order to reveal non-negligible R_{el} values.

The impedance for the generalized TLM model is:

$$Z_{TLM} = \frac{R_{el}*R_{ion,L}}{R_{el}+R_{ion,L}}\left(L + \frac{2\lambda}{\sinh(L/\lambda)}\right) + \lambda_{TLM}\frac{R_{el}^2+R_{ion,L}^2}{R_{el}+R_{ion,L}}\coth(L/\lambda_{TLM}) \qquad (3.11)$$

With:

$$\lambda_{TLM} = \sqrt{\zeta/\left(R_{el}+R_{ion,L}\right)} \qquad (3.12)$$

As mentioned above the electrode/electrolyte interface is modeled with the Randles circuit ζ which includes the charge transfer resistance R_{ct}, a constant phase element (CPE) Q and the general finite space Warburg element $W_{GFS,1D}$. The latter element models a diffusion process along a one-dimensional diffusion path terminated by an impermeable boundary [55]–[57], having the impedance:

$$Z_{WGFS,1D} = R_w\frac{\coth[(j\omega\tau_w)^{n_w}]}{(j\omega\tau_w)^{n_w}} \qquad (3.13)$$

with the time constant:

$$\tau_w = \frac{r^2}{D} \qquad (3.14)$$

R_w is polarization resistance, n_w is an exponent ($0<n_w<0.5$), r is the particle radius and D is the diffusion coefficient of Lithium ion within $LiFePO_4$.

The units of R_{ct} and C_{dl} in the TLM are respectively Ωcm^3 and Fcm^{-3} and, in order to be converted in the more usual Ωcm^2 and Fcm^{-2}, need to be divided and multiplied respectively by the cylindrical pore length L (expressed in cm). The effective double layer capacitance C_{dl} is calculated according to [58] using the expression:

$$C_{dl} = Q^{1/n} \left(R_e^{-1} + R_t^{-1}\right)^{(n-1)/n} \quad (3.15)$$

where Q is the CPE, n the exponent of the CPE, R_e is the ohmic resistance and R_t the resistance associated with the CPE.

Fig. 3.6 shows a simulation of the generalized TLM, varying values for $R_{ion,L}$ and R_{el}.

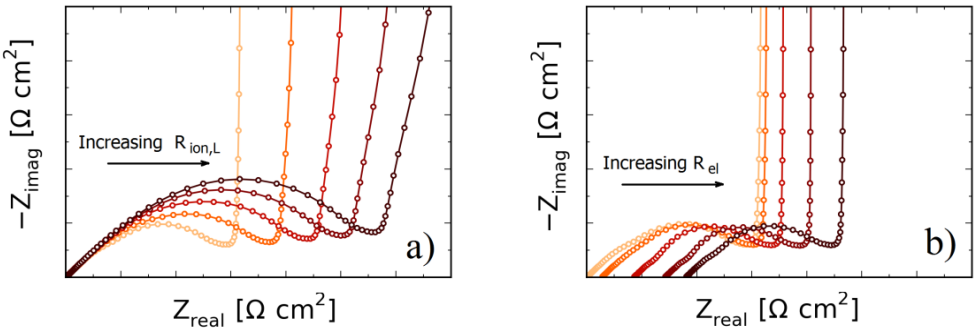

Figure 3.6. Impedance simulation of the generalized TLM varying values of (a) $R_{ion,L}$ and (b) R_{el}

3.2.3. The Transmission Line Model (TLM) – Simplified

In the case of a negligible R_{el}, a simplified version of the TLM could be used. Equation 3.11 is then reduced to:

$$Z_{TLMs} = \lambda_{TLMs} R_{ion,L} \coth(L/\lambda_{TLMs}) \quad (3.16)$$

With:

$$\lambda_{TLMs} = \sqrt{\zeta/R_{ion,L}} \quad (3.17)$$

This is usually the case of a highly electron conductive electrode, such as the graphite one.

It is also important to remember that in the case of a graphite (layered-structure electrode) the general finite space Warburg element has a 2D geometry and describes a two-dimensional diffusion path, $W_{GFS,2D}$ [55]–[57] with the impedance:

$$Z_{WGFS,2D} = R_w \frac{I_0[(j\omega\tau_w)^{n_w}]}{(j\omega\tau_w)^{n_w} I_1[(j\omega\tau_w)^{n_w}]} \quad (3.18)$$

where I_0 and I_1 are modified zero and first-order Bessel functions of the first kind.

3.3. Focused Ion Beam/Scanning Electron Microscopy (FIB/SEM)

The FIB/SEM is one of the most interesting electron microscopes, since it is a dual platform system that includes an ion column (FIB) and a scanning electron microscope (SEM). This combination allows cross-section sample imaging with the SEM as the ion beam mills normal to the surface.

Figure 3.7 shows a typical configuration for a FIB/SEM, where is possible to notice a vertical electron column and a tilted ion column (54°). In this case the specimen stage will also be tilted at 54° to mill normal to the specimen surface.

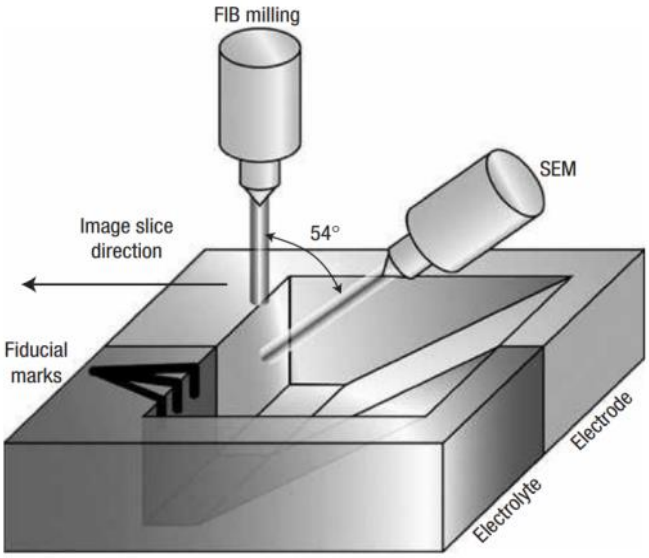

Fig. 3.7. Schematical representation of a FIB/SEM. Adapted with permission from [59]. Copyright © 2006 Nature Publishing Group.

The FIB/SEM is an instrument that uses a focus beam of ions (usually Gallium ions) and, unlike an electron microscope, is a destructive technique. The FIB system is often used for its sputtering capability and combined with an SEM forms a dual-beam platform that provides enhanced capabilities and could be used for tomographic analysis and 3D reconstruction of porous electrodes [60].

In this work FIB tomography and SEM imaging was carried out on a Zeiss 1540XB CrossBeam microscope, using a lateral E-T (Everhart-Thornley) detector and an In-lens detector.

3.3.1. The Scanning Electron Microscope (SEM)

The scanning electron microscope (SEM) is considered to be one of the most poweful instrument for morphological analysis and chemical composition characterization. It operation principle is based on the scanning of a specimen with a focused beam of electrons, and the imaging through the acquisition of signals produced by the interaction of electrons with it. The SEM mainly consists of two parts, the microscope column and the specimen chamber [61].

1. **Microscope column.** On top of the microscope column an electron gun is located. It purpose is to generate a stable electron beam with high current, adjustable energy and small energy dispersion. Many SEM use tungsten or lanthanum hexaboride cathodes, but modern microscopes also use field emission sources. Down through the colum there are also two pairs of alignment coil (for beam deflection), two condenser lens, the objective lens and the apertures.
2. **Specimen chamber.** It is located at the bottom of the microscope column and consists of the specimen holder, a stage (able to move in x,y,z direction, tilt and rotate) and the detectors for the different signals generated by interaction of electrons with the specimen.

Both microscope column and speciment chamber should be evacuate with a high vacuum pumps, in order to reduce interaction of electron beam with gas molecules [61].

3.3.2. Interaction of the electrons with the specimen

Once the specimen has been hit by the electron beam, this will result in a variety of interactions that could be divided in two main categories: elastic and inelastic interactions.

Elastic interactions are those resulting from collision of electrons that are deflected by the specimen atomic nucleus with a neglectable energy loss an a wide angle. All the electrons elastically scattered with an angle of more than 90° could be categorized as a backscattered electron (BSE), and they yield a useful signal for imaging the sample.

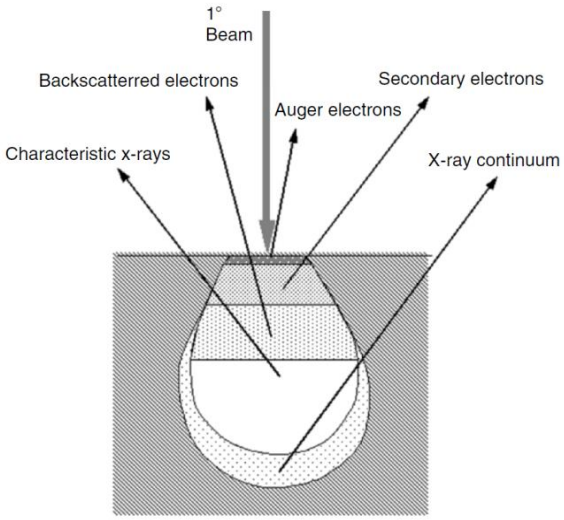

Fig. 3.8. Illustration of several signals generated by the electron beam–specimen interaction in the scanning electron microscope and the regions from which the signals can be detected. Reprinted with permission from [61]. Copyright © 2006 Springer.

If the collision occurs with a transfer of energy from the primary beam to the specimen atoms, this is the case of an inelastic interaction. This energy loss usually depends on the specimen electrons excitation and their binding energy to the atoms. Electrons excitation leads to the generation of secondary electrons (SE) that will be used for imaging as well. Furthermore, a lot of other signals, such as characteristic x-rays, Auger electrons and cathodoluminescence, are produced. This is due to the fact that most electrons penetrate into the sample for a huge distance before collide with an atom creating a zone of primary excitation (or interaction volume) from which the above mentioned signals are generated (Fig. 3.8). The size and shape of this region depends on beam elecron energy and the atomic number. It is usually teardrop shaped for low atomic number and hemispherical for specimens with high atomic number. Beam energy will instead affect depth of penetration [61].

3.3.3. Low-Voltage Scanning

This technique was first used and fully described by Thydén et al. [18] to identify percolation in SOFC anode Ni-network and in this work it has been applied for the first time in combination with a FIB for the 3D electron percolation analysis of a CB additive in a laboratory $LiFePO_4$/CB positive electrode.

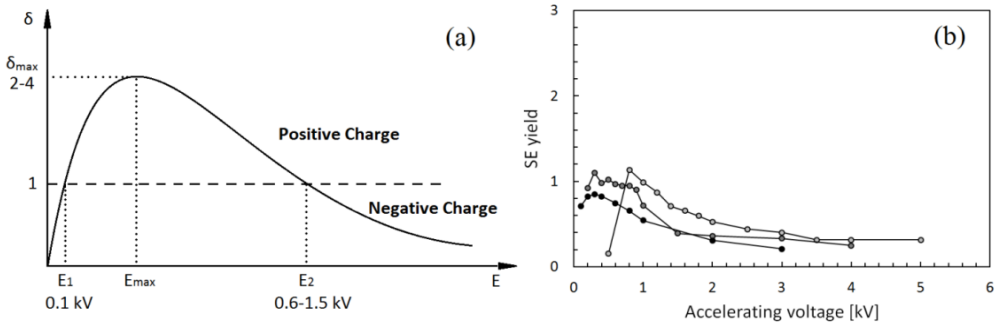

Figure 3.8. a) General SE yield curve in the low-voltage range and b) SE yield for carbon according to data compiled by D.C. Joy [62]. Reproduced from **paper I**.

The theory behind the low-voltage scanning is based on the interactions of the electron beam with different samples when the acceleration voltage approaches low values (1 kV). When the electron beam hits a sample, a variety of elastic and inelastic scattering of the electrons occurs, resulting in backscattered and secondary electrons respectively (BSE and SE). The SEs have by definition energies <50 eV and their detection gives useful information about the material properties. At such low voltage many materials have in fact a SE yield different than 1 [19], [20], resulting either in positive or negative charges that occur at the sample surface when imaged (Fig.3.9). If the material is not conductive enough, or not electron connected to the ground, will not be able to dissipate the charge to the ground. The In-lens detector, situated in the electron column, detects low energy electrons very efficiently due to the beambooster of the GEMINI column (Carl Zeiss, Germany) [21], acting as a low energy filter for the E-T detector, such that it primarily detects higher energy electrons. According to this the contrast changes, due to induced charging effects, are almost exclusively seen in the In-lens detector images.

3.4. Transmission Electron Microscopy (TEM)

The Transmission Electron Microscopy (TEM) is a powerful technique whereby an electron beam is transmitted through an ultra-thin sample, interacting with the specimen when passing through it. A TEM is similar to an optical microscope but the illumination system is replaced by an electron beam, while the glassy lens is replaced by electromagnetic lens in a high-vacuum column. The electrons are generated by either a thermionic filament or a field emission gun, then accelerated through a voltage of few hundreds of keV and condensed to a narrow and parallel beam by a condenser lens system. The electron beam hit the sample and most of the electrons are transmitted. The transmitted electron beam passes through the objective lens and an image, together with a diffraction pattern in back focal plane, are produced. The electron beam in the TEM is focused by electromagnetic lenses and the resolution of the TEM is limited not only by the diffraction but also by aberrations, which are intrinsic artefact of the electromagnetic lenses.

3.4.1. Scanning Transmission Electron Microscopy (STEM)

The Scanning Transmission Electron Microscopy (STEM) is a combination of both the SEM and the TEM and, thanks to the use of deflection coils, permits a high resolution scanning with a focused electron probe across the surface of a thin specimen. The rastering of the beam across the sample makes these microscopes suitable for analytical techniques such as mapping by energy dispersive X-ray (EDX) spectroscopy, electron energy loss spectroscopy (EELS) and annular dark-field imaging (ADF).

In this work, STEM imaging (bright-field, high-resolution, and high annular angle dark-field imaging) of few specimens was performed on a JEOL JEM 3000F equipped with a 300-kV field emission gun, high annular angle dark-field (HAADF) STEM detector.

Cell Designs and Battery Assembly 4

In this chapter are shown the different cell designs used to characterize the different electrode materials and a brief overview on the battery assembly procedures.

4.1. EL – CELL (Three-electrode setup)

The ECC-Combi test cell with reference eletrode (EL-CELL GmbH) is a standard test cell, hermetically sealed, suitable for the characterization of LIBs electrode materials in aprotic environment. Fig 4.1(a,b) show a schematic representation and all the components of the ECC-Combi. This particular cell allows the insertion of a reference electrode (RE) in contact with the electrolyte filled separator, placed in the sandwich working electrode (WE) – counter electrode (CE), through the use of a PEEK sleeve (Fig. 4.1b). The importance of having a RE, already discussed in section 3.1, resides in the resolution of working and counter electrodes potential in a GCPL analysis, for a better tracking of the single electrode overpotentials, and in the resolution of single electrode impedance in an EIS analysis.

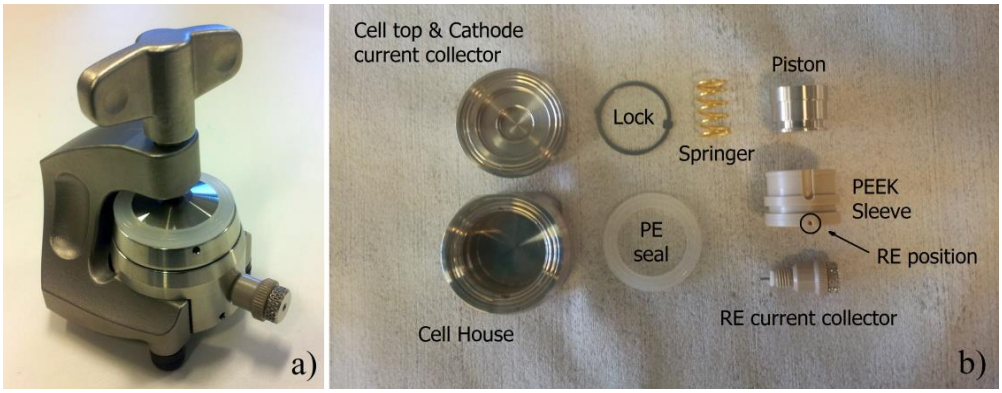

Fig. 4.1. Image of an (a) assembled and (b) de-assembled EL-CELL.

The position of RE becomes then important, since it needs to be placed at same distance from WE and CE. The cell is assembles in an Ar-filled glovebox, to avoid any H2O or O2 contamination, inserting first the lithium metal (RE) in the PEEK sleeve. A lithium metal disk electrode (CE, Ø = 18mm) is then attached to the bottom of the cell house (made of stainless steel 316L) which works as current collector for the CE. A glass fiber separator disk (Ø = 18mm, thickness = 1.55mm), soaked with 200 µl of the electrolyte solution, is placed on top of the CE and finally the WE on top closes the sandwich. A stainless steel

piston, working as current collector for the WE, presses the sandwich and the cell house is after closed and sealed.

The ECC-Combi is then tested using a Biologic VMP3 with Potentiostat/Galvanostat (Psta/Gstat) boards, connecting two channels of the potentiostat in stack mode. Channel 1 functions as a normal two-electrode setup, and controls the current and the potential of the cell, while channel 2 reads the potential difference between WE and RE, and between CE and RE. Thanks to the stack mode configuration, a resolution of the single electrodes impedance is also possible.

4.2. Pouch Cell (Two-electrode setup)

The pouch cell is one of the simplest two-electrode configurations for testing of battery electrode materials. Fig. 4.2 shows a typical pouch cell. The external case consists of an aluminum laminated film foil, folded on itself and sealed on one side. Two strips of aluminum and copper foil are used as current collector for positive and negative electrode respectively. The full battery is then assembled in an Ar-filled glovebox inserting a lithium metal foil (CE) in contact with the copper trip, a glass fiber separator (from Whatman) soaked with 200 µl of electrolyte solution, and the WE in contact with the aluminum strip. The cell is finally sealed, under vacuum, to remove the Ar inside the pouch cell.

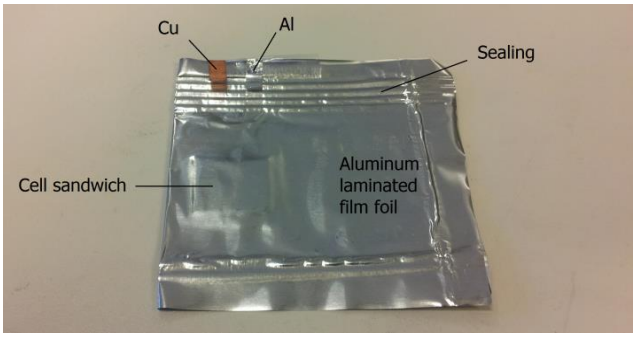

Fig. 4.2. Image of an assembled pouch cell.

4.3. Commercial 26650 Cylindrical Cell (Two-electrode setup)

In this work commercial $LiFePO_4$/C 26650 cylindrical cells (26650CC) are tested (in two-electrode configuration) and aged for several cycles to observe capacity fading. Fig. 4.3 shows a schematic representation of 26650CC.

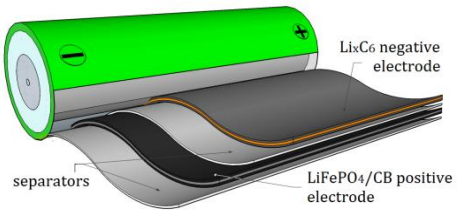

Fig. 4.3. Schematic representation of a $LiFePO_4$/C 26650 cylindrical cell. Adapted from **paper VI**.

The cylindrical cell consists of a 1.5 m $LiFePO_4$/carbonaceous additive (LFP/CB) positive electrode cast on either sides of an Aluminum foil, a 1.5 m Graphite (Gr) negative electrode cast on either sides of a Copper foil and 2 polymeric separators soaked with liquid electrolyte, as schematically represented in Fig. 4.3.

Summary of Results and Discussion 5

5.1. Laboratory Scale Li-ion batteries

Section 5.1 contains a collection of results and discussion of **papers I – IV** on degradation studies of laboratory Li-ion cells. **Papers I – III** cover a number of different characterization techniques in order to study degradation mechanisms that occur in a $LiFePO_4$/C cathode, mainly focusing in morphology and structural changes in Carbon Black (CB) additive. **Paper IV** is instead focused on the degradation of CB used as additive in high voltage batteries.

5.1.1. Low-kV FIB/SEM analysis for changes in morphology and conductivity of $LiFePO_4$/C electrodes

The structural degradation of a laboratory Li-ion battery $LiFePO_4$/Carbon Black (LFP/CB) composite cathode was studied by various microscopy techniques, including Focused Ion Beam (FIB)/Scanning Electron Microscopy (SEM) 3D tomography and Transmission Electron Microscopy (TEM). A new technique was also developed relying on the combination of low-accelerating voltage SEM imaging [63] with FIB milling, in order to study the electron percolation in the CB network in three dimensions.

After preparing and testing two LFP/CB electrodes, as described in Table 5.1, low-kV FIB/SEM tomography has been performed collecting two 3D datasets (see Table 5.2) from the fresh electrode (labeled as F1 and F2) and three from the aged one (labeled as A1, A2 and A3). Conventional SEM imaging has also been performed in another region of the aged sample (A4).

Table 5.1. Test conditions for the examined laboratory LFP electrodes.

Electrode	Current (mA g^{-1})	Total cycle number	Remaining capacity
Fresh	17	2	~ 100%
Aged	17	100	~ 30%

Table 5.2. Volumes of collected datasets.

Dataset	Volume (voxels) X x Y x Z	Volume (µm^3) X x Y x Z
F1	250 x 683 x 341	10 x 10 x 5
F2	141 x 683 x 341	5.6 x 10 x 5
A1	250 x 683 x 341	10 x 10 x 5
A2	131 x 683 x 341	5.2 x 10 x 5
A3	150 x 683 x 341	6 x 10 x 5

Fig. 5.1 shows SEM images after FIB slicing recorded at 1 kV of the fresh electrode (region F1, Fig. 5.1 a,b) and aged electrode (region A1, Fig. 5.1 c,d), and recorded at 10 kV of the aged electrode (region A4, Fig. 5.1 e,f). The images were recorded with the Everhart-Thornley (E-T) detector (Fig. 5.1 a,c,e) and with In-lens detector (Fig. 5.1 b,d,f). In the images recorded at 1 kV with the E-T detector (Fig. 5.1 a,c) it is possible to distinguish three different phases: the grains with the brightest contrast corresponding to LFP particles, the almost black regions corresponding to CB and the large grey areas in-between corresponding to pores filled with silicon resin. The fresh electrode (Fig. 5.1a) shows a relatively homogeneous distribution of sub-micrometer LFP grains and CB particles. The aged sample (Fig. 5.1c) has a less homogeneous distribution of both LFP and CB and an increased porosity. The aged sample is further characterized by the presence of larger CB agglomerates surrounding some LFP grains, which is not observed in the two images of the fresh electrode. The increased agglomeration is expected to result in a decrease in the percolation of the CB network [37], [64].

The E-T and In-lens detectors give different type of contrast and sensitivity to charging, as discussed in Paragraph 2.3 of **paper I**. In the images recorded at 1 kV with the In-lens detector it is observed that the silicon resin has high intensity in the parts of the sample not adjacent to electron conducting phases (Fig. 5.1b). This indicates that the silicon resin is charging negatively due to low conductivity to the ground [65]. The CB network, expected to have a good conductivity and connectivity to ground, shows instead a dark contrast, indicating a minimal charging (Fig. 5.1b). However, in the aged electrode on (Fig. 5.1d) large agglomerations (circled in red) of what appears to be CB is brighter than other CB regions. This indicates that those agglomerations are charging negatively i.e. have lost connection to ground and/or have low conductivity.

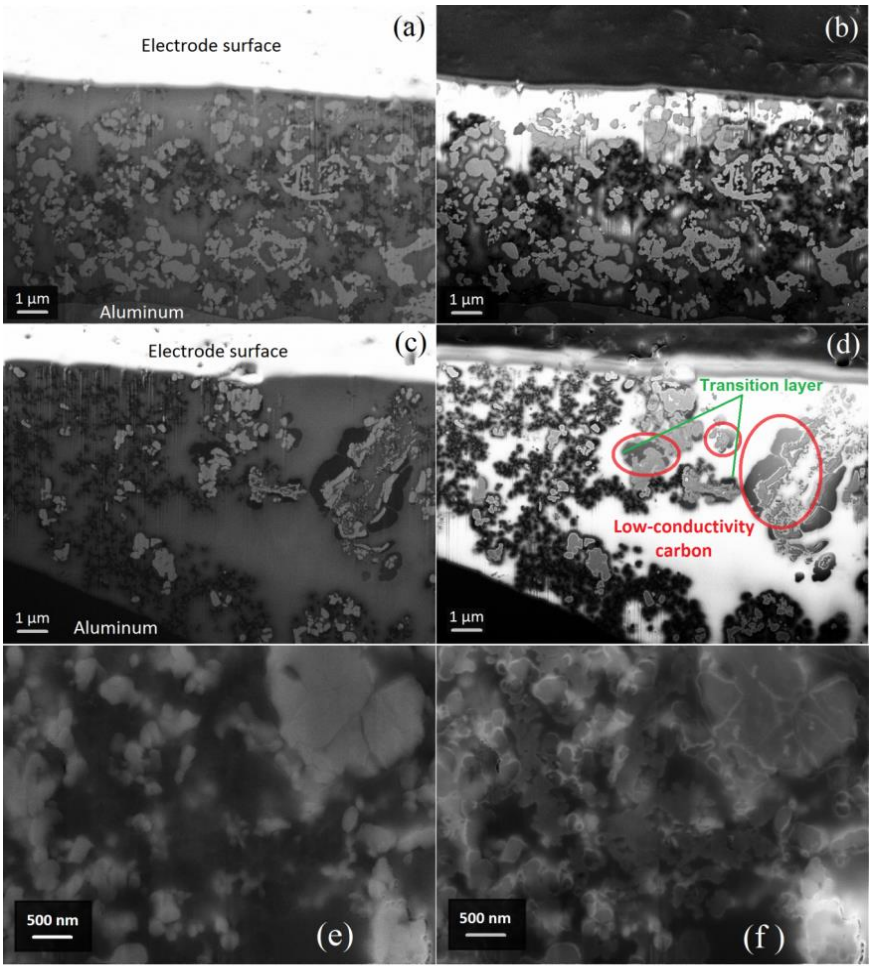

Figure 5.1. SEM images at 1 kV of the (a-b) fresh and (c-d) aged electrode recorded with the (a,c) Lateral E-T and (b,d) In-lens detector. SEM images at 10 kV of the (e-f) aged electrode (A4) recorded with the (e) lateral E-T and (f) In-lens detector. Reproduced from **paper I**.

Furthermore, a transition layer (pointed out by green arrows) with intermediate intensity between the CB agglomerates and the silicon resin is also observed as rims around the CB agglomerates in Fig. 5.1d. This indicates a transition zone where the silicon is able to dissipate charge to the CB phase.

In the images recorded with the In-lens detector, the LFP particles have a brighter contrast than the CB, which, as one would expect, indicate low electronic conductivity of the LFP particles. Fig. 5.1 (e,f) shows SEM images of the aged electrode, at higher magnification recorded at 10 kV. With the relatively high energy of 10 kV, the electrons penetrate app. 2-3 µm into the sample surface and the images therefore give insight into the internal structure of the particles. SEM images at 10 kV show cracks in some of the LFP

grains in area (A4) of the aged electrode (e.g. the large grain in the top right corner of Fig. 5.1e). The cracks are expected to be caused by expansion/contraction of the particle during the lithiation/delithiation process. In the In-lens detector image (Fig. 5.1f) many of the cracks appear as bright highlights due to the easier escape path of secondary electrons at topological LFP edges through the epoxy.

The SEM images from the five datasets F1, F2, A1, A2 and A3 have been used for three-dimensional reconstructions (Fig. 5.2) and statistical analysis such as particle size distribution (PSD) of the LFP phase and connectivity analysis of CB network.

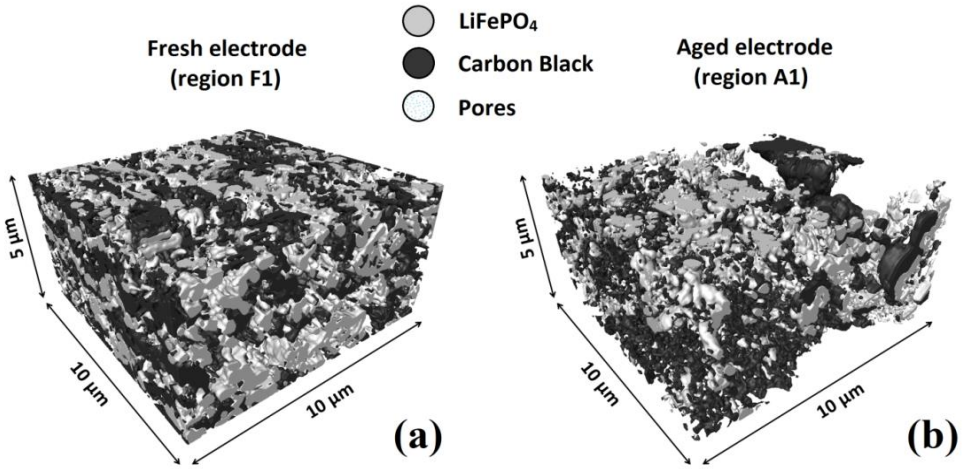

Figure 5.2. A segmentation of the 3D FIB tomography reconstruction of a) the fresh (F1) and b) aged (A1) electrode. Adapted from **paper I**.

Table 5.3. Phase volume fraction for fresh and aged electrode.

Phase	F1	F2	Fresh (Av. and Deviation)	A1	A2	A3	Aged (Av. and Deviation)
$LiFePO_4$	23%	17%	20% ± 3%	12%	18%	12%	14% ± 3%
CB	16%	15%	15.5% ± 0.5%	16%	5%	26%	16% ± 9%
Pores	61%	68%	64.5% ± 3.5%	72%	77%	62%	70% ± 6%

According to the results from the statistical analysis, shown in Table 5.3, some morphological changes are observed. The PSD of LFP particles show in fact a slight shift towards smaller grains in the aged sample, compared to the fresh one, probably due to cracking of particles, as observed in Fig. 5.1 (e,f). This creates new secondary smaller particles not connected or poorly connected to the CB network. The CB connectivity

analysis shows instead a lower connectivity for regions A1 and A2 from the aged electrode, because of relative big carbon agglomerates disconnected from the CB network. This continuous CB agglomeration on LFP surface upon cycling could be an effect of either mechanical stress or Iron dissolution [33] from LFP particles.

Another important aspect observed with cycling is the change in electron conductivity of the CB agglomerates, as revealed by low-kV FIB/SEM tomography. The fresh electrode is characterized by high conductivity CB, while localized charging is observed in the aged one. The amount of the apparently non-percolated CB is observed to be around 25% of total CB network in A1, 29% in A2 and 0% in A3, denoting a heterogeneous degradation in the LFP electrode. However, the assumption that the CB agglomerate brightness correlates with electronic percolation seem to be problematic. Fig. 5.3a shows a 3D reconstruction of the CB network in A1. The black particles represent the apparently electronically percolated CB, while the grey ones show the apparently insulated CB agglomerates. Fig 5.3 (b,c) show a zoom on a sub-volume and Fig.5.3 (d) show the corresponding raw images. From the inspection of the raw images in the 3D data Fig. 5.3d, the CB agglomerate brightness is seen to flicker between the grounded intensity level and the insulated (charged) intensity level. The flickering rules out that the increased intensity is due to the entire CB agglomerate being conducting and disconnected from ground. Further, the CB agglomerates appear dark (slices 114 and 116, Fig. 5.3d) where it has a surface connection (in the slicing plane) to grounded CB particles. Additionally, if the CB agglomeration is isolated in the slicing plane the CB agglomeration appears bright (slices 110 and 120). Such intensity flicker was observed to be a general behavior of the examined CB agglomerates. For this reason, we propose that the intensity flipping is attributed to the buildup of electrons on the CB agglomerate/vacuum interface resulting in a brighter contrast, and discharge across the slicing plane surface when adjacent to grounded CB, resulting in the darker contrast. This leads us to suggest that these large CB agglomerations are not grounded. But we can't fully determine whether this is due to disconnection from the conductive bulk or due to a lower bulk electronic conduction in the agglomerates.

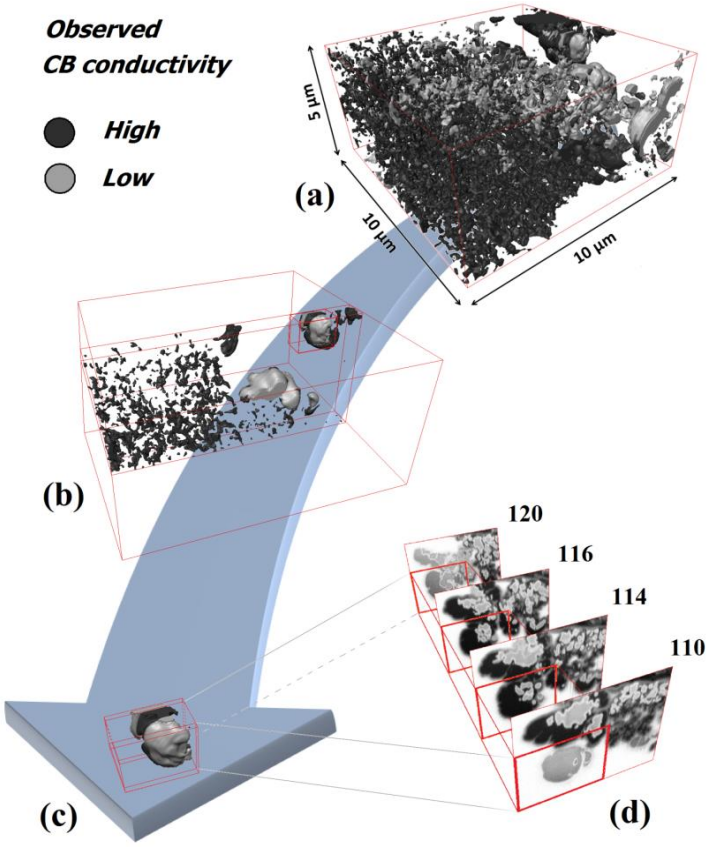

Figure 5.3. a) Segmentation of apparently percolated (black) and non-percolated (grey) CB from a 3D FIB tomography reconstruction of sample A1 based on SEM images recorded with an In-lens detector at 1 kV. b) and c) shows a zoom on a smaller section of the volume and d) examples of slices (raw SEM images) in the 3D dataset. Slice numbers are indicated in the figure. Reproduced from **paper I**.

A lower electronic bulk conductivity in the CB agglomerates could be possible due to observed structural degradation. TEM analysis of a sample (Fig. 8 in **paper I**) from the aged electrode show carbon surrounding the LFP particles that seems to be amorphous, in contrast to the quasi-crystalline fresh CB particles.

In conclusion **paper I** presents a degradation study of a laboratory $LiFePO_4$/C cathode by microscopy investigation. Changes in morphology were studied in 3D by FIB/SEM tomography and the degraded sample showed a higher amount of smaller LFP particles due to cracking of LFP grains upon cycling. The CB particle were seen to agglomerate and accumulate on the LFP surface in some parts of the aged electrode, increasing heterogeneity of the CB network and reducing electron percolation thereby decreasing the amount of electrochemically active LFP particles. The low accelerating voltage (1kV) provided a useful contrast between high-conductivity carbon phases and low-conductivity

carbon phases with no electronic percolation to high-conductivity carbon phases at the carbon/vacuum interface. We observed from the contrast difference that many CB agglomerates are not anymore grounded either because of disconnection from the conductive bulk or due to lower bulk electron conduction in the agglomerates. The presence of a different structure was also observed by TEM analysis, and the poor electronic conductivity of the CB agglomerates could be attributed to a change in the structure from quasi-crystalline to amorphous, which was supported by HRTEM analysis of the degraded cathode.

5.1.2. A transmission line model (TLM) for laboratory $LiFePO_4$/C electrodes

Paper II is an *ECS Transactions* manuscript presenting a thorough characterization of fresh and aged electrodes by Electrochemical Impedance Spectroscopy (EIS), with relative equivalent circuit modeling. Fitted values are nicely correlated to structural changes observed by low-kV FIB/SEM tomography.

Fig. 5.4 shows the equivalent circuit used to model the EIS spectra from both fresh and aged electrodes. The R_E-$R_{Al}Q_{Al}$ elements, Fig. 5.4a model the high-frequency region where R corresponds to a resistance and Q corresponds to a constant phase element. R_E represents the ionic resistance of the electrolyte, while the $R_{Al}Q_{Al}$ element denotes the aluminum/electrode polarization impedance [66]. The low-frequency region was modeled with a generalized transmission line model (TLM) for a porous electrode [49], [53], [54], Fig. 5.4b. This model involves a cylindrical pore (filled with the electrolytic solution) with length L, electronic resistance of the electrode R_{el}, ionic resistance of the solution in the pore $R_{ion,L}$ and an equivalent circuit Ç to model the interface electrode/electrolyte, including charge transfer resistance, double layer capacitance and solid state diffusion. The electronic resistance is often assumed to be much lower than the ionic resistance of the solution ($R_{el}<<R_{ion,L}$) for which reason a simplified transmission line without the electronic rail is used [49], [52]. However, assuming to find a higher R_{el} non-negligible electronic resistance in the aged electrode, the generalized version of the transmission line model is used. The electrode/electrolyte interface, Fig. 5.4c, has been modeled with a Randles circuit which includes the charge transfer resistance R_{ct}, a constant phase element Q (from which the effective double layer capacitance C_{dl} is calculated according to [58]) and the general finite space Warburg element W_{fs} [55]–[57].

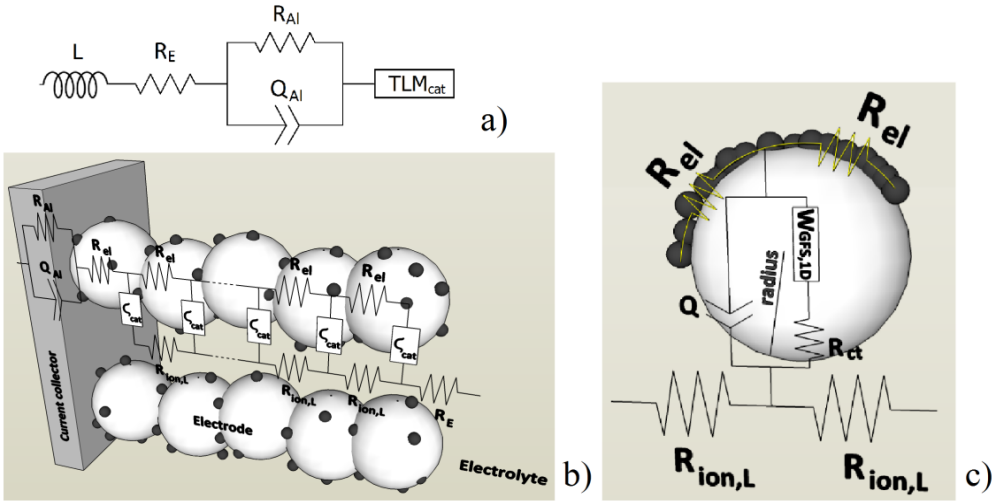

Figure 5.4. a) Equivalent circuit used to model the impedance spectra, b) Generalized Transmission Line model, c) Randles Circuit used to model electrode/electrolyte interface with Li+ Warburg Finite Space diffusion within a particle with radius r. Reproduced from **paper V**.

An impedance spectrum from the fresh electrode and the modeling result is presented in Fig. 5.5 (a,b), while the comparison of the impedance response of both fresh and aged electrodes, at the discharged state, is shown in Fig. 5.5 (c,d). Results from EIS fitting are reported in Table 5.4.

The impedance spectra modeling, indicates that most of the electrode degradation is due to changes in electrical conductivity in the CB additive phase. Presence of low-conductive and/or non-percolated carbon particles and agglomerates, as shown by low-voltage FIB/SEM tomography in **papers I** and **II**, is found to lead to an increase in electric resistivity both at the aluminum/electrode interface and throughout the CB network. This is seen by a larger R_{Al} and R_{el} for the aged electrode relative to the fresh electrode. The drop in C_{dl}, calculated from Q according to Brug et al. [58], is also expected after CB agglomeration, having a smaller surface in contact between the CB network and the current collector, and being C_{dl} directly proportional to the surface area. The lithium ion R_{ct} is also found to increase in the Randles circuit which models the electrode/electrolyte interface: it is an effect of lower electron transport by carbon, which should foster (de)lithiation process. The Li^+ ion diffusion coefficient within $LiFePO_4$ seems to not be affected. This could be an indication of almost no degradation occurring in the $LiFePO_4$ lattice. The rise in $R_{ion,L}$ in the infiltrated pores, as shown by the TLM, is not clearly understood, but it may be caused by formation of micropores, with a higher ion resistivity, after LFP cracking and/or increased tortuosity to electrochemically active sites. The most important result from the EIS model is the huge increase in electron resistance R_{el} throughout the CB network, of about two orders of magnitude. This higher resistance correlates with the presence of the non-electron percolating and/or non-conducting carbon phase which prevents the electron transfer within

the electrode, in agreement with the results from the low-kV FIB/SEM tomography, previously showed in **paper I**.

Table 5.4 Results from EIS fitting.

	RQ element		Transmission Line				
	R_{Al} (Ωcm^2)	C_{Al} (μF)	R_{ct} (Ωcm^3)	C_{dl} (F)	D ($cm^2 s^{-1}$)	$R_{ion,L}$ (Ωcm^{-1})	R_{el} (Ωcm^{-1})
Fresh	68	4.2	0.66	0.75	$2.7 \cdot 10^{-11}$	8760	21
Aged	142	3	3.27	0.64	$2.9 \cdot 10^{-11}$	17260	1546

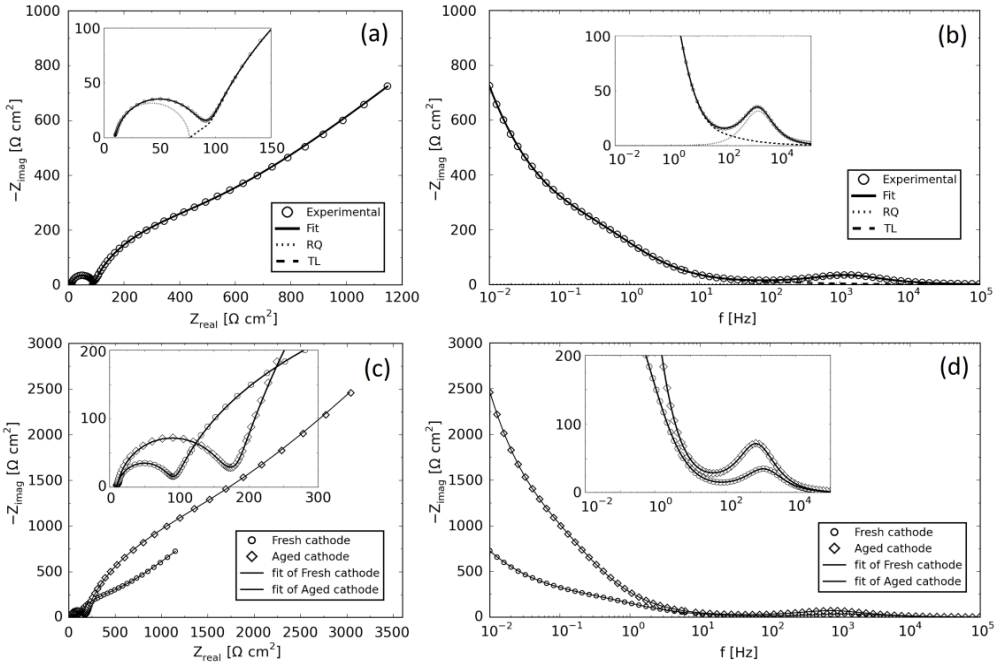

Figure 5.5. a) Nyquist and b) Bode plot of the Fresh electrode at 0% SOC including fit using the equivalent circuit in equation 1. c) Nyquist and d) Bode plot of Fresh and Aged cathodes at 0% SOC. The EIS measurements are performed at OCV after relaxation. All insets show a zoomed view of the high frequency region. Reproduced from **paper II**.

5.1.3. A TEM study of morphological and structural degradation phenomena in $LiFePO_4$-CB cathodes

Paper III consists of a thorough TEM analysis of morphological and structural degradation phenomena observed in laboratory LFP/CB cathodes investigated at different preparation, storage and cycling stage, as shown in Table 5.5.

Table 5.5. Overview of the investigated LFP-CB samples.

Number	Name	Description	Sample
1	Pristine CB	As-received CB powder	Powder (TEM)
2	Pristine LFP	As-received LFP powder	Powder (TEM)
3	Fresh cathode	LFP-CB (+ binder)	Powder (TEM)
4	Stored cathode	Sample 3 stored in electrolyte for 72 h	Powder (TEM)
5	Reference cathode	After 2 charge/discharge cycles	FIB/SEM
6	Aged cathode	After 100 charge/discharge cycles	FIB/SEM + TEM lamella

Fig. 5.6a displays a bright- and a dark-field (inset) TEM image of pristine off-the-shelf LFP nanoparticles deposited on a lacey carbon grid. A high-resolution TEM (HRTEM) image of one of the LFP particles is presented in Fig. 5.6b. A thin amorphous coating with a thickness of ~1 nm is observed at the particle surface. Fig. 5.6 (c,d) show respectively a bright-field TEM and a HRTEM image of pristine CB nanoparticles. The inset in Fig. 5.6c shows a selected area electron diffraction (SAED) pattern of the CB particles.

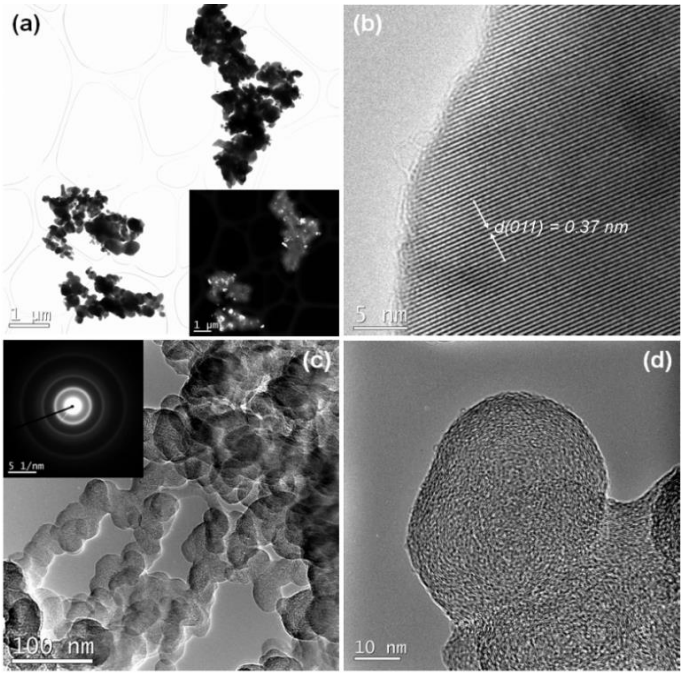

Figure 5.6. (a) Bright-field TEM image of pristine (off-the-shelf) LFP nanoparticles on lacey carbon grid, the inset shows a (200)-reflected dark-field image of the corresponding area; (b) HRTEM image of a single-crystal LFP nanoparticle; (c) Bright-field TEM image of pristine (off-the-shelf) CB nanoparticles. The inset shows a selected area electron diffraction pattern of the corresponding CB nanoparticles; (d) HRTEM image of a typical CB nanoparticle. Reproduced from **paper III**.

Fig. 5.7 presents bright-field TEM images of the (a) fresh, (b) stored and (c) aged cathode microstructures with LFP (dark contrast, large particles) and CB nanoparticles (light contrast, smaller particles) distinguished by amplitude contrast [67]. In Fig. 5.7c, the relatively dark LFP particles are indicated by black arrows and the lighter CB particles are indicated by white arrows. In Fig. 5.7c the grey contrast background arises from the Si resin stabilizing the TEM lamella.

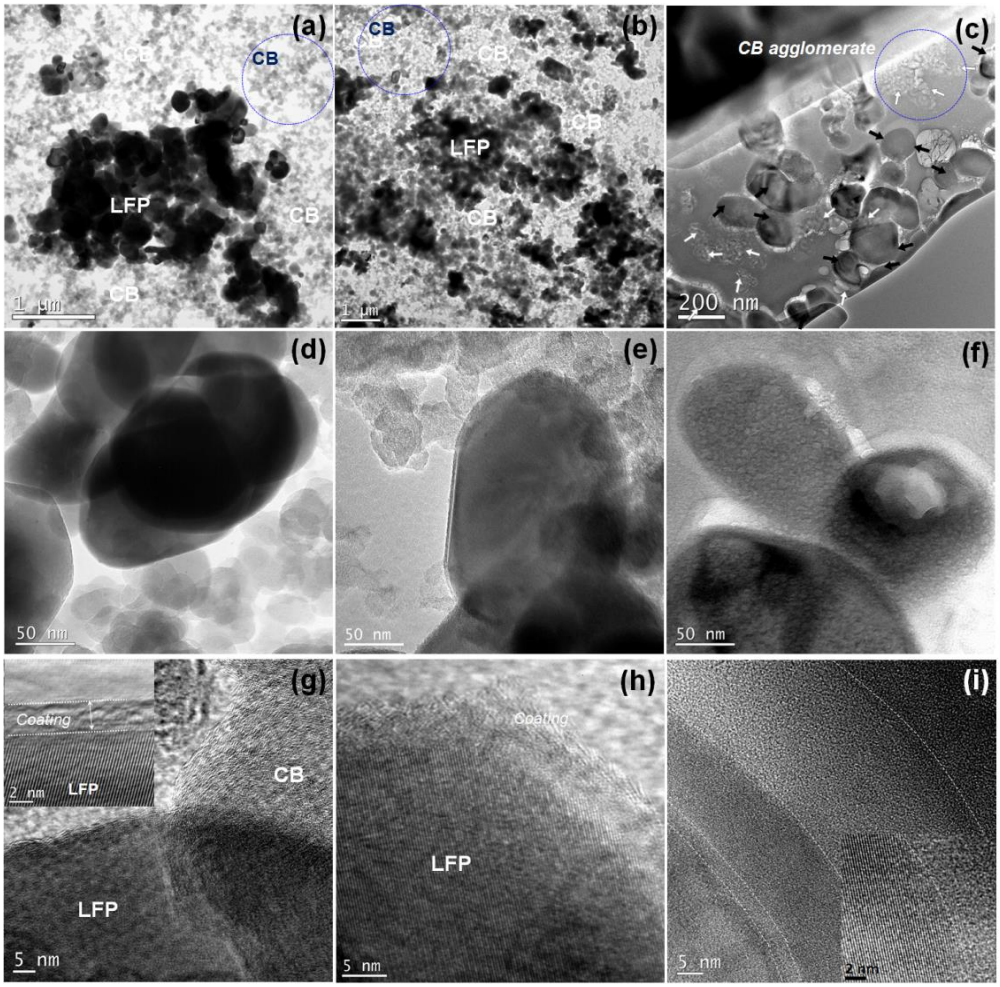

Figure 5.7. TEM images of the (a,d,g) fresh (b,e,h) stored and (c,f,i) aged LFP-CB cathode. The inset in (g) presents the magnified primary coating layer on LFP nanoparticles, and inset in (i) shows the magnified LFP/SEI layer interface. Reproduced from **paper III**.

Changes in the coating layer at the LPF particles surfaces are observed in the magnified TEM images, Fig. 5.7(d-f). It is seen that the thickness of the layers formed at the LFP particle surface increases from the fresh (Fig. 5.7d) to the stored (Fig. 5.7e) and further to the aged (Fig. 5.7f) cathode. Representative HRTEM images are shown for the fresh (Fig.

5.7g), stored (Fig. 5.7h) and aged (Fig. 5.7i) cathode. The thickness of the amorphous layer at the LFP particle surfaces increases from ~3 nm for the fresh cathode to ~9 nm for the stored cathode and ~30 nm for the aged cathode. It is observed that while the coating layers in the fresh and stored cathodes appear as one single amorphous layer, the coating layer in the aged cathode seems to consist of several layers distinguishable by different contrast levels, supposed to include primary coating layer and different SEI layers formed when the cathode was stored and cycled. According to an interesting complementary X-ray photoelectron spectroscopy (XPS) and in-situ Atomic Force Microscopy (AFM) study, SEI layers formed on a Highly Oriented Pyrolytic Graphite (HOPG) electrode in 1 M $LiPF_6$ in EC:DMC (1:1 by weight) consist of a thin and scattered top layer with a dense and more continuous bottom layer [68]. Importantly, the layer formation was observed to dynamically depend on the anodic/cathodic electrode operation. In other words the electrolyte composition, the use of additives and the electrode charge/discharge history was shown to be important for the morphology of decomposition compounds and SEI layer formation on $LiFePO_4$ surfaces.

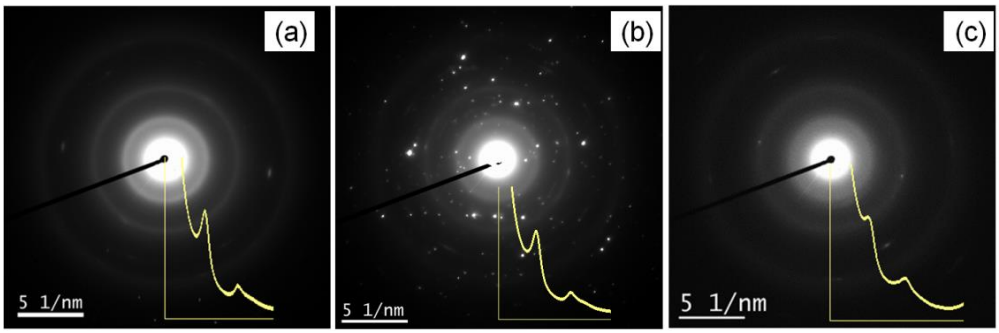

Figure 5.8. SAED electron diffraction patterns of CB particles for: (a) fresh cathode, (b) stored cathode and (c) aged cathode recorded inside the dotted blue rings in Fig. 5.7a, Fig. 5.7b and Fig. 5.7c respectively. The insets show normalized intensity profiles. Reproduced from **paper III**.

Changes in CB crystallinity and increased agglomeration of CB network are also observed in the cycled electrode. Fig. 5.8 shows the SAED profile from the fresh (Fig. 5.8a), stored (Fig. 5.8b) and cycled (Fig. 5.8c) cathode. The peak broadening and peak intensity decrease indicates the CB crystallinity decreases during storage in electrolyte and during cycling. This, combined with the CB agglomeration (see supplementary informations in **paper III**), are expected to decrease the electrical conductivity in the CB network. This is in agreement with the results fitted in **paper II**.

5.1.4. Analysis of the Interphase on Carbon Black Formed in High Voltage Batteries

Paper IV is a manuscript focused on the study of electrolyte decomposition in the surface region of carbon black (CB) additive in lithium-ion cells at high voltage up to 4.9 V.

Some Li-ion cells were assembled in a pouch cell, two-electrode setup, using Super P carbon black electrodes as positive electrode, Li metal as negative electrode and Celgard 2500 (monolayer Polypropylene) membrane as separator. Two different electrolyte mixture were used, consisting of 1 M of either $LiPF_6$ or $LiClO_4$ salts dissolved in EC:DEC (vol. 1:1). They were cycled with a constant current of 5 µA in a voltage range 2.5 – 4.9 V and 2.5 – 4.3 V and characterized by SOXPES and TEM analysis. Electrochemical Impedance Spectroscopy (EIS) was also performed in three-electrode setup on a Super P positive electrode, using lithium metal as counter and reference electrodes, and 1 M $LiPF_6$ in EC:DEC 1:1 v/v electrolyte solution.

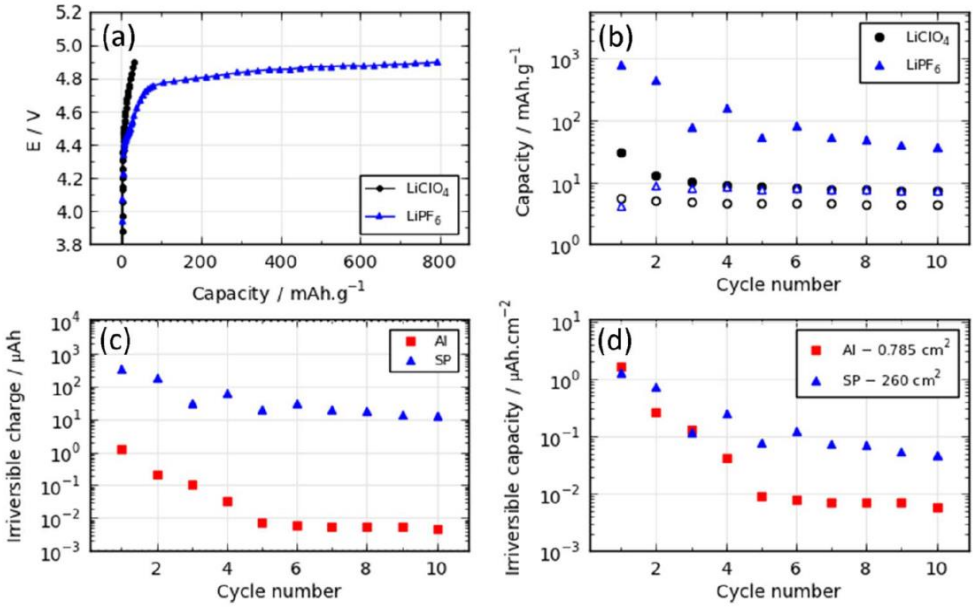

Figure 5.9. (a) First charge curves of Li-ion cells using CB cathode with LiPF6 or LiClO4 as electrolyte salt dissolved in EC:DEC (1:1) solvent. (b) Charge/discharge capacities for the first 10 cycles of CB cathode cycled between 4.9–2.5 V using the same electrolytes. Solid points are for charge while open points are for discharge capacities. (c) Logarithmic irreversible capacity vs. cycle number for a CB electrode and a bare Al electrode using LiPF6 salt. (d) Same as (c), but divided by surface area of the electrodes. Reproduced from **paper IV**.

Fig. 5.9a shows the first charge curves up to 4.9 V of the li-ion cells using Super P as cathode and $LiPF_6$ or $LiClO_4$ as electrolyte salts. The $LiClO_4$ based cell provided a capacity of around 50 mAh g^{-1}, while the $LiPF_6$ cell yielded a larger capacity of around 800 mAh g^{-1}.

The cells were then discharged to 2.5 V, and the cycled 10 times between 4.9 V and 2.5 V, to investigate the reversibility of these capacities. As shown in Fig. 5.9b the charge capacities were significantly higher than the discharge capacities, indicating irreversible electrochemical processes during charge, and they decrease significantly after the first cycle. The small discharge capacity is instead the same over the 10 cycles, indicating a reversible reaction occurring at the CB cathodes. This reversible capacity is due to the sum of accumulated surface capacitance and the charge transfer from intercalation/deintercalation of PF_6^- or ClO_4^- anions to/from the positive electrode. The large irreversible capacity can be instead explained by either formation of AlF_3 passivation layer on the aluminum current collector or reaction between the electrolyte and the surface functional groups on the carbon surface. In order to clarify this, identical cells were assembled and tested, using an Al disk as cathode. Fig. 5.9c shows that the irreversible capacity is order of magnitudes higher in the CB electrode than in an Al electrode in cells with LiPF6 electrolyte salt, and Fig. 5.9d shows the same results normalized for surface area of CB and Al (260 cm^2 and 0.785 cm^2 respectively).

To investigate a possible formation of electrolyte decomposition species in or on CB particles at high voltages, CB electrodes were analyzed using synchrotron-based SOXPES. Figure 5.10a shows C1s spectra of a CB cathode cycled 10 times between 4.9–2.5 V using $LiPF_6$ as the electrolyte salts. Also, C1s spectra of a CB cathode that was cycled between 4.3–2.5 V, as well as, C1s spectra of pristine and stored CB electrodes are presented in the Figure 5.10a. The C1s spectrum of the pristine sample contains 4 main contributions at the binding energies of 284.6 eV, 285 eV, 286.5 eV, and 290.9 eV assigned to Super P, hydrocarbons, CH_2 (from binder), and CF_2 (from binder), respectively [69], [70]. Interestingly, the C1s spectrum of the stored sample shows different features compared to the spectrum of the pristine sample, as the stored sample has a higher intensity/contribution of the hydrocarbon peak (red peak at 285 eV). Also, the intensity of the peak at 286.5 eV (green peak) is increased, which indicates presence of C–O bond in the surface region of the stored CB particles. The changes in the spectrum of the stored sample compared to the pristine sample shows that the electrolyte solution partially decomposes in/at the surface of CB particles when the electrode is immersed in the electrolyte. It should be mentioned again that all the electrodes were washed with DMC before SOXPES measurements to make sure no electrolyte remained on the surface of electrodes. The formation of decomposition species in the stored sample may take place by a redox reaction as the cells have open circuit voltage about 3 V vs. Li/Li^+ [71]. Surprisingly, the C1s spectrum of the CB cathode cycled 10 times up to 4.3 V present similar features to the C1s spectrum of pristine sample indicating that no major decomposition product is present in the CB cathode when cycled up to 4.3 V. The C1s spectrum consists of extra minor contribution from O–C–O and/or C=O bonds compared to the pristine sample. The results could suggest that the decomposition species in the surface of the stored CB diminishes when the CB cathode is cycled up to 4.3V. This can, for example, occur by oxidation and/or dissolution/desorption [72], [73]. Cycling the CB cathode between 4.9–2.5 V using $LiPF_6$ electrolyte, we could detect an increase in the relative intensity of peaks at 287.5 eV and 290.9 eV. The former

originates from O-C-O and/or C=O bonds while the latter from carbonate species (CO_3) [69], [70], [72].

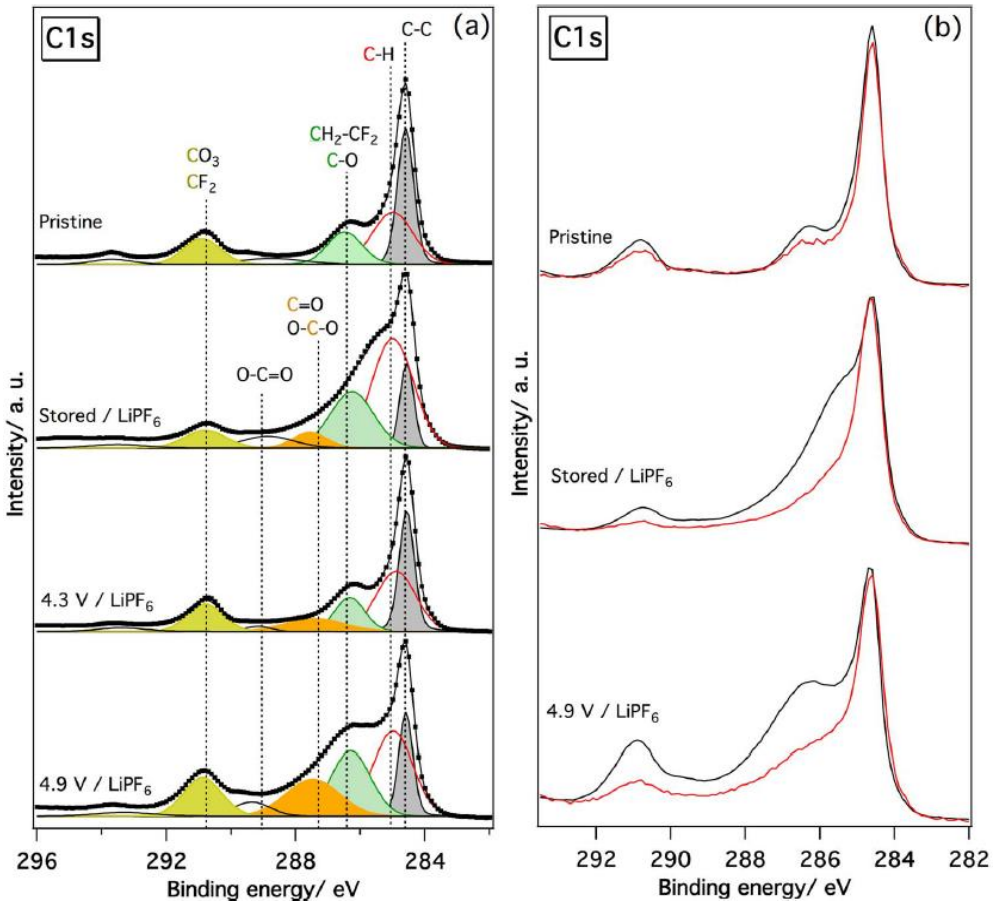

Figure 5.10. (a) Deconvoluted C1s spectra of pristine, stored, and cycled CB cathodes using LiPF6 in EC:DEC electrolyte. The spectra were measured by photon energy of 430 eV. (b) C1s spectra of the same samples measured using two photon energies of 430 eV (black) and 835 eV (red). Reproduced from **paper IV**.

To obtain a depth profiling of the surface layer, the CB cathodes were analyzed using two different photon energies of 430 eV and 835 eV, as presented by the black and red spectra, respectively, in Figure 5.10b. For the pristine CB electrode, the C1s spectra look similar using these two photon energies, as expected. A minor difference is that the C1s spectrum measured with lower photon energy shows slightly more contribution from binder (peaks at 286.5 eV, and 290.9 eV), indicating that concentration of binder is slightly higher on top surface. The stored and cycled samples display that the C1s spectra are more similar to the pristine sample for the higher photon energy of 835 eV. The spectra obtained with the higher photon energy are originated from increased depth of about 5–7 nm [74]. Therefore, the highest concentration of electrolyte decomposition species are found in a thin, about 1–

3 nm, surface region of the CB. SOXPES analysis of the CB electrode in $LiClO_4$ salts, as reported in **paper IV**, shows instead less degree of difference between the spectra of the cycled and pristine electrode, indicating less electrolyte degradation at the CB electrode surface. This is in agreement with capacity results showed in Fig. 5.9.

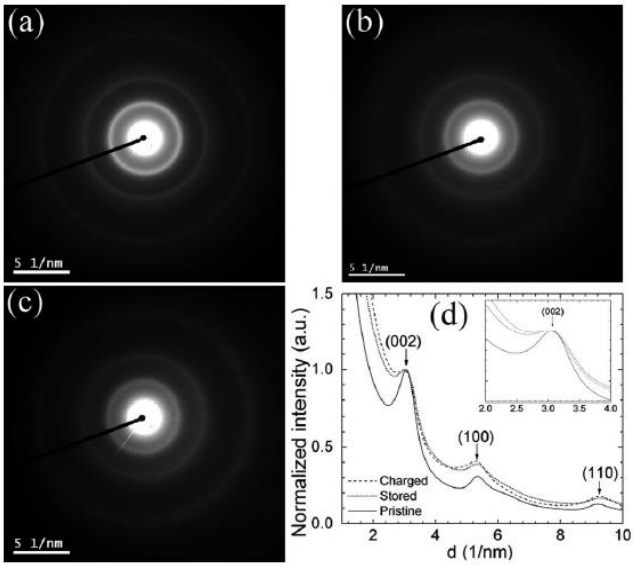

Figure 5.11. SAED patterns of (a) pristine, (b) stored, and (c) charged CB samples. Corresponding intensity profiles from the SAED patterns are shown in frame (d). The intensities are normalized to the intensity of the first diffraction ring (002). Inset of frame (d) shows a zoom-in of the first diffraction peak. Reproduced from **paper IV**.

To evaluate the possible loss of crystallinity indicated from the HRTEM images, SAED data for all three electrodes are presented in Fig. 5.11 along with normalized circular integration of the SAED patterns. Three main peaks can be distinguished in the pristine electrode corresponding to the (002), (100) and (110) reflections indicating that a partially graphitic structure exists in SP. The broad peaks are indicative of low-graphitized CB with short-range crystalline domains [75]. Fig. 5.11 shows that storing and charging CB leads to broadening of the diffraction peaks which indicates a loss in crystallinity, consistent with the HRTEM images. The distance between the sheets in the graphitic domains, which is obtained by the position of the d002 reflection, is determined to 3.3 ± 0.1 Å for the pristine electrode. This value is slightly increased to 3.5 ± 0.1 Å for the charged electrodes. This increase is much smaller than the increase expected for complete intercalation of PF_6^- anions into the graphitic domain (i.e. 4.5 Å) [76]. Finally, TEM images were recorded at lower magnification to evaluate the overall structure of the three samples. This analysis showed that the mean particle sizes slightly changed (see Fig. 5.12). In the pristine electrode, the mean particle size is 33.2 ± 1.2 nm, in the stored electrode it is 35.3 ± 1.0 nm and after cycling (at the charged stat) the value has increased to 40.2 ± 1.6 nm. The loss of crystallinity and particle swelling of the stored and charged CB samples could possibly be

explained partly by absorption of electrolyte solution followed by structural rearrangement of the internal CB structure. Also, the integration of decomposed electrolyte species to CB particles could influence CB particles.

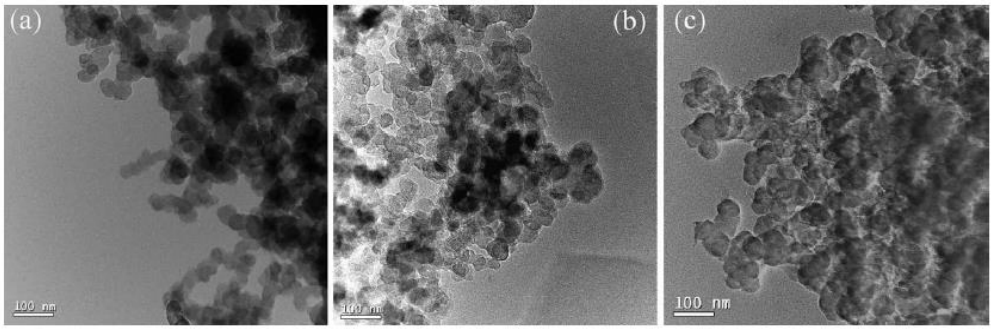

Figure 5.12. TEM images of (a) pristine, (b) stored, and (c) charged CB electrodes. Reproduced from **paper IV**.

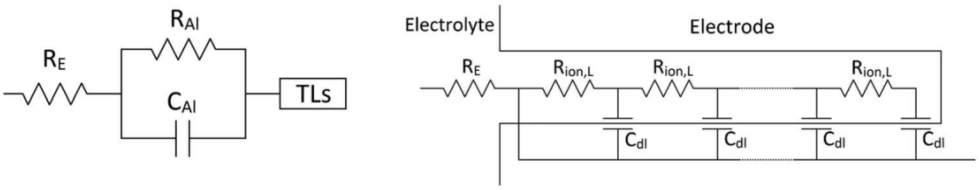

Figure 5.13. Equivalent circuit used for the analysis of the impedance spectra (left) including equivalent circuit of a pore described by a transmission line (right). Reproduced from **paper IV**.

The impedance results were modeled using the equivalent circuit presented in Fig. 5.13. The R_E-$R_{Al}C_{Al}$ elements model the high-frequency region where R corresponds to a resistance and C corresponds to a capacitor. These values have been normalized to the geometrical surface area of the electrode (0.785 cm2). The low-frequency region has been modeled with a simplified transmission line (TL) for a porous electrode, according to De Levie model [49], [54]. This model involves a cylindrical pore with lenght *L* and radius *r*, filled with the electrolytic solution, and the electronic resistance of the electrode is assumed to be much lower than the ionic resistance of the solution ($R_E << R_{ion}$). In case of a non-faradaic process, the overall impedance inside the pore is equal to:

$$Z = \sqrt{\frac{R_{ion,L}}{j\omega C_{dl,A} 2\pi r}} \coth \sqrt{R_{ion,L} * j\omega C_{dl,A} 2\pi r} \qquad (5.1)$$

where $R_{ion,L}$ is the ionic resistance of the electrolyte per unit pore length (Ωcm^{-1}) and $C_{dl,A}$ is the electrical double layer capacitance per unit surface area (Fcm^{-2}). From this model we calculated the total double layer capacitance of the CB electrode C_{dl} (F). The

uniform transmission line for a flooded ideally polarized porous electrode can be seen in Fig. 5.13 This model makes a good fit of the high- and low-frequency regions of the experimental data, but shows a small deviation in the mid-frequency part. Despite this, the model has been chosen as it provides an acceptable fit with a meaningful physical interpretation to the interface between CB surface and electrolyte in the extended porous network.

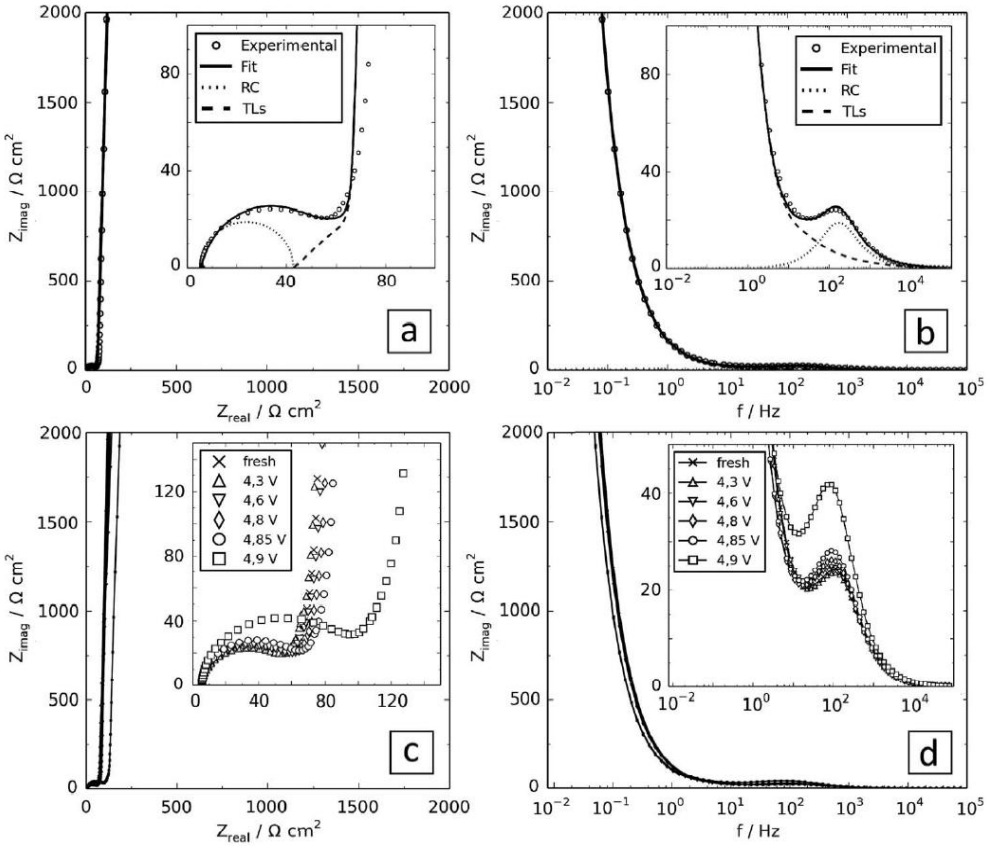

Figure 5.14. (a) Nyquist and (b) Bode plots of a stored CB electrode including fit using the equivalent circuit in equation 1. (c) Nyquist and (d) Bode plots of a CB cathode before, during and after stepwise charge to 4.9 V. The EIS measurements are performed atOCV after relaxation. All insets show a zoomed view of the high frequency region. Reproduced from **paper IV**.

The impedance results of stored and cycled CB electrodes are presented in Fig. 5.14. The Nyquist plots, Fig. 5.14(a,c), consist of a large semicircle in the high frequency range (between 10 kHz and 10 Hz) and an almost vertical tail in the low frequency range. The semicircle ($R_{Al}C_{Al}$) can be assigned to the interface between the aluminum current collector and the porous carbon network [77]. The low-frequency part (TLs) of the Nyquist plot shows a long capacitive tail, which refers to the double layer capacitance of the ion-blocking CB surface in the porous electrodes [49]. From modelling results (see **paper IV**)

is possible to notice that the Al/CB interface resistance R_{Al} remains constant up to 4.3 V, after which increase slowly until 4.85 V and suddenly increases significantly at 4.9 V. It could be explained by the growing of resistive surface layers (i.e. AlF_3) between aluminum and carbon particles [78], [79]. The ionic resistance of the electrolyte in the pores $R_{ion,L}$ is almost constant until 4.85 V after which it suddenly increases at 4.9 V. This increase is possibly linked to a change in the pore structure induced by the particle growth. Finally, the carbon surface double layer capacitance C_{dl} increases steadily from 0.95 to 1.25 mF at 4.85 V after which it keeps a constant value (see **paper IV**). Normalization of the initial carbon double layer capacitance to the total surface area of the electrode (260 cm^2), gives an $C_{dl,A}$ equal to 3.6 μF cm−2. This value is close to the values found in literature, i.e. 5 to 10 $\mu F cm^{-2}$ [80]. The actual surface area is slightly smaller due to blocking with PVDF binder and isolated particles not connected to the conductive network, and this can explain the smaller value. The capacitance is directly correlated to a change in the surface area and, as indicated from TEM analysis the CB particles swell from 35 to 40 nm, increasing their surface area with 30%. This is in agreement with the observed increase of C_{dl} by assuming that the conductive network is intact.

In conclusion the findings in **paper IV** suggest that the cathode/electrolyte interphases commonly observed on high voltage cathodes may originate from reactions between carbon black and electrolyte and not necessarily between active material and electrolyte.

5.2. Commercial $LiFePO_4$/C 26650 cylindrical cells

Section 5.2 contains a collection of results and discussion of **papers V** and **VI** on degradation studies of commercial $LiFePO_4$/C 26650 cylindrical cells. In **Papers V** a combined Transmission Line Model (TLM) has been proposed and implemented in an Equivalent Circuit Model (ECM) to describe the impedance spectra of a commercial 26650 $LiFePO_4$/C cylindrical cell. **Paper VI** focus on the analysis of aging mechanisms by low – voltage FIB/SEM tomography.

5.2.1. A transmission line model for a full $LiFePO_4$/C 26650 cylindrical cell derived by combined single-electrode Impedance and FIB/SEM tomography analysis

In **Paper V** a new equivalent circuit model (ECM), which includes a Transmission Line Model (TLM) for porous electrodes, is proposed and validated for commercial $LiFePO_4$/C 26650CC cylindrical cells.

A fresh $LiFePO_4$/C 26650 cylindrical cell with a nominal capacity of 2.5 Ah, denoted "26650CC", was cycled five times at a constant C-rate of 0.1 (250 mA) and characterized

by Electrochemical Impedance Spectroscopy (EIS) in a two-electrode setup using a Biologic VMP3 with Pstat/Gstat boards (test conditions shown in Table 5.6).

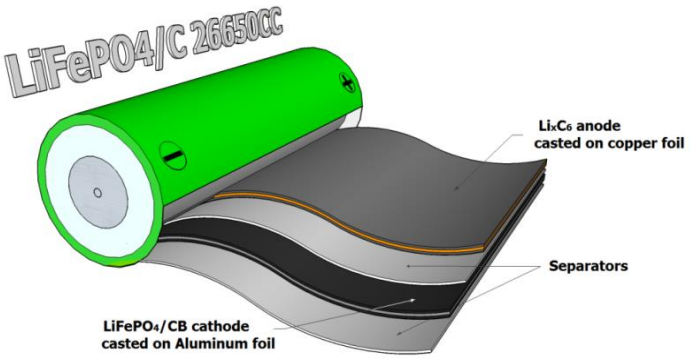

Figure 5.15. Schematic representation of the 26650CC $LiFePO_4$/C battery packaging design. Reproduced from **paper V**.

In order to test electrochemically the cathode and anode in a three-electrode configuration and resolve impedance contributions from each of the two electrodes, the 26650CC battery was dis-assembled in a glovebox in the discharged state and the cathode and anode were unrolled. The cylindrical cell consists of a 1.5 m $LiFePO_4$/carbonaceous additive (LFP/CB) positive electrode cast on either sides of an Aluminum foil, a 1.5 m Graphite (Gr) negative electrode cast on either sides of a Copper foil and 2 polymeric separators soaked with liquid electrolyte. The battery is schematically presented in Fig. 5.15. After proper rinsing of the electrode foils, four circular electrodes with a diameter of 18 mm (area = 2.55 cm^2) were punched out and used for three – electrode testing and FIB/SEM tomography. The test conditions for the four electrode samples are specified in Table 5.6.

Table 5.6. Test conditions for the examined samples

Sample	Current (mA)	Approx. C-rate	Total cycle number	Comment
26650CC	250	0.1	5	Cylindrical Cell, 2-electrode setup
LFP/CB1	0.33	0.1	5	Cathode, 3-electrode setup
LFP/CB2	-	-	-	Cathode, used for FIB/SEM analysis
Gr1	0.33	0.1	5	Anode, 3-electrode setup
Gr2	-	-	-	Anode, used for FIB/SEM analysis

FIB/SEM tomography was used to study the electrodes morphology. Results from statistical data analysis were implemented in the TLM and used to model the impedance spectra of LFP/CB1 and Gr1 electrodes. Figures 5.16 and 5.17 show Lateral E-T detector cross-section images of LFP/CB2 and Gr2 respectively, after ion milling. From Fig. 5.16a and Fig. 5.17 the cathode and anode thickness was estimated to 65 μm and 35 μm,

respectively. Fig. 5.16b shows a HR image recorded at the electrode/electrolyte interface. In the front face three different phases are distinguished: light gray $LiFePO_4$ particles, dark gray pores (infiltrated with silicon resin) and black CB particles. On the right side of the SEM image (Fig. 5a), where the electrolyte is supposed to be, there is a dark gray bulk of silicon resin with some LFP and CB particles, which probably detached during sample preparation.

In the Gr2 electrode (Fig. 5.17), only two phases can be distinguished: dark graphite particles and gray pores infiltrated with silicon resin. On the left side the copper/electrode interface is present, while on the right side the electrode/electrolyte interface is found. The darker gray bulk on the right is the epoxy resin, used for sample preparation, which has a different contrast than silicon resin. The region highlighted has been segmented for 3D reconstruction and PSD analysis.

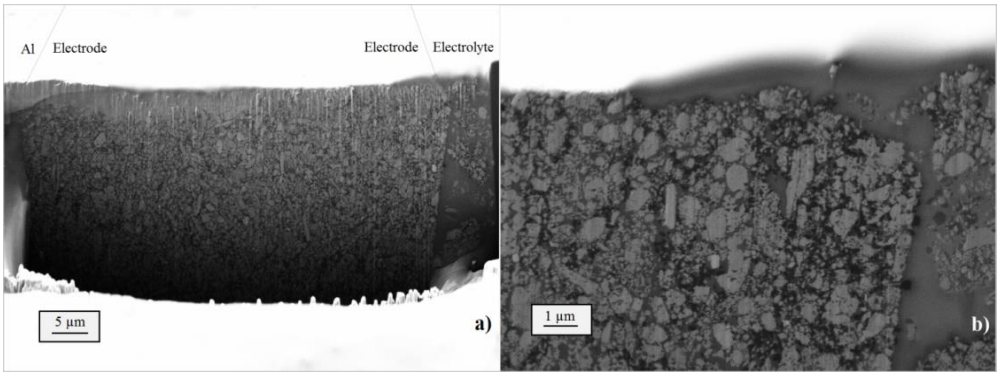

Figure 5.16. a) FIB/SEM cross-section image of the LFP/CB2 electrode, collected with lateral E-T detector. On the top, guidelines are shown to distinguish Al/Electrode and Electrode/Electrolyte interfaces, b) High resolution FIB/SEM cross-section image of Electrode/Electrolyte interface, used for 3D reconstruction and PSD.

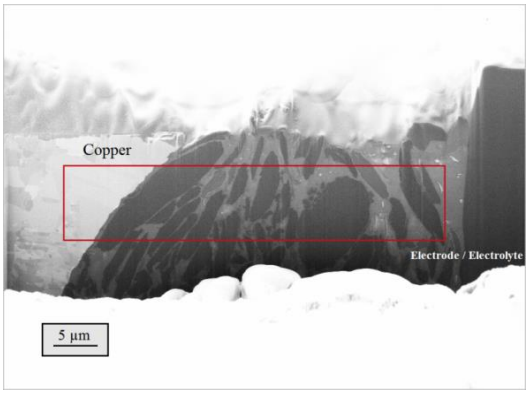

Figure 5.17. FIB/SEM cross-section image of the Gr2 electrode, obtained with a lateral E-T detector. On the left there is the copper current collector, on the right the Electrode/Electrolyte interface.

Figure 5.18 shows the 3D reconstruction of the LFP/CB2 electrode/electrolyte interface and of the Gr2 electrode. In the cathode 3D reconstruction (Fig. 18a) the grey phase is the $LiFePO_4$, the black phase is the CB additive network, while the electrolyte infiltrated pores are transparent blue. In the anode 3D reconstruction (Fig. 18b) the orange region represents the copper current collector, the black particles are graphite agglomerates and the transparent blue region is the pores network infiltrated with the electrolyte.

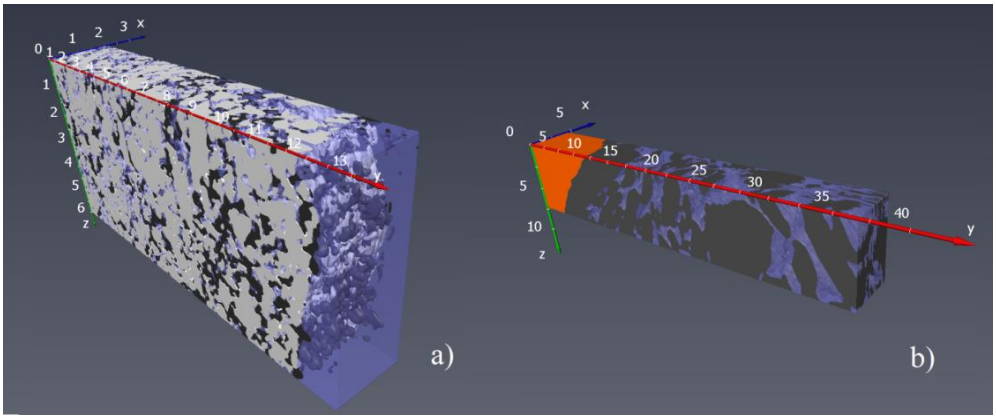

Figure 5.18. 3D reconstruction of a) LFP/CB2 electrode/electrolyte interface and b) Gr2 electrode. The scale bar units are [μm].

Fig. 5.19(a,b) show the PSD distribution for the three phases in LFP/CB2 electrode and for the two phases in Gr2 electrode. The average particle diameter for the active materials, $Li_{1-x}FePO_4$ and Li_xC_6, is respectively 76 nm and 1096 nm.

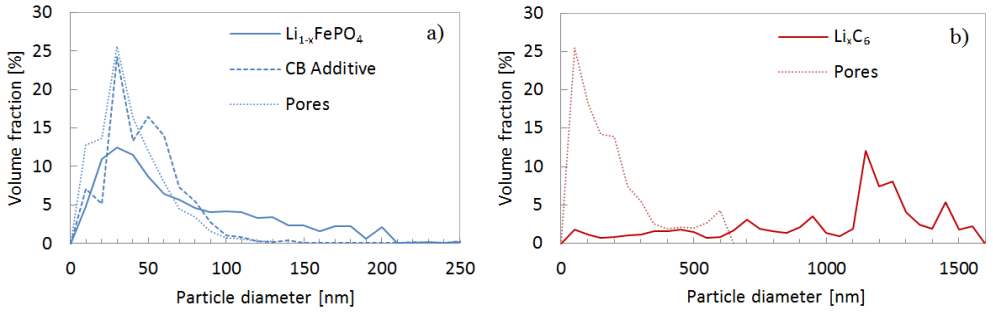

Figure 5.19. Particle size distribution for a) LFP/CB2 and b) Gr2 electrodes.

The 26650CC was cycled between 2.8 – 3.6 V as suggested from the commercial supplier, at a nominal C-rate of 0.1 C. The charge/discharge curve for 26650CC is shown in Fig.5.20a (black line).

In order to separate the electrode contributions single electrodes LFP/CB1 and Gr1 were prepared. Fig. 5.20b and 5.20c show respectively the charge/discharge curves for the

LFP/CB1 and Gr1 electrodes. The LFP/CB1 electrode is cycled between 3.0 – 3.7 V with a constant current of 330 µA, corresponding to a C-rate of 0.1, considering that its surface area is 2.55 cm^2 and that the unrolled battery electrode was 1950 cm2. The charge/discharge curve shows a typical flat plateau of a $Li_{1-x}FePO_4$ electrode (LFP/CB1, n.b.) at around 3.45 V (with $0 \leq x \leq 1$). Note that the discharge capacity of LFP/CB1 is 10% higher in the first cycle, when run vs lithium metal. This match with the typical amount of lithium lost for the building of SEI layer on Gr1 surface, inside 26650CC. The Gr1 electrode was cycled between 0.01 V and 0.45 V, also at 330 µA. Fig. 5.20c shows the charge/discharge curve of a Li_xC_6 electrode (Gr1, n.b.) with different intercalation steps of Li^+ ion (with $0 \leq x \leq 1$). Note that the charge/discharge curve of 26650CC resembles the voltage difference between the LFP/CB1 and Gr1 charge/discharge curves, as shown by the green curve in Fig. 5.20a.

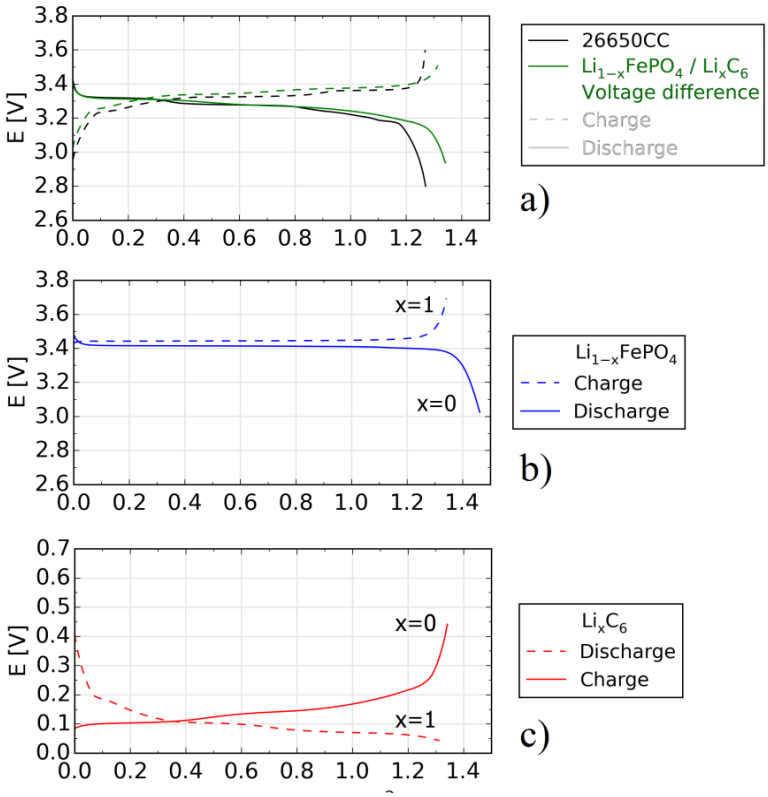

Figure 5.20. Charge/Discharge curves of a) 26650CC, b) LFP/CB1 and c) Gr1

The three-electrode EIS analysis was performed on LFP/CB1 and Gr1 electrodes and the impedance spectra were modelled using two similar ECMs which differ only for the TLM. Impedance spectra of LFP/CB1 were modelled by the ECM used in paper II, and already described in section 3.2.2. The spectra of Gr1 were instead modelled by the ECM shown in Fig. 5.21. It includes a simplified TLM, as described in section 3.2.3, where the

equivalent circuit which resembles the surface impedance ζ_{an} takes into account the presence of a thin layer (SEI) on the particle surface and a 2D geometry Warburg Finite Space Element is used.

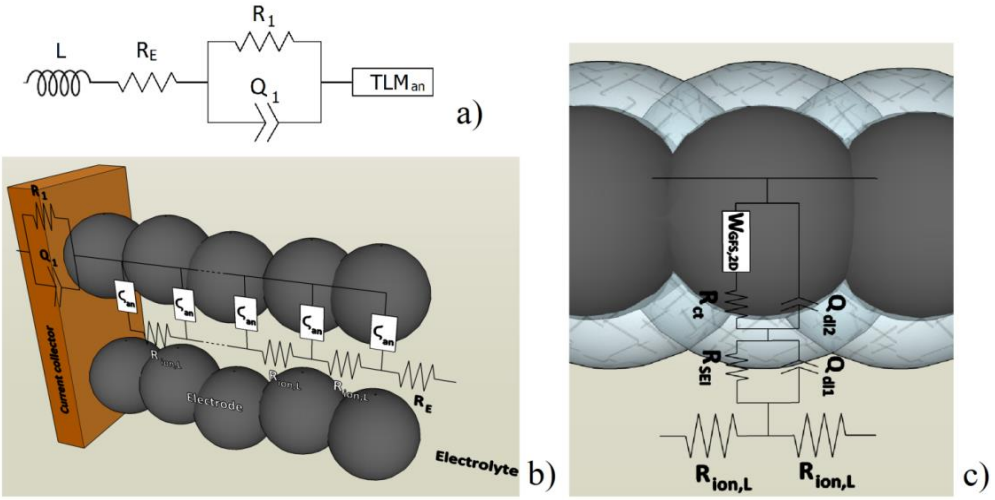

Figure 5.21. (a) Equivalent circuit used to model the impedance spectra, (b) Simplified Transmission Line Model resembling the element TLM_{an} in (a), (c) *RQ* element and Randles circuit used to model electrode/electrolyte interface with Li^+ diffusion (Warburg Finite Space element, $W_{GFS,2D}$) within a particle with radius *r*.

Fig. 5.22 and Fig. 5.23 show the normalized spectra measured for the LFP/CB1 and Gr1 electrodes respectively, with relative fitting. Both EIS spectra were measured either in the fully lithiated or delithiated state and results from EIS fitting are shown in Tables 5.7 and 5.8.

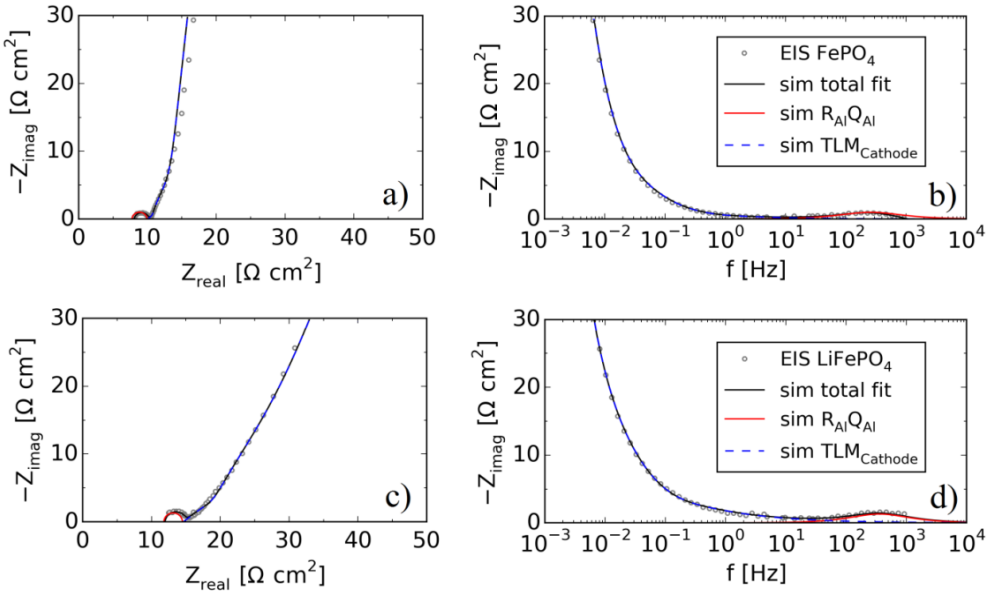

Figure 5.22. a) Nyquist and b) Bode plot of the $Li_{1-x}FePO_4$ electrode when the battery is at 100% SOC (x=1), c) Nyquist and d) Bode plot of the $Li_{1-x}FePO_4$ electrode when the battery is at 0% SOC (x=0). The black model curve is the sum of the red and blue model curves.

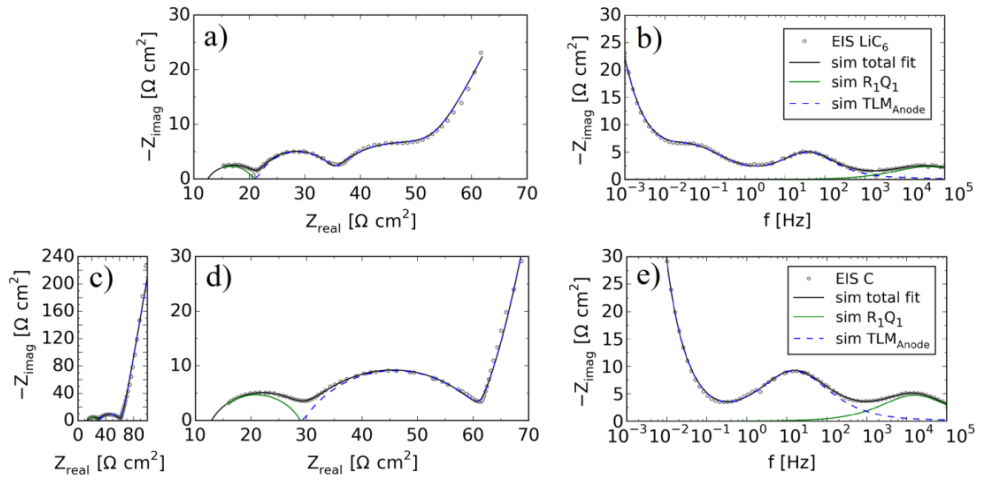

Figure 5.23. a) Nyquist and b) Bode plot of the Li_xC_6 electrode when the battery is at 100% SOC (x=1), c) Nyquist plot, d) zoomed view of high frequency region and e) Bode plot (zoomed view) of the Li_xC_6 electrode when the battery is at 0% SOC (x=0).

Both electrodes show a semicircle at relative high frequencies related to the current collector/electrode polarization. The mid- low-frequency region is instead different for the LFP/CB1 and Gr1 electrodes and has been modelled with a generalized and a simplified TLM respectively.

The values used in the TLM_{cat} (generalized TLM) for the electrode thickness L and the particle radius r are 65 µm and 38 nm, respectively, as obtained by FIB/SEM imaging and PSD analysis. The TLM_{an} (simplified TLM) has instead values of thickness L and particle radius r equal to 35 µm and 548 nm, respectively.

The fitted values from the TLM_{cat} (Table 5.7) show that R_{el} is not negligible compared to $R_{ion,L}$. Both resistances in the pore and the electrode are observed to decrease when the electrode is charged and mainly consists of $FePO_4$. $Li_{1-x}FePO_4$ particles are known to be subjected to expansion/contraction with cycling, and when the electrode is completely delithiated $FePO_4$ particles have a smaller volume and the pores increase in size, furnishing a smaller $R_{ion,L}$. R_{el} depends on the CB network tortuosity which changes due to particle movements during lithiation/delithiation process. Values of Li^+ diffusion coefficient D were calculated to be in the range $10^{-12} – 10^{-13}$ cm^2s^{-1}, in agreement with literature [38].

Values of $R_{ion,L}$ calculated from the TLM_{an} (Table 5.8) show to be comparable with the ones from the cathode, while the Li^+ diffusion coefficient D was estimated to be in the range $10^{-10} – 10^{-11}$ cm^2s^{-1}, around 2 orders of magnitude higher than LFP/CB1 [38]. Note that R_{el} is negligible for the graphite electrode.

Table 5.7. Results from EIS fitting of $Li_{1-x}FePO_4$ electrode.

	$R_{Al}Q_{Al}$ element		Generalized Transmission Line				
			Randles element			Pore	Electrode
	R_{Al} (Ωcm^2)	C_{Al} ($mFcm^{-2}$)	R_{ct} (Ωcm^2)	C_{dl} (Fcm^{-2})	D (cm^2s^{-1})	$R_{ion,L}$ (Ωcm)	R_{el} (Ωcm)
$FePO_4$	2.2	0.20	13.8	0.52	$8 \cdot 10^{-13}$	402	53
$LiFePO_4$	2.2	0.17	60	0.67	$4 \cdot 10^{-13}$	1538	113

Table 5.8. Results from EIS fitting of Li_xC_6 electrode.

	R_1Q_1 element		Simplified Transmission Line					
			$R_{SEI}Q_{dl1}$ element		Randles element			Pore
	R_1 (Ωcm^2)	C_1 (μFcm^{-2})	R_{SEI} (Ωcm^2)	C_{dl1} ($mFcm^{-2}$)	R_{ct} (Ωcm^2)	C_{dl} (Fcm^{-2})	D (cm^2s^{-1})	$R_{ion,L}$ (Ωcm)
LiC_6	8.3	0.40	14.3	0.28	14.3	0.10	$2 \cdot 10^{-11}$	745
C	16.0	0.43	31.4	0.35	40	0.57	$3 \cdot 10^{-10}$	500

Results from single-electrode EIS fitting were used in order to build a final ECM (Fig. 5.24) for the 26650CC, and some simplifications have been done in order to not have a model with too many variables which would destabilize the fitting routine.

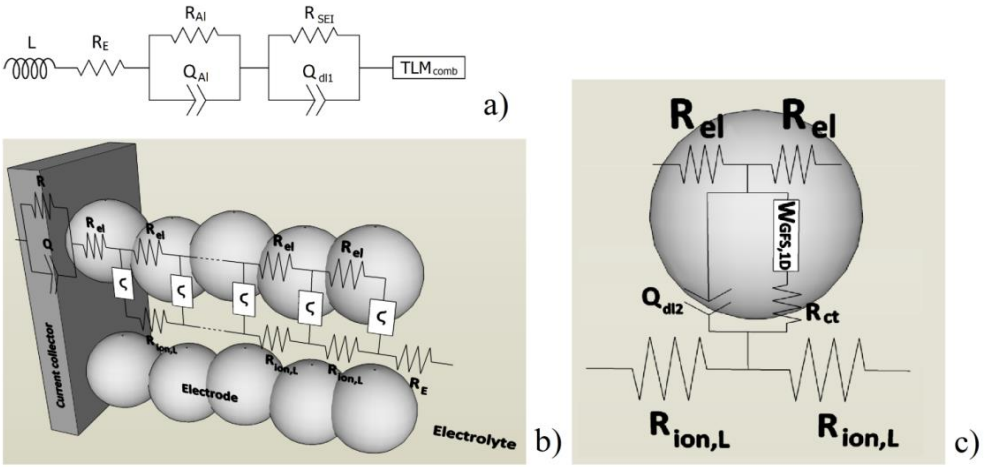

Figure 5.24 a) Equivalent circuit used to model the 2665CC impedance spectra, b) combined TLM_{comb} used to model porous electrode, c) single particle ECM.

The $R_E(R_{Al}Q_{Al})$ elements model the high-frequency region where R_E and R_{Al} are resistors and Q_{Al} a constant phase element (CPE). R_E models the ionic resistance of the electrolyte, while ($R_{Al}Q_{Al}$) represents the aluminum/cathode polarization [66], observed in the LFP/CB1 electrode in the frequency range 1 kHz – 100 Hz. The R_1Q_1 element, previously used to model the particle/particle contact in the Gr1 electrode, is not included in the total circuit since this process occurs at relative high frequency (>10 kHz). Above ~10 kHz the 26650CC is dominated by inductance.

The ($R_{SEI}Q_{dl1}$) element models the mid-frequency region (100 Hz – 10 Hz) and represents the SEI layer which covers the graphite particles in the anode. The TLM_{comb} in Fig. 16b combines the cathode and anode TLMs. The two single electrode TLMs have a Randles element in common to model the insertion or intercalation process at the electrolyte/electrode ($Li_{1-x}FePO_4$ or Li_xC_6) interface, but the *RQ* element representing the SEI layer on graphite is missing on the cathode model. For the 26650CC impedance model the ($R_{SEI}Q_{dl1}$) is placed outside the TLM_{comb} in order to have an equivalent circuit ς, to model the surface impedance inside the TLM_{comb}, which is equal for both cathode and anode particles ($\varsigma_{cat} = \varsigma_{an}$). No changes are observed in modelling the mid-frequency part of the spectra with a $R_{SEI}Q_{dl1}$ places either outside or inside the TLM, since comparable values have been found for both single-electrode impedance and 2-electrode configuration.

The TLM_{comb} variables are R_{ct}, C_{dl} (calculated from CPE according to Eq. 5) and D, $R_{ion,L}$ and R_{el}. The single electrode fitting (Table 3 and 4) shows R_{ct} and C_{dl} are not negligible for any of the two electrodes. However, the Li^+ ion diffusion coefficient D was observed to be around 2-3 orders of magnitude larger for Gr1 than for LFP/CB1, in agreement with previous findings [38]. This means diffusion in LFP/CB1 dominates the final part of the TLM_{comb} (the 45° line) and that the Warburg contribution from graphite can be neglected.

For this reason diffusion of Li^+ ion in LFP is modelled by a general finite space Warburg element with diffusion process along a one-dimensional diffusion path, $W_{GFS,1D}$, as used for the LFP cathode and the value used for r is the $Li_{1-x}FePO_4$/CB radius (22 nm, as calculated from PSD). R_{el} was also found to be negligible in the Li_xC_6 electrode, so the calculated electronic resistance R_{el} from the total TLM_{comb} is associated with the $Li_{1-x}FePO_4$/CB cathode, and more specifically the CB network. Finally, the ionic diffusion resistance per unit length in the pore $R_{ion,L}$ is seen to be highest when each electrode is in its fully lithiated state. This means the $R_{ion,L}$ contribution primarily comes from the cathode when the battery is discharged, and vice versa. From the single electrode modelling the cathode:anode contribution ratio was calculated to be 75:25 at 0% SOC, and 35:65 at 100% SOC.

The low frequency part of the 26650CC impedance spectra predominantly change at the lowest and highest SOC. For this reason the change this ratio is assumed to mainly occur at the lowest and highest SOC and consequently a ratio of 50:50 was simply used for all intermediate SOCs. The ratio was used to calculate an SOC dependent pore length L which is used as input for the TLM_{comb}; The values used for L are 57.5, 50 and 45.5 µm respectively for 0%, (12.5-87.5)%, and 100% SOC.

Fig. 5.25 shows the normalized EIS spectra measured for 26650CC at different SOC (dots), with the simulated fit (solid lines) for each spectrum. Results from EIS fitting are shown in Tables 5.9(a,b).

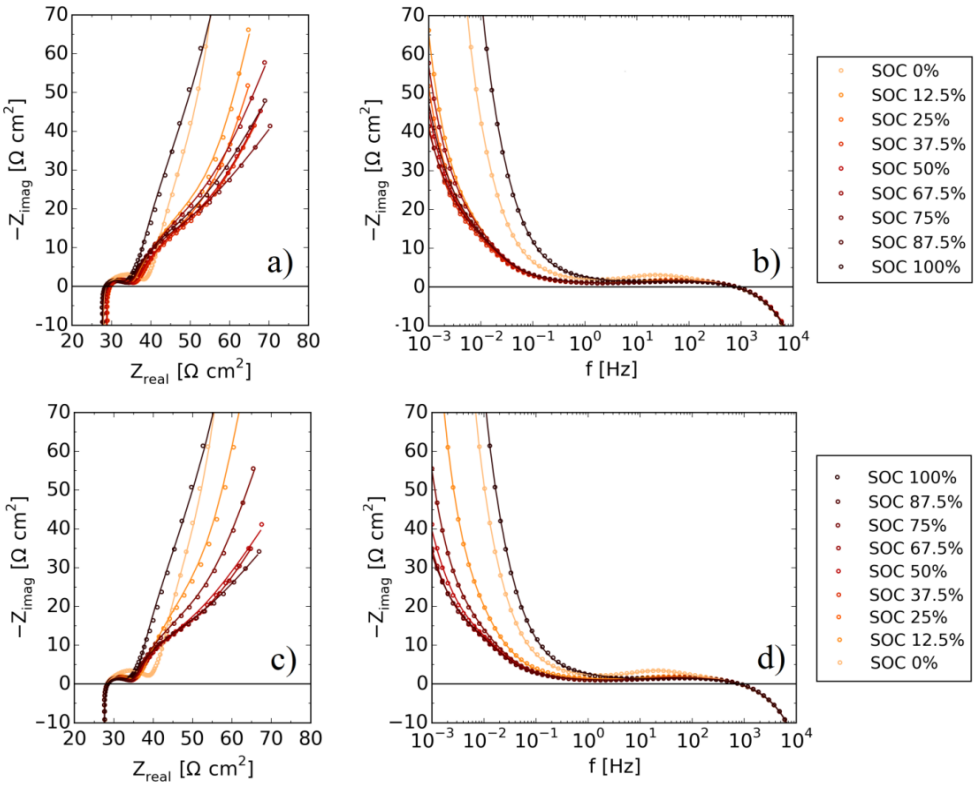

Figure 5.25 a) Nyquist and b) Bode plot of 26650CC at different SOC, measured in charging mode, with fitting c) Nyquist and d) Bode plot of 26650CC at different SOC, measured in discharging mode, with fitting. All spectra were measured at OCV after the cell had reached steady state defined by a change < 5 mV/h.

TABLE 5.9a Results from EIS fitting of 26650CC (charging mode).

	$R_{Al}Q_{Al}$ element		$R_{SEI}Q_{dl1}$ element		Combined Transmission Line				
					Randles element			Pores	Electrode
	R_{Al} (Ωcm^2)	C_{Al} ($mFcm^{-2}$)	R_{SEI} (Ωcm^2)	C_{dl1} ($mFcm^{-2}$)	R_{ct} (Ωcm^2)	C_{dl2} (Fcm^{-2})	D (cm^2s^{-1})	$R_{ion,L}$ (Ωcm)	R_{el} (Ωcm)
0%	1.81	0.17	7.18	0.54	87.0	0.24	$1.5 \cdot 10^{-13}$	1929	106
12.5%	1.76	0.17	4.58	0.50	64.0	0.72	$9.0 \cdot 10^{-14}$	927	79
25%	1.76	0.16	4.51	0.44	40.0	0.65	$8.8 \cdot 10^{-14}$	1040	92
37.5%	1.80	0.16	4.38	0.44	32.0	0.62	$8.9 \cdot 10^{-14}$	1025	71
50%	1.86	0.15	4.26	0.48	38.0	0.63	$8.9 \cdot 10^{-14}$	994	59
62.5%	1.80	0.16	4.27	0.44	42.0	0.58	$1.1 \cdot 10^{-13}$	997	64
75%	1.84	0.16	3.87	0.48	24.0	0.50	$1.5 \cdot 10^{-13}$	1144	58
87.5%	1.86	0.16	3.86	0.47	30.0	0.53	$1.3 \cdot 10^{-13}$	1071	46
100%	1.75	0.16	2.85	0.58	15.4	0.09	$1.4 \cdot 10^{-13}$	1826	46

TABLE 5.9b Results from EIS fitting of 26650CC (discharging mode).

	$R_{Al}Q_{Al}$ element		$R_{SEI}Q_{dl1}$ element		Combined Transmission Line				
					Randles element			Pores	Electrode
	R_{Al} (Ωcm^2)	C_{Al} ($mFcm^{-2}$)	R_{SEI} (Ωcm^2)	C_{dl1} ($mFcm^{-2}$)	R_{ct} (Ωcm^2)	C_{dl2} (Fcm^{-2})	D (cm^2s^{-1})	$R_{ion,L}$ (Ωcm)	R_{el} (Ωcm)
100%	1.75	0.16	2.85	0.58	15.4	0.09	$1.4\cdot10^{-13}$	1826	46
87.5%	1.82	0.16	4.14	0.43	20.0	0.55	$1.4\cdot10^{-13}$	1035	51
75%	1.82	0.16	4.10	0.44	44.0	0.63	$9.4\cdot10^{-14}$	1050	73
62.5%	1.84	0.15	4.50	0.44	26.0	0.59	$9.9\cdot10^{-14}$	1060	88
50%	1.82	0.16	4.68	0.43	24.0	0.55	$1.6\cdot10^{-13}$	1129	81
37.5%	1.80	0.16	4.69	0.44	42.0	0.62	$9.0\cdot10^{-14}$	1106	80
25%	1.80	0.17	4.68	0.47	58.0	0.66	$1.0\cdot10^{-13}$	1232	84
12.5%	1.78	0.17	4.62	0.53	58.0	0.50	$1.4\cdot10^{-13}$	1330	91
0%	1.83	0.17	7.82	0.58	88.7	0.20	$1.3\cdot10^{-13}$	2119	102

The values of the fitted parameters from TLM_{comb} are shown in Table 5.9(a,b). It is interesting to focus on the ionic resistance $R_{ion,L}$ of Li^+ ions diffusing into the electrode pores, the electron resistance R_{el} in the porous electrodes and Lithium diffusivity in the active materials in the electrodes. By comparing the obtained values with the values obtained from single electrode modeling, it is observed that the values for these variables can be ascribed to either the cathode or the anode. R_{el} was observed to be negligible for the anode such that R_{el} only depends on the cathode CB network. $R_{ion,L}$ was seen to consist of both cathode and anode contributions and to be dependent on the SOC. Specifically $R_{ion,L}$ was observed to be highest in each of the two electrodes when they were fully lithiated. The lithium diffusion coefficient D was much smaller in $LiFePO_4$ than in C which means D obtained from measurements of the full battery mainly reflects the lithium diffusion in $LiFePO_4$.

In conclusion the results from single-electrode impedance and FIB/SEM tomography in **Paper V** have been used to build a new ECM with a combined TLM for modelling of commercial $LiFePO_4$/C 26650 cylindrical cell impedance spectra. Combined with other characterization techniques, the combined ECM proposed here could be an important tool to study degradation mechanisms in $LiFePO_4$/C batteries when three-electrode impedance analysis in not possible.

5.2.2. Analysis of aging mechanisms in a commercial $LiFePO_4$/Graphite 26650 cylindrical cell by low – kV FIB/SEM tomography

In **Paper VI** the electrode degradation mechanisms in commercial 2.5 Ah $LiFePO_4$/Graphite 26650 cylindrical cells were examined. Aged and fresh electrode samples were prepared by cycling two cells respectively five and 22k times. Subsequently the cells were disassembled in a glovebox and electrode samples were rinsed and prepared for electrochemical testing in a 3-electrode setup, and for characterization with low-kV FIB/SEM tomography.

Table 5.10 shows the test conditions for the examined samples and Fig. 5.26 shows a schematic representation of the battery packaging design, the degraded graphite foil (from core and skin of the battery) and the regions where the electrode were punched out from.

Table 5.10. Test conditions for the examined samples

Sample	Current (mA)	Approx. C-rate	SOC range	Total cycle number	Comment
F26650CC	250	0.1	0 – 100 %	5	Cylindrical Cell, 2-electrode setup
A26650CC	10k	4	25 – 75 %	22k	Cylindrical Cell, 2-electrode setup
LFP1_F	0.33	0.1	0 – 100 %	1	Cathode, 3-electrode setup
LFP1_AB	0.33	0.1	0 – 100 %	1	Cathode, 3-electrode setup
LFP1_AR	0.33	0.1	0 – 100 %	1	Cathode, 3-electrode setup
Gr1_F	0.33	0.1	0 – 100 %	1	Anode, 3-electrode setup
Gr1_AB	0.33	0.1	0 – 100 %	1	Anode, 3-electrode setup
Gr1_AR	0.33	0.1	0 – 100 %	1	Anode, 3-electrode setup
LFP2_F	-	-	-	-	Cathode, used for FIB/SEM analysis
LFP2_AB	-	-	-	-	Cathode, used for FIB/SEM analysis
LFP2_AR	-	-	-	-	Cathode, used for FIB/SEM analysis
Gr2_F	-	-	-	-	Anode, used for FIB/SEM analysis
Gr2_AB	-	-	-	-	Anode, used for FIB/SEM analysis
Gr2_AR	-	-	-	-	Anode, used for FIB/SEM analysis

As shown in Fig. 5.26b, the negative graphite foil is characterized by a blue shadowed region in the part of the foil close to the skin of the battery and a red region close to the core. In the presented photo the colors are oversaturated to enhance the visibility of the blue and the red region. The color covers almost completely the center of the anode foil (Fig. 1b), with the exception of the sides of the electrode, where the original dark grey color of graphite is observed. Circular electrode samples from the center of the core and the skin of the graphite foil were punched out. Similar electrode samples were harvested from the adjacent sites at the LFP electrode. Additionally samples were collected from the fresh electrodes (labeled with F as suffix) to allow comparison of fresh and aged electrode

samples. The electrodes extracted from the skin of the aged battery are then labeled with AB (aged, blue) as suffix, while the ones from the core are labeled with AR (aged, red).

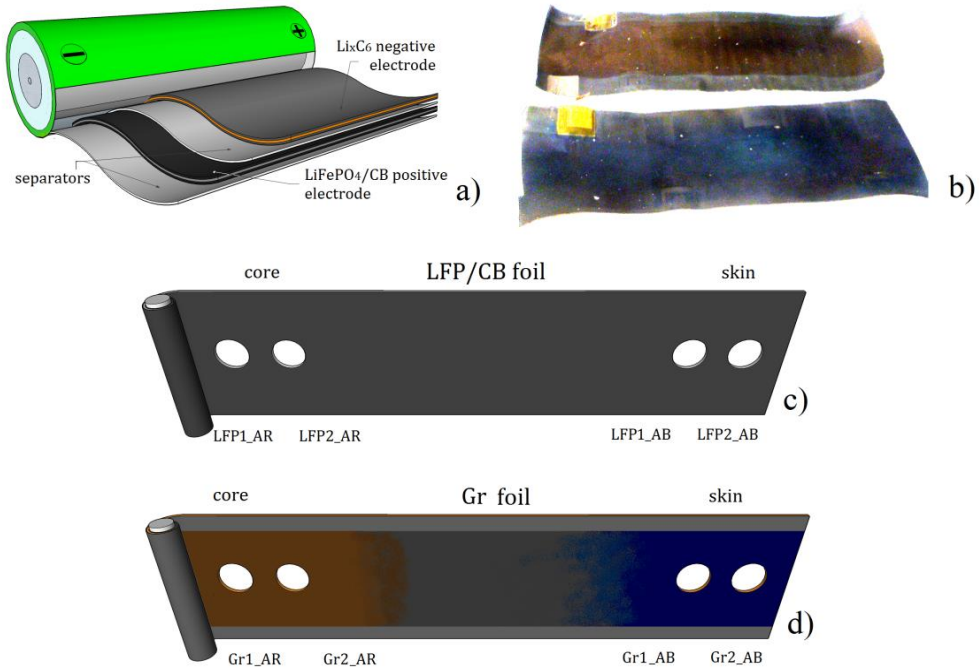

Figure 5.26. a) Schematic representation of the 26650CC $LiFePO_4$/C battery packaging design. b) Two pieces of the aged Li_xC_6 negative electrode (upper part from the core, lower part from the skin). The image has saturated colors to highlight the color contrast. c) Schematic representation of electrodes punched out from LFP/CB and d) Gr foils.

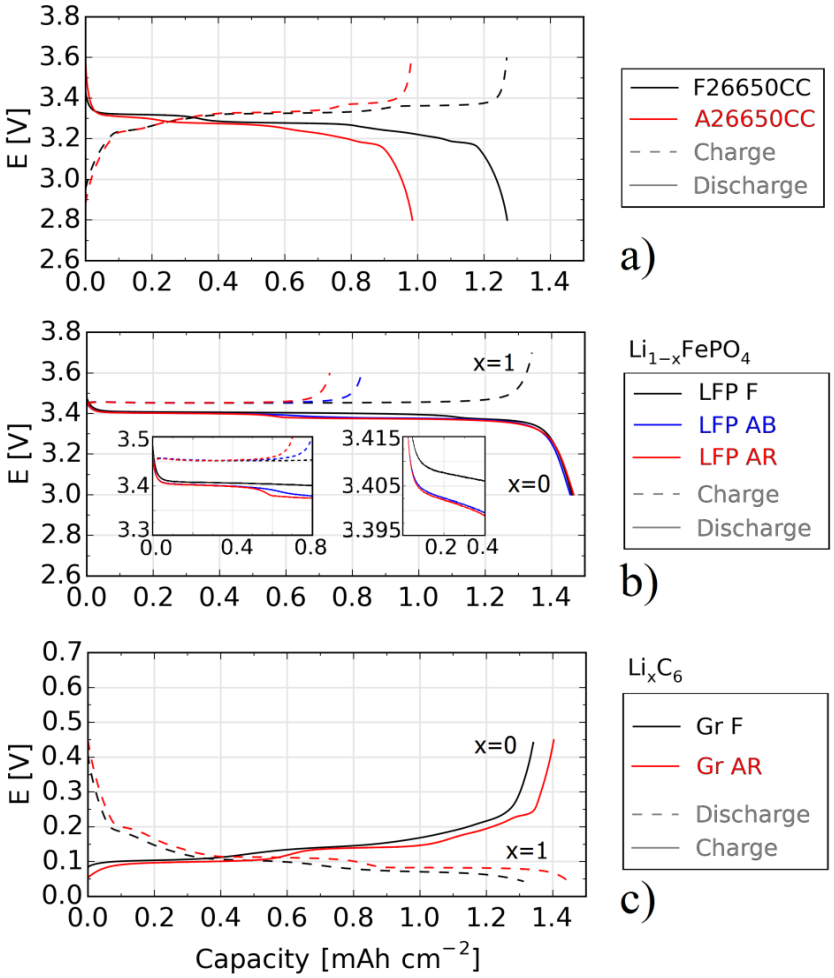

Figure 5.27. Charge/Discharge curves of a) F26650CC and A26650CC, b) LFP (fresh, aged blue and red) and c) Gr (fresh, aged blue and red)

Fig. 5.27a shows the charge/discharge curves for the fresh and aged cylindrical cell (F26650CC and A26650CC). To separate the single electrode contributions the two commercial cells have been subsequently de-assembled in the discharged state, fresh and aged LFP/CB1 and fresh and aged Gr1 were extracted and run in three-electrode setup with a lithium metal counter and reference electrode.

Fig. 5.27b and 5.27c show respectively the charge/discharge curves for the three LFP/CB1 and two Gr1 electrodes. LFP1_AB and LFP1_AR electrodes show capacity losses equal to 37% and 45% respectively. From the discharge curves however the aged electrodes are able to completely recover their initial capacity in both regions, showing that there are no electrochemically inactive regions. A little step in lithium intercalation is observed in the discharge curves of LFP1_AB and LFP1_AR, as shown in the left inset in

Fig. 5.27b. The right inset shows that the over polarization for the two aged samples is about 5 mV higher than that for LFP1_F. No big differences are instead observed between the charge/discharge curves of the Gr1_F and Gr1_AR, the aged sample even show a 4% higher capacity.

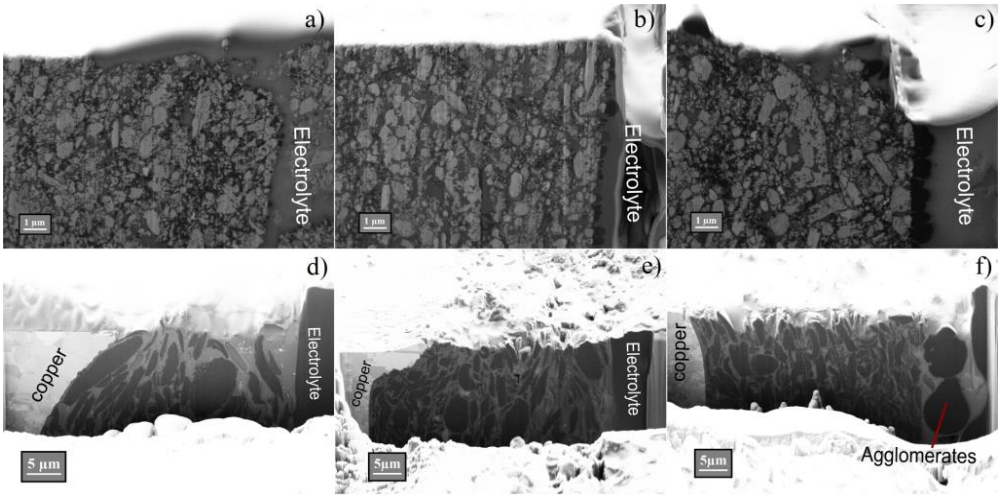

Figure 5.28. SEM images at 1 kV recorded with Lateral E – T detector of a) LFP2_F, b) LFP2_AB, c) LFP2_AR, d) Gr2_F, e) Gr2_AB and f) Gr2_AR electrodes.

The FIB/SEM analysis of the three LFP2 electrodes showed some changes in the morphology of the electrode with cycling (Fig. 5.28a,b,c). First of all the LFP particle are observed to slightly smaller in the two aged samples, as shown in PSD analysis in **paper VI**. This could probably be an effect of LFP cracking with cycling [30], [31], [81], [82]. The cracking may also increase the porosity of the aged electrodes, as observed by comparing the pore volumes for the three electrodes (see **paper VI**). The CB black particles are also observed to have a smaller size in the aged samples and their volume fraction is around a half of what is found in LFP2_F. The most important degradation process seems to be the formation of a layer at the electrode/electrolyte interface (Fig. 5.28b,c). The layer is possibly a mixture of carbon and electrolyte decomposition products [81], [82], [83], [84]. The layer is expected to partially block the electrolyte passage thereby increasing the ionic resistance, as also shown in the 3D reconstruction in Fig 5.29. This increases the over polarization of the aged electrodes during charge/discharge cycling (Fig. 5.27b, insets). CB agglomeration is influenced by the CB/LFP ratio in the electrode material [36]. The layer at the electrolyte/electrode interface is probably composed by a mixture of CB and decomposition products from the electrolyte, i.e. Li-organic species, fluorophosphates and LiF [35] and could thus in part explain the loss of lithium inventory (LLI) observed in Fig. 5.27b. The layer is found to be thickest in the sample collected from the core of the cylindrical battery, which could be an effect of the accelerated degradation of the electrolyte caused by the higher temperature [85], [86] developed in the core of the cylindrical cell [87].

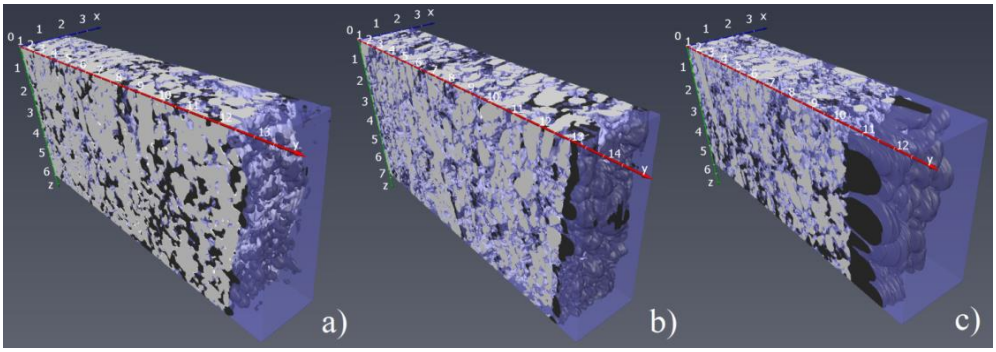

Figure 5.29. 3D reconstruction of a) LFP2_F, b) LFP2_AB and c) LFP2_AR electrodes. The scale bar units are [µm].

FIB/SEM tomography of the Gr2 electrodes also revealed formation of big agglomerates sitting at the electrode/electrolyte interface (Fig. 5.28f). The volume fraction between CB and pores (see PSD analysis in **paper VI**) is the same for the fresh and the aged sample, however from PSD analysis it is seen that the graphite particles are significantly smaller in Gr2_AR than in Gr2_F. This is probably an effect of cracking of Gr particles with cycling [88], [89].

Figures 5.30 shows cross-sectional In-lens images recorded a 1 kV after FIB milling of all LFP2 and Gr2 electrodes respectively. The low accelerating voltage enables a detection of charging effects on carbonaceous materials [81], [82]. The CB particles in the LFP2 electrodes do not seem to charge, however some of the agglomerates in LFP2_AB are noticed to charge (shown in the red rings, Fig 5.30b).

A few graphite grains are observed to charge in Gr2_F (shown in the red rings, Fig. 5.30d), and a higher amount of particles are observed to charge in Gr2_AB and Gr2_AR (Fig. 5.30e,f), in particular in the part of the electrodes closest to the electrode/electrolyte interface.

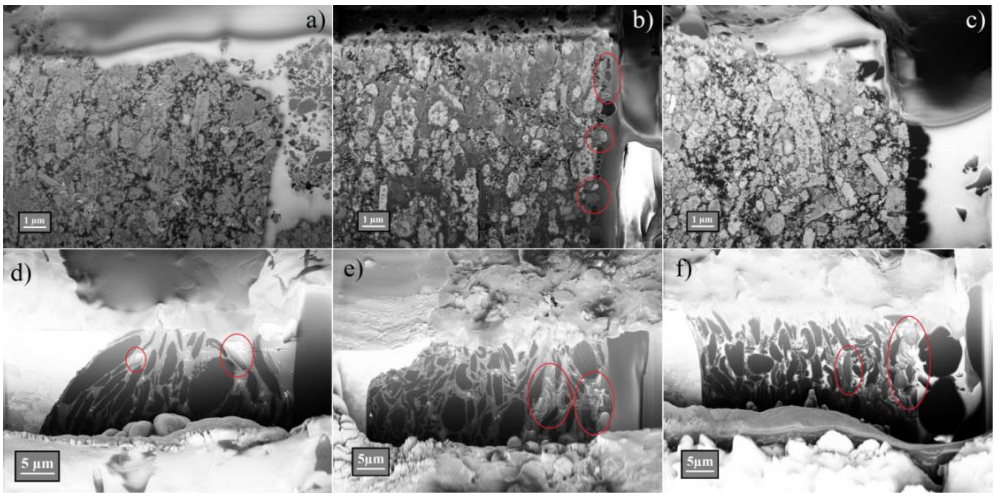

Figure 5.30 SEM images at 1 kV recorded with In-lens detector of a) LFP2_F, b) LFP2_AB, c) LFP2_AR, d) Gr2_F, e) Gr2_AB and f) Gr2_AR electrodes.

The low – kV analysis permitted the identification and quantification of locally charged Gr particles in the negative electrode sample, and a distinction between "percolating" and "non-percolating" graphite particles was possible. Non-percolating graphite particles count for 0.8% and 30% in Gr2_F and Gr2_AR respectively. The bright graphite particles are predominantly found in the region of the electrode closest to the electrode/electrolyte interface. This charging effect are not fully understood yet, however they are believed to describe graphite particles that are disconnected from the electron percolating network. Several Gr grains show in fact a flickering intensity between two consecutive images during the milling job. This is probably an effect of connection/disconnection of the same particle from the percolating network concurrently with the ion milling. Furthermore, cracking of graphite particles with cycling, as previously suggested by PSD calculation, would create new carbon/electrolyte interfaces which would be covered by SEI layer after electrolyte decomposition, which is known to be an electron insulator [11], [68], [90]. This would of course create new secondary smaller graphite grains with an increased electronic resistance.

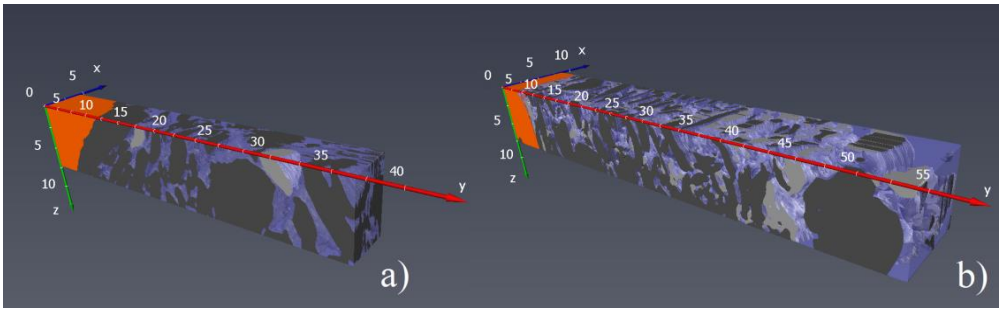

Figure 5.31. 3D reconstruction of a) Gr2_F and b) Gr2_AR electrodes. The scale bar units are [µm].

Fig. 5.31 shows the 3D reconstructions of low-kV In-lens images of Gr2_F and Gr2_AR electrodes. Large agglomerates with a diameter between 5-10 µm in diameter are seen at the Gr2_AR electrode/electrolyte interface. As already explained above this agglomerates, probably composed by a mixture of CB and decomposition products from the electrolyte, also contribute to the LLI.

In conclusion the degradation of a cylindrical cell has been analyzed in **paper VI** by electrochemical and physical-chemical characterization. Loss in performances could not be addressed to loss of electrochemically active material (LAM) from either positive or negative electrode, but is most likely due to LLI which occurs in relation to the deposition of a thick layer at the electrode/electrolyte interfaces. In addition a loss of electron dissipation capability is observed in the graphite electrode.

Concluding Remarks and Future Outlook 6

The aim of this thesis was to investigate the performance and lifetime limiting effects in Li-ion batteries, trying to understand the detailed coupling between degradation mechanisms and battery usage. The main focus has been the characterization of the cathode material $LiFePO_4$ (LFP) and carbon black (CB) additives, but the project was also used to study the degradation of graphite anodes. Several characterization techniques have been used to thoroughly study the morphological and structural degradation of the battery electrode materials and link the results to the loss in performance observed by electrochemical testing.

The PhD project has been divided in two main parts: The first part was dedicated to the study of the aging mechanisms that occur in laboratory batteries ($LiFePO_4$ cathode and Carbon Black additives) and the second part focused on the characterization of commercial $LiFePO_4$/Graphite 26650 cylindrical cells.

Laboratory batteries. The structural and morphological degradation of laboratory $LiFePO_4$/C cathodes subjected to cycling has been studied by Electrochemical Impedance Spectroscopy, low-kV FIB/SEM Tomography and TEM analysis. The two main degradation processes observed in the aged electrode were cracking of LFP particles and agglomeration of CB additive. The increased heterogeneity of the CB network reduces the electron percolation throughout the porous electrode thereby increasing the amount of electrochemically active LFP particles. The percolation analysis of the CB additive has been performed by low-voltage SEM analysis, combined for the first time with a FIB, and observing some localized charge phenomena on the surface non-percolated CB particles. This allowed to study the electron percolation in 3D, identifying and quantifying the amount of "non-percolating" CB, which was observed to be around 25% of the total network. These charging phenomena are not fully understood yet, but could be either correlated to disconnected CB particles from the conductive network or change in the bulk electron conductivity. TEM analysis of this agglomerates showed the presence of an amorphous structure of what seems to be a mixture of CB and decomposition products from the electrolyte, which could have lower electron conductivity than the quasi-crystalline fresh CB.

Impedance analysis of fresh and aged LFP cathode has been also performed and an equivalent circuit, consisting of a TLM for porous electrode, has been proposed and validated for the modelling of impedance spectra. From comparison of EIS spectra of fresh and degraded cathode an increase in electron resistivity R_{el} through the carbon black

network was observed by fitted results of the TLM, nicely correlating with main findings from microscopy analysis.

Commercial batteries. The EIS model developed for the laboratory LFP cathode has been applied to model the positive electrode of a commercial $LiFePO_4$/Graphite 26650 cylindrical cell. Furthermore another equivalent circuit, consisting of a different TLM, has been developed for the graphite negative electrode and, from the combination of these two TLMs, a final equivalent circuit model was proposed to model the commercial cell impedance spectra.

The analysis of the aging mechanisms occurring in the commercial cells was again performed by low-kV FIB/SEM tomography. Only 22.5% of capacity loss was observed after 22k cycles, but from GCPL analysis in three-electrode setup, both LFP and graphite seems to not be affected by degradation. However a thick layer of decomposition products possibly from the electrolyte and carbon in the electrodes is observed at the electrode/electrolyte interfaces. This degradation mechanism seems to be comparable with the one observed in the laboratory cell and could maybe be responsible for the loss of lithium inventory (LLI).

6.1. Outlook

The study of aging mechanisms occurring in Li-ion batteries is of vital importance for the development and improvement of future highly performing materials. The development of new advanced characterization techniques plays an important role in the battery failure analysis.

During this three years PhD project a new technique has been developed for the electron percolation analysis in CB network exploiting locally charging phenomena. However the explanation of the presence of “non-percolating” and “amorphous” carbon is still not fully understood. Furthermore the presence (and composition) of a thick carbonaceous layer on the commercial cell electrodes needs to be fully explained, since it could be either an effect of electrolyte decomposition or graphite cracking and exfoliation. A combined surface analysis (e.g. XPS) and high resolution TEM on a FIB lamella of the electrode/electrolyte interface could possibly give us more information about this.

Bibliography

[1] Z. Yang, J. Zhang, M. C. W. Kintner-meyer, X. Lu, D. Choi, and J. P. Lemmon, "Electrochemical energy storage for green grid.pdf," *Chem. Rev.*, pp. 3577–3613, 2011.

[2] H. Ibrahim, A. Ilinca, and J. Perron, "Energy storage systems-Characteristics and comparisons," *Renew. Sustain. Energy Rev.*, vol. 12, no. 5, pp. 1221–1250, 2008.

[3] M. Chowdhury, "Grid integration impacts and energy storage systems for wind energy applications—A review," *Power Energy …*, pp. 1–8, 2011.

[4] G. Coppez, S. Chowdhury, and S. P. Chowdhury, "The Importance of Energy Storage in Renewable Power Generation : A Review," *45th Int. Univ. Power Eng. Conf. (UPEC), 2010*, pp. 1–5, 2010.

[5] B. R. Alamri and a R. Alamri, "Technical Review of Energy Storage Technologies when Integrated with Intermittent Renewable Energy," *Int. Conf. Sustain. Power Gener. Supply*, pp. 1–5, 2009.

[6] B. Dunn, H. Kamath, and J.-M. Tarascon, "Electrical Energy Storage for the Grid: A Battery of Choices," *Science (80-.).*, vol. 334, no. 6058, pp. 928–935, 2011.

[7] B. Scrosati, J. Hassoun, and Y.-K. Sun, "Lithium-ion batteries. A look into the future," *Energy Environ. Sci.*, vol. 4, no. 9, p. 3287, 2011.

[8] B. Scrosati and J. Garche, "Lithium batteries: Status, prospects and future," *J. Power Sources*, vol. 195, no. 9, pp. 2419–2430, 2010.

[9] P. Van den Bossche, F. Vergels, J. Van Mierlo, J. Matheys, and W. Van Autenboer, "SUBAT: An assessment of sustainable battery technology," *J. Power Sources*, vol. 162, no. 2 SPEC. ISS., pp. 913–919, 2006.

[10] Huggins, *Advanced batteries*, vol. 276. 2009.

[11] S. C. Nagpure, B. Bhushan, and S. S. Babu, "Multi-Scale Characterization Studies of Aged Li-Ion Large Format Cells for Improved Performance: An Overview," *J. Electrochem. Soc.*, vol. 160, no. 11, pp. A2111–A2154, 2013.

[12] G. Amatucci, a Du Pasquier, a Blyr, T. Zheng, and J. Tarascon, "The elevated temperature performance of the LiMn 2 O 4 / C system : failure and solutions," *Electrochim. Acta*, vol. 45, pp. 255–271, 1999.

[13] K. S. Lee, H. J. Bang, S. T. Myung, J. Prakash, K. Amine, and Y. K. Sun, "Synthesis and electrochemical properties of spherical spinel Li1.05M0.05Mn1.9O4 (M = Mg and Al) as a cathode material for lithium-ion batteries by co-precipitation method," *J. Power Sources*, vol. 174, no. 2, pp. 726–729, 2007.

[14] Y.-K. Sun, S.-T. Myung, B.-C. Park, J. Prakash, I. Belharouak, and K. Amine, "High-energy cathode material for long-life and safe lithium batteries.," *Nat. Mater.*, vol. 8, no. 4, pp. 320–324, 2009.

[15] K. Zaghib, a. Guerfi, P. Hovington, a. Vijh, M. Trudeau, a. Mauger, J. B. Goodenough, and C. M. Julien, "Review and analysis of nanostructured olivine-based lithium recheargeable batteries: Status and trends," *J. Power Sources*, vol. 232, pp. 357–369, 2013.

[16] J. B. G. A. K. Padhi, K. S. Nanjundaswamy, "Phospho-olivines as Positive-Electrode Materials for Rechargeable Lithium Batteries," vol. 144, no. 4, pp. 1188–1194, 1997.

[17] Y. Zhang, Q. Huo, P. Du, L. Wang, A. Zhang, Y. Song, Y. Lv, and G. Li, "Advances in new cathode material LiFePO4 for lithium-ion batteries," *Synth. Met.*, vol. 162, no. 13–14, pp. 1315–1326, 2012.

[18] Y. Wang, P. He, and H. Zhou, "Olivine LiFePO4: development and future," *Energy Environ. Sci.*, vol. 4, no. 3, p. 805, 2011.

[19] W. J. Zhang, "Structure and performance of LiFePO4 cathode materials: A review," *J. Power Sources*, vol. 196, no. 6, pp. 2962–2970, 2011.

[20] C. V. Ramana, A. Mauger, F. Gendron, C. M. Julien, and K. Zaghib, "Study of the Li-insertion/extraction process in LiFePO4/FePO4," *J. Power Sources*, vol. 187, no. 2, pp. 555–564, 2009.

[21] C. Delmas, M. Maccario, L. Croguennec, F. Le Cras, and F. Weill, "Lithium deintercalation in LiFePO4 nanoparticles via a domino-cascade model.," *Nat. Mater.*, vol. 7, no. 8, pp. 665–71, 2008.

[22] Y. Liu and C. Cao, "Enhanced electrochemical performance of nano-sized LiFePO4/C synthesized by an ultrasonic-assisted co-precipitation method," *Electrochim. Acta*, vol. 55, no. 16, pp. 4694–4699, 2010.

[23] S. Lim, C. S. Yoon, and J. Cho, "Synthesis of nanowire and hollow LiFePO4 cathodes for high-performance lithium batteries," *Chem. Mater.*, vol. 20, no. 14, pp. 4560–4564, 2008.

[24] M. E. Spahr, D. Goers, A. Leone, S. Stallone, and E. Grivei, "Development of carbon conductive additives for advanced lithium ion batteries," *J. Power Sources*, vol. 196, no. 7, pp. 3404–3413, 2011.

[25] K. Sheem, Y. H. Lee, and H. S. Lim, "High-density positive electrodes containing carbon nanotubes for use in Li-ion cells," *J. Power Sources*, vol. 158, no. 2 SPEC. ISS., pp. 1425–1430, 2006.

[26] Y.-H. Chen, C.-W. Wang, G. Liu, X.-Y. Song, V. S. Battaglia, and a. M. Sastry, "Selection of Conductive Additives in Li-Ion Battery Cathodes," *J. Electrochem. Soc.*, vol. 154, no. 10, p. A978, 2007.

[27] X. L. Li, Y. L. Zhang, H. F. Song, K. Du, H. Wang, H. Y. Li, and J. M. Huang, "The comparison of carbon conductive additives with different dimensions on the electrochemical performance of LiFePO 4 Cathode," *Int. J. Electrochem. Sci.*, vol. 7, no. 8, pp. 7111–7120, 2012.

[28] N. H. Kwon, "The effect of carbon morphology on the LiCoO2 cathode of lithium ion batteries," *Solid State Sci.*, vol. 21, no. C, pp. 59–65, 2013.

[29] M-J. Wang, C.A. Gray, S.A. Reznek, K. Mahmud, Y. Kutsovsky, "Carbon Black," vol. 4, pp. 761–803, 2011.

[30] D. Wang, X. Wu, Z. Wang, and L. Chen, "Cracking causing cyclic instability of LiFePO4 cathode material," *J. Power Sources*, vol. 140, no. 1, pp. 125–128, 2005.

[31] H. Gabrisch, J. Wilcox, and M. M. Doeff, "TEM Study of Fracturing in Spherical and Plate-like LiFePO[sub 4] Particles," *Electrochem. Solid-State Lett.*, vol. 11, no. 3, p. A25, 2008.

[32] J. Wang, J. Yang, Y. Tang, R. Li, G. Liang, T.-K. Sham, and X. Sun, "Surface aging at olivine LiFePO4: a direct visual observation of iron dissolution and the protection role of nano-carbon coating," *J. Mater. Chem. A*, vol. 1, no. 5, p. 1579, 2013.

[33] X. Zhi, G. Liang, L. Wang, X. Ou, J. Zhang, and J. Cui, "The cycling performance of LiFePO4/C cathode materials," *J. Power Sources*, vol. 189, pp. 779–782, 2009.

[34] A. Barré, B. Deguilhem, S. Grolleau, M. Gérard, F. Suard, and D. Riu, "A review on lithium-ion battery ageing mechanisms and estimations for automotive applications," *J. Power Sources*, vol. 241, pp. 680–689, 2013.

[35] M. Cuisinier, N. Dupré, J. F. Martin, R. Kanno, and D. Guyomard, "Evolution of the LiFePO4 positive electrode interface along cycling monitored by MAS NMR," *J. Power Sources*, vol. 224, pp. 50–58, 2013.

[36] M. Zhu, J. Park, and a. M. Sastry, "Particle Interaction and Aggregation in Cathode Material of Li-Ion Batteries: A Numerical Study," *J. Electrochem. Soc.*, vol. 158, no. 10, p. A1155, 2011.

[37] X. Qi, B. Blizanac, A. Dupasquier, M. Oljaca, J. Li, and M. Winter, "Understanding the influence of conductive carbon additives surface area on the rate performance of LiFePO4 cathodes for lithium ion batteries," *Carbon N. Y.*, vol. 64, pp. 334–340, 2013.

[38] M. Gaberscek, J. Moskon, B. Erjavec, R. Dominko, J. Jamnik, C. Ho, P. Paolo, M. Lisi, D. Zane, M. Pasquali, M. Park, X. Zhang, M. Chung, G. B. Less, A. M. Sastry, M. Gaberscek, J. Moskon, B. Erjavec, R. Dominko, J. Jamnik, J. H. Sluyters, H. C. Shin, W. Il Cho, H. Jang, P. Paolo, M. Lisi, D. Zane, M. Pasquali, K. Bazzi, B. P. Mandal, M. Nazri, V. M. Naik, V. K. Garg, A. C. Oliveira, P. P. Vaishnava, G. A. Nazri, R. Naik, J. Illig, M. Ender, T. Chrobak, J. P. Schmidt, D. Klotz, E. Ivers-Tiffee, J. P. Meyers, M. Doyle, R. M. Darling, J. Newman, F. Gao, and Z. Tang, "A review of conduction phenomena in Li-ion batteries," *J. Power*

Sources, vol. 148, no. 24, pp. 7904–7929, 2002.

[39] P. Roy and S. K. Srivastava, "Nanostructured anode materials for lithium ion batteries," *J. Mater. Chem. A*, vol. 3, no. 6, pp. 2454–2484, 2015.

[40] Y. P. Wu, E. Rahm, and R. Holze, "Carbon anode materials for lithium ion batteries," *J. Power Sources*, vol. 114, no. 2, pp. 228–236, 2003.

[41] G. K. Simon and T. Goswami, "Improving anodes for lithium ion batteries," *Metall. Mater. Trans. A Phys. Metall. Mater. Sci.*, vol. 42, no. 1, pp. 231–236, 2011.

[42] D.D.L. Chung, "Review Graphite," *J. Mater. Sci.*, vol. 37, pp. 1475–1489, 2002.

[43] J. Yan, J. Zhang, Y. C. Su, X. G. Zhang, and B. J. Xia, "A novel perspective on the formation of the solid electrolyte interphase on the graphite electrode for lithium-ion batteries," *Electrochim. Acta*, vol. 55, no. 5, pp. 1785–1794, 2010.

[44] H. Wang, T. Umeno, K. Mizuma, and M. Yoshio, "Highly conductive bridges between graphite spheres to improve the cycle performance of a graphite anode in lithium-ion batteries," *J. Power Sources*, vol. 175, no. 2, pp. 886–890, 2008.

[45] A. a Franco, "Multiscale modelling and numerical simulation of rechargeable lithium ion batteries: concepts, methods and challenges," *Rsc Adv.*, vol. 3, no. 32, pp. 13027–13058, 2013.

[46] D. U. Sauer, "Charge – Discharge Curves," *Encycl. Electrochem. Power Sources*, pp. 443–451, 2009.

[47] H. Nara, D. Mukoyama, T. Yokoshima, T. Momma, and T. Osaka, "Impedance Analysis with Transmission Line Model for Reaction Distribution in a Pouch Type Lithium-Ion Battery by Using Micro Reference Electrode," *J. Electrochem. Soc.*, vol. 163, no. 3, pp. A434–A441, 2016.

[48] J. Illig, M. Ender, a. Weber, and E. Ivers-Tiffée, "Modeling graphite anodes with serial and transmission line models," *J. Power Sources*, vol. 282, pp. 335–347, 2015.

[49] N. Ogihara, S. Kawauchi, C. Okuda, Y. Itou, Y. Takeuchi, and Y. Ukyo, "Theoretical and Experimental Analysis of Porous Electrodes for Lithium-Ion Batteries by Electrochemical Impedance Spectroscopy Using a Symmetric Cell," *J. Electrochem. Soc.*, vol. 159, no. 7, pp. A1034–A1039, 2012.

[50] J. Bisquert, G. Garcia-Belmonte, P. Bueno, E. Longo, and L. O. . Bulhões, "Impedance of constant phase element (CPE)-blocked diffusion in film electrodes," *J. Electroanal. Chem.*, vol. 452, no. 2, pp. 229–234, 1998.

[51] N. Ogihara, S. Kawauchi, C. Okuda, Y. Itou, Y. Takeuchi, and Y. Ukyo, "Theoretical and Experimental Analysis of Porous Electrodes for Lithium-Ion Batteries by Electrochemical Impedance Spectroscopy Using a Symmetric Cell," vol. 159, no. 7, pp. 1034–1039, 2012.

[52] R. Younesi, a. S. Christiansen, R. Scipioni, D.-T. Ngo, S. B. Simonsen, K. Edstrom, J. Hjelm, and P. Norby, "Analysis of the Interphase on Carbon Black Formed in High Voltage Batteries," *J. Electrochem. Soc.*, vol. 162, no. 7, pp. A1289–A1296, 2015.

[53] G. Garcia-Belmonte, F. Fabregat-Santiago, J. Bisquert, M. Yamashita, E. C. Pereira, and S. Castro-Garcia, "Frequency dispersion in electrochromic devices and conducting polymer electrodes: A generalized transmission line approach," *Ionics (Kiel).*, vol. 5, pp. 44–51, 1999.

[54] R. D. Levie, "On porous electrodes," *Electrochim. Acta*, vol. 9, no. November 1963, p. 1231, 1964.

[55] F. Gao and Z. Tang, "Kinetic behavior of LiFePO4/C cathode material for lithium-ion batteries," *Electrochim. Acta*, vol. 53, no. 15, pp. 5071–5075, 2008.

[56] J. P. Meyers, M. Doyle, R. M. Darling, and J. Newman, "The Impedance Response of a Porous Electrode Composed of Intercalation Particles," *J. Electrochem. Soc.*, vol. 147, no. 8, p. 2930, 2000.

[57] J. Song and M. Z. Bazant, "Effects of Nanoparticle Geometry and Size Distribution on Diffusion Impedance of Battery Electrodes," *J. Electrochem. Soc.*, vol. 160, no. 1, pp. A15–A24, 2013.

[58] G.J.Brug; A.L.G. Van den Eeden; M. Sluyters-Rehbach; J.H. Sluyters, "The Analysis of Electrode Impedances Complicated by the Presence of a Constant Phase Element," *J. Electroanal. Chem.*, vol. 176, pp. 275–295, 1984.

[59] J. R. Wilson, W. Kobsiriphat, R. Mendoza, H.-Y. Chen, J. M. Hiller, D. J. Miller, K. Thornton, P. W. Voorhees, S. B. Adler, and S. a Barnett, "Three-dimensional reconstruction of a solid-oxide fuel-cell anode.," *Nat. Mater.*, vol. 5, no. 7, pp. 541–544, 2006.

[60] L. a. Giannuzzi and F. a. Stevie, *Introduction To Focused Ion*. 2005.

[61] W. Zhou, R. P. Apkarian, and Z. L. Wang, "Fundamentals of Scanning Electron Microscopy," *Scanning Microsc. Nanotechnol.*, pp. 1–40, 2007.

[62] D. Joy, "A database on electron- • solid interactions," *Scanning*, vol. 17, pp. 270–275, 1995.

[63] K. Thydén, Y. L. Liu, and J. B. Bilde-Sørensen, "Microstructural characterization of SOFC Ni-YSZ anode composites by low-voltage scanning electron microscopy," *Solid State Ionics*, vol. 178, no. 39–40, pp. 1984–1989, 2008.

[64] D. Y. Zhang, L. Zhang, P. X. Zhang, M. C. Lin, X. Q. Huang, X. Z. Ren, and Q. M. Xu, "Modification of $LiFePo_4$ by Citric Acid Coating and Nb^{5+} Doping," *Adv. Mater. Res.*, vol. 158, pp. 167–173, 2010.

[65] J. Cazaux, "A new model of dependence of secondary electron emission yield on primary electron energy for application to polymers," *J. Phys. D. Appl. Phys.*, vol.

38, no. 14, pp. 2433–2441, 2005.

[66] J. Illig, M. Ender, T. Chrobak, J. P. Schmidt, D. Klotz, and E. Ivers-Tiffee, “Separation of Charge Transfer and Contact Resistance in LiFePO4-Cathodes by Impedance Modeling,” *J. Electrochem. Soc.*, vol. 159, no. 7, pp. A952–A960, 2012.

[67] D. B. Williams and C. B. Carter, *The Transmission Electron Microscope*. 2009.

[68] C. Shen, S. Wang, Y. Jin, and W. Q. Han, “In Situ AFM Imaging of Solid Electrolyte Interfaces on HOPG with Ethylene Carbonate and Fluoroethylene Carbonate-Based Electrolytes,” *ACS Appl. Mater. Interfaces*, vol. 7, no. 45, pp. 25441–25447, 2015.

[69] R. Younesi, M. Hahlin, M. Treskow, J. Scheers, P. Johansson, and K. Edstro, “Ether Based Electrolyte , LiB (CN)4 Salt and Binder Degradation in the Li − O2 Battery Studied by Hard X-ray Photoelectron Spectroscopy,” *J. Phys. Chem. C*, vol. 116, pp. 18597–18604, 2012.

[70] R. A. Quinlan, Y.-C. Lu, Y. Shao-Horn, and A. N. Mansour, “XPS Studies of Surface Chemistry Changes of LiNi0.5Mn0.5O2 Electrodes during High-Voltage Cycling,” *J. Electrochem. Soc.*, vol. 160, no. 4, pp. A669–A677, 2013.

[71] J. Demeaux, M. Caillon-Caravanier, H. Galiano, D. Lemordant, and B. Claude-Montigny, “LiNi0.4Mn1.6O4/Electrolyte and Carbon Black/Electrolyte High Voltage Interfaces: To Evidence the Chemical and Electronic Contributions of the Solvent on the Cathode-Electrolyte Interface Formation,” *J. Electrochem. Soc.*, vol. 159, no. 11, pp. A1880–A1890, 2012.

[72] R. Younesi, M. Hahlin, M. Roberts, and K. Edstr??m, “The SEI layer formed on lithium metal in the presence of oxygen: A seldom considered component in the development of the Li-O2 battery,” *J. Power Sources*, vol. 225, pp. 40–45, 2013.

[73] M. Onuki, S. Kinoshita, Y. Sakata, M. Yanagidate, Y. Otake, M. Ue, and M. Deguchi, “Identification of the Source of Evolved Gas in Li-Ion Batteries Using 13C-labeled Solvents,” *J. Electrochem. Soc.*, vol. 155, no. 11, p. A794, 2008.

[74] S. Malmgren, K. Ciosek, M. Hahlin, T. Gustafsson, M. Gorgoi, H. Rensmo, and K. Edström, “Comparing anode and cathode electrode/electrolyte interface composition and morphology using soft and hard X-ray photoelectron spectroscopy,” *Electrochim. Acta*, vol. 97, pp. 23–32, 2013.

[75] X. Qi, B. Blizanac, A. DuPasquier, P. Meister, T. Placke, M. Oljaca, J. Li, and M. Winter, “Investigation of PF6− and TFSI− anion intercalation into graphitized carbon blacks and its influence on high voltage lithium ion batteries,” *Phys. Chem. Chem. Phys.*, vol. 16, no. 46, pp. 25306–25313, 2014.

[76] J. a. Seel and J. R. Dahn, “Electrochemical Intercalation of PF[sub 6] into Graphite,” *J. Electrochem. Soc.*, vol. 147, no. 3, p. 892, 2000.

[77] M. Gaberscek, J. Moskon, B. Erjavec, R. Dominko, and J. Jamnik, “The Importance of Interphase Contacts in Li Ion Electrodes: The Meaning of the High-

Frequency Impedance Arc," *Electrochem. Solid-State Lett.*, vol. 11, p. A170, 2008.

[78] A. H. Whitehead and M. Schreiber, "Current Collectors for Positive Electrodes of Lithium-Based Batteries," *J. Electrochem. Soc.*, vol. 152, p. A2105, 2005.

[79] Z. Yang, B. J. Ingram, and L. Trahey, "Interfacial Studies of Li-Ion Battery Cathodes Using In Situ Electrochemical Quartz Microbalance with Dissipation," *J. Electrochem. Soc.*, vol. 161, no. 6, pp. A1127–A1131, 2014.

[80] O. Barbieri, M. Hahn, A. Herzog, and R. Kötz, "Capacitance limits of high surface area activated carbons for double layer capacitors," *Carbon N. Y.*, vol. 43, no. 6, pp. 1303–1310, 2005.

[81] R. Scipioni, P. S. Jørgensen, D.-T. Ngo, S. B. Simonsen, Z. Liu, K. J. Yakal-kremski, H. Wang, J. Hjelm, P. Norby, S. A. Barnett, and S. H. Jensen, "Electron microscopy investigations of changes in morphology and conductivity of LiFePO4/C electrodes," *J. Power Sources*, vol. 307, pp. 259–269, 2016.

[82] R. Scipioni, P. S. Jørgensen, D. T. Ngo, S. B. Simonsen, J. Hjelm, P. Norby, and S. H. Jensen, "Low-voltage FIB/SEM Tomography for 3D Microstructure Evolution of LiFePO4/C Electrode," *ECS Trans.*, vol. 69, no. 18, pp. 71–80, 2015.

[83] M. Klett, R. Eriksson, J. Groot, P. Svens, K. Ciosek Högström, R. W. Lindström, H. Berg, T. Gustafson, G. Lindbergh, and K. Edström, "Non-uniform aging of cycled commercial LiFePO4//graphite cylindrical cells revealed by post-mortem analysis," *J. Power Sources*, vol. 257, pp. 126–137, 2014.

[84] E. Sarasketa-Zabala, F. Aguesse, I. Villarreal, L. M. Rodriguez-Martinez, C. M. López, and P. Kubiak, "Understanding lithium inventory loss and sudden performance fade in cylindrical cells during cycling with deep-discharge steps," *J. Phys. Chem. C*, vol. 119, no. 2, pp. 896–906, 2015.

[85] L. Zhao, I. Watanabe, T. Doi, S. Okada, and J. ichi Yamaki, "TG-MS analysis of solid electrolyte interphase (SEI) on graphite negative-electrode in lithium-ion batteries," *J. Power Sources*, vol. 161, no. 2, pp. 1275–1280, 2006.

[86] M. H. Ryou, J. N. Lee, D. J. Lee, W. K. Kim, Y. K. Jeong, J. W. Choi, J. K. Park, and Y. M. Lee, "Effects of lithium salts on thermal stabilities of lithium alkyl carbonates in SEI layer," *Electrochim. Acta*, vol. 83, pp. 259–263, 2012.

[87] L. H. Saw, Y. Ye, and A. A. O. Tay, "Electrochemical-thermal analysis of 18650 Lithium Iron Phosphate cell," *Energy Convers. Manag.*, vol. 75, pp. 162–174, 2013.

[88] D. Liu, Y. Wang, Y. Xie, L. He, J. Chen, K. Wu, R. Xu, and Y. Gao, "On the stress characteristics of graphite anode in commercial pouch lithium-ion battery," *J. Power Sources*, vol. 232, pp. 29–33, 2013.

[89] S. Bhattacharya, A. R. Riahi, and A. T. Alpas, "A transmission electron microscopy study of crack formation and propagation in electrochemically cycled graphite electrode in lithium-ion cells," *J. Power Sources*, vol. 196, no. 20, pp. 8719–8727,

2011.

[90] V. a. Agubra and J. W. Fergus, “The formation and stability of the solid electrolyte interface on the graphite anode,” *J. Power Sources*, vol. 268, pp. 153–162, 2014.

Appendix 7

I

Journal of Power Sources 307 (2016) 259–269

Contents lists available at ScienceDirect

Journal of Power Sources

journal homepage: www.elsevier.com/locate/jpowsour

Electron microscopy investigations of changes in morphology and conductivity of $LiFePO_4$/C electrodes

Roberto Scipioni [a, *], Peter S. Jørgensen [a], Duc-The Ngo [a, c], Søren B. Simonsen [a], Zhao Liu [b], Kyle J. Yakal-Kremski [b], Hongqian Wang [b], Johan Hjelm [a], Poul Norby [a], Scott A. Barnett [b], Søren H. Jensen [a]

[a] Department of Energy Conversion and Storage, Technical University of Denmark, DTU Risø Campus, Frederiksborgvej 399, 4000 Roskilde, Denmark
[b] Department of Material Science and Engineering, Northwestern University, 2220 Campus Drive, Evanston, IL 60208, USA
[c] School of Materials, The University of Manchester, Oxford Road, Manchester M13 9PL, United Kingdom

HIGHLIGHTS

- Low-kV FIB/SEM is used for first time to analyze degraded $LiFePO_4$/C cathode.
- Contrast difference allow identification of low-conductive carbon at low-kV.
- $LiFePO_4$ cracking and carbon agglomeration observed by conventional FIB/SEM.

GRAPHICAL ABSTRACT

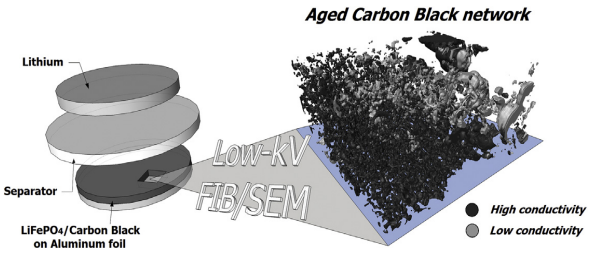

ARTICLE INFO

Article history:
Received 7 September 2015
Received in revised form
24 November 2015
Accepted 23 December 2015
Available online xxx

Keywords:
Low accelerating voltage
Focused ion beam scanning electron microscopy
Three-dimensional analysis of $LiFePO_4$/Carbon electrode
Degradation mechanism
Loss in electron percolation

ABSTRACT

In this work we study the structural degradation of a laboratory Li-ion battery $LiFePO_4$/Carbon Black (LFP/CB) cathode by various electron microscopy techniques including low kV Focused Ion Beam (FIB)/Scanning Electron Microscopy (SEM) 3D tomography. Several changes are observed in FIB/SEM images of fresh and degraded cathodes, including cracks in the LFP particles, secondary disconnected particles, and agglomeration of CB. Low voltage (1 kV) SEM images show that the CB agglomerates have a different brightness than the fresh CB, due to charging effects. This suggests that the electronic conductivity of the CB agglomerates is low compared to that of the fresh CB particles. HRTEM analysis shows that fresh CB particles are quasi crystalline, whereas the LFP/CB interface in the degraded electrode shows amorphous carbon surrounding the LFP particles. The presence of the amorphous carbon is known to impede the electronic conductivity and thereby decreasing percolation in the cathode and reducing the electrode capacity.

1. Introduction

Lithium-ion batteries find widespread use in many electricity storage applications, from portable devices to electric vehicles (EV), because of their high energy density and design flexibility [1–3].

* Corresponding author.
E-mail address: roscip@dtu.dk (R. Scipioni).

http://dx.doi.org/10.1016/j.jpowsour.2015.12.119

However, limited lifetime is still a challenge for several Lithium-ion battery materials. To understand the degradation mechanisms and increase the performance of these materials, the development of improved characterization methods is crucial.

$LiFePO_4$ (LFP) is an interesting material for lithium-ion battery porous cathodes because of its long durability and inherent safety [4,5]. Since LFP is a poor ion and electron conductor, it is usually mixed with carbon black (CB) additives to increase electronic percolation in the electrode. It is well known that mechanical stress related to expansion/contraction of the LFP particles during charging/discharging cycles leads to the formation of micro-cracks inside the LFP particles [6–8], so electronic conductivity and homogeneous dispersion of CB play an important role for long term performance and durability [9,10]. The formation of cracks in the LFP grains leads to disconnected secondary particles, resulting in an increased ionic resistivity and a capacity drop of the electrode. Agglomeration of the CB particles decreases electronic percolation, *i.e.* increasing the electric resistivity in the CB network from the current collector to the LFP particles [10].

Techniques that can directly quantitatively observe the morphology and structure of the CB phase are limited, however. FIB/SEM tomography has been successfully used to quantify the 3D microstructure of porous electrodes [11–15], and to observe changes in porosity, crack formation, and grain agglomeration [16,17] but, to our best knowledge, no one have used low-kV FIB/SEM tomography to study electron percolation in CB phase. *Thydén* et al. showed that low-kV SEM imaging is an excellent technique on conventional polished cross-sections for studying electron percolation in the Ni-network in solid oxide fuel cells (SOFC) [18] but it has never been combined with a FIB to study three-dimensionally the electron percolation.

In this work, the degradation of a laboratory-made LFP/CB porous cathode is studied using various electron microscope techniques, including low-kV FIB/SEM tomography. The low-voltage percolation contrast technique shows that the CB agglomerates have lower electronic conductivity in the bulk than that of the fresh CB particles. HRTEM analysis of the LFP/CB interface indicates that the CB agglomerates are amorphous, in contrast to fresh CB particles which are quasi-crystalline. This explains the low CB agglomerate bulk electronic conductivity [19,20].

2. Methods and materials

2.1. Electrode fabrication and test conditions

Slurry was made of commercial $LiFePO_4$ powder (already carbon coated, from MTI), Super C65 carbon black (from Timcal) and Polyvinylidene Fluoride (PVdF) as binder, with the ratio 80:10:10. From this slurry the electrode material was prepared by casting on aluminum foil. After drying, the thickness was approximately 22 μm thick and two electrodes with a diameter of 18 mm were punched out. The two electrodes were tested in an EL-CELL® ECC-Combi 3-electrode setup, using lithium metal foils counter electrodes, lithium metal as reference electrode and a glass fiber separator soaked with a standard 1 M $LiPF_6$ in 1:1 EC/DMC electrolyte. Both cells were cycled at constant C-rate using a Biologic VMP3 with Pstat/Gstat boards. Table 1 shows the test conditions for the two electrodes.

The first electrode, denoted “Fresh”, was cycled just two times while the second one, denoted “Aged”, was cycled 100 times. Both cells were cycled between 3 and 4 V at a constant current of 17 mA g^{-1}, corresponding to approximately 0.1 C-rate for the fresh electrode. Both electrodes were left in the discharged state before being de-assembled for microscopy analysis.

Table 1
Test conditions for the examined laboratory LFP electrodes.

Electrode	Current (mA g^{-1})	Total cycle number	Remaining capacity
Fresh	17	2	~100%
Aged	17	100	~30%

2.2. FIB/SEM microscopy

FIB tomography and SEM imaging was carried out on a Zeiss 1540XB CrossBeam microscope, using a lateral E-T (Everhart-Thornley) detector and an In-lens detector. Two 3D datasets were collected from the fresh electrode (labeled as F1 and F2) and three from the aged one (labeled as A1, A2 and A3). Conventional SEM imaging has been also performed in another region of the aged sample (A4). Table 2 shows the volume sizes of the 5 different 3D datasets. A Gallium FIB slicing probe of 2 nA was used and the thickness of each slice was estimated to be 40 nm. The serial sectioning imaging was performed at 1 kV with a pixel size of 15 × 15 nm^2, i.e. the voxel size in the 5 3D-data sets was 40 × 15 × 15 nm^3. Conventional SEM imaging was performed at 10 kV, with a pixel size of 15 × 15 nm^2. The electrodes were prepared for the FIB tomography by rinsing with diethyl carbonate and vacuum infiltrated with a silicon resin (Wacker Chemie) for 30 min to improve phase contrast between CB particles and pores as described by *Ender* et al. [13]. Subsequently the sample was infiltrated with epoxy resin to enable high-quality grinding and polishing of the sample.

2.3. Low-voltage percolation contrast

Thydén et al. [18] previously used low-voltage SEM imaging to identify percolation in SOFC anode Ni-network. Here we briefly describe the theory behind the percolation contrast.

As the electron beam hit the specimen, a variety of elastic and inelastic scattering of the electrons in the specimen occurs. The elastic and inelastic scattered electrons produce respectively backscattered and secondary electrons (BSE and SE). SEs have by definition energies <50 eV. BSEs have energies close to the acceleration voltage (in our case 1 kV). The SE signal is typically divided into three different kinds of secondary electrons [18,21,22]:

1. SE_1, generated by interaction of the primary electron beam with the specimen.
2. SE_2, generated by outgoing BSE.
3. SE_3, generated by the interaction of BSEs with the internal components of the chamber.

The In-lens detector, situated in the electron column, detects low energy electrons very efficiently due to the beambooster of the GEMINI column (Carl Zeiss, Germany) [23]. This means that the In-lens detector signal contains a high fraction of SE_1 and SE_2 electrons. At the same time the In-lens detector acts as a low energy filter for the E-T detector such that it primarily detects higher

Table 2
Volumes of collected datasets.

Dataset	Volume (voxels) X × Y × Z	Volume (μm^3) X × Y × Z
F1	250 × 683 × 341	10 × 10 × 5
F2	141 × 683 × 341	5.6 × 10 × 5
A1	250 × 683 × 341	10 × 10 × 5
A2	131 × 683 × 341	5.2 × 10 × 5
A3	150 × 683 × 341	6 × 10 × 5

energy electrons (>40 eV) [24].

The interaction volume decreases with the electron acceleration voltage. The visualization of electron percolation in materials is possible at low-kV due to the smaller interaction volume. At higher accelerating voltages the penetration depth of the primary beam is significantly larger (2–3 μm at 10 kV and 20–40 nm at 1 kV). For this reason observation of local small-feature charge phenomena is only possible at a low (~1 kV) acceleration voltage.

Fig. 1a shows a general trend of how the SE yield varies in the low-voltage range for a number of materials comparable to the Si-resin [25,26]. For beam energies higher than E_2 and lower than E_1 (the crossover voltages) less than 1 secondary electron is generated per incident electron. For beam energies between E_1 and E_2 more than 1 secondary electron is generated per incident electron. If the total electron yield (SE and BSE) differs from 1 a surplus or deficit of electrons will build up locally in the specimen. For many polymers E_1 is usually equal to or lower than 0.1 kV, while E_2 is in the range 0.6–1.5 kV, and δ_{max} is between 2 and 4 [23,27]. Fig. 1b presents carbon SE yield data compiled from data presented by D.C. Joy [28]. The SE yield curves follow the same general trend as observed for polymers [25,26] as depicted in Fig. 1a. Based on Fig. 1b, unfortunately it cannot be concluded whether the yield is higher or lower than 1 at 1 kV based on the presented knowledge for Carbon SE and BSE coefficients. From Fig. 1a Si-resin is expected to charge positively.

BSE coefficient for carbon is reported to be quite low, varying between 0.05 and 0.15 [28]. Additionally, a Monte Carlo simulation performed with Casino [29] software indicates that the BSE coefficient for Carbon is 0.06–0.11. BSE values for silicon resin have not been found in literature but a Monte Carlo simulation [29] indicates that they are in the range 0.1–0.12. According to these values, the SE coefficient contributes the most to the total electron yield.

For electron conducting phases with a connection to ground the local buildup of charge is rapidly equalized and no charging effects will occur. For insulators, the lack of charge dissipation means that balancing of the ingoing and outgoing electrons will occur mainly through charging of the particles which changes the secondary electron yield:

- Total electron yield >1: the sample will charge positively. Emission of low energy electrons will be impeded to balance the yield.
- Total electron yield <1: the sample will charge negatively. Deceleration or deflection of the incident beam and emission of additional low energy electrons will balance the yield.

To sum up sufficiently accurate yield-coefficient-values at 1 kV for the carbon black are not readily available and the best indication of the charging regime (positive, negative or not charging) for the two phases of carbon (non-electron-dissipating and electron-dissipating) is thus to observe their characteristic intensities. As mentioned, the silicon resin used to infiltrate the specimens has a total electron yield higher than 1, meaning that it is expected to charge positively and appear bright, when imaged at 1 kV.

As described above, the result of beam induced charging in an insulator will primarily change the yield of the lowest energy electrons. The contrast changes due to charging are thus almost exclusively seen in the In-lens detector images and the E-T detector images are largely unaffected. It is important to note that this technique only allows us to determine relative differences in the yield and conductivity of each phase; it does not allow a direct quantification of the conductivity.

2.4. Image processing

Segmentation of the 3D FIB/SEM image data was performed with the program ImageJ (NIH). Because of uneven illumination, setting a single threshold for entire micrographs was not feasible. Therefore the Sauvola algorithm [30,31] was so used to perform local thresholds of the data. The Sauvola algorithm works by dividing the input image into square windows ($n \times n$ pixel) and setting thresholds for each of them based on the mean and standard deviation of the pixel intensities. Visualizations of the 3D reconstructions of the analyzed data were performed with the program Avizo (FEI).

The particle size distributions (PSD) of LFP and CB phases in both fresh and aged samples were analyzed based on the method introduced by Münch et al. [32]: The segmented 3D volumes are filled with spheres of a given radius. By reducing the radius incrementally, more volumes will be filled. The cumulative PSD is then obtained by correlating the incrementally filled volume with corresponding radii.

2.5. Transmission electron microscopy

TEM specimen of the fresh sample was prepared by dropping a small drop of cathode solution on an Au TEM grid supported with a holey carbon film, and naturally drying at 120 °C in the air. TEM specimen of the age sample cured in Si resin was prepared by FIB. Transmission electron microscopy (TEM) characterizations (including HRTEM, STEM and X-ray spectroscopy analysis) were conducted on a JEOL JEM 3000F equipped with a 300 kV field emission gun (FEG), high annular angle dark field (HAADF) STEM detector, and an Oxford Instruments X-ray detector with an ultra-thin window for EDX analysis.

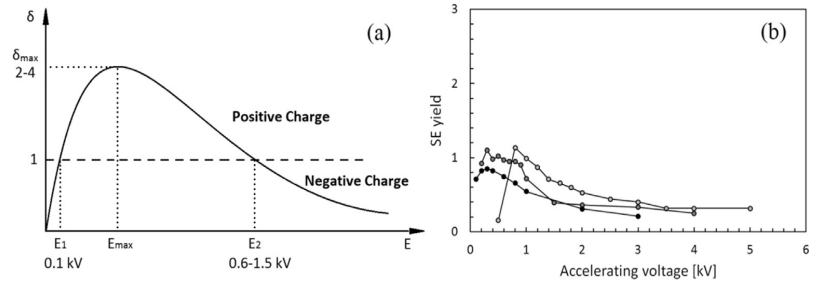

Fig. 1. a) General SE yield curve in the low-voltage range and b) SE yield for carbon according to data compiled by D.C. Joy [28].

3. Results

3.1. SEM images

Fig. 2 shows SEM images after FIB slicing recorded at 1 kV of the fresh electrode (region F1, Fig. 2 a,b) and aged electrode (region A1, Fig. 2 c,d), and recorded at 10 kV of the aged electrode (region A4, Fig. 2 e,f). The images were recorded with the E-T detector (Fig. 2 a,c,e) and with the In-lens detector (Fig. 2 b,d,f).

In the images recorded at 1 kV with the E-T detector (Fig. 2 a,c) it is possible to distinguish three different phases: the grains with the brightest contrast correspond to LFP particles, the almost black regions correspond to CB and the large gray areas in-between correspond to pores filled with silicon resin. The fresh electrode (Fig. 2a) shows a relatively homogeneous distribution of sub-micrometer LFP grains and CB particles. On the contrary, the aged sample (Fig. 2c) has a less homogeneous distribution of both LFP and CB and an increased porosity. The aged sample is further characterized by the presence of larger CB agglomerates surrounding some LFP grains, which is not observed in the two images of the fresh electrode. The increased agglomeration is expected to result in a decrease in the percolation of the CB network [9,10].

In the images recorded at 1 kV with the In-lens detector it can further be observed that the silicon resin has high intensity in the parts of the sample not adjacent to electron conducting phases (Fig. 2b). The two detectors give different type of contrast and sensitivity to charging, as discussed in the theory section. This indicates that the silicon resin is charging negatively due to low conductivity to the ground [23]. It is expected that the CB network has a good conductivity and connectivity to ground. Consistent with this expectation, the CB in the fresh sample has a dark contrast, which indicates minimal charging (Fig. 2b). However, in the aged electrode on (Fig. 2d) large agglomerations (circled in red) of what appears to be CB are brighter than other CB regions. This indicates that those agglomerations are charging negatively i.e. have lost connection to ground and/or have low conductivity.

Furthermore, a transition layer (pointed out by green arrows) with intermediate intensity between the CB agglomerates and the silicon resin is also observed as rims around the CB agglomerates in Fig. 2d. This indicates a transition zone where the silicon is able to

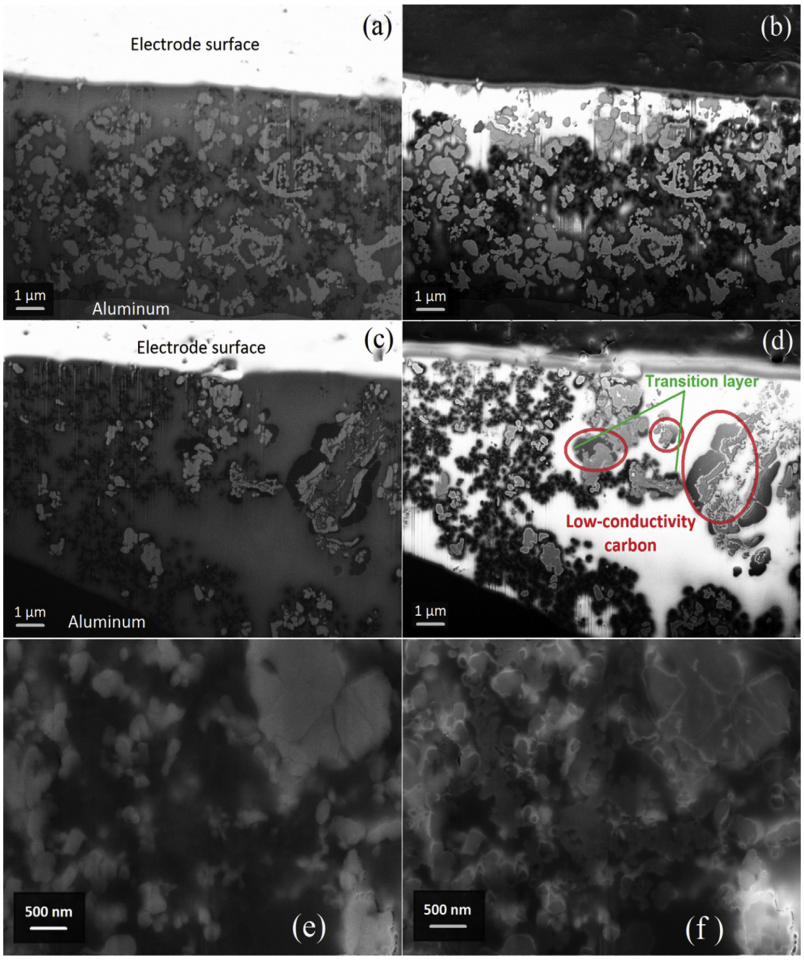

Fig. 2. SEM images at 1 kV of the (a–b) fresh and (c–d) aged electrode recorded with the (a,c) Lateral E-T and (b,d) In-lens detector. SEM images at 10 kV of the (e–f) aged electrode (A4) recorded with the (e) lateral E-T and (f) In-lens detector.

dissipate charge to the CB phase. In the images recorded with the In-lens detector, the LFP particle has a brighter contrast than the CB, which, as one would expect, indicate low electronic conductivity of the LFP particles.

Fig. 2 (e,f) shows SEM images of the aged electrode, at higher magnification recorded at 10 kV. With the relatively high energy of 10 kV, the electrons penetrate app. 2–3 μm into the sample surface and the images therefore give insight into the internal structure of the particles.

SEM images at 10 kV show cracks in some of the LFP grains in area (A4) of the aged electrode (e.g. the large grain in the top right corner of Fig. 2e). The cracks are expected to be caused by expansion/contraction of the particle during the lithiation/delithiation process. In the In-lens detector image (Fig. 2f) many of the cracks appear as bright highlights due to the easier escape path of secondary electrons at topological LFP edges through the epoxy.

3.2. FIB tomography

The SEM images from the five datasets F1, F2, A1, A2 and A3 are used for three-dimensional reconstructions. Fig. 3 shows the 3D FIB tomography reconstruction after image segmentation of the 1 kV Lateral E-T image dataset from the fresh (F1) and aged (A1) electrodes, respectively. LFP grains are represented as gray, CB as black, while pores are shown as transparent. From the figure it can be observed again that compared to F1, all phases are less homogeneously distributed in A1. Further, the presence of large CB agglomerates are seen in A1.

From the segmentation of the 3D datasets presented in Fig. 3 it is possible to extract and calculate statistical data. Table 3 shows calculated phase fractions for all the analyzed volumes. Relative to the fresh electrode, the aged electrode is characterized by a larger variation in the volume fraction of pores and of CB. This is in agreement with the 2D SEM analysis, where the aged sample was observed to be less homogeneous (Fig. 2).

Particle size distribution (PSD) for the LFP phase in the five 3D dataset is presented in Fig. 4. It shows a slight shift towards smaller grains in the aged samples compared to the fresh ones and this could be explained by cracking of the particles. The PSD of CB has not been calculated because of the size of the majority of the CB particles is below or comparable to the slicing resolution (~40 nm), which results in considerable uncertainty in determining the particle size.

From the segmented 3D datasets it is also possible to analyze the CB connectivity. In this analysis, a CB voxel is considered connected when it has a pathway to the bottom side of the reconstructed data cube (the direction of the aluminum current collector) through the carbon network. Unknown connectivity is defined as only being connected to one of the other sides of the reconstructed data cube.

Fig. 5 shows the analysis of connected CB in the five 3D data sets. Statistical results of the connectivity analysis are reported in Table 4. Both for F1 and F2, the CB networks are highly (97%) connected to the aluminum current collector. Regions from the three aged sample are instead characterized by large variations in connected and isolated fractions. Note that the precision of the connectivity analysis is also affected by the slicing resolution which is not included in the uncertainties given in Table 4.

3.3. Charge contrast FIB tomography

As presented in Fig. 2b and d, CB with two different contrast levels, apparently revealing the electronically percolated and non-percolated CB, can be obtained when recording the SEM images using an acceleration energy of 1 kV in combination with the in-lens detector. To analyze the two types of CB in 3D, the 1 kV in-lens SEM images were used for an additional segmentation. Fig. 6a shows a 3D reconstruction of the CB network in A1. The black particles represent the apparently electronically percolated CB, while the gray ones show the apparently insulated CB agglomerates.

However, the assumption that the CB agglomerate brightness correlates with electronic percolation seem to be problematic. Fig. 6 (b, c) show a zoom on a sub-volume and Fig. 6 (d) show the corresponding raw images.[1] From the inspection of the raw images in the 3D data (Fig. 6d), the CB agglomerate brightness is seen to flicker between the grounded intensity level and the insulated (charged) intensity level. The flickering rules out that the increased intensity is due to the entire CB agglomerate being conducting *and* disconnected from ground. Further, the CB agglomerates appear dark (slices 114 and 116, Fig. 6d) where it has a surface connection (in the slicing plane) to grounded CB particles. Additionally, if the CB agglomeration is isolated in the slicing plane the CB agglomeration appears bright (slices 110 and 120). Such intensity flicker was observed to be a general behavior of the examined CB agglomerates. For this reason, we propose that the intensity flipping is attributed to the buildup of electrons on the CB agglomerate/vacuum interface resulting in a brighter contrast, and discharge across the slicing plane surface when adjacent to grounded CB, resulting in the darker contrast. Importantly, and as mentioned above, if the CB agglomerates had sufficient electronic conductivity to dissipate the charge the intensity would not flip from bright to dark on subsequent images. This leads us to suggest that these large CB agglomerations have lower bulk electron conduction. However, the CB agglomerate/vacuum interface seems to be sufficiently conducting to dissipate the SE electrons.

As described above, the apparent percolated and non-percolated CB should rather be interpreted as CB agglomerates with low bulk electric conductivity as opposed to the fresh CB particles with high bulk conductivity. Table 5 shows the ratio of observed high- and low-conductivity CB for all the analyzed regions. Note that due to the surface discharge of the low-conductivity CB, a part of the low-conductivity CB has a low intensity and is thus not interpreted as low-conductivity CB. For this reason the actual amount of CB with low conductivity might be higher than the observed amount and correspondingly the amount of CB with high electronic conductivity might be lower than the observed amount. No attempts were made to quantify the amount surface-connected low-conductivity CB which could have quantified the difference between the observed and the actual amount of low-conductivity CB.

Supplementary data related to this article can be found online at http://dx.doi.org/10.1016/j.jpowsour.2015.12.119.

3.4. TEM images

Fig. 7a show a TEM image of fresh CB where it can be seen that the primary particles have an almost spherical shape with an average diameter of ~40 nm. The selected area electron diffraction (SAED) pattern in the inset of Fig. 7a reveals a quasi-crystal structure of CB nanoparticles and from Fig. 7b the graphitic sheets oriented concentrically approximately tangent to the CB surface is observed. The distance to the brightest ring in the SAED pattern in Fig. 7a is 2.95 nm^{-1} corresponding to (002) planes with a spacing of 0.34 nm. From Fourier transforms of HRTEM images like the one presented in Fig. 7b, the mean distance between the graphitic

[1] Additional parts of the raw images, not used for 3D reconstruction, are also shown in the raw images. Further, the raw images also contain the LFP phase which is not shown in the 3D reconstruction of the CB network.

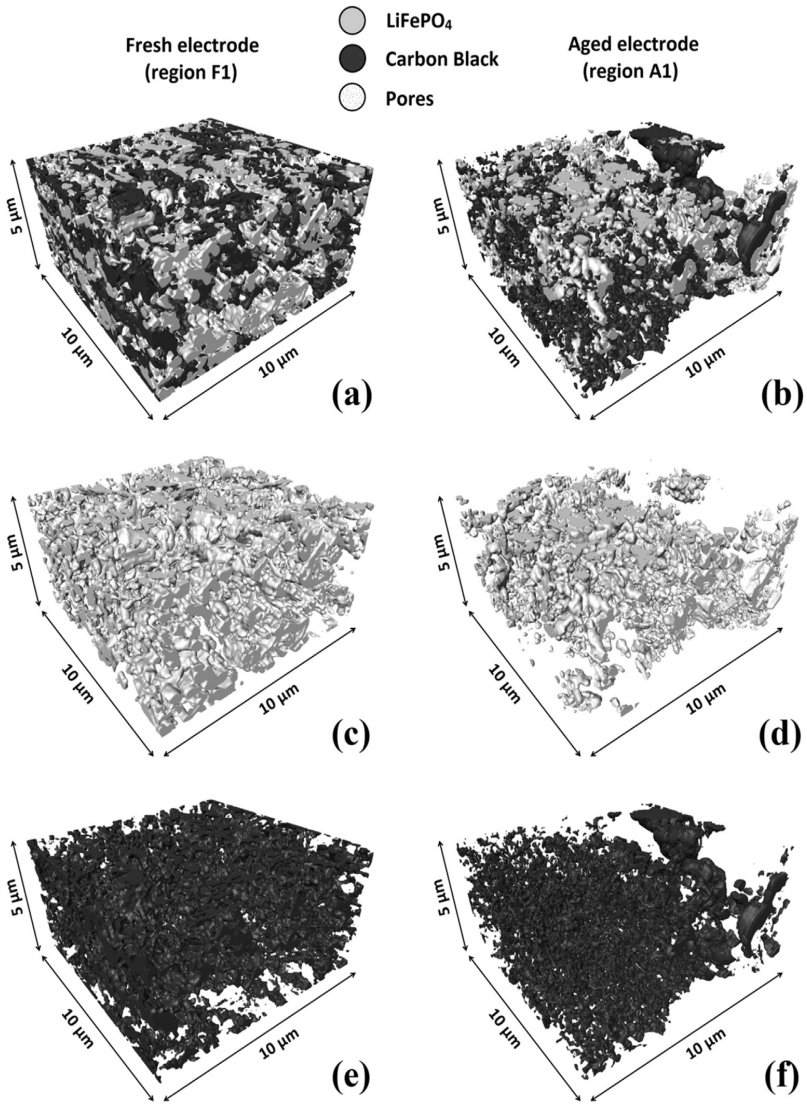

Fig. 3. A segmentation of the 3D FIB tomography reconstruction of a) the fresh (F1) and b) aged (A1) electrode. (c, d) show only the LFP phase and (e, f) show only the CB phase of (F1) and (A1), respectively.

Table 3
Phase volume fraction for fresh and aged electrode.

Phase	F1	F2	Fresh (av. and deviation)	A1	A2	A3	Aged (av. and deviation)
$LiFePO_4$	23%	17%	20% ± 3%	12%	18%	12%	14% ± 3%
CB	16%	15%	15.5% ± 0.5%	16%	5%	26%	16% ± 9%
Pores	61%	68%	64.5% ± 3.5%	72%	77%	62%	70% ± 6%

sheets is determined to 0.34 nm consistent with the characteristic distance of the CB (002) planes calculated from the SAED data.

The morphology of the pristine $LiFePO_4$ nanoparticles can be seen in the TEM images shown in Fig. 7 (c,d). LFP nanoparticles with a size of 200–300 nm are visible in a TEM image in Fig. 7c. Fig. 7d shows a close-up of a typical LFP particle with a lattice spacing of 0.37 nm corresponding to the (011) lattice distance of orthorhombic $LiFePO_4$. The carbon coating prepared by the commercial supplier is observed as a thin amorphous layer (~2 nm) at the edge.

HRTEM analysis has also been performed on a FIB lamellar specimen of the aged cathode. Fig. 8 shows TEM (a,b) and HRTEM (c,d) images of the LFP/CB aged cathode. A bright-contrast layer is

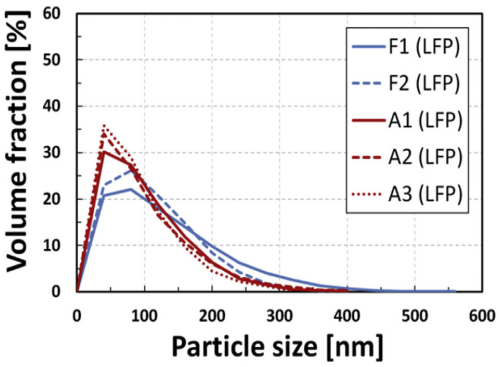

Fig. 4. Particle size distribution for LFP.

visible near the edges of the LFP particles (Fig. 8a,b). The bright contrast near the edges of the LFP particle indicates a coating layer with a light atomic weight relative to the darker LFP core. High resolution images (Fig. 8c,d) reveal contrast details of the coating layer on the LFP particle at an atomic level:

1. A thin layer carbon coating layer with average thickness of 2–4 nm (labeled as (1) in Fig. 8c,d). This layer has the same thickness as that observed in the fresh sample, as shown in Fig. 7d, and is most likely the carbon coating already present in the commercial LFP powder.
2. A dark layer, labeled as (2) in Fig. 8 (c,d), with thickness of 10–15 nm. It appears darker than the first one which indicates that it is composed by heavier elements.
3. A bright layer (3) with a thickness of 20–25 nm.
4. A dark layer (4) with a thickness of 2–4 nm.

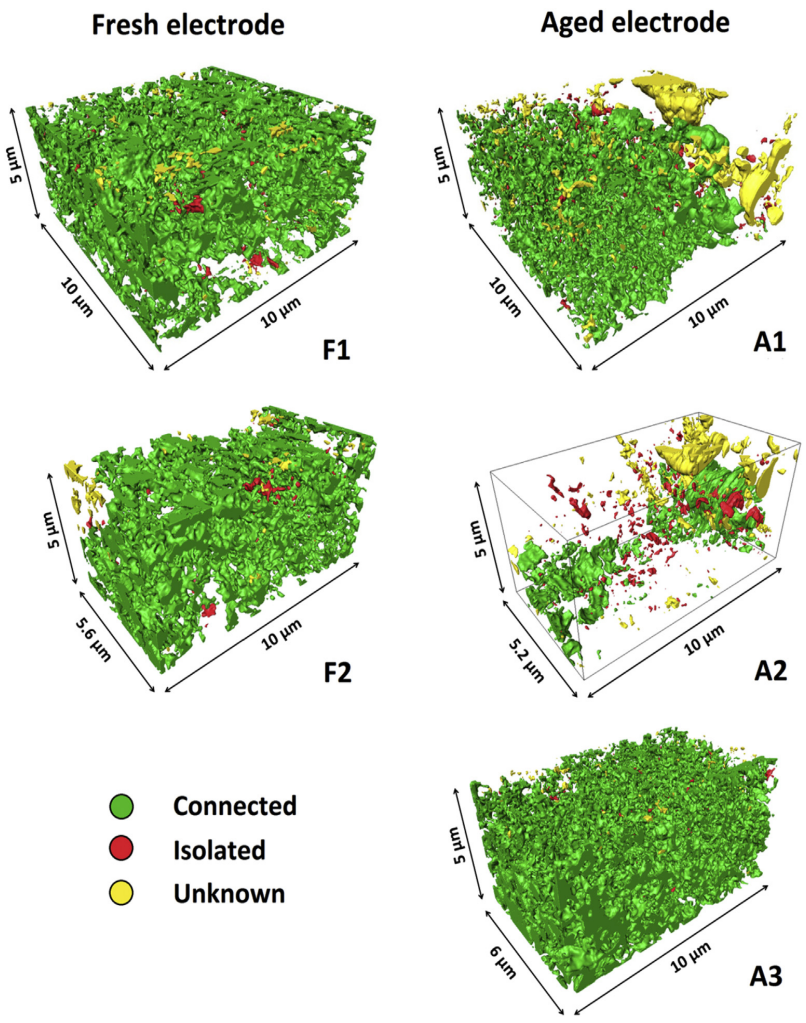

Fig. 5. Connectivity analysis of CB in the five 3D data sets. Green particles are connected with the bottom of the segmented volume (closest to the aluminum current collector). Red particles are unconnected and yellow particles are unknown (could be connected outside the segmented volume).

Table 4
Connectivity volume fraction for fresh and aged electrode.

Connectivity	F1	F2	Fresh (av. and deviation)	A1	A2	A3	Aged (av. and deviation)
Connected	97%	97%	97% ± 0%	78%	64%	98%	80% ± 14%
Isolated	2%	2%	2% ± 0%	5%	16%	1%	7% ± 6%
Unknown	1%	1%	1% ± 0%	17%	20%	1%	13% ± 8%

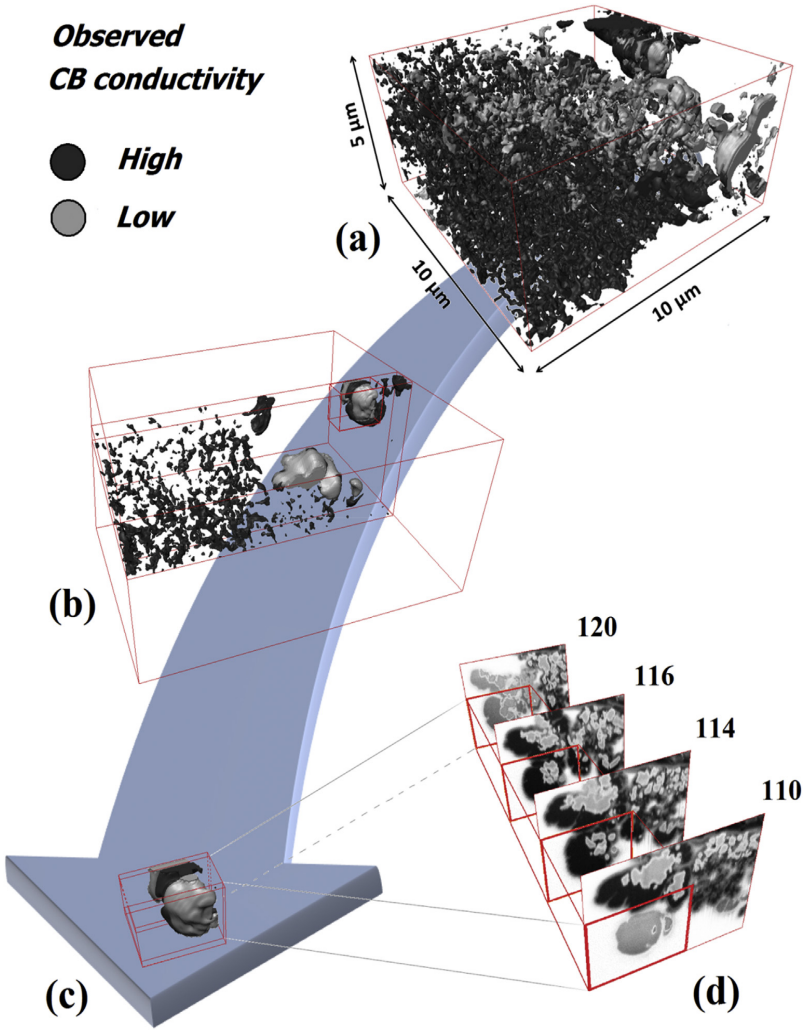

Fig. 6. a) Segmentation of apparently percolated (black) and non-percolated (gray) CB from a 3D FIB tomography reconstruction of sample A1 based on SEM images recorded with an In-lens detector at 1 kV b) and c) shows a zoom on a smaller section of the volume and d) examples of slices (raw SEM images) in the 3D dataset. Slice numbers are indicated in the figure.

Table 5
Observed high- and low-conductivity in the fresh and aged electrode samples.

Observed CB conductivity	F1	F2	Fresh (av. and deviation)	A1	A2	A3	Aged (av. and deviation)
High	100%	100%	100% ± 0%	75%	71%	100%	82% ± 13%
Low	0%	0%	0% ± 0%	25%	29%	0%	18% ± 13%

HRTEM imaging combining with Fourier transform deduced from HRTEM images indicates that the LFP particle cores preserve

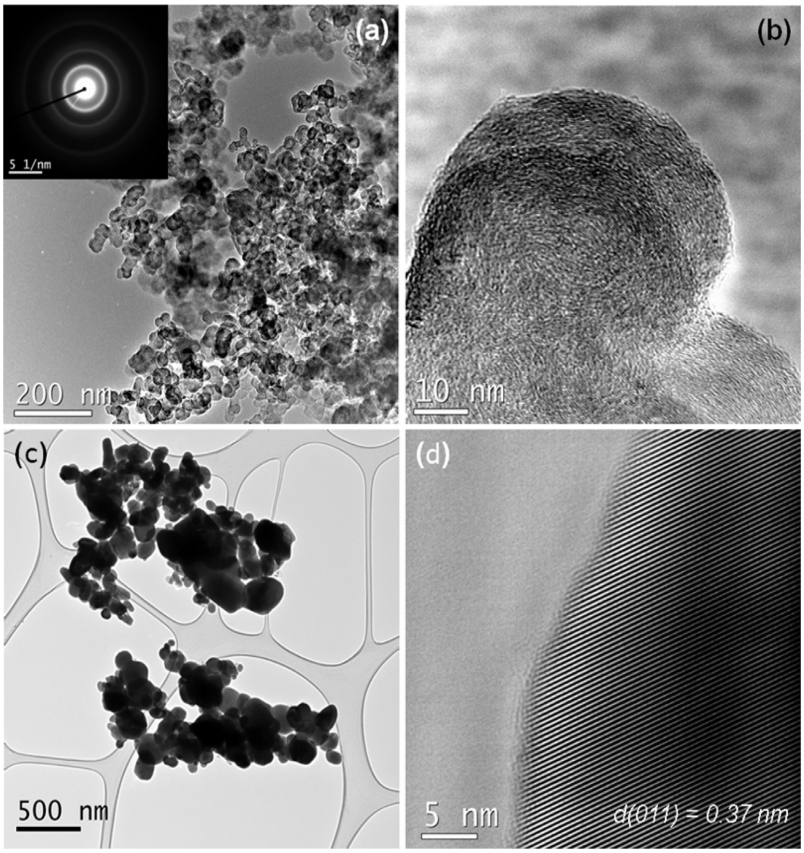

Fig. 7. (a) TEM image of fresh CB. The inset shows SAED pattern from the corresponding area. (b) HRTEM image of fresh CB nanoparticles indicating quasi-crystalline structure of graphene sheets in the particles. (c) TEM image of LFP nanoparticles on lacey carbon film, and (d) HRTEM image of a LFP nanoparticle with contrast from (011) lattice planes (d = 0.37 nm) and with a thin coating layer.

their crystalline structure (orthorhombic structure) denoted by crystal planes visible in Fig. 8d whereas the coating layer on the LFP particles are amorphous.

4. Discussion

4.1. Morphological changes

PSD calculation of LFP and connectivity analysis of CB has been used to study morphological degradation in a LFP/CB electrode. The LFP PSD in Fig. 4 shows a slight shift towards smaller grains in the aged samples compared to the fresh samples, probably due to cracking of the particles (Fig. 2 e,f). This creates new secondary smaller particles which are not connected or poorly connected to the carbon black network. Due to low ionic and electronic conduction of LFP, the cracks will likely cause parts of the old particles and some of the new LFP particles formed by cracking to become electrochemically inactive such that they cannot participate in the overall (de)lithiation reaction in the electrode, resulting in a drop in electrode capacity. Furthermore, olivine $LiMPO_4$ (with M = Fe, Mn, Co) in presence of HF, developed by $LiPF_6$ electrolyte decomposition, are known to be subjected to M dissolution, which leads to capacity fading [33,34]. This process is usually accelerated if the active material is not protected by a carbon coating [34], thus the particle cracking observed by PSD distribution (Fig. 4) and SEM images at 10 kV (Fig. 2 e,f) suggests that the increased surface area of non-carbon coated LFP accelerates the iron dissolution.

Regions A1 and A2 are characterized by the worst CB connectivity to the current collector (Fig. 5 and Table 4), because of relatively big carbon agglomerates disconnected from the CB network. On the other hand, no significant changes are observed between A3 and the fresh electrode. This suggests that CB degradation occurs heterogeneously throughout the sample and that carbon particles probably tend to agglomerate with cycling, reducing the electron supply needed for LFP (de)lithiation. *Zhu* et al. [9] showed that CB additive tends to aggregate and attach on the active material surface (n.b. LFP), especially with a high CB/LFP mass ratio as in our cathodes (10%:80%). However the continuous CB agglomeration on LFP surface upon cycling could be an effect of two different kind of degradation:

1. Mechanical stress, due to expansion/contraction of LFP during charging/discharging cycling, which would cause CB attachment on LFP surface and detachment from other sites;
2. Iron dissolution [34]. It is believed that this process causes the loss of contact between active materials (LFP) and conductive CB [34] with consequent agglomeration on other LFP grains.

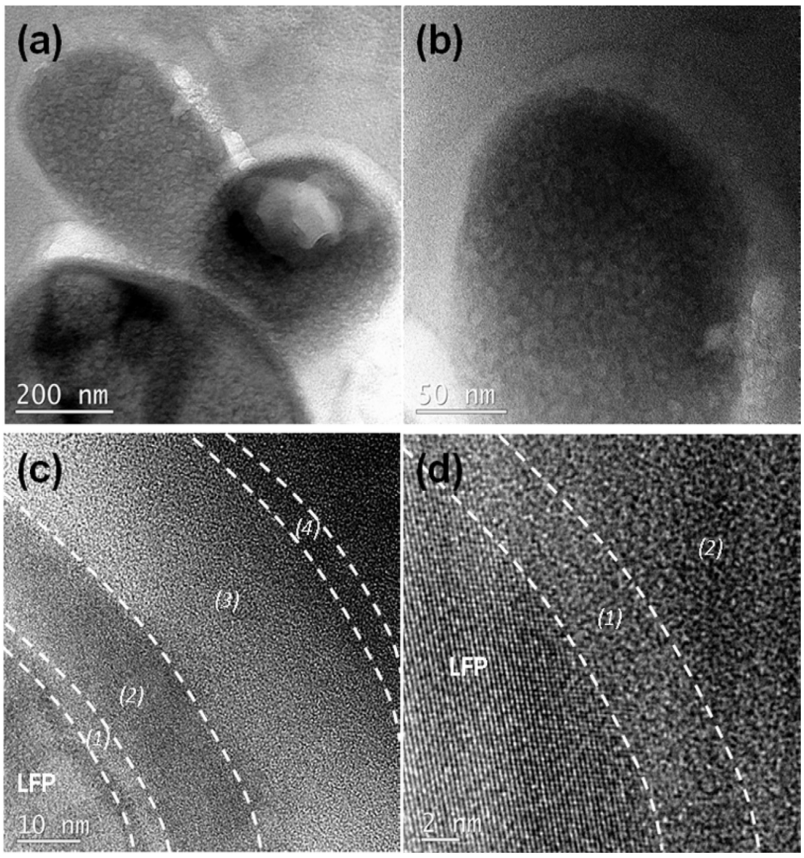

Fig. 8. (a, b) TEM images of LFP/CB aged cathode, (c, d) HRTEM images of the edge of the LFP particle presented in (b).

4.2. Charge contrast

Morphological changes are not the only degradation mechanism observed with cycling. Another important aspect is the observed change in the electronic conductivity of the CB agglomerates. Charge contrast FIB/SEM tomography was used to resolve high- and low-conductivity CB. The fresh electrode is characterized by high-conductivity CB, whereas localized charging is observed in the aged samples, A1 and A2. A3 does not show any charging phenomena, confirming that degradation of the LFP/CB electrode occurs heterogeneously.

The reason for the low electronic bulk conductivity in the CB agglomerates is probably due to structural degradation. TEM images of a sample from the aged electrode show carbon surrounding the LFP particles that seems to be amorphous, in contrast to the quasi-crystalline fresh CB particles. The reason for the formation of the large amorphous structures in the degraded electrode is currently not known by the authors. A possible reason for structural changes of CB during charge/discharge cycling could be its dissolution and subsequent agglomeration in the amorphous form at other sites in the electrode [35]. The change from a quasi-crystalline structure to an amorphous structure is known to decrease the electronic conductivity [19,20] several orders of magnitude [36,37]. It is reported in literature that the electrical resistivity of crystalline graphite is around $10^{-5} - 10^{-3}$ Ωm, while in bulk amorphous carbon is around 10^{3}–10^{13} Ωm [37].[2]

4.3. SEI-like layer

It is well known that the positive electrode materials are reactive with the most common electrolyte solutions, forming SEI phases at the interphase between salt-based and solvent-based species [38]. Specifically, the $LiFePO_4$ electrode material, in the presence of 1 M $LiPF_6$ in 1:1 EC:DMC electrolyte reacts, creating an SEI-like layer composed by different species, such as Li-organic species, Fluorophosphates and LiF [38]. This is likely what we observed in our LFP particles, as the first SEI layer denoted (2) in Fig. 8c,d possibly formed once the electrode has been soaked into the electrolyte. This layer can be distinguished from the first carbon layer because appears darker, being composed by heavier element such as F, P, O coming from electrolyte decomposition.

As discussed above, cycling the battery for 100 cycles, causes carbon agglomeration on the LFP surface, it could therefore be suggested that the 3rd relatively thick and bright layer, denoted (3) in Fig. 8c, is the initiation of the carbon agglomeration. This carbon layer appears amorphous in contrast to the crystallinity of the fresh Super C65 structure. If the original CB particles, with degradation,

[2] A video showing rotations of the 3D structures is available as supplementary material.

dissolves and agglomerate as amorphous structures on LFP surfaces, this could partly explain the reduced the electrical conductivity and decreased cathode performance. It can be speculated that the 4th relatively thin and dark layer in Fig. 8c is an SEI-like layer which deposited after the battery cycling was ended. It should, however be emphasized that further characterization is needed to verify the composition of the amorphous layers.

5. Conclusions

In this work a fresh and a degraded laboratory-made Li-ion battery LFP/CB cathode were characterized by SEM, TEM and low-kV FIB/SEM analysis. Five samples, two from the fresh cathode and three from the degraded cathode were analyzed.

Lateral E-T detector imaging provided brightness contrast between LFP, CB and pores, which allowed phase separation and segmentation of the electrode samples.

LFP particle size distribution analysis revealed that the aged cathode had a higher amount of smaller LFP particles than the amount observed in the fresh electrode, probably due to cracking of the LFP particles during cycling. This was supported by the observation of visible cracks in the bigger LFP particles in the degraded electrode using 10 kV SEM imaging.

The CB particles were seen to agglomerate and accumulate on the LFP surface in some parts of the aged electrode, increasing heterogeneity of the CB network and reducing electron percolation thereby decreasing the amount of electrochemically active LFP particles.

Low accelerating voltage (1 kV) permitted a detailed study of charging effects in CB agglomerates observed in the aged cathode. The interpretation of low-kV SEM imaging, that charging effects correlate with electronic percolation, was shown to be incomplete in the analysis of the CB agglomerates. A careful analysis of the 3D low-kV images indicated that the CB agglomerates do not have a sufficient bulk electronic conductivity to dissipate the electrons induced by the SEM imaging. However, the CB/vacuum interface seems to have sufficient conductivity to dissipate the electrons induced by the SEM imaging. In conclusion the low-kV SEM in-lens imaging can provide a useful contrast between high-conductivity carbon phases and low-conductivity carbon phases with no electronic percolation to high-conductivity carbon phases at the carbon/vacuum interface. We can observe from the contrast difference that the CB is moving toward lower conductivity, indicating the presence of a different structure as later confirmed by TEM analysis. The poor electronic conductivity of the CB agglomerates is attributed to a change in the structure from quasi-crystalline to amorphous, supported by HRTEM analysis of the degraded cathode, which would increase the electrical resistivity of carbon from 10^{-5}–10^{-3} Ωm to around 10^{3}–10^{13} Ωm [37].

The presented method combining low-kV SEM in-lens imaging with FIB 3D tomography can yield detailed information about the amount of low-conductivity carbon in aged LFP/CB electrodes and we hope the method will prove valuable in failure analysis of battery electrodes, thereby assisting in improving existing and future battery technologies.

Acknowledgments

The authors gratefully acknowledge financial support from the Danish strategic research council through the project “Advanced Lifetime Prediction of Battery Energy Storage” (contract no. 0603-00589B). The authors wish to thank Ebtisam Abdellahi for laboratory assistance and sample preparation. The authors at Northwestern gratefully acknowledge the financial support from the Office of Naval Research Grant #N00014-12-1-0713.

References

[1] M. Armand, J.M. Tarascon, Nature 451 (2008) 652–657.
[2] B. Scrosati, J. Hassoun, Y.K. Sun, Energy Environ. Sci. 4 (2011) 3287–3295.
[3] J.M. Tarascon, M. Armand, Nature 414 (2001) 359–367.
[4] A.K. Padhi, K.S. Nanjundaswamy, J.B. Goodenough, J. Electrochem. Soc. 144 (1997) 1188–1194.
[5] Y. Wang, P. He, H. Zhou, Energy Environ. Sci. 4 (2010) 805–817.
[6] H. Gabrisch, J. Wilcox, M.M. Doeff, Electrochem. Solid-State Lett. 11 (2008) A25–A29.
[7] H.Y.S. Huang, Y.X. Wang, J. Electrochem. Soc. 159 (2012) A815–A821.
[8] D. Wang, X. Wu, Z. Wang, L. Chen, J. Power Sources 140 (2005) 125–128.
[9] M. Zhu, J. Park, A.M. Sastry, J. Electrochem. Soc. 158 (2011) A1155–A1159.
[10] X. Qi, B. Blizanac, A. DuPasquier, M. Oljaca, J. Li, M. Winter, Carbon 64 (2013) 334–340.
[11] J.R. Wilson, W. Kobsiriphat, R. Mendoza, H.Y. Chen, J.M. Hiller, D.J. Miller, K. Thornon, P.W. Voorhees, S.B. Adler, S.A. Barnett, Nat. Mater. 5 (2006) 541–544.
[12] T. Hutzenlaub, S. Thiele, R. Zengerle, C. Ziegler, Electrochem. Solid-State Lett. 15 (2012) A33–A36.
[13] M. Ender, J. Joos, T. Carraro, E. Ivers-Tiffée, J. Electrochem. Soc. 159 (2012) A972–A980.
[14] Z. Liu, J.S. Cronin, Y.K. Chen-Wieart, J.R. Wilson, K.J. Yakal-Kremski, J. Wang, K.T. Faber, S.A. Barnett, J. Power Sources 227 (2013) 267–274.
[15] M. Ender, J. Joos, T. Carraro, E. Ivers-Tiffée, Electrochem. Commun. 13 (2011) 166–168.
[16] J.S. Cronin, J.R. Wilson, S.A. Barnett, J. Power Sources 196 (2011) 2640–2643.
[17] J.S. Cronin, Y.K. Chen-Wiegart, J. Wang, S.A. Barnett, J. Power Sources 233 (2013) 174–179.
[18] K. Thydén, Y.L. Liu, J.B. Bilde-Sørensen, Solid State Ionics 178 (2008) 1984–1989.
[19] M.M. Doeff, J.D. Wilcox, R. Kostecki, G. Lau, J. Power Sources 163 (2006) 180–184.
[20] R. Kostecki, B. Schnyder, D. Alliata, X. Song, K. Kinoshita, R. Kötz, Thin Solid Films 396 (2001) 36–43.
[21] M.T. Postek, Rev. Sci. Instrum. 61 (1990) 3750.
[22] J. Cazaux, J. Microsc. 214 (2004) 341–347.
[23] J. Cazaux, J. Phys. D. Appl. Phys. 38 (2005) 2433–2441.
[24] K. Kumagai, T. Sekiguchi, Ultramicroscopy 109 (2009) 368–372.
[25] J. Cazaux, Microsc. Microanal. 10 (2004) 670–684.
[26] D.J. Stokes, Philos. Trans. R. Soc. Lond. A 361 (2003) 2771–2787.
[27] W. Li, W. Bauhofer, Carbon 49 (2011) 3891–3898.
[28] D.C. Joy, Scanning 17 (1995) 270. Data available at: http://web.utk.edu/~srcutk/htm/interact.htm.
[29] P. Hovington, D. Drouin, R. Gauvin, D.C. Joy, N. Evans, Scanning 19 (1997) 29–35.
[30] J. Sauvola, M. Pietikäinen, Pattern Recognit. 33 (2000) 225–236.
[31] T. Kryjak, M. Gorgoń, Int. J. Appl. Math. Comput. Sci. 20 (2010) 571–580.
[32] B. Münch, L. Holzer, J. Am. Ceram. Soc. 91 (2008) 4059–4067.
[33] B.S.M. Oh, S.W. Oh, C.S. Yoon, B. Scrosati, K. Amine, Y.K. Sun, Adv. Funct. Mater. 20 (2010) 3260–3265.
[34] X. Zhi, G. Liang, L. Wang, X. Ou, J. Zhang, J. Cui, J. Power Sources 189 (2009) 779–782.
[35] M. Kerlau, M. Marcinek, R. Kostecki, J. Power Sources 174 (2007) 1046–1051.
[36] M.M. Doeff, Y. Hu, F. McLarnon, R. Kostecki, Electrochem. Solid-State Lett. 6 (2003) A207–A209.
[37] K. Saito, J. Fujii, T. Kizuka, Jpn. J. Appl. Phys. 48 (2009) 010218.
[38] M. Cuisinier, N. Dupré, J.F. Martin, R. Kanno, D. Guyomard, J. Power Sources 224 (2013) 50–58.

II

ECS Transactions, 69 (18) 71-80 (2015)
10.1149/06918.0071ecst ©The Electrochemical Society

Low-voltage FIB/SEM Tomography for 3D Microstructure Evolution of $LiFePO_4$/C Electrode

R. Scipioni, P. S. Jørgensen, D. T. Ngo, S. B. Simonsen, J. Hjelm, P. Norby, and S. H. Jensen

Department of Energy Conversion and Storage, Technical University of Denmark, DTU Risø Campus, Frederiksborgvej 399, 4000 Roskilde, Denmark

This work presents an investigation of the degradation mechanisms that occur in $LiFePO_4$/C battery electrodes during charge/discharge cycling. Impedance spectra were measured on a fresh electrode and an electrode aged by cycling. The spectra were modeled with an equivalent circuit which indicates that both the ionic and electronic pathways in the electrode were negatively affected by the cycling. Focused Ion Beam/Scanning Electron Microscopy (FIB/SEM) tomography of both electrodes shows that cycling causes agglomerations of Carbon black (CB). In addition to this, Low-voltage FIB/SEM revealed non-conductive CB in the aged electrode.

Introduction

Li-ion batteries find widespread use in many applications, from portable devices to electric vehicles [1-3], and $LiFePO_4$ (LFP) is one of the most common cathode materials because of its long durability and high safety [4, 5]. Since LFP is a poor electronic conductor, it is always mixed with carbon black (CB) additives to increase electronic percolation in the electrode. LFP is known to be subjected to expansion/contraction with cycling. The resulting mechanical stress leads to formation of micro-cracks inside the LFP particles [6-8] and aggregation of CB [9]. FIB/SEM tomography is one of the most used techniques for quantitative observations of electrode morphology and structure [10-12]. SEM imaging at low-kV has previously been used to study electron percolation in solid oxide fuel cell Ni/YSZ-electrodes [13]. Here we combine low-kV SEM imaging with FIB to study electron percolation in three dimensions (3D) in two laboratory $LiFePO_4$/C electrodes; one fresh and one degraded by cycling. A loss of electron percolation was observed in the degraded electrode, correlating with modeling of impedance spectra recorded on the two electrodes.

Experimental

Cell assembly and testing

The electrodes were prepared by casting, on aluminum foil, a slurry made of commercial $LiFePO_4$ powder (already carbon coated, from MTI), Super C65 carbon black (from Timcal) and Polyvinylidene Fluoride (PVdF) as binder, with the ratio 80:10:10. After drying, two electrodes with a diameter of 18 mm and thickness of 22 μm

were punched out. The electrodes were tested in an EL-CELL® ECC-Combi 3-electrode setup, using lithium metal foil counter electrodes, lithium metal as reference electrode and a glass fiber separator soaked with a standard 1M $LiPF_6$ in 1:1 EC/DMC electrolyte. Both cells were cycled at constant C-rate using a Biologic VMP3 with Pstat/Gstat boards. Table 1 shows the test conditions for the two electrodes.

TABLE I. Test conditions.

Electrode	Current (mA g^{-1})	Voltage limits	Total cycle number	Remaining capacity
Fresh	17	3 – 4 V	2	~ 100%
Aged	17	3 – 4 V	100	~ 30%

Impedance spectroscopy

The 3-electrode setup combined with the Biologic VMP3 enabled electrochemical impedance spectroscopy (EIS) measurements of the $LiFePO_4$/C electrodes. EIS measurements in a frequency range from 100 kHz to 10 mHz of both the fresh and the aged electrode were obtained after discharging the cells at 3V with a calculated 0.1 C-rate. All measurements were performed at OCV after the cell had reached steady state defined by a change < 5 mV/h. The impedance results were modeled using the equivalent circuit presented in Fig. 1.

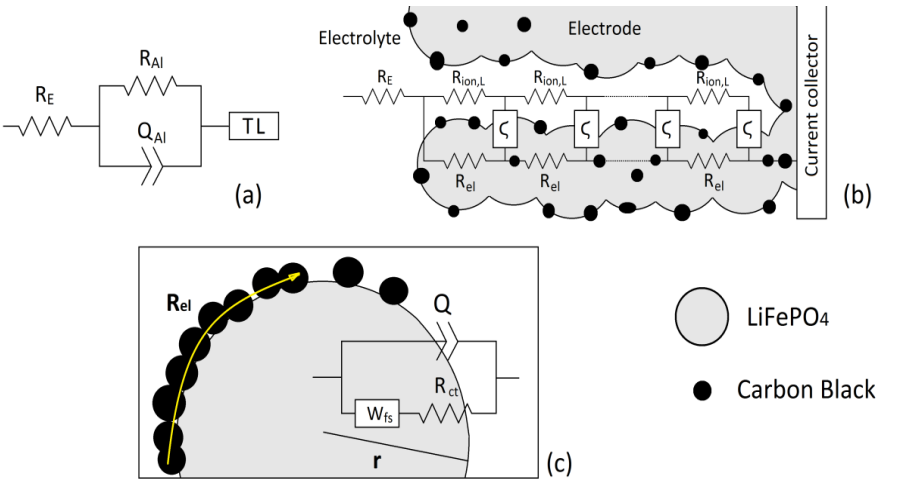

Figure 1. (a) Equivalent circuit used to model the impedance spectra, **(b)** Generalized Transmission Line model resembling the element TL in (a), **(c)** Randles circuit used to model electrode/electrolyte interface with Li^+ diffusion (Warburg Finite Space element, W_{fs}) within a particle with radius r. The Randles circuit resembles the element ζ in (b). The yellow arrow in (c) indicates the electron pathway on the surface of the LFP particle.

The R_E-$R_{Al}Q_{Al}$ elements, Fig. 1(a) model the high-frequency region where R corresponds to a resistance and Q corresponds to a constant phase element. R_E represents the ionic resistance of the electrolyte, while the $R_{Al}Q_{Al}$ element denotes the aluminum/electrode polarization impedance [14]. The low-frequency region was modeled with a generalized transmission line (TL) for a porous electrode [15-17], Fig. 1(b). This model involves a cylindrical pore (filled with the electrolytic solution) with length L,

electronic resistance of the electrode R_{el}, ionic resistance of the solution in the pore $R_{ion,L}$ and an equivalent circuit ς to model the interface electrode/electrolyte, including charge transfer resistance, double layer capacitance and solid state diffusion. The electronic resistance is often assumed to be much lower than the ionic resistance of the solution (R_{el}<<$R_{ion,L}$) for which reason a simplified transmission line without the electronic rail is used [17, 18]. However, assuming to find a higher R_{el} non-negligible electronic resistance in the aged electrode, the generalized version of the transmission line model is used [15-17], where the overall impedance is:

$$Z_{TL} = \frac{R_{el} * R_{ion,L}}{R_{el} + R_{ion,L}}\left(L + \frac{2\lambda}{\sinh(L/\lambda)}\right) + \lambda\frac{R_{el}^2 + R_{ion,L}^2}{R_{el} + R_{ion,L}}\coth(L/\lambda) \quad [1]$$

With:

$$\lambda = \sqrt{\varsigma/\left(R_{el} + R_{ion,L}\right)} \quad [2]$$

The electrode/electrolyte interface, Fig. 1(c), has been modeled with a Randles circuit which includes the charge transfer resistance R_{ct}, a constant phase element Q (from which the effective double layer capacitance C_{dl} is calculated according to [19]) and the general finite space Warburg element W_{GFS} [20-22], with the impedance:

$$Z_{WGFS} = R_w\frac{\coth[(j\omega\tau_w)^{n_w}]}{(j\omega\tau_w)^{n_w}} \quad [3]$$

With time constant:

$$\tau_w = \frac{r^2}{D} \quad [4]$$

R_w is polarization resistance, n_w is an exponent ($0<n_w<0.5$), r is the particle radius and D is the diffusion coefficient of Lithium ion within $LiFePO_4$.

FIB/SEM Tomography

FIB tomography and SEM imaging was carried out on a Zeiss 1540XB CrossBeam microscope, using a lateral E-T (Everhart-Thornley) detector and an In-lens detector. Two 3D datasets were collected from the fresh electrode (labeled as F1 and F2) and three from the aged one (labeled as A1, A2 and A3). Table 2 shows the volume sizes of the 5 different 3D datasets. A gallium FIB slicing probe of 2nA was used and the thickness of each slice was estimated to be 40 nm. The serial sectioning imaging was performed at 1 kV with a pixel size of 15x15 nm^2, and the voxel size in the five 3D-data sets was therefore 40x15x15 nm^3. The electrodes were prepared for FIB tomography by rinsing with diethyl carbonate and vacuum infiltrated with a silicon resin (Wacker Chemie) for 30 minutes to improve phase contrast between CB particles and pores as described by Ender et al [11]. Subsequently the samples were infiltrated with epoxy resin to enable high-quality grinding and polishing of the sample.

TABLE II. Volumes of collected datasets.

Dataset	Volume (voxels) X x Y x Z	Volume (µm3) X x Y x Z
F1	250 x 683 x 341	10 x 10 x 5
F2	141 x 683 x 341	5.6 x 10 x 5
A1	250 x 683 x 341	10 x 10 x 5
A2	131 x 683 x 341	5.2 x 10 x 5
A3	150 x 683 x 341	6 x 10 x 5

Low-voltage FIB/SEM

The low-voltage SEM technique has previously been used to study electron percolation by Thydén et al [13] and is here combined with a FIB to study the three-dimensional electron percolation in the CB network.

A low accelerating voltage (in our case 1 kV) causes a high secondary electron (SE) yield thereby charging the investigated specimen (depending on the examined material) [23, 24]. For electron conducting phases with a connection to ground, the local buildup of charge is rapidly equalized and no charging effects are observed. For insulators, the lack of charge dissipation means that a 1-1 balance between ingoing and outgoing electrons is rapidly established, mainly through charging of the insulator since the charging results in deflection/attraction of electrons. The silicon resin used to infiltrate the specimens (to fill out pores in the electrode) has a total electron yield higher than 1 [23, 24], meaning that it is expected to charge positively and appear bright, when imaged at 1 kV.

Electron conducting carbon was observed to be darker than non-electron-dissipating carbon particles, indicating that the later carbon type tends to charge positively.

Image processing

Segmentation and statistical data analysis of the 3D FIB/SEM image data was performed with the program ImageJ (NIH). Because of uneven illumination, setting a single threshold for entire micrographs was not feasible. Therefore the Sauvola algorithm [25, 26] was used to perform local thresholds of the data. The Sauvola algorithm works by dividing the input image into square windows (n x n pixel) and setting thresholds for each of them based on the mean and standard deviation of the pixel intensities. Visualizations of the 3D reconstructions of the data were performed with the program Avizo (FEI).

Results

Impedance spectra modeling

The normalized[1] impedance of the fresh electrode (dots) with the modeling result (line) using the model presented above is shown in Fig. 3(a,b). The Nyquist plot, Fig. 3(a), consists of a small semicircle in the high frequency range (between 10 kHz and 10 Hz) and a low frequency branch characterized by a diffusive tail (with an angle close to 45°). Modelling values are given in Table 3.

[1] Normalized to the geometrical surface area 2.545 cm^2

The high frequency side of the semicircle intersects with the x-axis at 9 Ωcm^2 (R_E). This value originates mainly from the ionic resistance of the electrolyte between the cathode and the Li reference electrode. As mentioned above, the semicircle ($R_{Al}Q_{Al}$) can be assigned to the interface between the Aluminum current collector and the porous cathode [14], where R_{Al} corresponds to the contact resistance between current collector and the $LiFePO_4$/C network, while Q_{Al} is the constant phase element which represents the double layer capacitance at this interface. The effective double layer capacitance C_{Al} is subsequently calculated [19] and presented in Table 3. The low-frequency part (TL) of the Nyquist plot models the electrode/electrolyte interface (with R_{ct}, C_{dl} and Finite Space Warburg diffusion of Li^+ ions inside the LFP particle with radius r) [20-22] including the electron resistivity through the Carbon Black and the ion resistivity into the pore (with lenght L) filled with the electrolyte [15-17]. The LFP particle radius used in this fitting are 55 and 40 nm for fresh and aged electrode respectively, while the pore length L is 22 μm. The particle size values were obtained by particle size distribution analysis reported elsewhere [28].

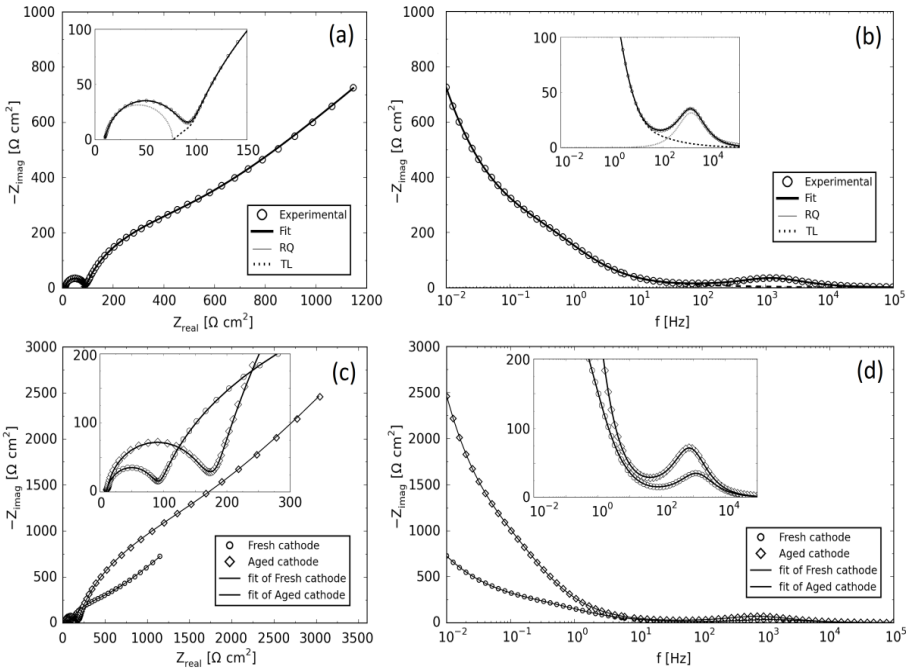

Figure 2. (a) Nyquist and (b) Bode plot of the fresh electrode at 0% SOC including fit using the equivalent circuit in equation 1. (c) Nyquist and (d) Bode plot of fresh and aged electrode at 0% SOC. The EIS measurements are performed after discharging the electrodes at 3V, at OCV after relaxation. All insets show a zoomed view of the high frequency region.

Figure 2 (c,d) shows the impedance response of both fresh and aged electrodes at the discharged state. Comparing the two impedance response is possible to observe an increase in the size of the first semicircle and of the transmission line. As seen in Table 3, the modelling suggests that these increases are mainly due to a raise in the electric and the ion resistivity in the porous electrode.

TABLE III. Results from EIS fitting.

	RQ element		Transmission Line				
	R_{Al} (Ωcm^2)	C_{Al} (μF)	R_{ct} (Ωcm^2)	C_{dl} (F)	D ($cm^2 s^{-1}$)	$R_{ion,L}$ (Ωcm^{-1})	R_{el} (Ωcm^{-1})
Fresh	68	4.2	0.66	0.75	$2.7 \cdot 10^{-11}$	8760	21
Aged	142	3	3.27	0.64	$2.9 \cdot 10^{-11}$	17260	1546

The aged electrode shows a big rise in the contact resistance R_{Al} between current collector and porous electrode and slight decrease in double layer capacitance C_{dl}. The charge transfer resistance R_{ct} at the interface between electrode material and electrolyte, is observed to be higher in the aged electrode than in the fresh electrode, while C_{dl} is smaller. As expected, the Li^+ ion diffusion coefficient was relatively constant, and it is in agreement with value found in literature [27]. Interestingly, the ionic resistance is seen to double, while the electron resistance within carbon black additive drastically increases.

Low-voltage FIB/SEM

Figure 3 shows SEM images after FIB slicing, recorded at low accelerating voltage (1 kV), of the fresh electrode (region F2, Fig 3(a,b)) and of the aged electrode region A2, Fig. 3(c,d). SEM images of other regions are reported by *Scipioni et al* [28]. The images were recorded with E-T detector Fig. 3(a,c) and with the In-lens detector Fig. 3(b,d).

In the images recorded at 1 kV with the E-T detector Fig. 3 (a,c) we can observe a very bright area on the top, which is the electrode surface. It is possible to distinguish three different phases: the grains with the brightest contrast are LFP particles, the almost black regions are CB and the large grey areas in-between are pores filled with silicon resin. The fresh electrode, Fig. (3a) shows a relatively homogeneous distribution of sub-micrometer LFP grains and CB particles. On the contrary, the aged sample (Fig. 3c) has a less homogeneous distribution of both LFP and CB and an increased porosity. The aged sample is further characterized by the presence of larger CB agglomerates surrounding some LFP grains, which is not observed in the fresh electrode.

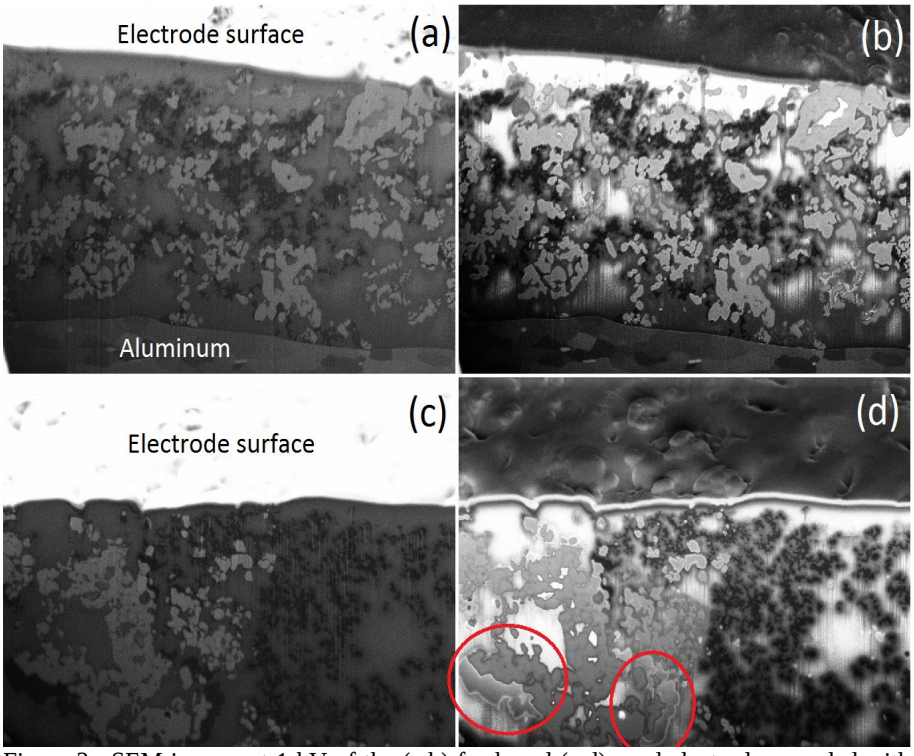

Figure 3. SEM images at 1 kV of the (a,b) fresh and (c,d) aged electrode recorded with the (a,c) Lateral E-T and (b,d) In-lens detector.

In the images recorded at 1 kV with the In-lens detector it can be observed that the silicon resin has high intensity in the parts of the sample not adjacent to electron conducting phases. This indicates that the silicon resin is charging negatively due to low conductivity to the ground. The CB network is instead expected to have a good conductivity and connectivity to the ground. Consistent with this expectation, the CB in the fresh sample has a dark contrast, which indicates minimal charging Fig. (3b). However, in the aged electrode on Fig. (3d) large agglomerations (circled in red) of what appears to be CB are brighter than other CB regions. This indicates that those agglomerations are charging negatively i.e. have lost connection to ground and/or have low conductivity. In other words, these CB regions appear not to be electron percolating.

3D Reconstruction

The SEM images, recorded after FIB slicing from the five dataset F1, F2, A1, A2 and A3 have been used for three dimensional reconstructions. Fig 4 shows a volume rendering of the 3D FIB tomography reconstruction after image segmentation of the 1 kV Lateral E-T image dataset from F2 and A2. Other 3D reconstructions can be found in [28]. From the figure it can be observed that all phases are less homogeneously distributed in A2 in all three dimensions, and not only in the single slice presented in fig. 2. Furthermore large CB agglomerates are seen in the aged electrode [28].

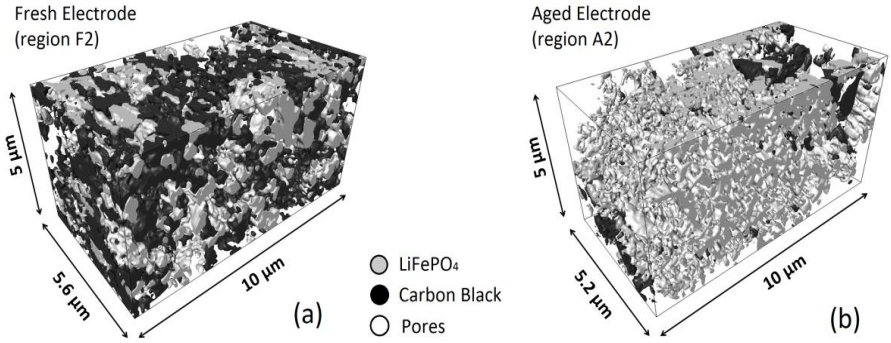

Figure 4. Volume rendering of the 3D reconstruction of a) fresh and b) aged electrode, after segmentation of Lateral E-T images.

The segmented regions from the 5 dataset have been used to extract and calculate statistical data. Table 4 shows the calculated phase fraction for all the volumes. Furthermore the average LFP particles size for the fresh and the aged electrode were calculated equal to 110 and 80 nm, respectively. More results from the particle size distribution analysis can be found in [28].

TABLE IV. Phase volume fraction for fresh and aged electrode.

Phase	F1	F2	Fresh (Av. and Deviation)	A1	A2	A3	Aged (Av. and Deviation)
$LiFePO_4$	23%	17%	20% ± 3%	12%	18%	12%	14% ± 3%
CB	16%	15%	15.5% ± 0.5%	16%	5%	26%	16% ± 9%
Pores	61%	68%	64.5% ± 3.5%	72%	77%	62%	70% ± 6%

As described in relation to Fig. 2, by using the images recorded by the In-lens detector for 3D segmentation we can distinguish between percolating and non-percolating CB. Fig. 5 shows a volume rendering of the 3D reconstruction of the CB network in F2 and A2. The amount of non-percolating CB was 29% in A2 and 0% in F2.

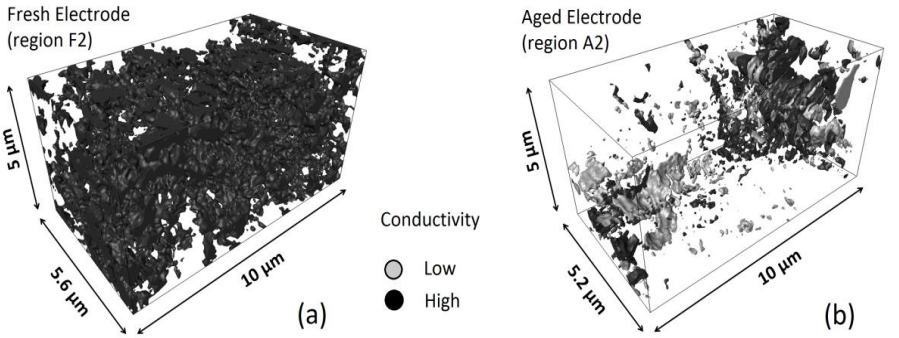

Figure 5. Volume rendering of the 3D reconstruction of a) fresh and b) aged carbon network, after segmentation of In-lens images.

Discussion

The impedance spectra modeling, indicates that most of the electrode degradation is due to changes in morphology and electrical conductivity of CB additive. Presence of low-conductive carbon, as shown by low-voltage FIB/SEM tomography, is clearly found to lead to an increase in electric resistivity both at the aluminum/electrode interface and throughout the CB network. This is suggested by the rise in R_{Al} in the first semicircle in the aged electrode. The drop in C_{dl} is also expected after CB agglomeration, having a smaller surface in contact between the CB network and the current collector, and being C_{dl} directly proportional to the surface area. The lithium ion R_{ct} is also found to increase in the Randles circuit which models the electrode/electrolyte interface: it is an effect of lower electron transport by carbon, which should foster (de)lithiation process. The C_{dl} is again observed to decrease, because of a smaller electrode surface area after CB agglomeration, while the Li^+ ion diffusion coefficient within $LiFePO_4$ seems to not be affected. This could be an indication of almost no degradation occurring in the $LiFePO_4$ lattice. The rise in $R_{ion,L}$ in the infiltrated pores, as shown by the Transmission Line, is not clearly understood, but it may be caused by formation of micropores, with a higher ion resistivity, after LFP cracking and/or increased tortuosity to electrochemically active sites. The most important result from the EIS model is the huge increase in electron resistance R_{el} throughout the CB network, of about two orders of magnitude. This higher resistance correlates with the presence of the non-conducting carbon phase which prevents the electron transfer within the electrode.

Conclusion

In this work a fresh and a degraded laboratory-made Li-ion battery $LiFePO_4$/C electrode were characterized by impedance spectroscopy (EIS) and low-voltage FIB/SEM analysis to correlate degradation mechanisms to observed loss in capacity.

Modeling of the EIS indicates a large increase with cycling in the electron resistance in the Carbon Black (CB) network in both the aluminum/electrode interface and the electrode/electrolyte interface.

The electron percolation in the CB network was studied with low-voltage FIB/SEM tomography. Low acceleration voltage (1 kV) permitted a detailed study of charging effects in CB agglomerates observed in the aged cathode, indicating that they have a low electronic conductivity.

The presented method combining low-kV SEM in-lens imaging with FIB 3D tomography can yield detailed information about the amount of low-conductivity carbon in aged $LiFePO_4$/C electrodes and we hope the method will prove valuable in failure analysis of battery electrodes, thereby assisting in improving existing and future battery technologies.

Acknowledgments

The authors gratefully acknowledge financial support from the Danish strategic research council through the project “Advanced Lifetime Prediction of Battery Energy Storage” (contract no. 0603-00589B). The authors wish to thank Ebtisam Abdellahi for laboratory assistance and sample preparation and the Scott Barnett group at Department of Material Science and Engineering at Northwestern University for the assistance in image segmentation and three-dimensional reconstruction.

References

1. M. Armand, J. M. Tarascon, *Nature*, **451**, 652-657 (2008).
2. B. Scrosati, J. Hassoun, and Y.K. Sun, *Energy Environ. Sci.*, **4**, 3287-3295 (2011).
3. J.M. Tarascon, M. Armand, *Nature*, **414**, 359-367 (2001).
4. A.K. Padhi, K.S. Nanjundaswamy, and J. B. Goodenough, *J. Electrochem. Soc.*, **144**(4), 1188-1194 (1997).
5. Y. Wang, P. He, and H. Zhou, *Energy Environ. Sci.*, **4**, 805-817 (2010).
6. H. Gabrisch, J. Wilcox, M.M. Doeff, *Electrochem. and Solid-State Letters*, **11**, A25-A29 (2008).
7. H.Y.S. Huang, Y.X. Wang, *J. Electrochem. Soc.*, **159**, A815-A821 (2012).
8. D. Wang, X. Wu, Z. Wang, L. Chen, *J. Power Sources*, **140**, 125-128 (2005).
9. M. Zhu, J. Park, A.M. Sastry, *J. Electrochem. Soc.*, **158**, A1155-A1159 (2001).
10. T. Hutzenlaub et al., *Electrochemical and Solid-State Letters*, **15** (3), A33-A36 (2012).
11. M. Ender et al, *J. Electrochem.* Soc., **159**(7), A972-A980 (2012).
12. Z. Liu et al., *J. Power Sources*, **227**, 267-274 (2013).
13. K. Thydén, Y.L. Liu, and J.B. Bilde-Sørensen, *Solid State Ionics*, **178**, 1984-1989 (2008).
14. J. Illig et al, *J. Electrochem. Soc.*, **159**(7), A952-A960 (2012).
15. G. Garcia-Belmonte et al, *Ionics*, **5**, 44 – 51 (1999).
16. R. De Levie, Electrochimica Acta, **9**, 1231-1245 (1964).
17. N. Ogihara, S. Kawauchi, C. Okuda, Y. Itou, Y. Takeuchi, and Y. Ukyo, *J. Electrochem. Soc.*, **159**, A1304-A1309 (2012).
18. R. Younesi et al, *J. Electrochem. Soc.*, **162**(7), A1289-A1296 (2015).
19. G.J. Brug et al, *J. Electroanal. Chem.*, **176**, 275-295 (1984).
20. F. Gao, Z. Tang, *Electrochimica Acta*, **53**, 5071-5075 (2008).
21. J.P. Meyers et al, *J. Electrochem. Soc.*, **147**(8), 2930-2940 (2000).
22. J. Song, M. Bazant, *J. Electrochem. Soc.*, **160**(1), A15-A24 (2013).
23. J. Cazaux, *Microsc. Microanal.*, **10**, 670-684 (2004).
24. D.J. Stokes, *Phil. Trans. R. Soc. Lond. A* **361,** 2771–2787 (2003).
25. J. Sauvola, M. Pietikäinen, *Pattern Recognition*, **33**, 225-236 (2000).
26. T. Kryjak, M. Gorgoń, *Int. J. Appl. Math. Comput. Sci.*, **20**, 571-580 (2010).
27. M. Park et al, *Journal of Power Sources*, **195**, 7904–7929 (2010).
28. R. Scipioni et al, *"Electron Microscopy Investigations of Changes in Morphology and Conductivity of $LiFePO_4$/C Electrodes"*, submitted to *J. Power Sources*.

III

International Journal of Energy Research

INTERNATIONAL JOURNAL OF ENERGY RESEARCH
Int. J. Energy Res. (2016)
Published online in Wiley Online Library (wileyonlinelibrary.com). DOI: 10.1002/er.3575

SHORT COMMUNICATION

A TEM study of morphological and structural degradation phenomena in $LiFePO_4$-CB cathodes

Duc-The Ngo[1,2,*,†], Roberto Scipioni[1], Søren Bredmose Simonsen[1], Peter Stanley Jørgensen[1] and Søren Højgaard Jensen[1,*,†]

[1]DTU Energy, Department of Energy Conversion and Storage, Technical University of Denmark, Frederiksborgvej 399, Roskilde, 4000, Denmark
[2]Electron Microscopy Centre, School of Materials, University of Manchester, Oxford Road, Manchester, M13 9PL, United Kingdom

SUMMARY

$LiFePO_4$-based cathodes suffer from various degradation mechanisms, which influences the battery performance. In this paper, morphological and structural degradation phenomena in laboratory cathodes made of $LiFePO_4$ mixed with carbon black (CB) in a 1 mol/L $LiPF_6$ in EC : DMC (1:1 by weight) electrolyte are investigated by transmission electron microscopy at various preparation, assembling, storage, and cycling stages. High-resolution transmission electron microscopy imaging shows that continuous SEI layers are formed on the $LiFePO_4$ particles and that both storage and cycling affect the formation. Additionally, loss of CB crystallinity, CB aggregation, and agglomeration is observed. Charge–discharge curves and impedance spectra measured during cycling confirm that these degradation mechanisms reduce the cathode conductivity and capacity. Copyright © 2016 John Wiley & Sons, Ltd.

KEY WORDS

lithium ion battery; cathode degradation; nanoparticles; transmission electron microscopy; high-resolution transmission electron microscopy

Correspondence

*Duc-The Ngo, Electron Microscopy Centre, School of Materials, University of Manchester, Oxford Road, Manchester M13 9PL, UK. Søren Højgaard Jensen, DTU Energy, Department of Energy Conversion and Storage, Technical University of Denmark, Frederiksborgvej 399, Roskilde 4000, Denmark.

†E-mail: duc-the.ngo@manchester.ac.uk

Received 28 January 2016; Revised 17 May 2016; Accepted 17 May 2016

1. INTRODUCTION

Lithium iron phosphate, $LiFePO_4$ (LFP), is a common cathode material in lithium-ion batteries [1,2]. It combines reasonably good cycle life, low cost and toxicity, high open-circuit voltage around 3.4 V versus Li^+/Li, and a theoretical charge/discharge capacity of ~170 mAh/g [3–5]. LFP has a low electronic conductivity, which requires mixing with carbon or a conductive polymer to ensure good electric conductivity and power density [6–8].

Several degradation phenomena can occur in this type of cathode. Among these, cycling-related micro-cracks in larger LFP grains [9–11], loss of crystallinity [12], and active material [9] as well as carbon aggregation and agglomeration [13,14] are known to negatively affect the electrode performance and cause capacity fading. LFP nanoparticles are surface sensitive to modifying additives [15–19]. The electrolyte composition, the use of additives, and the electrode charge/discharge history affect the morphology of decomposition compounds, the solid electrolyte interface (SEI) layer formation, and the related electrode performance [20–23].

Here, we present a study of laboratory LFP electrodes in 1 mol/L $LiPF_6$ in EC : DMC (1:1 by weight) at different preparation, assembling, and testing stages. Transmission electron microscopy (TEM) of as-received LFP and carbon black (CB) powders, as-prepared LFP-CB, LFP-CB stored in the electrolyte, and LFP-CB after 100 charge/discharge cycles is used to investigate nanostructural changes including SEI layer formation. A heterogeneous electrode structure, formation of secondary phases, and multilayered SEI are observed in the cycled electrode. Although not investigated in detail in this paper, the latter interestingly indicate that the electrode history – to some extent – is stored and can be detected in the SEI layers.

2. EXPERIMENTAL DETAILS

Laboratory LFP-CB cathode specimens were prepared from LFP nanoparticles (MTI Corp., Richmond, CA,

USA), Super C65 CB (Timcal, Bodio, Switzerland), and polyvinylidene fluoride (PVdF). The microstructure of as-received LFP and CB nanoparticles was studied separately and referred to as 'pristine' samples. The LFP, CB, and PVdF were mixed with a ratio of 80:10:10 and dissolved in *N*-methyl-2-pyrrolidone (NMP) solvent by magnetic stirring for 10 h. The PVdF was used as binder to enhance the adhesion to the current collector. After magnetic stirring, a TEM specimen was prepared by putting a small drop of the cathode mixture on Au TEM grids with a holey carbon support film. Subsequently, it was dried at 120 °C under vacuum. The sample was investigated in the TEM microscope and is referred to as the 'fresh cathode'. After TEM characterization, the fresh cathode was kept in a standard 1 M $LiPF_6$ in 1:1 EC/DMC electrolyte for 72 h, rinsed with diethyl carbonate, and dried at 120 °C under vacuum. The sample was investigated once again in the TEM and referred to as the 'stored cathode'.

Two electrodes were prepared by drying the LFP, CB, and PVdF solution in NMP solvent (described earlier) on an Al current collector at 120 °C under vacuum. The electrodes were then subjected to respectively 2 and 100 charge/discharge cycles in a three-electrode EL-CELL® ECC-Combi cell house at 0.1 °C using lithium metal foil as counter and reference electrodes and a glass fiber separator soaked with the standard 1 M $LiPF_6$ in 1:1 EC/DMC electrolyte. After cycling, the cell houses were disassembled in a glove box, and the two electrodes were rinsed with diethyl carbonate to remove the remaining electrolyte before being dried at 120 °C under vacuum and subsequently embedded in silicon resin. The electrodes cycled two times and 100 times are referred to as the 'reference cathode' and 'aged cathode', respectively. After curing of the resin, a TEM lamellar specimen of the aged cathode was prepared by focused ion beam (FIB) milling using a 30-kV Ga ion beam (Zeiss Crossbeam XB1540; Germany). Scanning electron microscopy (SEM) images of the reference and aged cathodes were also obtained using FIB/SEM imaging with the same Crossbeam XB1540 equipment. An overview of the studied samples is presented in Table I.

(Scanning) transmission electron microscopy, (S)TEM imaging (bright-field, high-resolution, and high annular angle dark-field imaging) of the LFP-CB cathode specimens was performed on a JEOL JEM 3000F equipped with a 300-kV field emission gun, high annular angle dark-field (HAADF) STEM detector, and an Oxford Instruments X-ray detector (Abingdon, UK) with an ultra-thin window for X-ray energy dispersive spectroscopy (EDX) analysis.

Electrochemical impedance spectroscopy measurements were performed on the two cycled cathodes in the three-electrode EL-CELL® ECC-Combi using lithium metal as counter and reference electrodes. Electrochemical impedance spectroscopy measurements in a frequency range from 10 mHz to 10 kHz were obtained from the LFP-CB reference and aged electrodes in the discharged state at open-circuit voltage, after the cells had reached a steady state defined by a voltage change less than 5 mV/h.

3. RESULTS

3.1. SEI layers

Figure 1(a) displays a bright-field image and a dark-field (inset) TEM image of pristine off-the-shelf LFP nanoparticles deposited on a lacey carbon grid. A high-resolution TEM (HRTEM) image of one of the LFP particles is presented in Figure 1(b). A thin amorphous coating with a thickness of ~1 nm is observed at the particle surface. Figure 1(c) and (d) shows respectively a bright-field TEM and a HRTEM image of pristine CB nanoparticles. The inset in Figure 1(c) shows a selected area electron diffraction pattern of the CB particles.

Figure 2(a)–(c) presents bright-field TEM images of the (a) fresh, (b) stored, and (c) aged cathode microstructures with LFP (dark contrast and large particles) and CB nanoparticles (light contrast and smaller particles) distinguished by amplitude contrast [24]. In Figure 2(c), the relatively dark LFP particles are indicated by black arrows, and the lighter CB particles are indicated by white arrows. In Figure 2(c), the gray contrast background arises from the Si-resin stabilizing the TEM lamella.

Changes in the coating layer at the LPF particles surfaces are observed in the magnified TEM images [Figure 2(d)–(f)]. It is seen that the thickness of the layers formed at the LFP particle surface increases from the fresh [Figure 2(d)] to the stored [Figure 2(e)] and further to the aged [Figure 2(f)] cathode. Representative

Table I. Overview of the investigated LFP-CB samples.

Number	Name	Description	Sample
1	Pristine CB	As-received CB powder	Powder (TEM)
2	Pristine LFP	As-received LFP powder	Powder (TEM)
3	Fresh cathode	LFP-CB (+ binder)	Powder (TEM)
4	Stored cathode	Sample 3 stored in electrolyte for 72 h	Powder (TEM)
5	Reference cathode	After 2 charge/discharge cycles	FIB/SEM
6	Aged cathode	After 100 charge/discharge cycles	Lamellar (TEM) + FIB/SEM

TEM, transmission electron microscopy; CB, carbon black; LFP, $LiFePO_4$; FIB, focused ion beam; SEM, scanning electron microscopy.

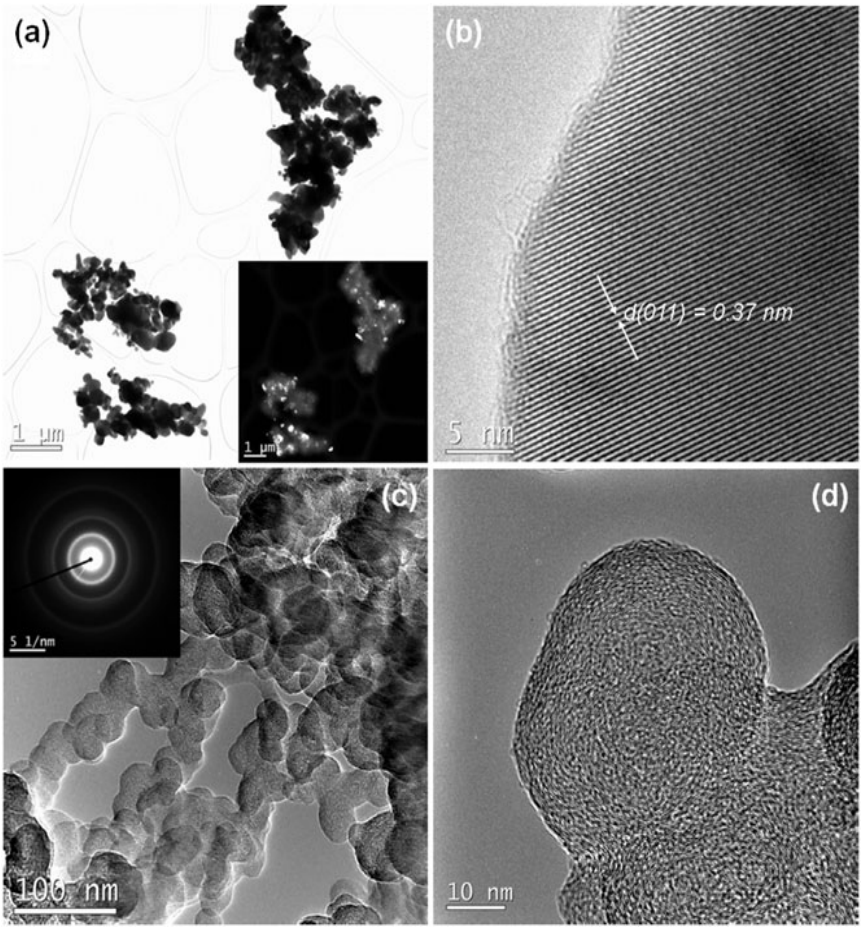

Figure 1. (a) Bright-field transmission electron microscopy (TEM) image of pristine (off-the-shelf) $LiFePO_4$ nanoparticles on lacey carbon grid: The inset shows a (200)-reflected dark-field image of the corresponding area. (b) High-resolution TEM image of a single-crystal $LiFePO_4$ nanoparticle. (c) Bright-field TEM image of pristine (off-the-shelf) carbon black (CB) nanoparticles. The inset shows a selected area electron diffraction pattern of the corresponding CB nanoparticles. (d) High-resolution TEM image of a typical CB nanoparticle.

HRTEM images are shown for the fresh [Figure 2(g)], stored [Figure 2(h)], and aged [Figure 2(i)] cathode. The thickness of the amorphous layer at the LFP particle surfaces increases from ~3 nm for the fresh cathode [Figure 2(g)] to ~9 nm for the stored cathode [Figure 2 (h)] and ~30 nm for the aged cathode [Figure 2(i)]. In the latter sample, the SEI consists of distinct layers. The relation to the cathode history is debated further in the discussion section. The inset in Figure 2 (g) shows a magnification of one of the LFP/SEI layer interfaces for the fresh sample. Further magnification of one of the LFP/SEI interfaces for the aged cathode sample can be seen in the Supporting Information, Figure S1(a). Fourier transforms of areas within the LFP particle and coating layer are presented in Figure S1(b) and (c), respectively. Area selections for the Fourier transforms are shown with dotted squares in Figure S1(a).

3.2. Carbon crystallinity

Selected area electron diffraction patterns of CB from the fresh, stored, and aged samples are presented in Figure 3 (a), (b), and (c), respectively. The diffraction patterns were obtained from the areas inside the dotted blue rings in Figure 2(a)–(c) respectively. Diffraction intensity profiles are shown as insets in the figure. The diffraction intensity profiles are obtained by rotationally averaging the diffraction patterns and normalizing. A quantitative analysis of the peaks in the diffraction profile is provided in Table II.

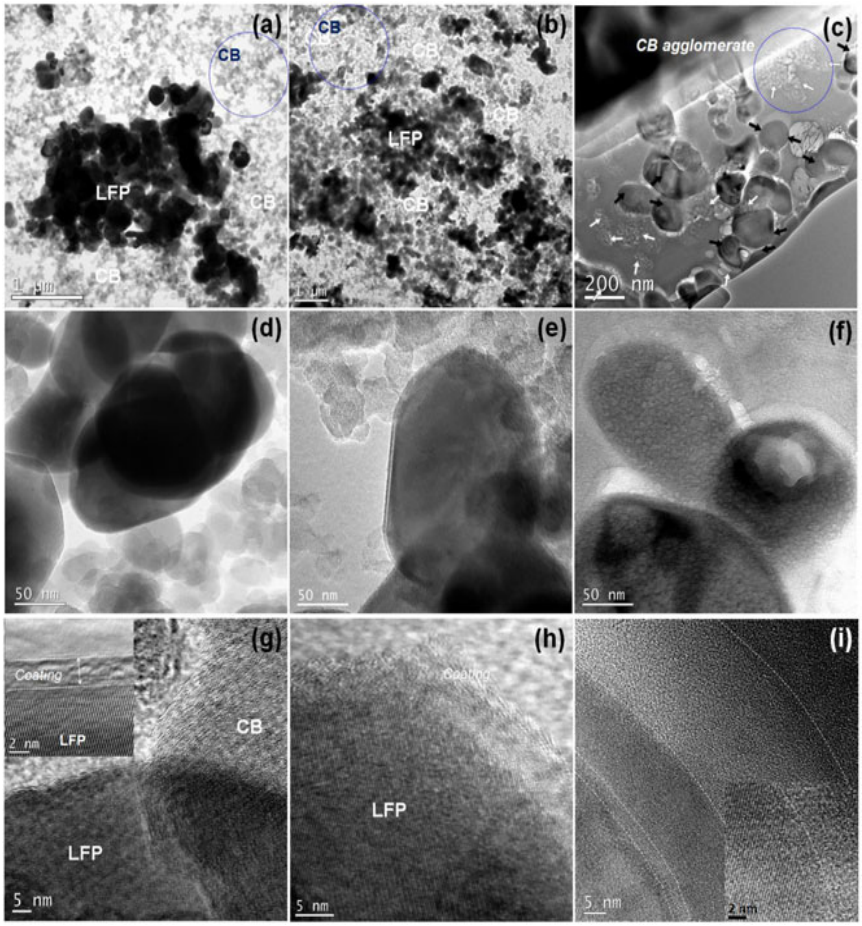

Figure 2. Transmission electron microscopy images of the (a,d,g) fresh, (b,e,h) stored, and (c,f,i) aged $LiFePO_4$ (LFP)-carbon black (CB) cathode. The inset in (g) presents the magnified primary coating layer on LFP nanoparticles, and the inset in (i) shows the magnified LFP/SEI layer interface.

3.3. Carbon agglomeration

A STEM-HAADF image of the aged sample is presented in Figure S2(a). Elemental maps of the sample using STEM-EDX are presented in Figure S2(b)–(f), and an average EDX spectrum showing apparent presence of C, O, Fe, P, Al, and Si is illustrated in Figure S2(g). It is noteworthy that Fluorine (F) is presumably present in the sample denoted by a shoulder (~677 eV) nearby the Fe peak (704 eV). However, it is likely impossible to resolve the F-presence because of small difference between Fe and F peaks (27 eV) compared with measurement resolution of our EDX detector (~140 eV). Fe is known to be part of LFP and thus present in the sample firmly, whereas it cannot be concluded from the EDX map whether F is present in the sample. Additionally, the Al map is not provided because the Al counts were too weak to form a clear visible spatial distribution.

In the STEM-HAADF image, carbon appears as dark contrast areas, whereas the Si-epoxy resin is visible as grey contrast and the LFP is bright-contrast, in accordance with the Z-contrast rule in HAADF imaging. A high-magnification BF-TEM image of the carbon as seen in the upper part of Figure S2 is presented in Figure S3(a), and a STEM-HAADF image of the same region is shown in Figure S3(b).

Scanning electron microscopy images of the reference and aged electrode are presented in Figure S4. Relative to the reference electrode, increased heterogeneity and formation of agglomerates are observed in the aged electrode.

3.4. Charge–discharge cycling

Figure 4 displays 0.1 °C charge–discharge curves for the reference and aged LFP-CB cathode. The two cathodes show similar initial charge capacity, but the aged cathode shows a

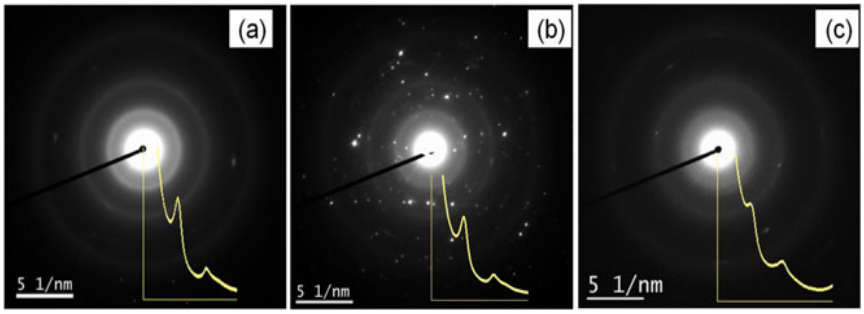

Figure 3. Selected area electron diffraction electron diffraction patterns of carbon black particles for (a) fresh cathode, (b) stored cathode, and (c) aged cathode recorded inside the dotted blue rings in Figure 2(a)–(c), respectively. The insets show normalized intensity profiles.

Table II. Selected area electron diffraction peak data.

Diffraction quantity	(002) peak			(101) peak		
	Fresh	Stored	Aged	Fresh	Stored	Aged
Intensity (a.u.)	1.13 ± 0.02	0.96 ± 0.02	0.15 ± 0.02	0.47 ± 0.02	0.36 ± 0.02	0.30 ± 0.02
FWHM (a.u.)	0.22 ± 0.02	0.25 ± 0.02	0.35 ± 0.02	0.36 ± 0.02	0.47 ± 0.02	0.58 ± 0.02

FWHM, full width at half maximum.

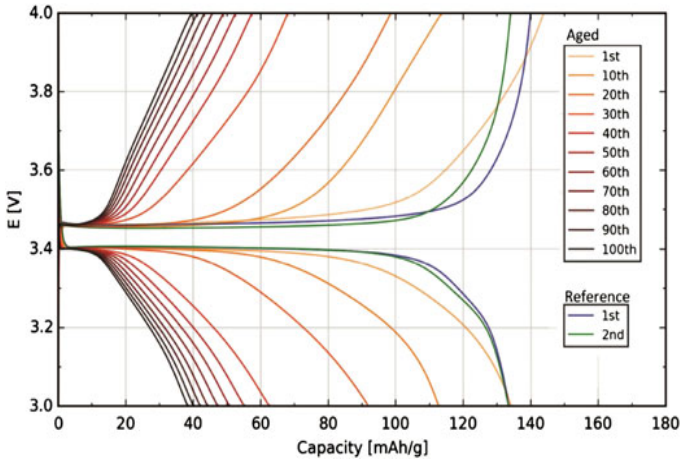

Figure 4. Charge/discharge curves for the reference and aged cathodes recorded at 0.1 °C.

significant reduction of charge capacity during cycling, ending at ~40 mAh/g after 100 cycles. The DC resistance – here calculated as the difference between the horizontal voltage level during charging and discharging (i.e., two times a DC overvoltage of 37 mV), divided with two times the applied DC current – is fairly constant with cycling around 2000 $\Omega\,cm^2$.

3.5. Impedance analysis

Figure 5 shows impedance spectra recorded for the reference cathode and for the aged cathode at various state of charge (SOC) and cycling number. The equiaxial Nyquist plot, Figure 5(a), shows impedance spectra for the aged

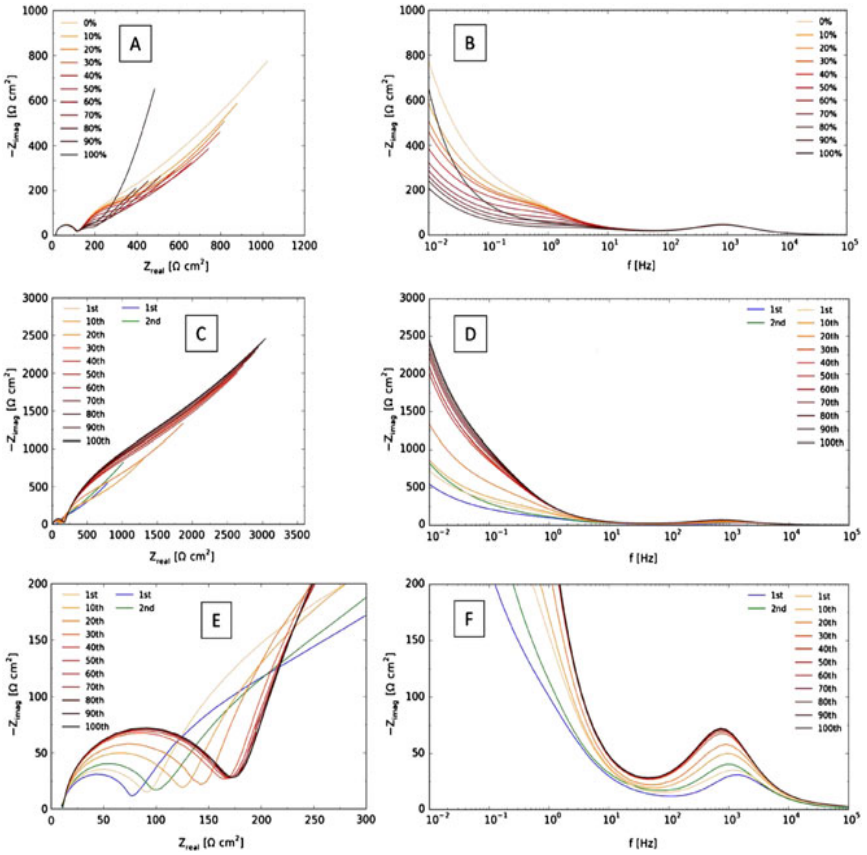

Figure 5. (a) Nyquist and (b) Bode plots of impedance spectra recorded at various state of charge with the aged electrode after five cycles. (c) Nyquist and (d) Bode plots of impedance spectra recorded with the reference electrode (blue and green spectra) and with the aged electrode (yellow–red–black spectra). (e) Nyquist and (f) Bode plots showing a zoom of the high-frequency part of the spectra presented in (c) and (d).

cathode recorded at decreasing SOC from 100% to 0% SOC after five full cycles at 0.1 °C. Figure 5(b) shows a Bode plot of the same spectra. A Nyquist plot of impedance spectra for both the reference and aged cathode at various cycling number is presented in Figure 5(c). The spectra were recorded at 0% SOC, that is, at 3 V. A Bode plot of the same spectra is presented in Figure 5(d). Zooms of the spectra are presented in Figure 5(e) and (f).

4. DISCUSSION

4.1. SEI Layer formation

From Figure 1(b), it is seen that the pristine LFP particle is crystalline and has a thin amorphous coating with a thickness of ~1 nm at the surface. The coating is an electron conductive amorphous carbon layer deposited by the supplier.

The relatively distinct thin circles in the inset in Figure 1(c) show that CB is quasi-crystalline in agreement with previously findings [25,26]. Figure 1(d) reveals concentric single-crystal sheets in CB particles oriented approximately parallel to the electron beam. A distance of 0.34 ± 0.02 nm between the sheets was obtained from a Fourier transform of the HRTEM image. This is in agreement with the previously reported distance of 0.36 nm between CB(002) planes [26–28].

The overall contrast and morphology of the aged cathode [Figure 2(c)] seem to be different from that of the fresh [Figure 2(a)] and stored [Figure 2(b)] cathodes. However, at this magnification, the main difference in appearance is due to the difference in sample preparation. The fresh and stored cathode samples were prepared on Lacey carbon grids, whereas the aged cathode sample was a TEM lamella from the cycled cathode. In the lamella [Figure 2 (c)], the gray contrast background arises from the Si-resin filling the pores between the LFP and CB particles while stabilizing the TEM lamella.

The measured difference in the thickness of the amorphous layer on the surface of the LFP particles in the pristine (~1 nm) and fresh sample (~3 nm) [Figure 1(b) and Figure 2(g)] could possibly be ascribed to the electrode preparation [29]; however, it should be noted that the difference is comparable with the measurement uncertainty.

The Fourier transform of the LFP coating layer in [Figure S1(c)] shows broad diffuse rings thus confirming that the coating is amorphous. The Fourier transform of the LFP particle in [Figure S1(b)] shows bright spots. The measured lattice spacing agrees with the distances between LFP lattice planes within an estimated measuring error of 6%. This confirms that the crystalline structure of the LFP particle survived the cathode preparation and subsequent cycling.

The composition of the coating on the pristine LFP particles was not provided by the manufacturer. The EDX Al signal was too weak to provide a map with enough spatial resolution; however, from the EDX spectrum [Figure S2 (g)], Al is seen to be present in the aged sample. This indicates that the coating on the pristine LFP particles could be an Al-containing coating such as AlF_3, which are known to suppress iron dissolution and improve the cycling capability [30,31].

It is observed that while the coating layers in the fresh [Figure 2(g)] and stored [Figure 2(h)] cathodes appear as one single amorphous layer, the coating layer in the aged cathode [Figure 2(i)] seems to consist of several layers distinguishable by different contrast levels.

The observation of a growing amorphous SEI layers on LFP during exposure to the electrolyte agrees with previous reports [32,33]. It has also been reported that SEI layers can grow during battery charge/discharge cycling and dismantling [33,34].

Specifically, LFP nanoparticles are surface sensitive to modifying additives, which means the electrolyte composition is important for the morphology of decomposition compounds and SEI layers formed on LFP surfaces [15–18]. For instance, continuous SEI layer formation on LFP using 1 mol/L $LiPF_6$ in EC/PC/EMC (0.14/0.18/0.68 wt. %) has previously been observed by Borong W. *et al.* [19] The addition of fluoroethylene carbonate to the electrolyte was observed to maintain layer continuity while affecting the SEI morphology and the impedance associated with the SEI layer. Contrary to this, heterogeneous formation of electrolyte decomposition compounds such as Li_2CO_3 and LiF was observed on LFP in 1.2 mol/L $LiPF_6$ in EC : DMC (1:1 by weight) electrolyte by C. C. Chang *et al*. [20]. It was noted that the addition of tris (pentafluorophenyl) borane suppresses this heterogeneous formation. Similarly, heterogeneous deposition of surface compounds was observed on LFP using 1 mol/L LiPF6 in EC : DEC (2:1 by weight) as electrolyte [21,22].

An interesting complementary X-ray photoelectron spectroscopy and *in-situ* atomic force microscopy study suggested that SEI layers formed on a highly oriented pyrolytic graphite electrode in 1 mol/L LiPF6 in EC : DMC (1:1 by weight) consist of a thin and scattered top layer with a dense and more continuous bottom layer [23]. Importantly, the layer formation was observed to dynamically depend on the anodic/cathodic electrode operation. In other words, the electrolyte composition, the use of additives, and the electrode charge/discharge history were shown to be important for the morphology of decomposition compounds and SEI layer formation on LFP surfaces. This indicates that the layers observed in Figure 2(i) could include the primary coating layer and different SEI layers formed when the cathode was stored and cycled.

4.2. CB crystallinity

Relative to the selected area electron diffraction profile from the fresh cathode [Figure 3], a reduction of peak intensity and peak broadening is observed for both the stored and in particular the aged sample. Decreasing CB crystallinity during storage has previously been observed [35], and the peak broadening and peak intensity decrease indicates that the CB crystallinity decreases during storage in electrolyte and during cycling. It should be noted that in the aged cathode, the amorphous Si-resin – to some extend – tends to smear out the electron diffraction pattern thereby causing additional peak intensity reduction and peak broadening.

4.3. CB agglomeration

The area within the blue dotted circle in Figure 2(c) shows an aggregate of particles. Here, it is important to distinguish between aggregation (gathering of carbon particles) and agglomeration (nucleation of new amorphous phases) [13]. A zoom on the aggregated particles is presented in the upper left part of the BF-TEM image [Figure S3(a)]. Here, it is seen that the aggregated particles have partly nucleated to form an agglomerate. The same area is shown in the STEM-HAADF image in Figure S3(b). Here, the carbon (black), Si-resin (grey), and the LFP (white) can be distinguished by brightness contrast, which confirms that the agglomerate primarily consists of carbon. The area shown in Figure S3 is part of the larger area mapped in Figure S2 (upper, right part). Figure S2(f) shows that the Si-resin contains more carbon than the LFP particles and that the agglomerate contains more carbon than the Si-resin.

It should be noted that TEM images only show smaller parts of the cathodes and are therefore prone to severe statistical errors. SEM images [Figure S4(a) and (b)] show larger parts of the reference and aged electrode with improved statistical information. Comparing the two SEM images, we observe that, relative to the reference electrode, a more heterogeneous structure and larger agglomerates are observed in the aged cathode.

It has previously been suggested that Brownian motion may cause aggregation of CB particles [36,37]. The CB aggregation is most likely enhanced by mechanical stress, because of expansion/contraction of LFP upon cycling and/or Fe dissolution from LFP grains [38]. Self-agglomeration of

C_{65} and Super P is previously observed in $LiCoO_2$ cathode systems [29,39]. Similarly, C_{65} agglomeration has been observed in cycled LMNO/C_{65} electrodes where Fourier transform infrared spectroscopy analysis of the cycled electrode indicated decomposition reactions and possible formation of alkyl carbonates [40]. Thus, in the present study, the observed decrease of CB crystallinity is likely related to the formation of carbon agglomerates.

It should be noted that pristine CB consists of particles that have grown into each other as part of the combustion process so that they share graphitic sheets. This means that the pristine CB – to some extent – already forms agglomerates. However, the agglomerates observed in the aged sample [Figure S4(b)] are significantly larger than the agglomerates in the pristine CB. Specifically, quasi-crystalline round-shaped CB nanoparticles are observed in both the fresh and the stored cathode, whereas spherical CB nanoparticles are difficult to find in the TEM specimen from the aged sample. Here, the carbon has primarily formed amorphous chains rather than spherical particles.

Relative to commercial cathodes, the investigated laboratory-made cathode has a rather poor particle packing with large open pores, which enhances carbon particle aggregation and subsequent formation of large agglomerates [14]. Amorphous carbon has a lower electric conductivity than the quasi-crystalline CB [8,41,42], which means that the formation of large carbon agglomerates with decreased crystallinity along with the increased heterogeneity in the aged sample will likely decrease the electric conductivity in the carbon network.

4.4. Charge–discharge cycling

The capacity loss observed in LFP batteries is normally ascribed to the negative graphite electrode [43], and related to the thick SEI layers of several hundredth of nm that can be formed here [44]. However, the thickness of the SEI layers formed on the LFP particles in this study is much smaller [Figure 2(f) and (i), ~30 nm] than the thickness of the SEI layers normally formed at the negative graphite electrode. For this reason, the SEI layer formation at the LFP surface is not expected to contribute significantly to the observed capacity fade seen for the aged LFP electrode in Figure 4.

In commercial batteries, the resistance of the LFP electrode is normally significantly larger than the resistance at the graphite electrode [45]. Thus, for such batteries, SEI layer formation at the LFP is likely to affect the battery resistance rather than the battery capacity. The DC resistance (before onset of concentration polarization) is fairly constant [Figure 4] around $2000\,\Omega\,cm^2$ ($=37\,mV/40\,\mu A\cdot\pi\cdot 9\,mm^2$), so the SEI layers formed on the LFP particles during storage and cycling do not seem to affect the DC resistance.

At the low C-rate used in this manuscript, the DC overpotentials are related to the critical over-potential required to initiate lithiation/delithiation in the LFP particles [46]. It is believed that this over-potential is not affected by the local increase in current density with capacity fading at the individual LFP particles, because the applied current densities are relatively small – even after the observed capacity fade.

4.5. Impedance analysis

The semi-circle in Figure 5(a) occurring between 10 kHz and 100 Hz [Figure 5(b)] is independent of SOC. This is in agreement with the conventional assumption that this arc is related to the interface between the current collector and the cathode materials [47–51]. The mid-low frequency range (between 10 Hz and 10 kHz) [Figure 5(b)] is characterized by a larger semicircle [Figure 5(a)] that transitions into a low-frequency tail with an angle of 45° in the Nyquist plot [Figure 5(a)], which is usually related to respectively electrode/electrolyte interface reactions and diffusion of lithium ions in the LFP particles [52,53]. This part of the spectra is seen to be dependent of SOC in particular at low and high SOC.

Figure 5(c) and (d) (zoom in (e) and (f)) shows that both the high-frequency part and the low frequency part increase because of cycling. Relative to the reference cathode, the aged cathode exhibited increased heterogeneity in the carbon network, carbon agglomeration, and decreased carbon crystallinity. Additionally, loss of electric percolation has been reported for the aged LFP CB electrode using low-kV FIB/SEM [11,14]. These degradation mechanisms are expected to decrease the electric conductivity in the CB network, thereby increasing the size of the high-frequency arc.

The resistance related to the low-frequency part of the impedance spectra in Figure 5 is also observed to increase with cycling. The value of the real part of the lowest-frequency impedance in part (c) is larger than the ~$2000\,\Omega\,cm^2$ DC resistance. This is because the impedance is measured at 0% SOC where the overvoltage deviates from the DC overvoltage of 37 mV.

It is important to note that the resistance associated with the high-frequency arc is in the order of 75–$175\,\Omega\,cm^2$, which is small relative to the DC resistance of ~$2000\,\Omega\,cm^2$. Thus, the increase with cycling of the size of the high-frequency arc does not significantly affect the DC resistance.

5. CONCLUSIONS

Laboratory assembled electrodes of LFP-CB were investigated at different preparation, storage, and cycling stages by complementary TEM and SEM microscopy techniques, charge–discharge capacity curves, and impedance spectroscopy.

Decreased crystallinity of CB particles was observed in an electrode cycled 100 times. Additionally, agglomeration of carbon was seen in the electrode. The decrease in the crystallinity and CB agglomeration is expected to decrease the electrical conductivity in the CB network. Impedance

spectroscopy was performed on the cycled electrode every 10 cycles. The spectra showed an increasing resistance with cycling in the high-frequency impedance arc. This arc was independent of SOC and associated with the CB network – current collector interface. The increase in the arc resistance was linked to a decrease in the conductivity/percolation of the CB network.

Storage in electrolyte and charge/discharge cycling was shown to increase the thickness of amorphous SEI layers formed at the LFP surfaces. Interestingly, a multilayered SEI was formed on the cycled electrode. This suggests that the operational history of the electrode to some extent is recorded by the SEI layer and points towards research that can 'read' this history. More systematic studies of the correlation between SEI layer formation and changes in the electrode impedance are required to quantify and solidify these conclusions.

ACKNOWLEDGEMENTS

The authors gratefully acknowledge the financial support from the Danish Strategic Research Council through the project 'Advanced Lifetime Predictions of Battery Energy Storage' (contract no. 0603-00589B).

REFERENCES

1. Whittingham MS. Lithium batteries and cathode materials. *Chemical Reviews* 2004; **104**:4271–4301.
2. Wang J, Sun X. Olivine LiFePO4: the remaining challenges for future energy storage. *Energy and Environmental Science* 2015; **8**:1110.
3. Padhi AK, Nanjundaswamy KS, Goodenough JB. Phospho-olivines as positive-electrode materials for rechargeable lithium batteries. *Journal of The Electrochemical Society* 1997; **144**:1188.
4. Yamada A, Chung SC, Hinokuma K. Optimized LiFePO4 for lithium battery cathodes. *Journal of The Electrochemical Society* 2001; **148**:A224.
5. Niu J *et al.* In situ observation of random solid solution zone in LiFePO4 electrode. *Nano Letters* 2014; **14**:4005–4010.
6. Liao X-Z *et al.* LiFePO4 Synthesis routes for enhanced electrochemical performance. *Journal of The Electrochemical Society* 2005; **152**:A231.
7. Gao H *et al.* High rate capability of Co-doped LiFePO4/C. *Electrochimica Acta* 2013; **97**:143–149.
8. Spahr ME, Goers D, Leone A, Stallone S, Grivei E. Development of carbon conductive additives for advanced lithium ion batteries. *Journal of Power Sources* 2011; **196**:3404.
9. Liu P *et al.* Aging mechanisms of LiFePO4 batteries deduced by electrochemical and structural analyses. *Journal of The Electrochemical Society* 2010; **157**:A499.
10. Wang J, Sun X. Olivine LiFePO4: the remaining challenges for future energy storage. *Energy and Environmental Science* 2015; **8**:1110–1138.
11. Scipioni R *et al.* Degradation studies on LiFePO 4 cathode. *ECS Transactions* 2015; **64**:97.
12. Roberts MR *et al.* Direct observation of active material concentration gradients and crystallinity breakdown in LiFePO4 electrodes during charge / discharge cycling of lithium batteries. *The Journal of Physical Chemistry C* 2014; **118**:6548–6557.
13. Nichols G *et al.* A review of the terms agglomerate and aggregate with a recommendation for nomenclature used in powder and particle characterization. *Journal of Pharmaceutical Sciences* 2002; **91**:2103–2109.
14. Scipioni R *et al.* Electron microscopy investigations of changes in morphology and conductivity of LiFePO4/C electrodes. *Journal of Power Sources* 2016; **307**:259–269.
15. Wu J *et al.* In situ Raman spectroscopy of LiFePO4: size and morphology dependence during charge and self-discharge. *Nanotechnology* 2013; **24**:424009.
16. Sacci RL *et al.* Direct visualization of initial SEI morphology and growth kinetics during lithium deposition by in situ electrochemical transmission electron microscopy. *Chemical Communications* 2014; **50**:2104.
17. Sugar JD *et al.* High-resolution chemical analysis on cycled LiFePO4 battery electrodes using energy-filtered transmission electron microscopy. *Journal of Power Sources* 2014; **246**:512.
18. Samadani E, Mastali M, Farhad S, Fraser RA, Fowler M. Li-ion battery performance and degradation in electric vehicles under different usage scenarios. *International Journal of Energy Research* 2015. doi:10.1002/er.3378.
19. Wu B *et al.* Enhanced electrochemical performance of LiFePO4 cathode with the addition of fluoroethylene carbonate in electrolyte. *Journal of Solid State Electrochemistry* 2013; **17**:811–816.
20. Chang CC, Chen TK. Tris(pentafluorophenyl) borane as an electrolyte additive for LiFePO4 battery. *Journal of Power Sources* 2009; **193**:834–840.
21. Herstedt M *et al.* Surface chemistry of carbon-treated LiFePO4 particles for Li-ion battery cathodes studied by PES. *Electrochemical and Solid-State Letters* 2003; **6**:A202.
22. Stjerdmdahl M. *Stability Phenomena in Novel Electrode Materials for Lithium-ion Batteries*. *Acta Universitatis Upsaliensis* Uppsala University: Sweden, 2007.
23. Shen C, Wang S, Jin Y, Han WQ. In situ AFM imaging of solid electrolyte interfaces on HOPG with

ethylene carbonate and fluoroethylene carbonate-based electrolytes. *ACS Applied Materials and Interfaces* 2015; **7**:25441–25447.
24. William DB, Carter CB. *Transmission Electron Microscopy: A Textbook for Materials Science*. Springer, 2006. DOI:10.1007/978-0-387-76501-3.
25. Ugarte D. Curling and closure of graphitic networks under electron-beam irradiation. *Nature* 1992; **359**:707.
26. Vander Wal RL, Tomasek AJ, Pamphlet MI, Taylor CD, Thompson WK. Analysis of HRTEM images for carbon nanostructure quantification. *Journal of Nanoparticle Research* 2004; **6**:555.
27. Belenkov E. Formation of graphite structure in carbon crystallites. *Inorganic Materials* 2001; **37**:928–934.
28. Bi H, Kou KC, Ostrikov K, Zhang JQ. Graphitization of nanocrystalline carbon microcoils synthesized by catalytic chemical vapor deposition. *Journal of Applied Physics* 2008; **104**:1–7.
29. Kwon NH. The effect of carbon morphology on the LiCoO2 cathode of lithium ion batteries. *Solid State Sciences* 2013; **21**:59–65.
30. Song GM, Wu Y, Liu G, Xu Q. Influence of AlF3 coating on the electrochemical properties of LiFePO4/graphite Li-ion batteries. *Journal of Alloys and Compounds* 2009; **487**:214–217.
31. Xu B, Qian D, Wang Z, Meng YS. Recent progress in cathode materials research for advanced lithium ion batteries. *Materials Science and Engineering: R: Reports* 2012; **73**:51–65.
32. Lawder MT, Northrop PWC, Subramanian VR. Model-based SEI layer growth and capacity fade analysis for EV and PHEV batteries and drive cycles. *Journal of The Electrochemical Society* 2014; **161**: A2099–A2108.
33. Li D *et al.* Modeling the SEI-formation on graphite electrodes in LiFePO4 batteries. *Journal of The Electrochemical Society* 2015; **162**:A858–A869.
34. Yamamoto K *et al.* Dynamic visualization of the electric potential in an all-solid-state rechargeable lithium battery. *Angewandte Chemie International Edition* 2010; **49**:4414–4417.
35. Younesi R *et al.* Analysis of the interphase on carbon black formed in high voltage batteries. *Journal of The Electrochemical Society* 2015; **162**:A1289–A1296.
36. Zhu M, Park J, Sastry AM. Particle interaction and aggregation in cathode material of Li-ion batteries: a numerical study. *Journal of The Electrochemical Society* 2011; **158**:A1155.
37. Li J, Armstrong BL, Daniel C, Kiggans J, Wood DL. Optimization of multicomponent aqueous suspensions of lithium iron phosphate (LiFePO4) nanoparticles and carbon black for lithium-ion battery cathodes. *Journal of Colloid and Interface Science* 2013; **405**:118–124.
38. Zhi X *et al.* The cycling performance of LiFePO4/C cathode materials. *Journal of Power Sources* 2009; **189**:779–782.
39. Hong JK, Lee JH, Oh SM. Effect of carbon additive on electrochemical performance of LiCoO2 composite cathodes. *Journal of Power Sources* 2002; **111**:90–96.
40. Arbizzani C, Da Col L, De Giorgio F, Mastragostino M, Soavi F. Reduced graphene oxide in cathode formulations based on LiNi0.5Mn1.5O4. *Journal of The Electrochemical Society* 2015; **162**: A2174–A2179.
41. Chu PK, Li L. Characterization of amorphous and nanocrystalline carbon films. *Journal of Materials Chemistry* 2006; **96**:253–277.
42. Pandolfo AG, Hollenkamp AF. Carbon properties and their role in supercapacitors. *Journal of Power Sources* 2006; **157**:11–27.
43. Klett M *et al.* Non-uniform aging of cycled commercial LiFePO4//graphite cylindrical cells revealed by post-mortem analysis. *Journal of Power Sources* 2014; **257**:126–137.
44. Zhang HL, Li F, Liu C, Tan J, Cheng HM. New insight into the solid electrolyte interphase with use of a focused ion beam. *The Journal of Physical Chemistry B* 2005; **109**:22205–22211.
45. Belt JR, Bernardi DM, Utgikar V. Development and use of a lithium-metal reference electrode in aging studies of lithium-ion batteries. *Journal of The Electrochemical Society* 2014; **161**:A1116–A1126.
46. Cogswell DA, Bazant MZ. Theory of coherent nucleation in phase-separating nanoparticles. *Nano Letters* 2013; **13**:3036–3041.
47. Zhu Y, Xu Y, Liu Y, Luo C, Wang C. Comparison of electrochemical performances of olivine NaFePO4 in sodium-ion batteries and olivine LiFePO 4 in lithium-ion batteries. *Nanoscale* 2013; **5**:780–787.
48. Chang Y-C, Sohn H-J. Electrochemical impedance analysis for lithium ion intercalation into graphitized carbons. *Journal of The Electrochemical Society* 2000; **147**:50.
49. Liao X-Z *et al.* Electrochemical behavior of LiFePO4/C cathode material for rechargeable lithium batteries. *Journal of The Electrochemical Society* 2005; **152**:A1969.
50. Gaberscek M, Moskon J, Erjavec B, Dominko R, Jamnik J. The importance of interphase contacts in Li ion electrodes: the meaning of the high-frequency impedance arc. *Electrochemical and Solid-State Letters* 2008; **11**:A170.

51. Illig J *et al.* Separation of charge transfer and contact resistance in LiFePO4-cathodes by impedance modeling. *Journal of The Electrochemical Society* 2012; **159**:A952.
52. Meyers JP, Doyle M, Darling RM, Newman J. The impedance response of a porous electrode composed of intercalation particles. *Journal of The Electrochemical Society* 2000; **147**:2930.
53. Gao F, Tang Z. Kinetic behavior of LiFePO4/C cathode material for lithium-ion batteries. *Electrochimica Acta* 2008; **53**:5071.

SUPPORTING INFORMATION

A TEM study of morphological and structural degradation phenomena in $LiFePO_4$-CB cathodes

IV

Analysis of the Interphase on Carbon Black Formed in High Voltage Batteries

Reza Younesi,[a,*,z] Ane Sælland Christiansen,[a] Roberto Scipioni,[a] Duc-The Ngo,[a] Søren Bredmose Simonsen,[a,*] Kristina Edström,[b,*] Johan Hjelm,[a,*] and Poul Norby[a]

[a]*Department of Energy Conversion and Storage, Technical University of Denmark, DK-4000 Roskilde, Denmark*
[b]*Department of Chemistry, Ångström Laboratory, Uppsala University, SE-751 21 Uppsala, Sweden*

Carbon black (CB) additives commonly used to increase the electrical conductivity of electrodes in Li-ion batteries are generally believed to be electrochemically inert additives in cathodes. Decomposition of electrolyte in the surface region of CB in Li-ion cells at high voltages up to 4.9 V is here studied using electrochemical measurements as well as structural and surface characterizations. $LiPF_6$ and $LiClO_4$ dissolved in ethylene carbonate:diethylene carbonate (1:1) were used as the electrolyte to study irreversible charge capacity of CB cathodes when cycled between 4.9 V and 2.5 V. Synchrotron-based soft X-ray photoelectron spectroscopy (SOXPES) results revealed spontaneous partial decomposition of the electrolytes on the CB electrode, without applying external current or voltage. Depth profile analysis of the electrolyte/cathode interphase indicated that the concentration of decomposed species is highest at the outermost surface of the CB. It is concluded that carboxylate and carbonate bonds (originating from solvent decomposition) and LiF (when $LiPF_6$ was used) take part in the formation of the decomposed species. Electrochemical impedance spectroscopy measurements and transmission electron microscopy results, however, did not show formation of a dense surface layer on CB particles.

 [DOI: 10.1149/2.0761507jes] All rights reserved.

Manuscript submitted December 23, 2014; revised manuscript received April 9, 2015. Published April 16, 2015.

The growth of earth's population with concomitant increase in energy consumption require development of renewable energy conversion technologies coupled with advanced energy storage systems like lithium batteries.[1,2] In order to increase the power density in Li-ion batteries, much research is focused on developing cathode materials that can operate at high voltages (above 4.5 V vs. Li/Li^+) with a high capacity, high cycling stability, and good rate capability.[3–5] However, at high voltages, all the components of positive electrodes including the Al current collector, polymer binders, conductive additives, and other possible additives have an increased risk of degradation. In addition, one of the main issues with high voltage batteries is the instability of common aprotic electrolytes at voltage above 4.5 V.[6,7] The stability of the electrolyte/cathode interphase is related to the chemistry of electrolyte solvents and salts and also to the chemistry of the components of the cathode.

Carbon black (CB) additives are one of the main constituents of cathodes, added to increase the electrical percolation and thus the electronic conductivity.[8,9] Though the weight percentage of CB in commercial batteries is generally very small, it composes a rather large part of the internal surface area of a cathode due to its small particle size (≈50 nm), low density, and high surface area. CBs are generally thought of being an electrochemically inert additive in cathodes, but few studies have investigated the role of CBs at high voltages and have indicated that CBs exhibit irreversible electrochemical reactions resulting in appreciable irreversible charge capacities.[10–18] This charge capacity is attributed to oxidation reactions, anodic degradation of aprotic electrolytes on the surface of CBs, side reactions involving binder and salt, and intercalation of anions such as PF_6^- (partly reversible) and solvent molecules into graphitic layers.[10–19] The oxidation voltage, decomposition products, and possible formation of a surface layer are dependent on the chemistry of electrolyte and the surface area and the surface functional groups of CBs.[10–14] This is similar, but not identical, to the concept of formation of solid electrolyte interphase (SEI) on anodes. This SEI-like layer is often referred to as a solid permeable interphase (SPI)[20] or cathode electrolyte interphase (CEI)[21] and can ideally prevent further parasitic reactions between electrolyte and cathode materials. According to La Mantia et al. the oxidation of surface active groups occurs around 4.5–4.6 V.[12] They showed that the first charge capacity is dependent on the charge rate, which could indicate the formation of a SPI layer. This surface layer was suggested to be made of Li_2CO_3, LiF, and polycarbonates, but was not analyzed to prove.[12] In two recent studies Demeaux et al. and Syzdek et al. suggested decomposition products from the electrolyte on the surface of carbon particles at high voltages using FT-IR.[11,14] A surface layer of decomposed electrolyte formed on carbon particles can decrease electronic conductivity, and thus, hinder the overall performance of the cathode.[22]

The aim of this work is to study parasitic reactions and possible formation of a surface layer on Super P, as one of the most common CB, in cathodes during the first few cycles at high voltages in Li-ion cells with two different electrolyte salts, $LiPF_6$ and $LiClO_4$. The surface layer on cathodes can be very thin, and thus, difficult to analyze by SEM, XRD,[14] or conventional X-ray photoelectron spectroscopy (XPS). Therefore, we used synchrotron-based soft X-ray photoelectron spectroscopy (SOXPES), which is one of the most powerful techniques for studying the outermost surface of compounds, to analyze the surface of CBs. We chose to use relatively low excitation photon energies to detect both crystalline and/or amorphous chemical compounds at shallow depths from the surfaces of the cathodes. Tuning the photon energies, we could achieve a nondestructive depth profiling of the surface layer. In addition electrochemical impedance spectroscopy (EIS), transmission electron microscopy (TEM) and energy-dispersive X-ray spectroscopy (EDS) were used to characterize the change in morphology, structure, and chemistry of CB before and after charging to high voltages.

Experimental

Li-ion cells were assembled in a "Coffee-bag" (pouch cell) configuration[23] using carbon black electrodes as the positive electrode, Li metal as the negative electrode, and two layers of Celgard 2500 (Monolayer Polypropylene) membrane (dried at 60°C overnight) as the separator. Cathodes were prepared by mixing Super P carbon black (purchased from Erachem Comilog N.V.) with Kynar binder (Kynar Flex 2801, Arkema) dissolved in (N-Methyl-2-Pyrrolidone) and casting on Al foil. The ratio of carbon:binder was 70:30 by weight. The electrodes were dried at 120°C overnight and were cut to discs of 10 mm in diameter. A total mass of 0.42 mg Super P was used for each electrode. The electrolyte mixture consisted of 1 M of either $LiPF_6$ or $LiClO_4$ salts dissolved in EC:DEC (vol. 1:1), where EC is ethylene carbonate and DEC is diethyl carbonate purchased from BASF. 200 µl of electrolyte were added to each cell. The electrochemical characterizations were performed using a BioLogic VMP3

*Electrochemical Society Active Member.
zE-mail: reyo@dtu.dk

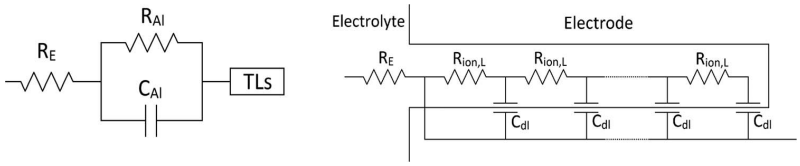

Figure 1. Equivalent circuit used for the analysis of the impedance spectra (right) including equivalent circuit of a pore described by a transmission line (left).

multichannel analyzer. A constant current of 5 μA yielding the current density of about 6.4 $\mu A.cm^{-2}$ and voltage limits of either 4.9–2.5 V or 4.3–2.5 V were applied for cycling cells used for SOXPES analysis. For comparison, identical cells were assembled and stored for 3 days without applying external current or voltage (hereafter referred to as "stored" electrodes). Similar cells were assembled and cycled between 5.2 V and 2.5 V for TEM and EDS analysis. Electrochemical impedance spectroscopy (EIS) measurements were performed in a three-electrode EL-CELL ECC-Combi using lithium metal as counter and reference electrodes. The cell was assembled inside the glove box using glass fiber separator (and 200 μl electrolyte solution. EIS measurements in a frequency range from 500 kHz to 10 mHz of CB electrodes were obtained before (stored) and after stepwise charge to 4.9 V. All measurements were performed at OCV after the cell had reached steady state defined by a change <5 mV/h. The impedance results were modeled using the equivalent circuit presented in Figure 1. The R_E-$R_{Al}C_{Al}$ elements model the high-frequency region where R corresponds to a resistance and C corresponds to a capacitor. These values have been normalized to the geometrical surface area of the electrode (0.785 cm^2). The low-frequency region has been modeled with a simplified transmission line (TL) for a porous electrode, according to De Levie model.[24,25] This model involves a cylindrical pore with lenght L and radius r, filled with the electrolytic solution, and the electronic resistance of the electrode is assumed to be much lower than the ionic resistance of the solution ($R_E \ll R_{ion}$). In case of a non-faradaic process, the overall impedance inside the pore is equal to:

$$Z = \sqrt{\frac{R_{ion,L}}{j\omega C_{dl,A} 2\pi r}} \coth\sqrt{R_{ion,L} * j\omega C_{dl,A} 2\pi r} \qquad [1]$$

where $R_{ion,L}$ is the ionic resistance of the electrolyte per unit pore length (Ωcm^{-1}) and $C_{dl,A}$ is the electrical double layer capacitance per unit surface area (Fcm^{-2}). From this model we calculated the total double layer capacitance of the CB electrode C_{dl} (F). The uniform transmission line for a flooded ideally polarized porous electrode can be seen in Figure 1. This model makes a good fit of the high- and low-frequency regions of the experimental data, but shows a small deviation in the mid-frequency part. Despite this, the model has been chosen as it provides an acceptable fit with a meaningful physical interpretation to the interface between CB surface and electrolyte in the extended porous network. The double layer capacitance is related to the total surface area A:

$$C_{dl} = \varepsilon\varepsilon_0 \frac{A}{l} \qquad [2]$$

where ε_0 is the electric constant, and ε and l is the dielectric constant and the thickness of a surface layer, respectively. After cycling, Li-ion cells were transferred to MAX-IV Laboratory where they were dismantled in an Ar-filled glove box (H_2O < 1 ppm). The carbon electrodes were washed with several drops of dimethyl carbonate (DMC). This washing is necessary to remove remaining electrolyte species in order to obtain spectra from the surface of the samples. The samples were mounted in a specially designed transfer chamber and transported to the analyzing chamber without exposure to the atmosphere. The measurements were performed using synchrotron radiation (beamline I-411) at the MAX IV Laboratory. Photons were monochromatized by a Zeiss SX-700 planar grating monochromator. Core level spectra of carbon (C 1s) spectra were measured using two different photon energies of 430 eV and 835 eV to obtain depth profile analysis of surface layer on carbon cathodes. Core level spectra of fluorine (F 1s) spectra were measured using photon energies of 835 eV. The spectra were energy calibrated using the hydrocarbon peak at 285.0 eV. The spectra were intensity normalized to 1. Curve fitting was performed using IGOR Pro, and a linear background was subtracted before the spectra were deconvoluted. TEM imaging and selected area electron diffraction (SAED) of CB was carried out by using a JEOL 3000 F equipped with a 300 kV FEG. EDS was carried out for compositional analysis by using an Oxford Instruments detector with an ultra-thin window. The analysis was performed using the Inca software. After opening the cells, the samples were washed by DMC to remove the electrolyte. All specimens were prepared for TEM by scratching electrode powders from the Al current collector and the powder was dispersed dryly onto Au TEM grids with a lacey carbon film. Particle sizes were analyzed from bright field TEM images using ImageJ software. To compare the intensities in the SAED data, the patterns were circularly integrated and the all intensities were normalized to the intensity of the first diffraction ring. XRD analyses was performed using a Bruker D8 TwinTwin X-ray diffractometer operating at 40 kV and 40 mA using Cu Kα radiation (λ = 1.5406 Å).

Results and Discussion

Figure 2a shows the first charge curves of Li-ion cells assembled using CB cathodes with $LiPF_6$ or $LiClO_4$ as the electrolyte salts. It can be seen that the $LiClO_4$-based cell reached the anodic limit of 4.9 V much faster than the $LiPF_6$-based cell. In other words, the $LiClO_4$ based cell provided a smaller charge capacity, about 50 $mAh \cdot g^{-1}$, while the $LiPF_6$ cell yielded a larger charge capacity of about 800 $mAh \cdot g^{-1}$. These capacities are comparable (considering differences in applied current densities) to previously reported results for Super P carbon black and noticeably smaller than capacities of similar cells with graphitic carbons or high surface area carbons like Ketjen black which provides irreversible charge capacity above 2000 $mAh \cdot g^{-1}$.[12,13]

To investigate the reversibility of these capacities, the cells were discharged to 2.5 V and then cycled 10 times between 4.9 and 2.5 V. Figure 2b shows that the charge capacities were significantly higher than the discharge capacities indicating irreversible electrochemical processes during charge. In addition, the charge capacity decreased significantly from the first cycle to the following cycles (note that the capacities are presented on a logarithmic scale). The small discharge capacity is the same in all cycles indicating that a minor reversible reaction occurs on the CB cathodes. This reversible capacity is due to the sum of the accumulated surface capacitance and the charge transfer from any reversible electrochemical processes. The latter could be intercalation/deintercalation of PF_6^- or ClO_4^- anions to/from the positive electrode, as this can provide a small reversible capacity.[8,15–19]

The large irreversible capacity (defined as the difference between the charge and the discharge capacity) can be explained by i) formation of a AlF_3 passivation layer on the aluminum current collector via decomposition of $LiPF_6$,[26,27] and ii) reactions between the electrolyte and the surface functional groups on the carbon surface. In order to clarify the contribution of Al current collector corrosion to the total irreversible capacities observed for CB cathodes, identical cells were assembled using only an Al disk (as it is without any carbon black or active material on it) as cathode. Figure 2c shows that the irreversible

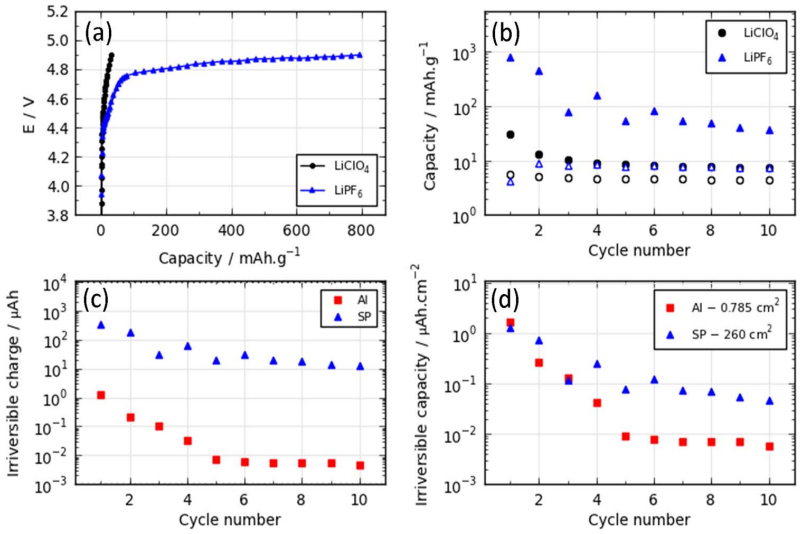

Figure 2. (a) First charge curves of Li-ion cells using CB cathode with $LiPF_6$ or $LiClO_4$ as electrolyte salt dissolved in EC:DEC (1:1) solvent. (b) Charge/discharge capacities for the first 10 cycles of CB cathode cycled between 4.9–2.5 V using the same electrolytes. Solid points are for charge while open points are for discharge capacities. (c) Logarithmic irreversible capacity vs. cycle number for a CB electrode and a bare Al electrode using $LiPF_6$ salt. (d) Same as (c), but divided by surface area of the electrodes.

charge (Q_{irr}) is order of magnitudes higher in the CB electrode than in an Al electrode in cells with $LiPF_6$ electrolyte salt, showing that the Al current collector corrosion is not the main origin of Q_{irr}. However, one may argue that the higher surface area of carbon particles causes the higher degree of Q_{irr} in the CB electrode. Figure 2d shows Q_{irr} per surface area of the electrodes. The surface area for the Al disk is estimated to be 0.785 cm^2, assuming a smooth surface. In case of CB electrodes, the surface area is estimated by using a BET value of 62 $m^2 \cdot g^{-1}$ for CB powder, assuming that all particles are available for charge accumulation i.e. no surface blocking due to binder etc. Thus, the total surface area of CB electrode is assumed to be equal to 260 cm^2. Figure 2d shows that Q_{irr}/cm^2 of Al disk is significantly deceased after few cycles, which is known to be due to formation of a passivation layer of AlF_3. However, Q_{irr}/cm^2 of CB electrode is still about one order of magnitude higher for CB in the following cycles. This finding confirms that Q_{irr} in long term cycling is originated from CB particles. Winter et al. have shown that the nature and properties of CBs such as presence of functional groups and graphitic structure influence irreversible capacities at high voltage.[16–18] They have shown that thermal treatment of CB results in graphitization of CB as well as removal of functional groups, which consequently can decrease Q_{irr} of CB.

To investigate a possible formation of electrolyte decomposition species in or on CB particles at high voltages, CB electrodes were analyzed using synchrotron-based SOXPES. Figure 3a shows C1s spectra of a CB cathode cycled 10 times between 4.9–2.5 V using $LiPF_6$ as the electrolyte salts. Also, C1s spectra of a CB cathode that was cycled between 4.3–2.5 V, as well as, C1s spectra of pristine and stored CB electrodes are presented in the Figure 3a. The C1s spectrum of the pristine sample contains 4 main contributions at the binding energies of 284.6 eV, 285 eV, 286.5 eV, and 290.9 eV assigned to Super P, hydrocarbons, CH_2 (from binder), and CF_2 (from binder), respectively.[28,29] There are also two small contributions at binding energies of 288.7 eV and 293.5 eV representing CF and CF_3, respectively, in Kynar binder.[28–30] Interestingly, the C1s spectrum of the stored sample shows different features compared to the spectrum of the pristine sample, as the stored sample has a higher intensity/contribution of the hydrocarbon peak (red peak at 285 eV). Also, the intensity of the peak at 286.5 eV (green peak) is increased, which indicates presence of C–O bond in the surface region of the stored CB particles. In addition, a small peak has appeared at 287.5 eV originating from O–C–O and/or C=O bonds.[28–30] The changes in the spectrum of the stored sample compared to the pristine sample shows that the electrolyte solution partially decomposes in/at the surface of CB particles when the electrode is immersed in the electrolyte. It should be mentioned again that all the electrodes were washed with DMC before SOXPES measurements to make sure no electrolyte remained on the surface of electrodes. Similar, but not identical, results regarding the surface degradation on stored carbon electrodes have been observed in other studies using FTIR.[11,14] Demeaux et al.[11] proposed that polyether and polycarbonate species form on the surface of CB samples stored for longer time (4 weeks) at higher temperature (40°C). While our SOXPES confirms formation of ether-based species, we did not observe formation of carbonate-based compound on the stored samples. Also, Demeaux et al.[11] suggested a formation of a surface layer based on scanning electron microscopy (SEM). However, Syzdek et al. did not detect any surface layer in SEM results, and this was explained by the possibly removal of any surface layer by DMC prior to imaging.[14] The formation of decomposition species in the stored sample may take place by a redox reaction as the cells have open circuit voltage about 3 V vs. Li/Li^+.[11] Compared to well-studied storage degradation of cathode materials,[31–34] less attention has been paid to spontaneous reaction occurring in the surface region of stored CB. Thus, the presented results are useful for detecting the origin of surface layer on stored cathodes, because decomposition products originated from active materials and carbon black may overlap with each other.[11]

Surprisingly, the C1s spectrum of the CB cathode cycled 10 times up to 4.3 V present similar features to the C1s spectrum of pristine sample indicating that no major decomposition product is present in the CB cathode when cycled up to 4.3 V. The C1s spectrum consists of extra minor contribution from O–C–O and/or C=O bonds compared to the pristine sample. The results could suggest that the decomposition species in the surface of the stored CB diminishes when the CB cathode is cycled up to 4.3 V. This can, for example, occur by oxidation and/or dissolution/desorption.[30,35]

Cycling the CB cathode between 4.9–2.5 V using $LiPF_6$ electrolyte, we could detect an increase in the relative intensity of peaks at 287.5 eV and 290.9 eV. The former originates from O-C-O and/or C=O bonds while the latter from carbonate species (CO_3).[28–30] The

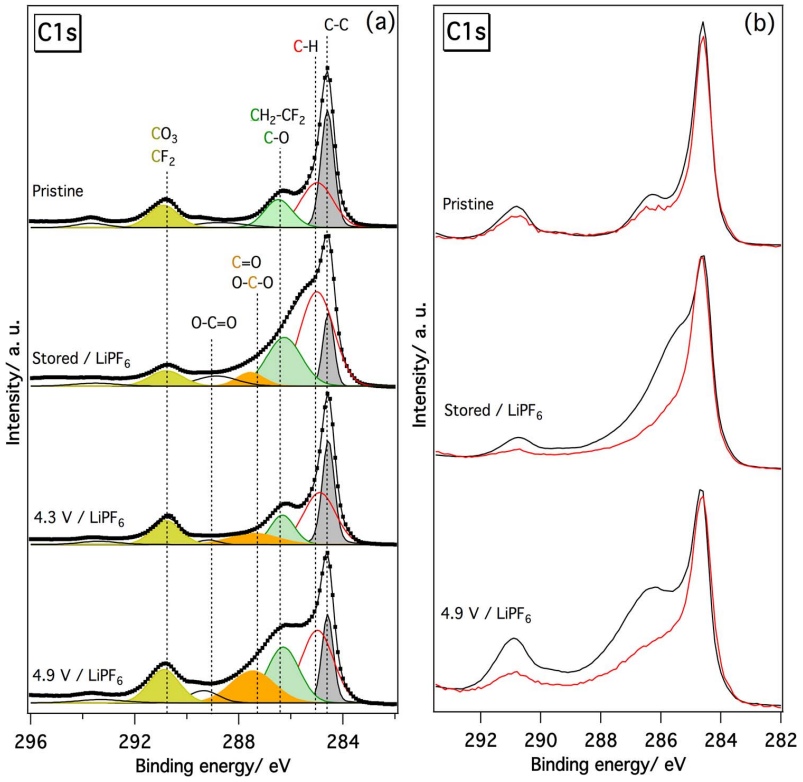

Figure 3. (a) Deconvoluted C1s spectra of pristine, stored, and cycled CB cathodes using $LiPF_6$ in EC:DEC electrolyte. The spectra were measured by photon energy of 430 eV. (b) C1s spectra of the same samples measured using two photon energies of 430 eV (black) and 835 eV (red).

increase in the relative intensity of these peaks implies that the CB cathode decompose EC:DEC solvent partially when the cell was cycled to 4.9 V.

To obtain a depth profiling of the surface layer, the CB cathodes were analyzed using two different photon energies of 430 eV and 835 eV, as presented by the black and red spectra, respectively, in Figure 3b. For the pristine CB electrode, the C1s spectra look similar using these two photon energies, as expected. A minor difference is that the C1s spectrum measured with lower photon energy shows slightly more contribution from binder (peaks at 286.5 eV, and 290.9 eV), indicating that concentration of binder is slightly higher on top surface. The stored and cycled samples display that the C1s spectra are more similar to the pristine sample for the higher photon energy of 835 eV. The spectra obtained with the higher photon energy are originated from increased depth of about 5–7 nm.[36] Therefore, the highest concentration of electrolyte decomposition species are found in a thin, about 1–3 nm, surface region of the CB.

Figure 4a shows C1s spectra of CB electrodes stored and cycled to 4.9 V using $LiClO_4$ in EC:DEC electrolyte. Both spectra demonstrate presence of decomposed electrolyte species on the surface of the sample. However, compared to the $LiPF_6$-based samples, the spectra of $LiClO_4$-based sample show a less degree of difference from the spectrum the pristine sample. Also, the spectra of $LiClO_4$-based samples measured by two photon energies of 430 eV and 835 eV (black and red spectra respectively in Figure 4b) are more similar than those for $LiPF_6$-based samples (Figure 3b). This means that a smaller amount of degradation products are formed in the surface of CB cathodes in $LiClO_4$-based cells compared to the $LiPF_6$-based cells. This is in agreement with the capacity results presented in Figure 2, which indicated that charge capacity of $LiClO_4$-based cells is smaller than that of $LiPF_6$-based cells.

The F1s spectra of all the samples look more or less similar since the peak in the spectra are substantially originated from binder of electrodes (Figure 5). The peak at 688 eV mainly represent bond between F and C in the Kynar binder. However, a closer look at the spectra reveals that a small shoulder is present at 685 eV in the spectra of stored and cycled samples when $LiPF_6$ was used as the electrolyte salt. This small contribution represents LiF formed due to partial decomposition of $LiPF_6$,[30] suggesting that decomposed $LiPF_6$ salt is found in the surface region of the CB.

As described in detail above decomposed electrolyte species are found in the surface region of the CB particle according to the SOXPES results. The structure of these decomposed electrolyte species is, however, not clear from the SOXPES results. It could for example be speculated that the species are present as layers partly covering the CB surfaces, or alternatively that the species are integrated into the CB top surface layer. To address this question, high-resolution TEM (HRTEM) was applied and HRTEM images of the pristine and charged CB electrodes are shown in Figure 6. From these images no surface layers on the CB particles can be observed in any of the samples. However, the internal structure of the pristine CB particles indicates the presence of graphitic structures approximately in the direction along the surface of the primary CB particles, while this structure is less pronounced for the charged sample (HRTEM image of the stored sample is presented in Figure S1 displaying slightly changes between pristine and stored CB particles). These results could indicate a loss in crystallinity after storing and charging. Also, for the charged sample the surface of particle became less sharp and in many areas the damaged graphitic was observed. EDS analysis showed that phosphorus and fluorine signals increase from stored to charged samples, suggesting that more PF_6^- originated compounds are present in the charged sample (see Figure 7). These results together with the

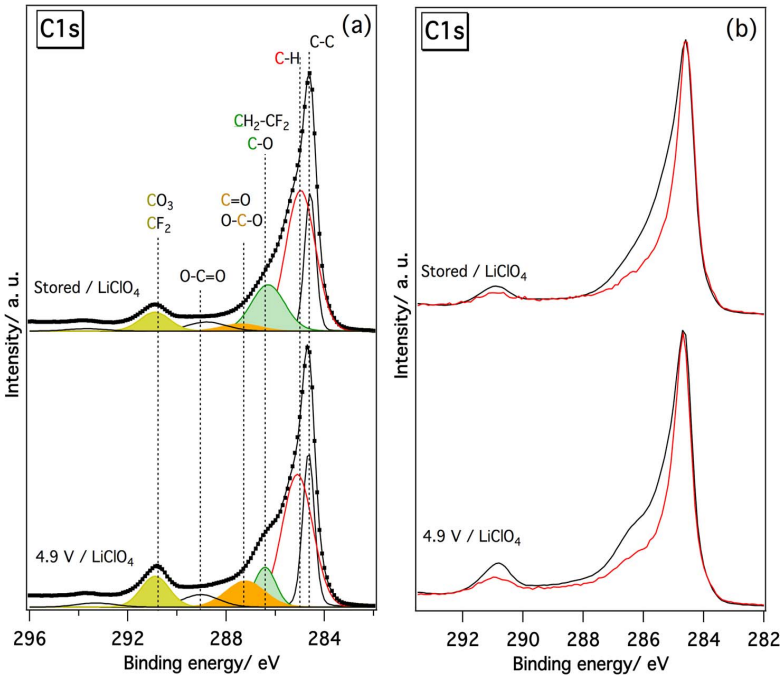

Figure 4. (a) Deconvoluted C1s spectra of stored and cycled CB cathodes using $LiClO_4$ in EC:DEC electrolyte. The spectra were measured by photon energy of 430 eV. (b) C1s spectra of the same samples measured using two photon energies of: 430 eV (black) and 835 eV (red).

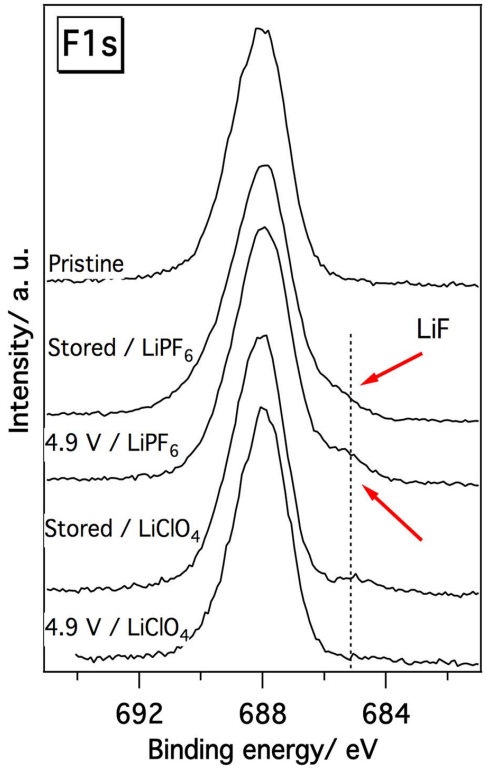

Figure 5. F1s spectra of pristine, stored, and cycled CB cathodes using $LiPF_6$ and $LiClO_4$ as the electrolyte salt.

SOXPES shows that the decomposed electrolyte species are present, not as layers partly covering the CB particles, but integrated into the surface of the CB. To evaluate the possible loss of crystallinity indicated from the HRTEM images, SAED data for all three electrodes are presented in Figure 8 along with normalized circular integration of the SAED patterns. Three main peaks can be distinguished in the pristine electrode corresponding to the (002), (100) and (110) reflections indicating that a partially graphitic structure exists in SP, which is in agreement with XRD results presented in Figure S2. The broad peaks are indicative of low-graphitized CB with short-range crystalline domains.[17] Figure 8 shows that storing and charging CB leads to broadening of the diffraction peaks which indicates a loss in crystallinity, consistent with the HRTEM images. The distance between the sheets in the graphitic domains, which is obtained by the position of the d_{002} reflection, is determined to 3.3 ± 0.1 Å for the pristine electrode. This value is slightly increased to 3.5 ± 0.1 Å for the charged electrodes. This increase is much smaller than the increase expected for complete intercalation of PF_6^- anions into the graphitic domain (i.e. 4.5 Å).[19] Finally, TEM images were recorded at lower magnification to evaluate the overall structure of the three samples. This analysis showed that the mean particle sizes slightly changed (see Figure 9). In the pristine electrode, the mean particle size is 33.2 ± 1.2 nm, in the stored electrode it is 35.3 ± 1.0 nm and after cycling (at the charged stat) the value has increased to 40.2 ± 1.6 nm. The loss of crystallinity and particle swelling of the stored and charged CB samples could possibly be explained partly by absorption of electrolyte solution followed by structural rearrangement of the internal CB structure. Also, the integration of decomposed electrolyte species to CB particles could influence CB particles.

The impedance result of a stored CB electrode is presented in Figures 10a and 10b. The Nyquist plot consists of a large semicircle in the high frequency range (between 10 kHz and 10 Hz) and an almost vertical tail in the low frequency range. The high frequency side of the semicircle intersects with the x-axis at 5 Ωcm^2 (R_E). This value originates mainly from the ionic resistance of the electrolyte between

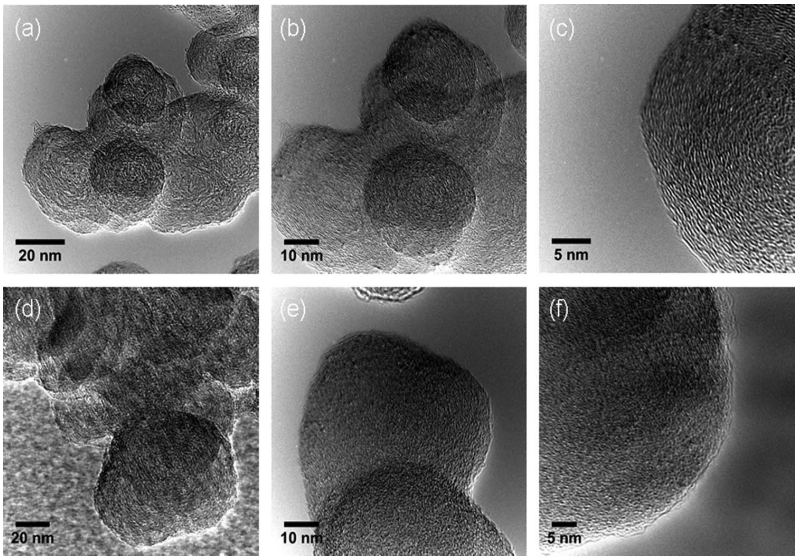

Figure 6. HRTEM images of CB samples: (a-c) pristine and (d-f) charged.

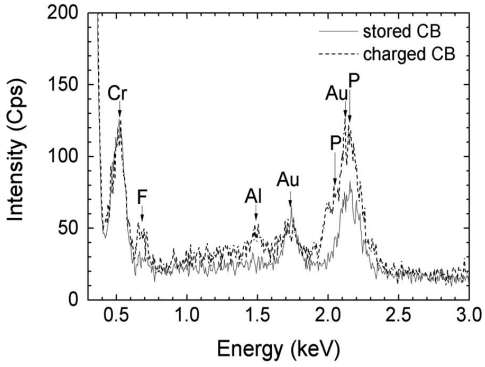

Figure 7. Normalized EDS spectra of stored (solid) and charged (dash) electrodes. A larger content of F and P was found in the charged electrode. Al originates from the preparation step when CB was scratched from the Al current collector. Cr and Au originate from the TEM grid.

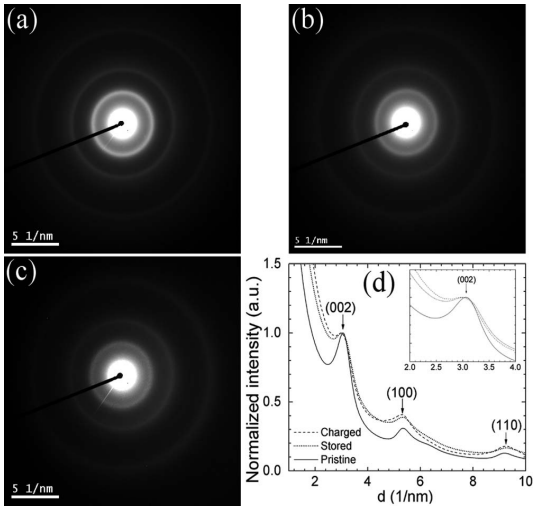

Figure 8. SAED patterns of (a) pristine, (b) stored, and (c) charged CB samples. Corresponding intensity profiles from the SAED patterns are shown in frame (d). The intensities are normalized to the intensity of the first diffraction ring (002). Inset of frame (d) shows a zoom-in of the first diffraction peak.

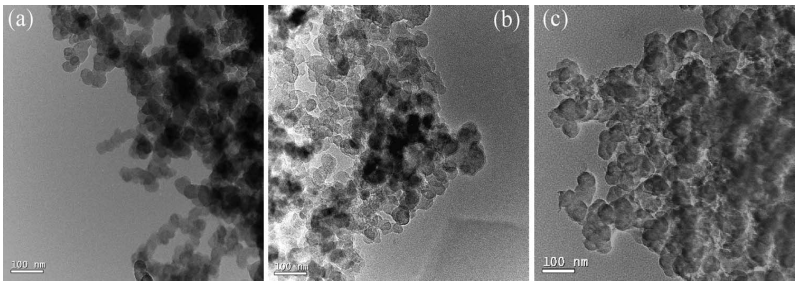

Figure 9. TEM images of (a) pristine, (b) stored, and (c) charged CB electrodes.

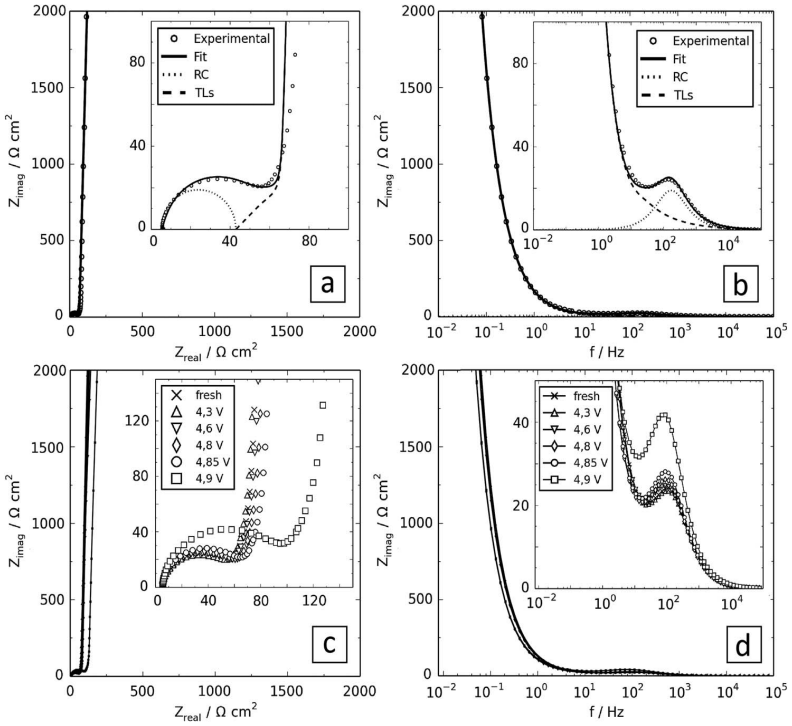

Figure 10. (a) Nyquist and (b) Bode plots of a stored CB electrode including fit using the equivalent circuit in equation 1. (c) Nyquist and (d) Bode plots of a CB cathode before, during and after stepwise charge to 4.9 V. The EIS measurements are performed at OCV after relaxation. All insets show a zoomed view of the high frequency region.

the cathode and the Li reference electrode. The semicircle ($R_{Al}C_{Al}$) can be assigned to the interface between the aluminum current collector and the porous carbon network.[37] The low-frequency part (TLs) of the Nyquist plot shows a long capacitive tail, which refers to the double layer capacitance of the ion-blocking CB surface in the porous electrodes.[25] Since the measurements are obtained at OCV no charge transfer reaction is expected. The Bode plot in Figure 10b shows the frequency domain of the impedance response. The impedance response from a CB electrode before, during, and after stepwise charge to 4.9 V is shown in Figure 10c. All measurements were performed at OCV after the cell had reached steady state. An increase in the semicircle and a small change in the angle of the tail are observed. Fitting of each plot was performed and the values for R_{Al}, C_{Al}, $R_{ion,L}$ and C_{dl} are extracted and shown as a function of the charge potential in Figure 11. The Al/CB interface resistance (R_{Al}) remains constant up to 4.3 V after which it increases slowly until 4.85 V and suddenly increases significantly at 4.9 V. The capacitance of the Al/CB interface (C_{Al}) is almost constant until 4.8 V after which it suddenly decreases. The increase in R_{Al} (Figure 11a) could be explained by the growing of resistive surface layers between aluminum and carbon particles. From 4.0 V and above an AlF_3 surface layer will form on aluminum which fits with the increase in the slope above 4.3 V.[26,27] A decrease in C_{Al}

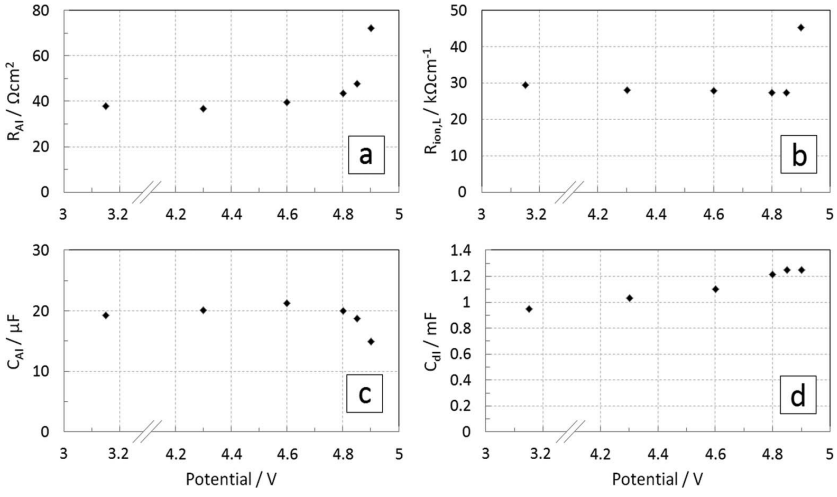

Figure 11. (a) Al/CB interface resistance R_{Al}, (b) Electrolyte resistance per unit pore length $R_{ion,L}$, (c) Al/CB interface capacitance C_{Al} and d) CB double layer capacitance C_{dl} as function of charging voltage.

(Figure 11c) after 4.8 V supports that an interphase layer is formed. A formation of an AlF_3 layer will lead to an increase of the thickness of double layer and to a reduction of dielectric constant ε (EC and DEC have ε equal to 89.6 and 3.12 respectively, while AlF_3 has a ε equal to 2.2[38]). According to equation 2 these factors will both lead to a reduction of C_{Al}. The ionic resistance of the electrolyte in the pores ($R_{ion,L}$) is almost constant until 4.85 V after which it suddenly increases at 4.9 V. This increase is possibly linked to a change in the pore structure induced by the particle growth. Finally, the carbon surface double layer capacitance (C_{dl}) increases steadily from 0.95 to 1.25 mF at 4.85 V after which it keeps a constant value (Figure 11d). Normalization of the initial carbon double layer capacitance to the total surface area of the electrode (260 cm^2), gives an $C_{dl,A}$ equal to 3.6 μF cm^{-2}. This value is close to the values found in literature i.e. 5 to 10 μFcm^{-2}.[39] The actual surface area is slightly smaller due to blocking with PVDF binder and isolated particles not connected to the conductive network, and this can explain the smaller value. According to equation 2, the capacitance is directly correlated to a change in the surface area. As indicated from TEM analysis the CB particles swell from 35 to 40 nm, increasing their surface area with 30%. This is in agreement with the observed increase of C_{dl} by assuming that the conductive network is intact. Alternatively, increased wetting of the electrode network could also explain such an increase in $C_{dl.}$ Therefore, since no decrease in double layer capacitance was observed, the EIS result cannot prove the formation of a surface layer on top of the CB particles.

Conclusions

Synchrotron-based SOXPES results revealed that spontaneous decomposition of electrolyte solution ($LiPF_6$ dissolved in EC:DEC) occurs in the surface region of carbon black particles stored in the electrolyte in the absence of external potential and current. Consequently, mainly hydrocarbons and ether species (C–O) originated from EC:DEC, and also, LiF originated from $LiPF_6$ decomposition are formed in the surface of the stored electrode. The decomposition species diminish when the electrode is cycled between 2.5–4.3 V, which suggests that they were oxidized/desorbed when electrochemical processes started. Increased anodic potential to 4.9 V leads to irreversible charges, and thus, to an increase in the impedance of the carbon cathode and to formation of a quite different composition of degraded electrolyte species compared to that formed in the stored electrode. The electrolyte/cathode interphase formed at high voltages consists of relatively higher contribution from O–C–O and/or C=O bonds as well as carbonates compounds (CO_3) originating from the solvent, in addition to hydrocarbons, ethers and LiF. Depth profile analysis of the interphase indicated that the concentration of the decomposed species is highest at the outermost CB surface (1–3 nm). TEM and EIS showed no distinctive surface layer indicating that the electrolyte degradation products are likely integrated into the surface region of the CB. The findings suggest that cathode/electrolyte interphases commonly observed on high voltage cathodes may originate from reactions between carbon black and electrolyte and not necessarily between active material and electrolyte.

Acknowledgments

The authors gratefully acknowledge financial support from the Danish Strategic Research Council through the project "Advanced Lifetime Predictions of Battery Energy Storage" (contract no. 0603-00589B). The EC FP7 project Hi-C (grant no. 608575) and Copenhagen Cleantech Cluster are also acknowledged for financial support. Kristian Bastholm Knudsen is acknowledged for help in the EIS analysis.

References

1. P. J. Hall and E. J. Bain, *Energy Policy*, **36**, 4352 (2008).
2. R. Younesi, *Front. Energy Res.*, **2**, 1 (2014).
3. D. Liu, W. Zhu, J. Trottier, C. Gagnon, F. Barray, A. Guerfi, A. Mauger, H. Groult, C. M. Julien, J. B. Goodenough, and K. Zaghib, *RSC Adv.*, **4**, 154 (2014).
4. A. Kraytsberg and Y. Ein-Eli, *Adv. Energy Mater.*, **2**, 922 (2012).
5. R. Younesi, S. Malmgren, K. Edström, and S. Tan, *J. Solid State Electrochem.*, **18**, 2157 (2014).
6. K. Xu, *Chem. Rev.*, **114**, 11503 (2014).
7. H. Duncan, N. Salem, and Y. Abu-Lebdeh, *J. Electrochem. Soc.*, **160**, A838 (2013).
8. A. Watanabe, K. Mori, H. Ishikawa, and Y. Nakamura, *J. Electrochem. Soc.*, **134**, 1318 (1987).
9. S. Mandal, J. M. Amarilla, J. Ibáñez, and J. M. Rojo, *J. Electrochem. Soc.*, **148**, A24 (2001).
10. L. Fransson, T. Eriksson, K. Edström, T. Gustafsson, and J. O. Thomas, *J. Power Sources*, **101**, 1 (2001).
11. J. Demeaux, M. Caillon-Caravanier, H. Galiano, D. Lemordant, and B. Claude-Montigny, *J. Electrochem. Soc.*, **159**, A1880 (2012).
12. F. La Mantia, R. A. Huggins, and Y. Cui, *J. Appl. Electrochem.*, **43**, 1 (2012).
13. J. Zheng, J. Xiao, W. Xu, X. Chen, M. Gu, X. Li, and J.-G. Zhang, *J. Power Sources*, **227**, 211 (2013).
14. J. Syzdek, M. Marcinek, and R. Kostecki, *J. Power Sources*, **245**, 739 (2014).
15. W. Märkle, N. Tran, D. Goers, M. E. Spahr, and P. Novák, *Carbon N. Y.*, **47**, 2727 (2009).
16. X. Qi, B. Blizanac, A. DuPasquier, A. Lal, P. Niehoff, T. Placke, M. Oljaca, J. Li, and M. Winter, *J. Electrochem. Soc.*, **162**, A339 (2015).
17. X. Qi, B. Blizanac, A. DuPasquier, P. Meister, T. Placke, M. Oljaca, J. Lie, and M. Winter, *Phys. Chem. Chem. Phys.*, **16**, 25306 (2014).
18. T. Placke, G. Schmuelling, R. Kloepsch, P. Meister, O. Fromm, P. Hilbig, H.-W. Meyer, and M. Winter, *Zeitschrift für Anorg. und Allg. Chemie*, **640**, 1996 (2014).
19. J. A. Seel and J. R. Dahn, *J. Electrochem. Soc.*, **147**, 892 (2000).
20. K. Edström, T. Gustafsson, and J. O. Thomas, *Electrochim. Acta*, **50**, 397 (2004).
21. H. Duncan, Y. Abu-Lebdeh, and I. J. Davidson, *J. Electrochem. Soc.*, **157**, A528 (2010).
22. K. J. Carroll, M.-C. Yang, G. M. Veith, N. J. Dudney, and Y. S. Meng, *Electrochem. Solid-State Lett.*, **15**, A72 (2012).
23. A. S. Andersson, B. Kalska, L. Häggström, and J. O. Thomas, *Solid State Ionics*, **130**, 41 (2000).
24. R. de Levie, *Electrochim. Acta*, **9**, 1231 (1964).
25. N. Ogihara, S. Kawauchi, C. Okuda, Y. Itou, Y. Takeuchi, and Y. Ukyo, *J. Electrochem. Soc.*, **159**, A1034 (2012).
26. A. H. Whitehead and M. Schreiber, *J. Electrochem. Soc.*, **152**, A2105 (2005).
27. Z. Yang, B. J. Ingram, and L. Trahey, *J. Electrochem. Soc.*, **161**, A1127 (2014).
28. R. Younesi, M. Hahlin, M. Treskow, J. Scheers, P. Johansson, and K. Edström, *J. Phys. Chem. C*, **116**, 18597 (2012).
29. R. A. Quinlan, Y.-C. Lu, Y. Shao-Horn, and A. N. Mansour, *J. Electrochem. Soc.*, **160**, A669 (2013).
30. R. Younesi, M. Hahlin, M. Roberts, and K. Edström, *J. Power Sources*, **225**, 40 (2013).
31. S. S. Zhang, K. Xu, and T. R. Jow, *J. Electrochem. Soc.*, **149**, A1521 (2002).
32. J. Lei, L. Li, R. Kostecki, R. Muller, and F. McLarnon, *J. Electrochem. Soc.*, **152**, A774 (2005).
33. D. Ostrovskii, F. Ronci, B. Scrosati, and P. Jacobsson, *J. Power Sources*, **94**, 183 (2001).
34. Z. Wang, X. Huang, and L. Chen, *J. Electrochem. Soc.*, **151**, A1641 (2004).
35. M. Onuki, S. Kinoshita, Y. Sakata, M. Yanagidate, Y. Otake, M. Ue, and M. Deguchi Onuki, *J. Electrochem. Soc.*, **155**, A794 (2008).
36. S. Malmgren, K. Ciosek, M. Hahlin, T. Gustafsson, M. Gorgoi, H. Rensmo, and K. Edström, *Electrochim. Acta*, **97**, 23 (2013).
37. M. Gaberscek, J. Moskon, B. Erjavec, R. Dominko, and J. Jamnik, *Electrochem. Solid-State Lett.*, **11**, A170 (2008).
38. M. Park, X. Zhang, M. Chung, G. B. Less, and A. M. Sastry, *J. Power Sources*, **195**, 7904 (2010).
39. O. Barbieri, M. Hahn, A. Herzog, and R. Kötz, *Carbon N. Y.*, **43**, 1303 (2005).

V

A transmission line model for a full $LiFePO_4$/C 26650 cylindrical cell derived by combined single-electrode Impedance and FIB/SEM-tomography analysis

Roberto Scipioni*, Peter S. Jørgensen, Johan Hjelm, and Søren H. Jensen**

DTU Energy, Department of Energy Conversion and Storage, Technical University of Denmark, Frederiksborgvej 399, 4000 Roskilde, Denmark

Keyword: Battery, Lithium, Ion, Electrochemical, Impedance, Spectroscopy, Degradation, Mechanisms, Focused, Ion, Beam, Scanning, Electron, Microscopy

Corresponding author: (*) roscip@dtu.dk (Roberto Scipioni), (**) shjj@dtu.dk (Søren Højgaard Jensen)

Abstract

In this work a combined Transmission Line Model (TLM_{comb}) has been proposed and implemented in an Equivalent Circuit Model (ECM) to describe the impedance spectra of a commercial 26650 $LiFePO_4$/C cylindrical cell. The derivation of the final ECM has been made possible by the application, and combination, of both generalized and simplified TLMs to model the impedance response of positive (LiFePO4) and negative (Graphite) electrodes, harvested from the commercial cylindrical cell. Microstructural parameters obtained from Focused Ion Beam (FIB)/Scanning Electron Microscopy (SEM) and 3-D reconstruction analysis of the electrodes were inserted and fixed in the TLMs. The single electrode impedance analysis gives important information about parameters, such as solid state diffusion in the solid intercalation particles, and electronic and ionic resistance of the porous composite electrodes. This analysis was crucial in order to make the final simplifications for the combined ECM here presented.

1. Introduction

The cylindrical cell continues to be one of the most widely used packaging styles for primary and secondary batteries. The advantages are ease of manufacture and good mechanical stability. The tubular cylinder can withstand high internal pressures without deforming [1]. Even though cylindrical cells does not fully utilize the space by creating air cavities on side-by-side placement, it has a higher energy density than prismatic/pouch Li-ion cells [1]. The higher energy density of the cylindrical cell compensates for its less ideal stacking abilities and the empty space can always be

used for cooling to improve thermal management. The smaller cousin to the 26650 cylindrical cell is the 18650 cylindrical cell which is used in e.g. Tesla cars.

Electrochemical Impedance Spectroscopy (EIS) is one of the most powerful tools for the study of electrochemical systems [2]–[4] and especially suited for extraction of kinetic and transport properties of the electrode materials and for studies of aging of the porous composite electrodes used in Lithium-ion batteries [5]–[9]. Many different equivalent circuit model (ECM) have been developed and proposed in literature to describe the impedance response of a single $LiFePO_4$ [8], [10], [11] or Graphite electrodes [12]–[16]. Most have them have been derived distinguishing the polarization process which occur at the single electrode using symmetrical cell configurations [10], [11], [17] or by use of a three-electrode configuration [15], [18], in order to resolve the impedance contribution from a single electrode in the cell.

The state of the art of EIS, used as tool to study aging mechanisms in porous electrodes, started to include in the last decades the use of Transmission Line Model (TLM) to study the response of porous electrodes, usually infiltrated by liquid electrolyte [12], [17], [19], [20]. The importance of these TLMs resides in the calculation of ionic resistance in the infiltrated pores $R_{ion,L}$ and the electronic resistance in the porous materials R_{el}. However the electronic resistance through the composite electrode is always considered negligible compared to the ionic one and most of these works use a simplified TLM. $LiFePO_4$ is however a poor ionic and electronic conductor [21], and is always carbon coated and mixed with carbon additives to improve its electronic conductivity [22]. Despite this, its electronic resistance is still not considered negligible and a generalized TLM has been successfully used by *Scipioni et al*. [18] to observe how R_{el} changes with degradation in a lab-scale battery electrode.

Furthermore the TLM incorporates an equivalent circuit element ζ which describes the surface reaction at the interface electrode/electrolyte [17]. For a complete description of all the reaction taking place at the porous electrode, an ECM which takes into account the solid state diffusion inside the particles would be needed, including a Warburg element.

In this work we set out to determine both kinetic and transport parameters of the intercalation electrode materials in electrodes harvested from a commercial 26650 $LiFePO_4$/C cylindrical cell, along with the ionic and electronic conductivity in the porous composite electrodes in the cell by using a classical transmission line model. A set of proposed equivalent circuits ζ were examined to model the interfacial reactions and solid state diffusion inside both a $LiFePO_4$ and Graphite particle. Two kinds of transmission line models have been used for the single electrode impedances, according to the properties of the two composite electrodes, and then combined in a final equivalent circuit model (ECM) which has been used to analyze the impedance response of the full cell. The simplified combined model incorporates elements describing the dominating losses in the cell and is shown to retain a high degree of physical relevance.

2. Methods and materials

2.1. Cell testing and disassembling

A fresh $LiFePO_4$/C 26650 cylindrical cell with a nominal capacity of 2.5 Ah, denoted "26650CC", was cycled five times at a constant C-rate of 0.1 (250 mA) and characterized by Electrochemical Impedance Spectroscopy (EIS) in a two-electrode setup using a Biologic VMP3 with Pstat/Gstat boards (test conditions shown in Table 1).

In order to test electrochemically the cathode and anode in a three-electrode configuration and resolve impedance contributions from each of the two electrodes, the 26650CC battery was disassembled in a glovebox in the discharged state and the cathode and anode were unrolled. The cylindrical cell consists of a 1.5 m $LiFePO_4$/carbonaceous additive (LFP/CB) positive electrode cast on either sides of an Aluminum foil, a 1.5 m Graphite (Gr) negative electrode cast on either sides of a Copper foil and 2 polymeric separators soaked with liquid electrolyte, schematically presented in Fig.1. The carbonaceous additive in the positive electrode is unknown, so we refer to it as Carbon Black (CB), in order to distinguish it from the Gr negative electrode. The total area of each of the battery electrodes and separators was 1950 cm^2. The two electrode foils were rinsed with diethyl carbonate and vacuum dried at 120°C in order to remove the liquid electrolyte. Subsequently four circular electrodes with a diameter of 18 mm (area = 2.55 cm^2) were punched out (two from LFP/CB foil and two from Gr foil) to be used for three-electrode testing and characterized by Focused Ion Beam (FIB)/ Scanning Electron Microscopy (SEM). Two out of the four circular electrodes (one LFP/CB and one Gr) were scratched with a spatula to remove the electrode layer on one side and then tested in two EL-CELL® ECC-Combi 3-electrode setups, using lithium metal foil counter electrodes, lithium metal as reference electrode and a glass fiber separator soaked with a standard 1M $LiPF_6$ in 1:1 v/v EC/DMC electrolyte (from Sigma-Aldrich). Both cells were cycled at a constant C-rate, calculated as 0.1 C, for few cycles to stabilize the electrode (see table 1 for test conditions). The two other electrode samples from the opened battery were prepared for microscopy analysis.

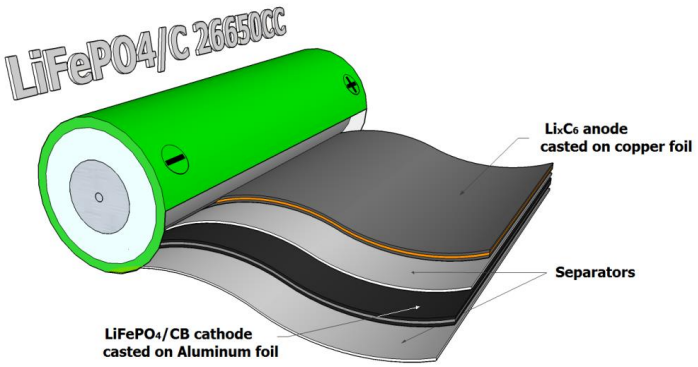

Figure 1. Schematic representation of the 26650CC $LiFePO_4$/C battery packaging design.

Table 1. Test conditions for the examined samples

Sample	Current (mA)	Approx. C-rate	Total cycle number	Comment
26650CC	250	0.1	5	Cylindrical Cell, 2-electrode setup
LFP/CB1	0.33	0.1	5	Cathode, 3-electrode setup
LFP/CB2	-	-	-	Cathode, used for FIB/SEM analysis
Gr1	0.33	0.1	5	Anode, 3-electrode setup
Gr2	-	-	-	Anode, used for FIB/SEM analysis

2.2. FIB/SEM tomography

The electrodes LFP/CB2 and Gr2 (Table 1) were prepared for the FIB tomography by rinsing with diethyl carbonate and vacuum infiltrated with a silicon resin (Wacker Chemie) for 30 minutes to improve phase contrast between CB particles and pores as described by Ender et al [23]. Subsequently the samples were infiltrated with epoxy resin to enable high-quality grinding and polishing of the sample.

FIB tomography and SEM imaging of the two electrode samples was carried out on a Zeiss 1540XB CrossBeam microscope, using a lateral E-T (Everhart-Thornley) detector and an In-lens detector. A 3D dataset was collected from each of the two electrodes. Table 2 shows the volume sizes of the two 3D datasets. A Gallium FIB slicing probe of 2nA was used to mill the LFP/CB electrode with a slice thickness of 27 nm. The slice thickness was calculated by measuring the progress of the milling front in each image during the stack alignment post processing step. For the GR electrode the current for the Gallium FIB slicing probe was reduced to 1nA and the thickness of each slice was estimated to be 14 nm. The Gr electrode is softer than the LFP/CB electrode. For this reason the current had to be reduced to enable high-quality imaging for the Gr electrode dataset.

The LFP particles in the positive electrode are much smaller than the Gr particles in the negative one. Thus, in order to perform an accurate image segmentation of LFP particles (to be used for 3D reconstruction and PSD analysis), it was necessary to collect high-resolution images with increased magnification. Specifically, the serial sectioning imaging was performed at 1 kV with a pixel size of 15x15 nm^2 for LFP/CB2 and 49x49 nm^2 for Gr2. The voxel size in the 3D-data sets was then 27x15x15 nm^3 for LFP/CB2 and 14x49x49 nm^3 for Gr2.

Table 2. Volumes of collected datasets.

Dataset	Volume (voxels) X x Y x Z	Volume (μm^3) X x Y x Z
LFP/CB2	80 x 850 x 400	2.2 x 12.5 x 5.9
Gr2	328 x 750 x 150	4.4 x 36.6 x 7.3

2.3. Image processing

Segmentation of the 3D FIB/SEM image data was performed with the program ImageJ (NIH). Because of uneven illumination, setting a single threshold for entire micrographs was not feasible. Therefore the Sauvola algorithm [24], [25] was used to perform local thresholds of the data. The Sauvola algorithm works by dividing the input image into square windows (n x n pixel) and setting thresholds for each of them based on the mean and standard deviation of the pixel intensities. Visualizations of the 3D reconstructions of the analyzed data were performed with the program Avizo (FEI).

The particle size distributions (PSD) of LFP/CB2 and Gr2 electrodes were analyzed based on the method introduced by Münch et al. [26]: The segmented 3D volumes are filled with spheres of a given radius. By reducing the radius incrementally, more volumes will be filled. The cumulative PSD is then obtained by correlating the incrementally filled volume with corresponding radii.

The geometrical tortuosity of the pore network, τ_g, is calculated by first calculating the length of the shortest path through the pore network between two opposite sides of the 3D data cuboid. This distance is then normalized by the distance between the two sides. Note that the geometrical tortuosity is a purely geometrical measure of how tortuous a pathway is. It does not take into account the constrictivity of the pore network (bottlenecks in the transport network).

2.4. Electrochemical Impedance Spectroscopy (EIS)

Electrochemical impedance spectroscopy (EIS) measurements were performed in two-electrode configuration for the 26650CC cylindrical cell and in three-electrode setup for the LFP/CB1 and Gr1 electrodes, using a Biologic VMP3 with Pstat/Gstat boards. Two-electrode EIS measurements of the cylindrical cell were obtained in a frequency range from 10 kHz to 1 mHz (10 points per decade) at different SOC (state-of-charge) from 0% to 100% SOC in the voltage range 2.8-3.6 V. Three-electrode measurements for both LFP/CB1 and Gr1 electrodes have been performed in a EL-CELL® ECC-Combi, using lithium metal as counter and reference electrodes. The cells were assembled inside the glove box using glass fiber separator (Whatman GF/A) and 200 µL electrolyte solution. The spectra were measured in the frequency range 100 kHz – 1 mHz (10 points per decade), when the electrodes were at 0% and 100% SOC. All measurements were performed at OCV after the cell had reached steady state defined by a change < 5 mV/h.

2.4.1. Cathode generalized Transmission Line Model (TLM_{cat})

The impedance results obtained from the LFP/CB1 electrode were modeled using the equivalent circuit model (ECM) shown in Fig. 2.

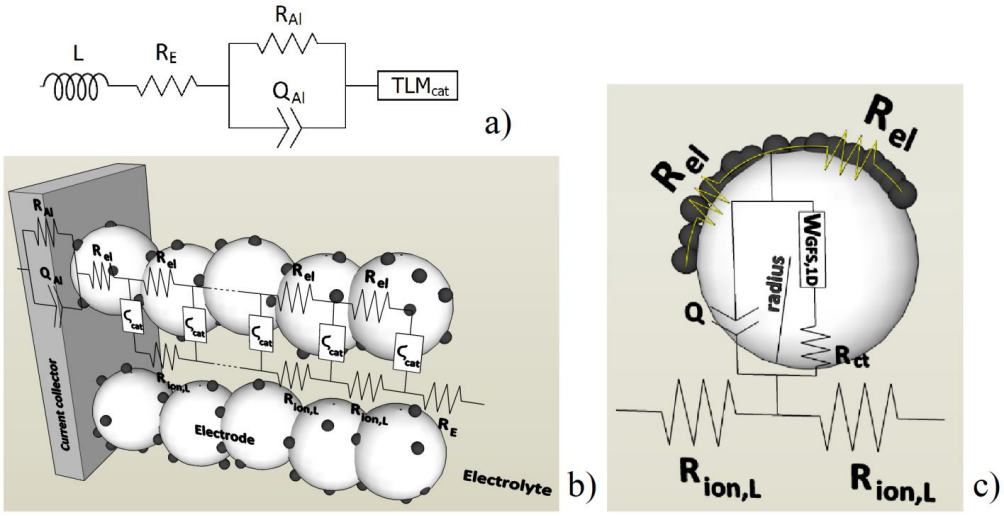

Figure 2. (a) Equivalent circuit used to model the impedance spectra, **(b)** Generalized Transmission Line model resembling the element TLM_{cat} in (a), **(c)** Randles circuit used to model electrode/electrolyte interface with Li^+ diffusion (Warburg General Finite Space element, $W_{GFS,1D}$) within a particle with radius r. The Randles circuit resembles the element ζ_{cat} in (b). The yellow resistors in (c) model the resistivity along the electron pathway on the surface of the LFP particles.

L_W is an inductor. The modelled inductance is primarily related to the leads of the test setup. R_E is a resistor modelling the ionic resistance of the electrolyte. Q_{Al} is a constant phase element and R_{Al} is a resistor. ($R_{Al}Q_{Al}$), where the brackets indicates a parallel connection between R_{Al} and Q_{Al}, which models the high-frequency part of the electrode impedance spectra associated with the aluminum/electrode interfacial polarization [11]. The low-frequency part of the electrode impedance spectra is modeled with a generalized transmission line model (TLM) for a porous electrode [17], [27], [28] (Fig. 2b). The model assumes cylindrical pores with length L filled with the electrolytic solution and oriented perpendicular to the current collector. $R_{ion,L}$ is the resistance associated with Lithium ions traveling in the pores. The pores are surrounded by carbon coated LFP particles mixed with carbon black particles. R_{el} is the resistance associated with electrons traveling in the surface coating. The equivalent circuit element ζ_{cat}, usually referred to as the surface impedance in the context of TLM_{cat}, which models the impedance of the electrode/electrolyte interface, however in this case we include the diffusion of lithium ions inside the LFP particles. ζ_{cat} consists of a charge transfer resistance R_{ct} in parallel with a constant phase element Q modeling the apparent double layer capacitance of the intercalation particles. Additionally R_{ct} is in series with a General Finite Space Warburg element $W_{GFS,1D}$ which models the impedance associated with lithium ion diffusion through the solid particle. The analysis carried out here neglects that the electrode materials are phase change materials, and consider them solid solutions. The electronic resistance is often assumed to be much lower than the ionic resistance of the solution ($R_{el}<<R_{ion,L}$) resulting in a simplified transmission line model where R_{el} is omitted [29], [30]. The generalized TLM_{cat} [17], [27], [28] was used in this study and reveal non-negligible R_{el} values. This is further detailed in the discussion section (Section 4).

The impedance of the generalized TLM_{cat} model is:

$$Z_{TLM} = \frac{R_{el}*R_{ion,L}}{R_{el}+R_{ion,L}}\left(L + \frac{2\lambda}{\sinh(L/\lambda)}\right) + \lambda_{TLM}\frac{R_{el}^2+R_{ion,L}^2}{R_{el}+R_{ion,L}}\coth(L/\lambda_{TLM}) \quad [1]$$

With:

$$\lambda_{TLM} = \sqrt{\varsigma_{cat}/\left(R_{el} + R_{ion,L}\right)} \quad [2]$$

As mentioned above the electrode/electrolyte interface (Fig. 2c) is modeled with the Randles circuit ς_{cat} which includes the charge transfer resistance R_{ct}, a constant phase element (CPE) Q and the general finite space Warburg element $W_{GFS,1D}$. The latter element models a diffusion process along a one-dimensional diffusion path terminated by an impermeable boundary [6], [8], [31], having the impedance:

$$Z_{WGFS,1D} = R_w\frac{\coth[(j\omega\tau_w)^{n_w}]}{(j\omega\tau_w)^{n_w}} \quad [3]$$

with the time constant:

$$\tau_w = \frac{r^2}{D} \quad [4]$$

R_w is polarization resistance, n_w is an exponent ($0<n_w<0.5$), r is the particle radius and D is the diffusion coefficient of Lithium ion within $LiFePO_4$.
The units of R_{ct} and C_{dl} in the TLM_{cat} are respectively Ωcm^3 and Fcm^{-3} and, in order to be converted in the more usual Ωcm^2 and Fcm^{-2}, need to be divided and multiplied respectively by the cylindrical pore length L (expressed in cm), which we set equal to the electrode thickness. The effective double layer capacitance C_{dl} is calculated according to [32] using the expression:

$$C_{dl} = Q^{1/n}\left(R_e^{-1} + R_t^{-1}\right)^{(n-1)/n} \quad [5]$$

where Q is the CPE, n the exponent of the CPE, R_e is the ohmic resistance and R_t the resistance associated with the CPE.

A 1D finite space Warburg element can be used for olivine-structure electrode materials $LiMPO_4$ (with M = Fe, Co, Mn), since they display a diffusion process along one-dimensional diffusion paths in the crystal lattice [33], [34].

2.4.2. Anode simplified Transmission Line Model (TLM_{an})

The impedance spectra measured on the Gr1 electrode were modeled using an ECM almost similar to the circuit used to model the LFP/CB1 electrode impedance. The $R_E(R_1Q_1)$ elements model the high frequency part of the impedance spectra. R_E models the ionic resistance of the electrolyte, while the R_1Q_1 element represents a combination of the copper current collector/electrode polarization and the particle/particle contact polarization. Similar to the model for the cathode, the mid- and low-frequency part of the anode spectra are modeled with a transmission line model for a porous electrode, however here the simplified version is used [17], [27], [28] (Fig. 3b), as the condition $R_{el} << R_{ion}$ holds for the graphite electrode [35]–[37]. The equivalent circuit to model the surface impedance of the TLM_{an} ζ_{an} is different from the one used for the positive electrode.

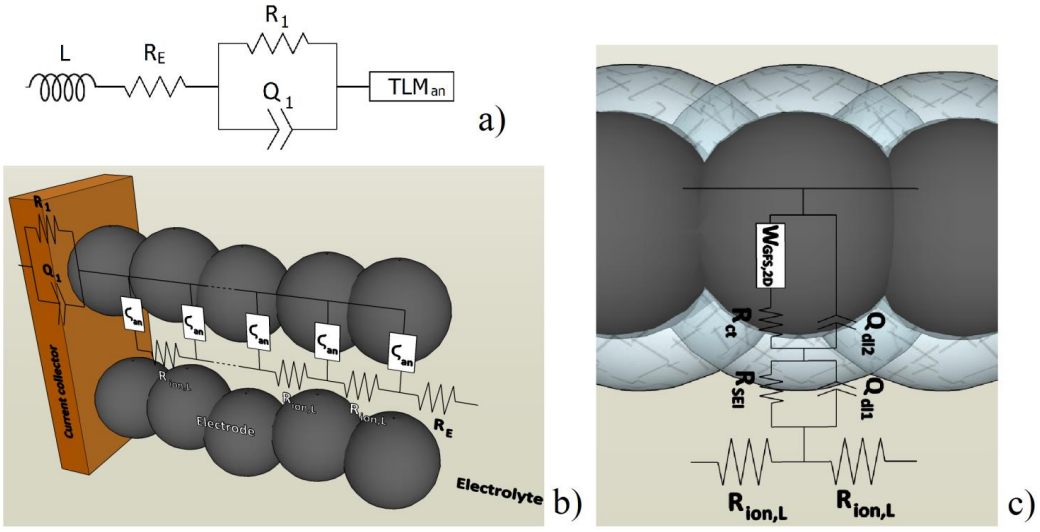

Figure 3. (a) Equivalent circuit used to model the impedance spectra, **(b)** Simplified Transmission Line Model resembling the element TLM_{an} in (a), **(c)** *RQ* element and Randles circuit used to model electrode/electrolyte interface with Li^+ diffusion (Warburg Finite Space element, $W_{GFS,2D}$) within a particle with radius *r*.

The ECM for the Gr1 electrode includes a simplified TLM_{an} since, on the contrary of LFP/CB1 electrode, R_{el} is found to be negligible. Equation 1 is then reduced to:

$$Z_{TLMs} = \lambda_{TLMs}\, R_{ion,L} \coth(L/\lambda_{TLMs}) \quad [6]$$

With:

$$\lambda_{TLMs} = \sqrt{\zeta_{an}/R_{ion,L}} \quad [7]$$

In the Gr1 electrode for the element ζ_{an} is constituted by a *RQ* element in series with a Randles circuit (Fig. 3c). The $R_{SEI}Q_{dl1}$ element models the impedance associated with the SEI layer which

covers each graphite particle. The Randles circuit includes the charge transfer resistance R_{ct}, a constant phase element Q_{dl2} (from which the effective double layer capacitance C_{dl2} is again calculated according to Eq. 5 [32]) and the general finite space Warburg element with a two-dimensional diffusion path, $W_{GFS,2D}$ [6], [8], [31] with the impedance:

$$Z_{WGFS,2D} = R_w \frac{I_0[(j\omega\tau_w)^{n_w}]}{(j\omega\tau_w)^{n_w} I_1[(j\omega\tau_w)^{n_w}]} \quad [8]$$

where I_0 and I_1 are modified zero and first-order Bessel functions of the first kind.

Here a 2D Warburg finite space element with cylindrical geometry is used. This geometry describes a diffusion along the radial axis, as usually occurs in the layered-structure electrodes (e.g. graphite) [38].

2.4.3. Considerations about ζ_{an}

Meyers et al. [6] studied the impedance response of a porous electrode, covered by a film (SEI layer in our case n.b.), and proposed different equivalent circuit models (Fig. 4b). They have been thoroughly analyzes and compared with our proposed model (Fig. 4a) to be implemented in the ζ_{an} of the TLM_{an} of the graphite electrode.

- Case 1: it is described as the most general case, since include internal (particle/film) and external (film/electrolyte) interfacial impedances, together with a resistive film. Results from our ECM and Meyers' one are comparable for internal impedance and film resistance. However a $R_{ct2}C_{dl2}$ circuit was found to be physically meaningful, because of the negligible value of charge transfer resistance R_{ct2} at the film/electrolyte interface and for value of *n* (exponent of the CPE which describes the internal double layer capacitance C_{dl2}) lower than 0.3.
- Case 2: it neglects the external interfacial impedance and the internal double layer. It seemed to be to most suitable ECM to model the graphite electrode impedance and modelling results are identical to our model.
- Case 3: it is the simplest case, but was not considered because it neglects the SEI layer entirely.

According to this, our model seems to be comparable with Case 2 proposed by *Meyers et al.* [6] although the double layer capacitance of the SEI layer Q_{dl1} (C_{film} in Meyers' model n.b.), is not positioned in parallel with R_{SEI} and the Randles, but only with R_{SEI}.

The choice of using our ECM is motivated by the need of moving the $R_{SEI}Q_{dl1}$ circuit out of the TLM_{an} in the simplified circuit that we are going to propose in section 4.3.1 for the full 26650CC cell.

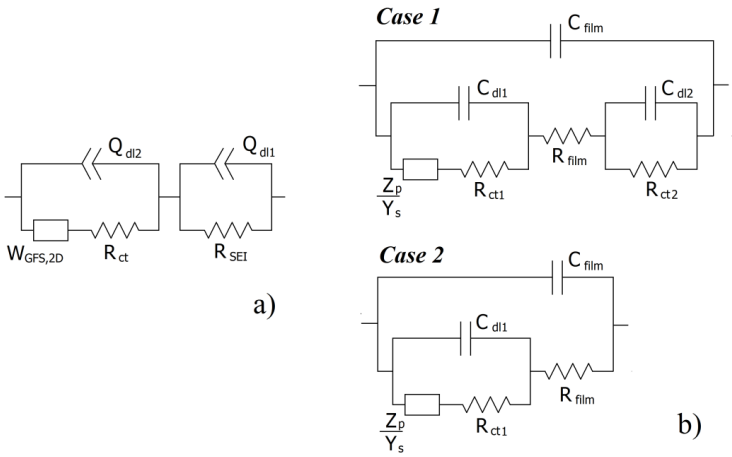

Figure 4. (a) Equivalent circuit ζ_{an} used to model the surface (and internal) impedance response of a single graphite particle, **(b)** different equivalent circuits used by *Meyers et al.* [6] to model the impedance of a porous electrode covered by a film (SEI layer in our case n.b.).

2.4.4. Tortuosity estimation from TLMs

The ionic resistance in the infiltrated pore with length L, $R_{ion,L}$ [Ωcm] calculated from the TLMs is correlated to the effective electrode pore tortuosity τ_{el} through the equation:

$$\tau_{el} = \sigma_{ion} R_{ion,L} \varepsilon_{el} \quad [9]$$

where σ_{ion} is the ionic conductivity [Scm^{-1}] of 1 M $LiPF_6$ in 1:1 EC/DMC and ε_{el} is the electrode porosity [12]. Values used for σ_{ion} is $1.18 \cdot 10^{-2}$ Scm^{-1}, as an average value reported by *Lombardo et al.* [36], and *Porion et al.* [37]. The tortuosity of the glass fiber separator τ_s has been also calculated using a similar equation, using instead the ohmic resistance R_E [Ωcm^2] found in the ECM, divided by the separator length l [cm], and the separator porosity ε_s furnished by the commercial supplier.

$$\tau_s = \sigma_{ion} \frac{R_E}{l} \varepsilon_s \quad [10]$$

The thickness of the separator is reported to be 0.155 cm, but the value used for l is just a half of it since the ohmic resistance R_E comes from a three-electrode measurement, where the reference electrode is placed exactly in the middle between working and counter electrode. The porosity of the separator used in the three electrode cell, ε_s, is 0.92.

3. Results

3.1. FIB/SEM Tomography

Figure 5 and 6 show respectively cross-section lateral E-T images after FIB milling of the LFP/CB2 and the Gr2 electrode. In the top region of the images it is possible to observe a very bright region, which is the sample surface after polishing. Looking inside the milled samples current collector/electrode and electrode/electrolyte interfaces can be distinguished for both samples. Guidelines are shown in Fig. 5a to indicate how the interfaces extend into the sample. From Fig. 5a and Fig. 6 the cathode and anode thickness is estimated to 65 µm and 35 µm, respectively. Fig. 5b show a HR image recorded at the electrode/electrolyte interface. In the front face three different phases are distinguished: light gray $LiFePO_4$ particles, dark gray pores (infiltrated with silicon resin) and black CB particles. On the right side of the SEM image (Fig. 5a), where the electrolyte is supposed to be, there is a dark gray bulk of silicon resin with some LFP and CB particles, which probably detached during sample preparation.

In the Gr2 electrode (Fig. 6), only two phases can be distinguished: dark graphite particles and gray pores infiltrated with silicon resin. On the left side the copper/electrode interface is present, while on the right side the electrode/electrolyte interface is found. The darker gray bulk on the right is the epoxy resin, used for sample preparation, which has a different contrast than silicon resin. The region highlighted has been segmented for 3D reconstruction and PSD analysis.

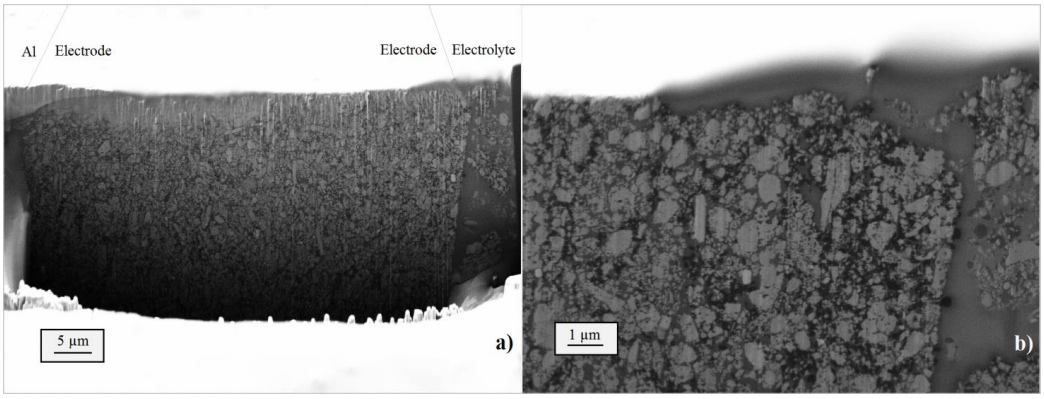

Figure 5. a) FIB/SEM cross-section image of the LFP/CB2 electrode, collected with lateral E-T detector. On the top, guidelines are shown to distinguish Al/Electrode and Electrode/Electrolyte interfaces, b) High resolution FIB/SEM cross-section image of Electrode/Electrolyte interface, used for 3D reconstruction and PSD.

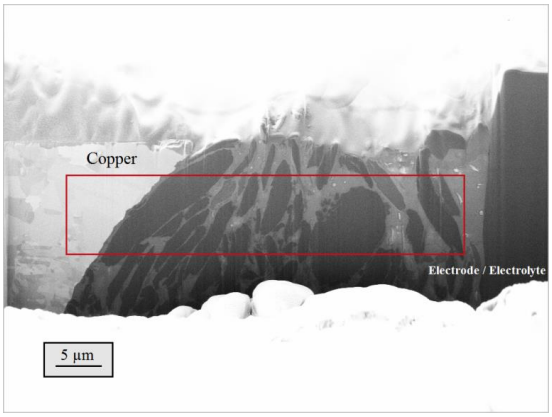

Figure 6. FIB/SEM cross-section image of the Gr2 electrode, obtained with a lateral E-T detector. On the left there is the copper current collector, on the right the Electrode/Electrolyte interface.

Figure 7 shows the 3D reconstruction of the LFP/CB2 electrode/electrolyte interface and of the Gr2 electrode. In the cathode 3D reconstruction (Fig. 7a) the grey phase is the $LiFePO_4$, the black phase is the CB additive network, while the electrolyte infiltrated pores are transparent blue. All phases (Fig. 8 a,b,c) seem quite homogeneously distributed. In the anode 3D reconstruction (Fig. 7b) the orange region represents the copper current collector, the black particles are graphite agglomerates and the transparent blue region is the pores network infiltrated with the electrolyte. The two phases in the Gr2 electrode are shown in Fig. 8(d,e).

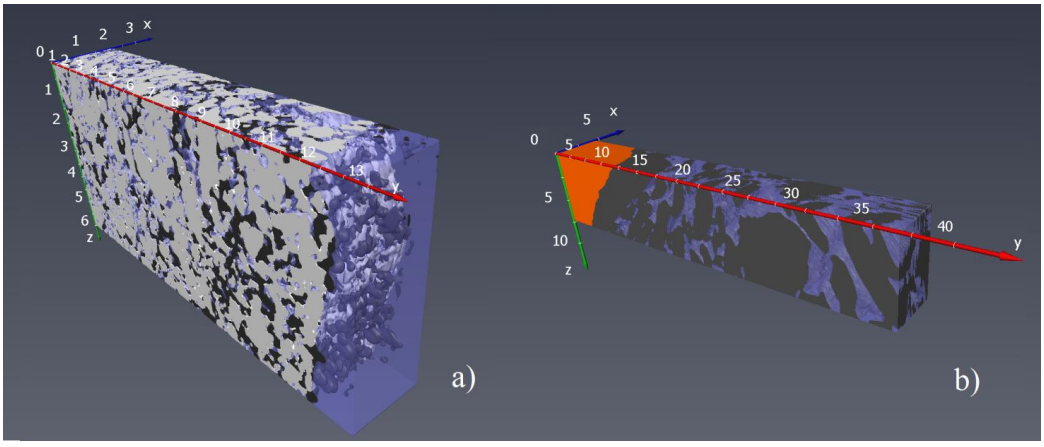

Figure 7. 3D reconstruction of a) LFP/CB2 electrode/electrolyte interface and b) Gr2 electrode. The scale bar units are [µm].

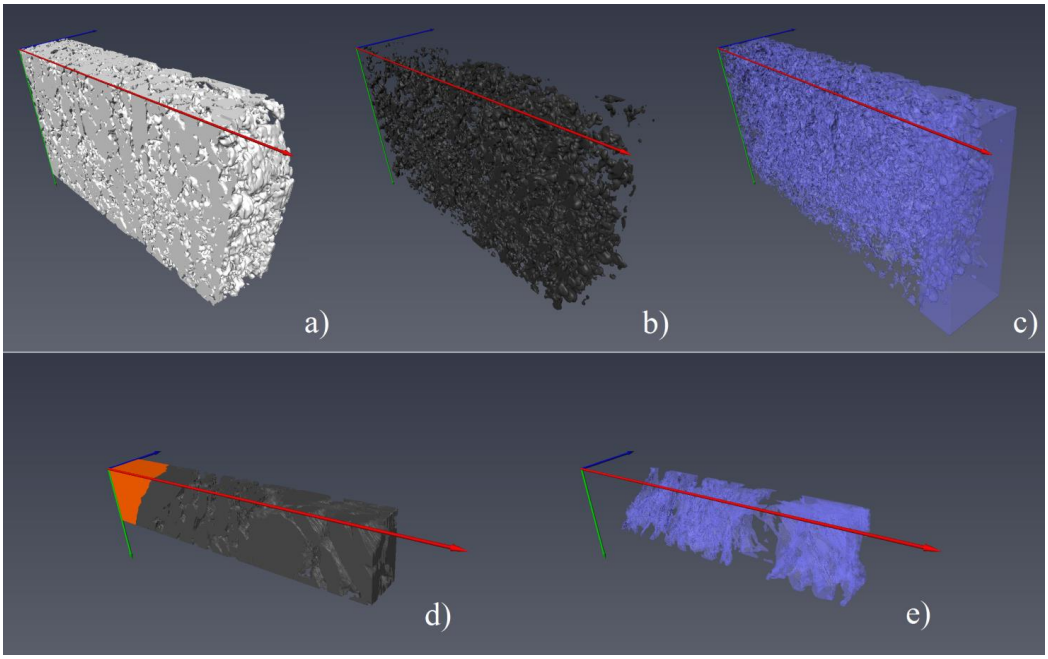

Figure 8. 3D reconstruction of a) LFP, b) CB and c) pores networks in LFP/CB2 electrode. 3D reconstruction of d) Graphite and e) pores networks in Gr2 electrode.

Fig. 9(a,b) show respectively the PSD distribution for the three phases in LFP/CB2 electrode and for the two phases in Gr2 electrode. The average particle size for the active materials, $Li_{1-x}FePO_4$ and Li_xC_6, is respectively 76 nm and 1096 nm. These values are subsequently implemented in the TLMs. Volume fraction values for all the phases are instead shown in Table 3.

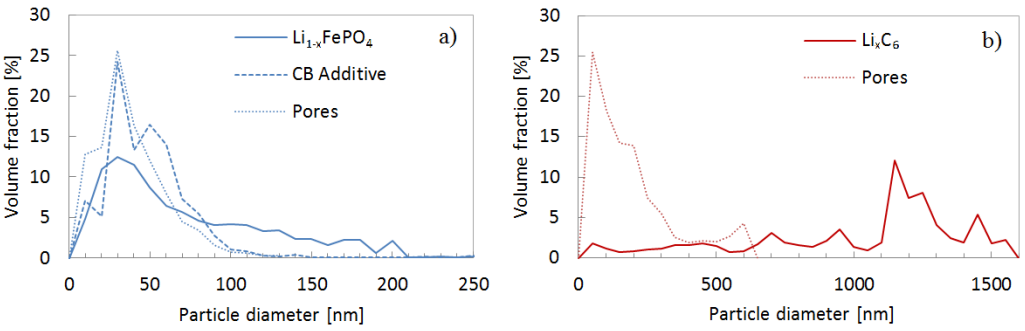

Figure 9. Particle size distribution for a) LFP/CB2 and b) Gr2 electrodes.

Table 3. Volume fraction and average particle size for the different phases

Phase	LFP/CB2		Gr2	
	Volume Fraction [%]	Avg. particle size [nm]	Volume Fraction [%]	Avg. particle size [nm]
Active Material	58	76	70	1096
CB Additive	17	49	-	-
Pores	25	39	30	159

In Fig. 10 are reported the propagation maps and the results for geometrical tortuosity found for the positive and the negative electrode. The cathode mean geometrical tortuosity is found to be 1.148, while the anode one is equal to 1.135.

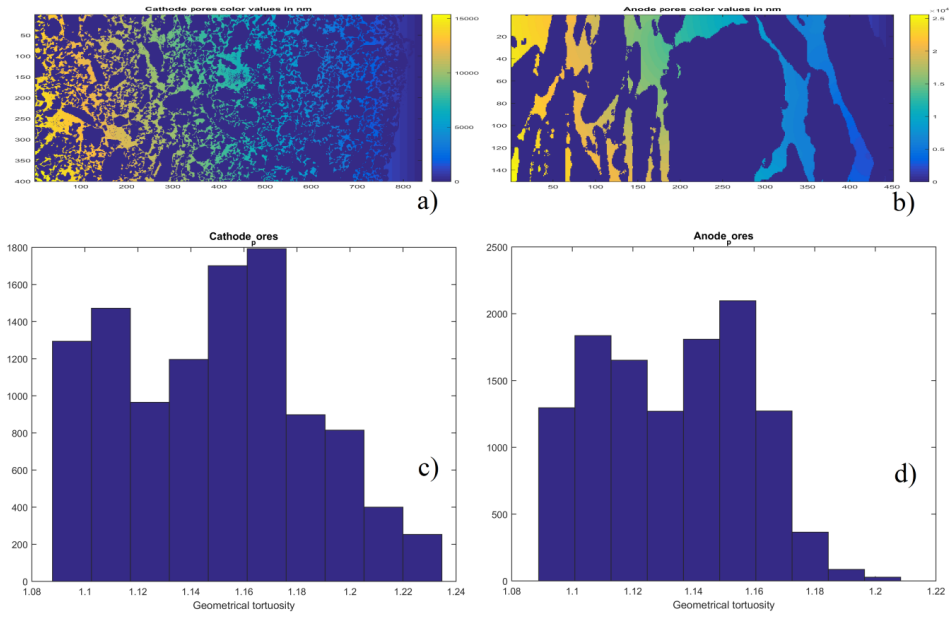

Figure 10. Propagation maps of a) LFP/CB2 and b) Gr2 electrodes. Geometrical tortuosity of c) LFP/CB2 and d) Gr2 electrodes.

3.2. Galvanostatic Cycling with Potentiostatic Limitation (GCPL)

The 26650CC was cycled between 2.8 – 3.6 V as suggested from the commercial supplier, at a nominal C-rate of 0.1 C. The charge/discharge curve for 26650CC is shown in Fig.11a (black line).

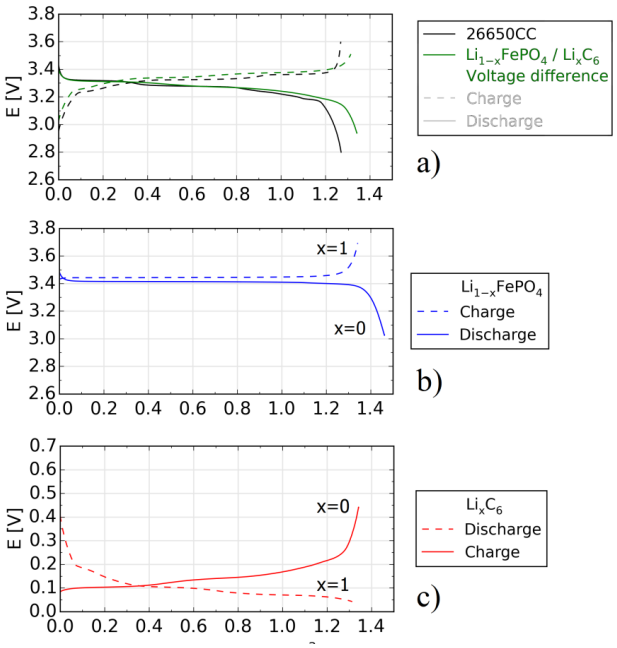

Figure 11. Charge/Discharge curves of a) 26650CC, b) LFP/CB1 and c) Gr1

In order to separate the electrode contributions single electrodes LFP/CB1 and Gr1 were prepared. Fig. 11b and 11c show respectively the charge/discharge curves for the LFP/CB1 and Gr1 electrodes. The LFP/CB1 electrode is cycled between 3.0 – 3.7 V with a constant current of 330 µA, corresponding to a C-rate of 0.1, considering that its surface area is 2.55 cm^2 and that the unrolled battery electrode was 1950 cm^2. The charge/discharge curve shows a typical flat plateau of a $Li_{1-x}FePO_4$ electrode (LFP/CB1, n.b.) at around 3.45 V (with $0 \leq x \leq 1$). Note that the discharge capacity of LFP/CB1 is 10% higher in the first cycle, when run vs lithium metal. This match with the amount of lithium lost for the building of SEI layer on Gr1 surface, inside 26650CC. The Gr1 electrode was cycled between 0.01 V and 0.45 V, also at 330 µA. Fig. 11c shows the charge/discharge curve of a Li_xC_6 electrode (Gr1, n.b.) with different intercalation steps of Li^+ ion (with $0 \leq x \leq 1$). Note that the charge/discharge curve of 26650CC resembles the voltage difference between the LFP/CB1 and Gr1 charge/discharge curves, as shown by the green curve in Fig. 11a.

3.3. EIS modelling of $Li_{1-x}FePO_4$ electrode (three-electrode configuration)

The three-electrode impedance spectra were measured in the frequency range 100 kHz – 1 mHz, however values over 1 kHz were found to be noisy for the LFP/CB1 electrode and were not included for the modeling. Fig. 12 shows the normalized[1] EIS spectra measured for the LFP/CB1

[1] Normalized to the geometrical surface area 2.55 cm^2

electrode in the charged (a, b) and discharged state (c, d). Fig. 12 (a, b) represent respectively a Nyquist and a Bode plot of the EIS spectrum measured at OCV after charging to 3.7 V and relaxation. Fig. 12 (c, d) show a Nyquist and Bode plot of the EIS spectrum measured at OCV after discharging the LFP electrode to 3.0 V followed by relaxation. Fig. 13 shows a zoomed view of the high frequency regions of the spectra. The measured data is modeled (black lines) and the model result is divided in an ($R_{Al}Q_{Al}$) part (red line) and a TLM_{cat} part (blue line). The most meaningful modelling results are presented in Table 4 and discussed in Section 4. All the parameters are instead reported in table S1 in the supplementary information.

Table 4. Results from EIS fitting of $Li_{1-x}FePO_4$ electrode.

	$R_{Al}Q_{Al}$ element		Generalized Transmission Line				
			Randles element			Pore	Electrode
	R_{Al} (Ωcm^2)	C_{Al} ($mFcm^{-2}$)	R_{ct} (Ωcm^2)	C_{dl} (Fcm^{-2})	D (cm^2s^{-1})	$R_{ion,L}$ (Ωcm)	R_{el} (Ωcm)
$FePO_4$	2.2	0.20	13.8	0.52	$8 \cdot 10^{-13}$	402	53
$LiFePO_4$	2.2	0.17	60	0.67	$4 \cdot 10^{-13}$	1538	113

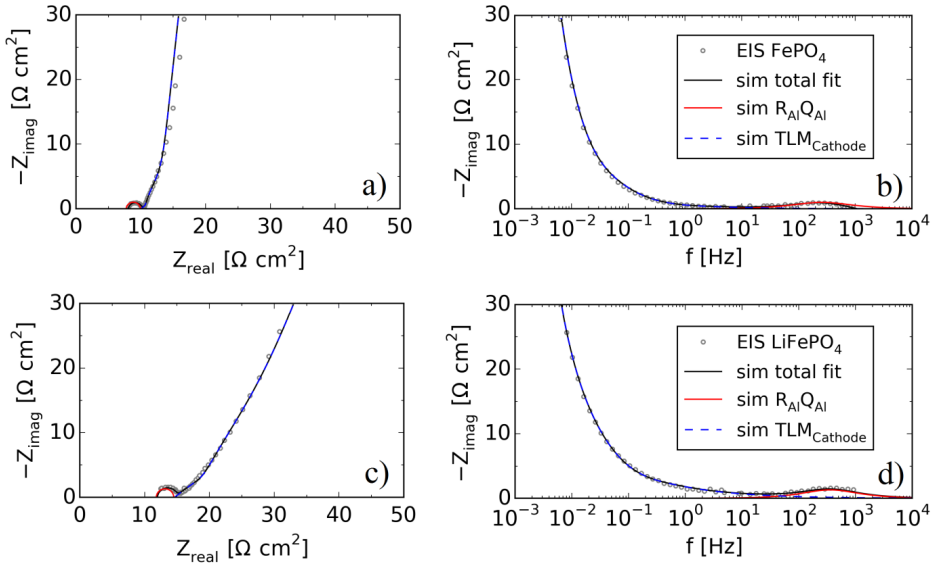

Figure 12. a) Nyquist and b) Bode plot of the $Li_{1-x}FePO_4$ electrode when the battery is at 100% SOC (x=1), c) Nyquist and d) Bode plot of the $Li_{1-x}FePO_4$ electrode when the battery is at 0% SOC (x=0). The black model curve is the sum of the red and blue model curves.

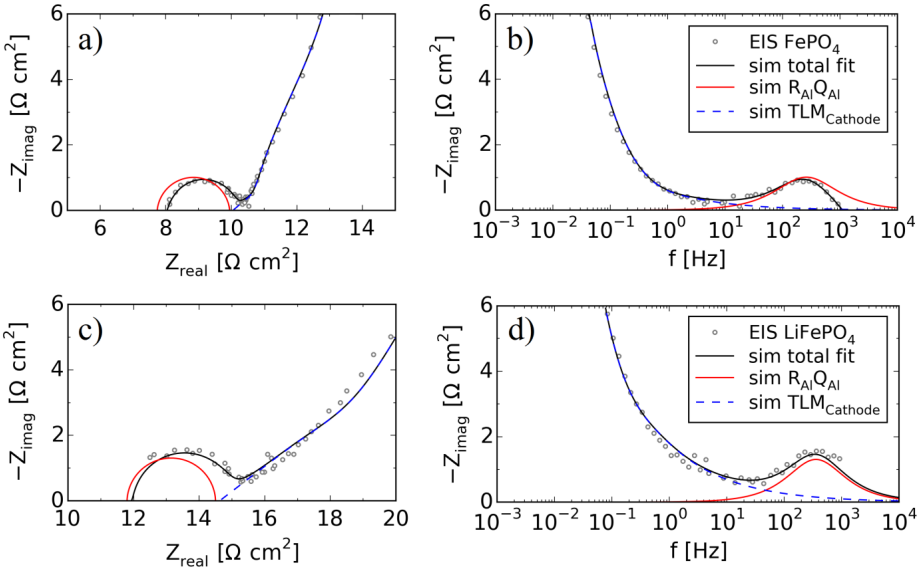

Figure 13. Zoom of the spectra presented in Fig. 10.

3.4. EIS modelling of Li_xC_6 electrode (three-electrode configuration)

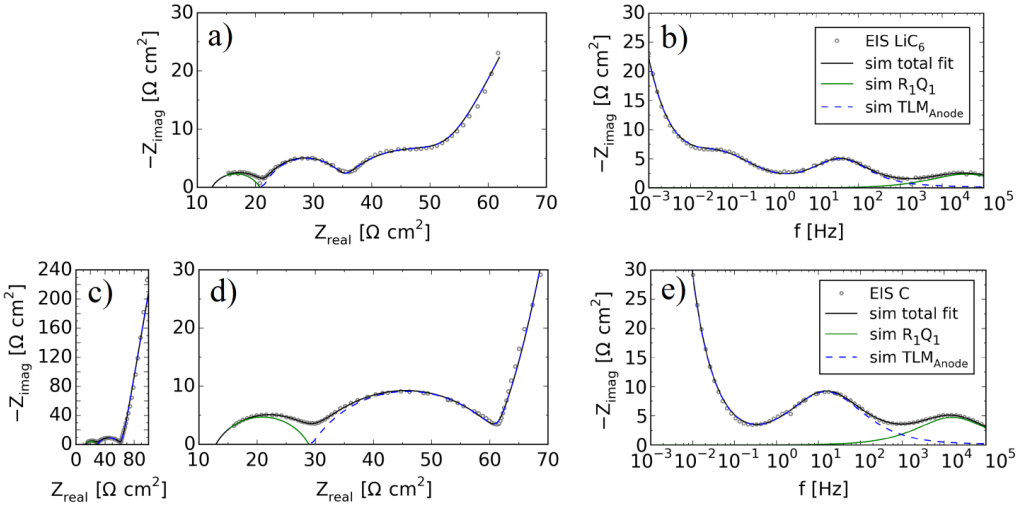

Figure 14. a) Nyquist and b) Bode plot of the Li_xC_6 electrode when the battery is at 100% SOC (x=1), c) Nyquist plot, d) zoomed view of high frequency region and e) Bode plot (zoomed view) of the Li_xC_6 electrode when the battery is at 0% SOC (x=0).

Fig. 14 show the normalized EIS spectra measured for Gr1 in the lithiated (a, b) and delithiated form (c, d, e). Fig. 14 (a, b) show Nyquist and Bode plot of the Gr1 spectrum measured at OCV after discharging the electrode to 0.01 V followed by relaxation. Fig. 14 (c, d, e) show Nyquist and Bode plots of the Gr1 spectrum measured after charging the electrode to 0.5 V and after relaxation.

The measured data is modeled (black lines) and the model result is divided in an (R_1Q_1) part (green line) and a TLM_{an} part (blue line). The most meaningful modelling results are presented in Table 5 and discussed in Section 4. All parameters are again reported in table S2 in the supplementary information.

Table 5. Results from EIS fitting of Li_xC_6 electrode.

	R_1Q_1 element		**Simplified Transmission Line**					
			$R_{SEI}Q_{dl1}$ element		**Randles element**			**Pore**
	R_1 (Ωcm^2)	***C_1 (μFcm^{-2})***	***R_{SEI} (Ωcm^2)***	***C_{dl1} ($mFcm^{-2}$)***	***R_{ct} (Ωcm^2)***	***C_{dl} (Fcm^{-2})***	***D (cm^2s^{-1})***	***$R_{ion,L}$ (Ωcm)***
LiC_6	8.3	0.40	14.3	0.28	14.3	0.10	$2 \cdot 10^{-11}$	745
C	16.0	0.43	31.4	0.35	40	0.57	$3 \cdot 10^{-10}$	500

3.5. EIS modelling of 26650CC (two-electrode configuration)

Impedance spectra obtained on the 26650CC were recorded at different SOC either in charging or discharging mode. Fig. 15 shows the normalized EIS spectra measured for 26650CC at different SOC (dots), with the simulated fit (solid lines) for each spectrum. A full description of the equivalent circuit used to model the spectra and results from the fitting are provided in paragraph 4.3.1 and 4.3.2 respectively.

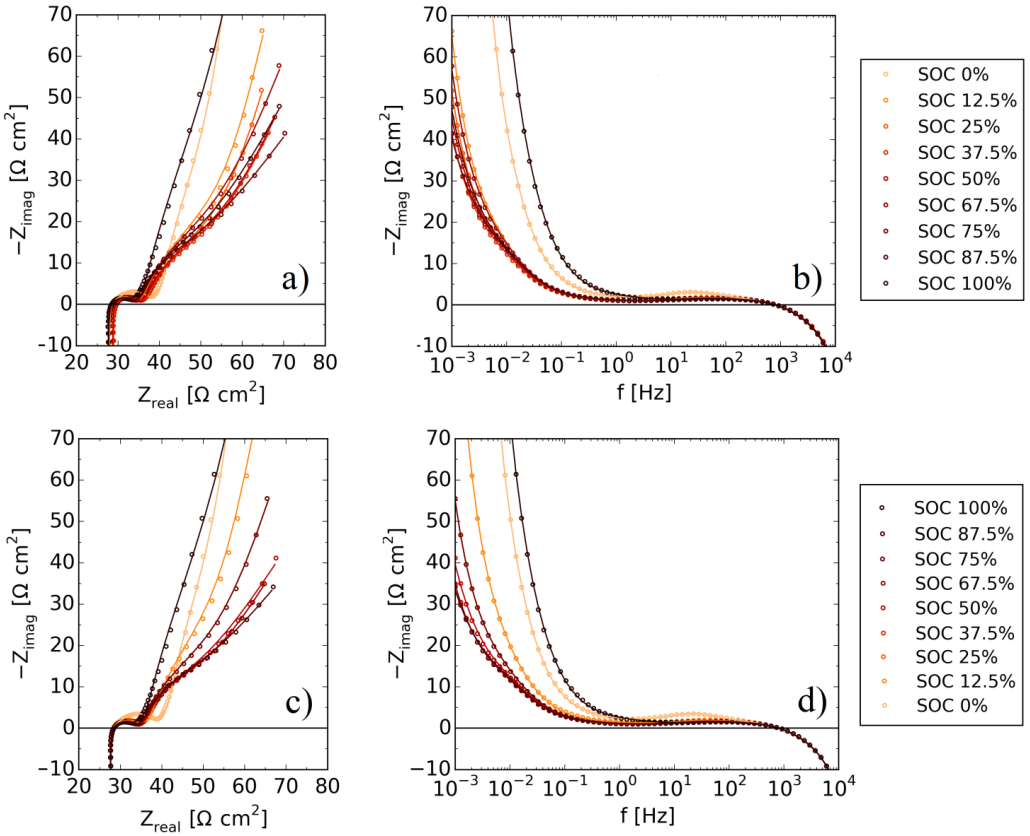

Figure 15. a) Nyquist and b) Bode plot of 26650CC at different SOC, measured in charging mode, with fitting c) Nyquist and d) Bode plot of 26650CC at different SOC, measured in discharging mode, with fitting. All spectra were measured at OCV after the cell had reached steady state defined by a change < 5 mV/h.

4. Discussion

4.1. Cathode Impedance Modelling: Three-electrode configuration

The Nyquist plot of $FePO_4$ and $LiFePO_4$, Fig. 12(a, c), consist of a small semicircle in the high frequency region between 1 kHz – 100 Hz and a low frequency branch characterized by an almost vertical tail in the charged state, and a less vertical tail in the discharged state.

The high frequency side of the semicircle intersects with the x-axis at 8.0 Ωcm^2 and 12.0 Ωcm^2 for $FePO_4$ and $LiFePO_4$ respectively. However, because of the inductance and of the electronic resistance R_{el} (in series with R_E, as shown in the ECM in Fig. 2), the real value of electrolyte

resistance (R_E) is 7.3 Ωcm^2 and 11.3 Ωcm^2, see Table 4. The value of R_E is not expected to change with SOC and the change is possibly related to measurement uncertainties; impedance measurements above 1 kHz were very noisy and therefore removed before the impedance was modeled. This was assumed due to some effect of the scratching out of active materials from the Al current collector.

R_{Al} models the charge transfer (contact) resistance between the Aluminum foil and $Li_{1-x}FePO_4$/CB network, and in the additive CB network, since $LiFePO_4$ is a poor electron conductor. From Table 4 it is seen that the R_{Al} values change very little for the two different SOCs, in agreement with literature [11].

The values used in the TLM_{cat} for the electrode thickness L and the particle radius r are 65 μm and 38 nm, respectively. These values were obtained from the presented FIB/SEM analysis and PSD calculation. When R_{el} is significant relative to $R_{ion,L}$ the generalized TLM_{cat} features a small Ohmic contribution which shift the starting point of the red semi-circle to the left in the Nyquist plot, Fig. 13(a, c). If this Ohmic contribution was placed on the left side of the red semi-circle it would be easier to see how the semi-circle contribute to the total spectrum, however the semi-circle is deliberately plotted with the TLM_{cat} shifted to the right side to highlight the small Ohmic contribution from the TLM_{cat} as this contribution also affects the value of R_E.

Diffusion of Li^+ ions through the liquid electrolyte in the electrode pores result in a 45° slope in the beginning of the TLM_{cat} curve. The length of the part of the TLM_{cat} curve resembling a line with a 45° slope is determined by $R_{ion,L}$ and the thickness of the electrode. Once a Li^+ ion has traveled through a pore and reached a coated LFP particle it reacts with an electron from the CB network and diffuses into the bulk of the LFP particle. This is modelled by ς_{cat} and results in a semicircle followed by a 45° curve terminating in a capacitive-like response, Fig. 13(a, c). The semicircle is the result of charge transfer resistance, $R_{ct,}$ of Li^+ at the particle/electrolyte interface and double layer capacitance C_{dl}, in parallel, calculated from the CPE used to model it. The 45° line followed by a capacitive-like curve corresponds to the finite space Warburg element $W_{GFS,1D}$ which represents diffusion of Li^+ ions in the electrode network, until all the active material is consumed.

The fitted values from the TLM_{cat} show that R_{el} is not negligible compared to $R_{ion,L}$. Both resistances in the pore and the electrode are observed to decrease when the electrode is charged and mainly consists of $FePO_4$. $Li_{1-x}FePO_4$ particles are known to be subjected to expansion/contraction with cycling, and when the electrode is completely delithiated $FePO_4$ particles have a smaller volume and the pores increase in size, furnishing a smaller $R_{ion,L}$. R_{el} depends on the CB network tortuosity which changes due to particle movements during lithiation/delithiation process. R_{ct} is observed to be significantly lower at 100% SOC.

4.2. Anode Impedance Modelling: Three-electrode configuration

The Nyquist plot of the impedance spectra for Gr1 Fig. 14(a, c, d), consist of a small semicircle in the high frequency region, between 100 kHz – 10 kHz, a second bigger semicircle in the mid-frequency range (100 Hz – 10 Hz) and – similar to the LFP/CB1 electrode – a low frequency branch (at frequencies lower than 1 Hz) characterized by an almost vertical tail, in the charged state, and a diffusive tail in the discharged state. Parameter values obtained from the modelling are given in table 5.

The high frequency side of the impedance curve does not intersect with the x-axis, so the electrolyte resistance (R_E) is obtained from the modeling and was 12.5 Ωcm^2 and 12.9 Ωcm^2 for LiC_6 and C respectively. The first semicircle (R_1Q_1) observed at high frequencies (higher than 10 kHz) can be assigned to the interface between the Copper current collector and/or the porous graphite anode or the graphite particle/particle contact resistance [12], with R_1 contact resistance and Q_1 constant phase element which represents the double layer capacitance at these interfaces. The value obtained for R_1 is observed to be significantly lower at 100% SOC than at 0% SOC. This is possibly related to the change in the particle/particle contact because of swelling of graphite grains after Li intercalation.

The second semicircle at 100 Hz – 10 Hz is modelled by ($R_{SEI}Q_{dl1}$) i.e. related to the SEI layer formed around each graphite particle and is a part of the Simplified Transmission Line Model (TLM_{an}) for a porous electrode [6], [8], [17], [27], [28], [31]. The values used for L and r are respectively 35 μm and 548 nm, obtained from the FIB/SEM analysis and PSD calculation. The fitting values for R_{SEI} and R_{ct} are highest for C in the delithiated form. Similarly D is highest for C in the delithiated form which means Li^+ ions travel faster through the graphene planes when they are delithiated. The lithium diffusivity in the negative electrode is observed to be is around 2 order of magnitude higher than D for the positive electrode.

R_{el} is extremely low and could be neglected, enabling the use of a Simplified Transmission Line Model [12], [17] for the graphite electrode. This is because the entire anode is made of C which is highly conductive. Contrary the cathode is a mixed $LiFePO_4$/CB electrode with a significant electronic resistance.

The values obtained for $R_{ion,L}$ for the Gr1 and LFP/CB1 electrode are comparable. This is in agreement with the expectations since the electrode pore volumes are comparable, see Fig. 9 and Table 3. Besides the pore diameter, indicated by the analysis presented in Fig. 8, the electrode pores tortuosity τ_{el}, and pore volume / solid phase volume ratio is important factors determining $R_{ion,L}$. τ_{el} has been calculated, using Eq. 9, for both positive and negative electrode. It has been found to be equal respectively to 4.54 and 1.77. Both results are higher than the values of geometrical tortuosity, but they probably better represent the real tortuosity values of the two electrodes. Furthermore a smaller τ_{el} for Gr1 is reasonable because of its higher porosity and bigger average pore size compare to LFP/CB1.

For both the anode and cathode $R_{ion,L}$ is observed to be higher in the lithiated state than in the delithiated state. This is believed to be related to the expansion/contraction of the lithiated/delithiated LFP or C particles. LFP particles are known to reduce their volume by approximately 6.8% [39], [40] with delithiation and the volume reduction of two close LFP particles could highly influence the pores dimension (found to be smaller than LFP), resulting in a huge drop of $R_{ion,L}$ as observes in the delithiated form. On the contrary the swelling decreases the pore volume thereby narrowing the electrolyte diffusion channels inside the electrodes which increases $R_{ion,L}$. The relative change in the obtained values for $R_{ion,L}$ in the lithiated and non-lithiated form is smaller for the anode than for the cathode. This is possibly because of a much bigger pores diameter and smaller tortuosity in the negative electrode, whose combined effect results in a smaller relative $R_{ion,L}$ change.

Note that the Ohmic contribution from the TLM_{an} is negligible since there is no gap on the x-axis in Fig. 14 a) and d) between the blue TLM_{an} impedance and the green (R_1Q_1) semi-circle. This is because $R_{el} << R_{ion,L}$ (i.e. R_{el} is insignificant) for the Gr1 electrode.

4.3. 26650CC Impedance Modelling: Two-electrode configuration

4.3.1. Equivalent Circuit Description

The number of variables in the model for the LFP/CB1 and Gr1 spectra is respectively 13 and 16. Ideally, the two single electrode impedance models should be put in series to model the 26650CC impedance spectra. Unfortunately this would result in a model with too many variables (more than 20) to allow a stable fitting of the model data to the measured 26650CC spectra.

Instead of adding the two single electrode models, a new equivalent circuit is proposed to model the 26650CC spectra. The model is presented in Fig. 16 and is a combination of the two single electrode equivalent circuits (Fig. 2 and 3) with a few simplifications, which keep the number of variables equal to 16.

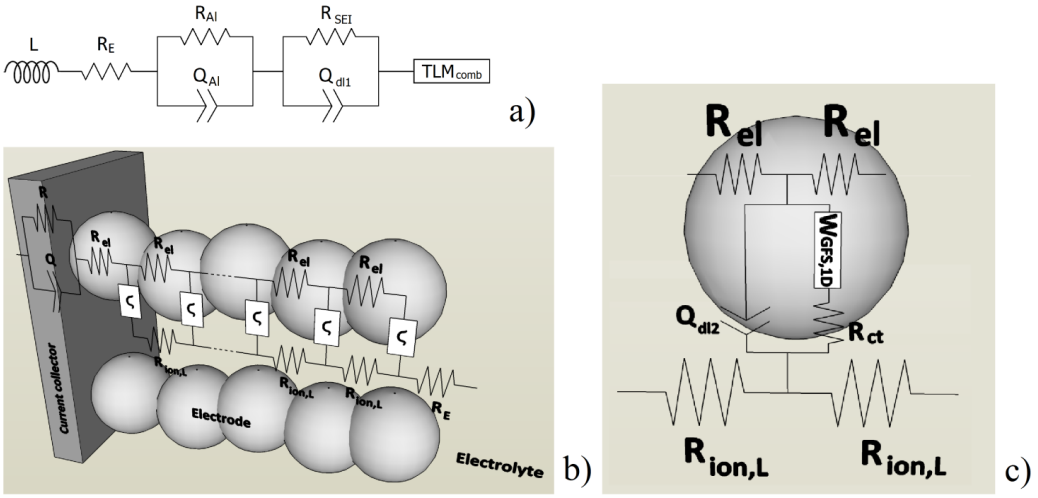

Figure 16. a) Equivalent circuit used to model the 2665CC impedance spectra, b) combined TLM_{comb} used to model porous electrode, c) single particle ECM.

The $R_E(R_{Al}Q_{Al})$ elements model the high-frequency region where R_E and R_{Al} are resistors and Q_{Al} a CPE. R_E models the ionic resistance of the electrolyte, while $(R_{Al}Q_{Al})$ represents the aluminum/cathode polarization [11], observed in the LFP/CB1 electrode in the frequency range 1 kHz – 100 Hz. The R_1Q_1 element, previously used to model the particle/particle contact in the Gr1 electrode, is not included in the total circuit since this process occurs at relative high frequency (>10 kHz). Above ~10 kHz the 26650CC is dominated by inductance and possibly beginning skin-effects or other processes yielding increased real resistance.

The $(R_{SEI}Q_{dl1})$ element models the mid-frequency region (100 Hz – 10 Hz) and represents the SEI layer which covers each graphite particle in the anode. The TLM_{comb} in Fig. 16b combines the cathode and anode TLMs. The two single electrode TLMs have a Randles element in common to model the insertion or intercalation process at the interface ($Li_{1-x}FePO_4$ or Li_xC_6), but the *RQ* element representing the SEI layer on graphite is missing on the cathode model. For the 26650CC impedance model the $(R_{SEI}Q_{dl1})$ is placed outside the TLM_{comb} in order to have an equivalent circuit ς, to model the surface impedance inside the TLM_{comb}, which is equal for both cathode and anode particles ($\varsigma_{cat} = \varsigma_{an}$). No changes are observed in modelling the mid-frequency part of the spectra with a $R_{SEI}Q_{dl1}$ places either outside or inside the TLM, since comparable values have been found for both single-electrode impedance and 2-electrode configuration. However, results of R_{SEI} and C_{dl1} calculated from the model are reported in Table 5(a,b), and as supplementary information, being normalized for both geometrical surface area and internal surface area.

From the single electrode modelling, it is possible to identify electrode specific contributions dominating the 26650CC EIS spectrum.

The TLM_{comb} variables are R_{ct}, C_{dl} (calculated from CPE according to Eq. 5) and D, $R_{ion,L}$ and R_{el}. The single electrode fitting (Table 3 and 4) shows R_{ct} and C_{dl} are not negligible for any of the two electrodes. However, the Li^+ ion diffusion coefficient D was observed to be around 2-3 orders of magnitude larger for Gr1 than for LFP/CB1, in agreement with previous findings [41]. This means diffusion in LFP/CB1 dominates the final part of the TLM_{comb} (the 45° line) and that the Warburg contribution from graphite can be neglected.

For this reason diffusion of Li^+ ion in LFP is modelled by a general finite space Warburg element with diffusion process along a one-dimensional diffusion path, $W_{GFS,1D}$, as used for the LFP cathode and the value used for r is the $Li_{1-x}FePO_4$/CB radius (22 nm, as calculated from PSD). R_{el} was also found to be negligible in the Li_xC_6 electrode, so the calculated electronic resistance R_{el} from the total TLM_{comb} is associated with the $Li_{1-x}FePO_4$/CB cathode, and more specifically the CB network. Finally, the ionic diffusion resistance per unit length in the pore $R_{ion,L}$ is seen to be highest when each electrode is in its fully lithiated state. This means the $R_{ion,L}$ contribution primarily comes from the cathode when the battery is discharged, and vice versa. From the single electrode modelling the cathode:anode contribution ratio was calculated to be 75:25 at 0% SOC, and 35:65 at 100% SOC.

The low frequency part of the 26650CC impedance spectra predominantly change at the lowest and highest SOC. For this reason the change this ratio is assumed to mainly occur at the lowest and highest SOC and consequently a ratio of 50:50 was simply used for all intermediate SOCs. The ratio was used to calculate an SOC dependent pore length L which is used as input for the TLM_{comb}; The values used for L are 57.5, 50 and 45.5 µm respectively for 0%, (12.5-87.5)%, and 100% SOC.

4.3.2. EIS spectra fitting

The normalized EIS spectrum measured for 26650CC at 50% SOC, after inductance removal, is shown in Fig. 17(a, b). Fig. 17(c, d) show respectively Nyquist and Bode plot of the EIS spectrum, with relative fitting, measured after charging 26650CC at 50% SOC, at OCV after relaxation, while Fig. 17(e, f) show a zoomed view of the high frequency region. The values obtained by EIS modelling at different SOC (see Fig. 15) are instead reported in tables 5(a, b) and plotted in image 18. All parameters are again reported in Table S3 in the supplementary information.

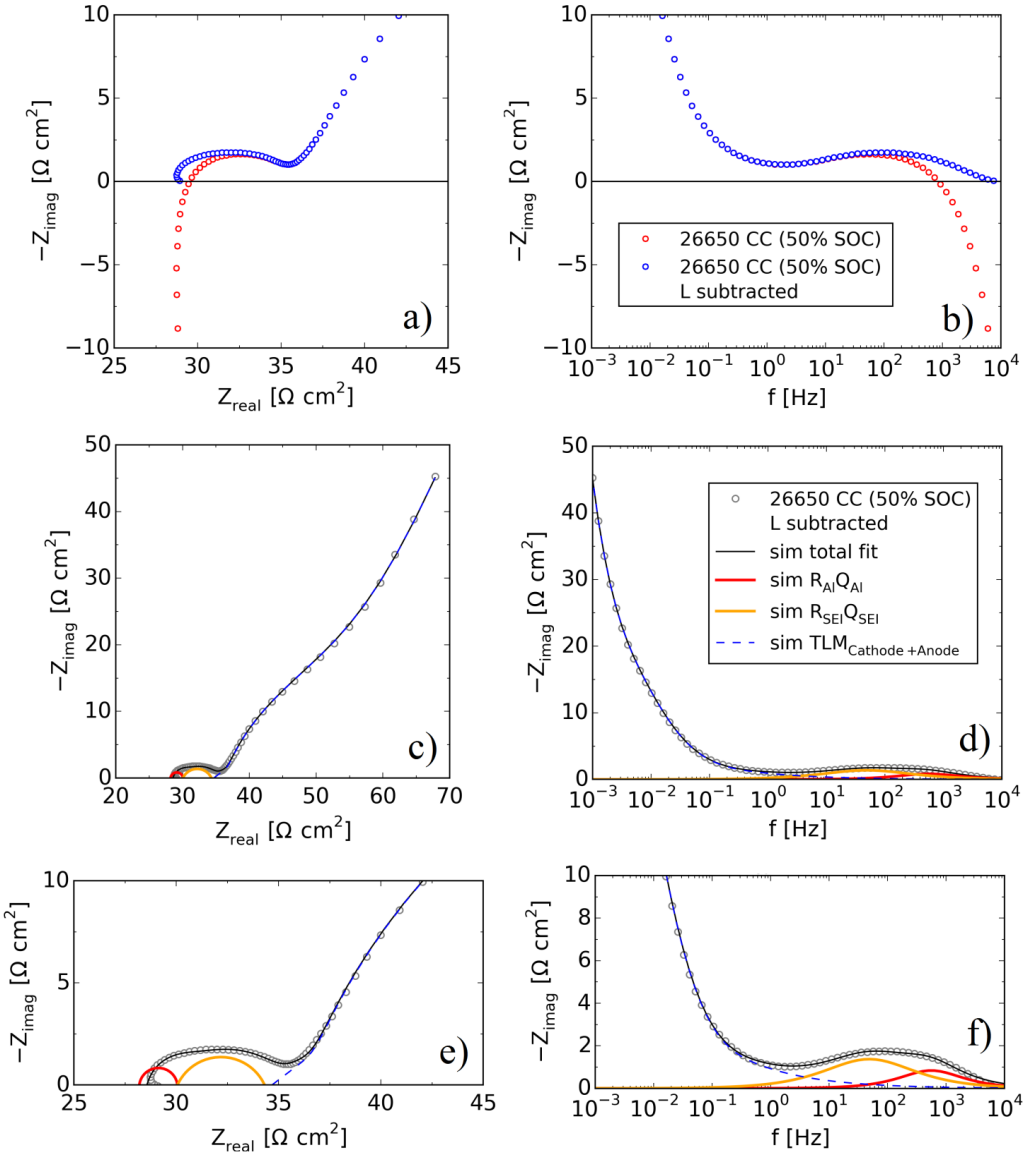

Figure 17. a) Nyquist and b) Bode plot of 26650CC impedance spectra measured after charging to 50% SOC with and without subtraction of inductance. Full view of c) Nyquist and d) Bode plot of the same spectra subtracted inductance including fitted model data (black line) and separate parts of the model data (blue, yellow, red). Zoomed view of e) Nyquist and f) Bode plot of the same as in c) and d).

The red semicircle seen in Fig 17(c, e) show the impedance for the ($R_{Al}Q_{Al}$) element assigned to the interface between the Aluminum current collector and the porous cathode [11]. As reported in Table

5(a, b) and presented in Fig. 18, R_{Al} is independent of SOC and the values obtained for R_{Al} and C_{Al} are comparable to the values obtained for the same variables from the $Li_{1-x}FePO_4$/CB EIS modelling (Table 3).

The yellow semicircle in Fig 17(c, e) shows the ($R_{SEI}Q_{dl1}$) element impedance. From the fitted values, R_{SEI} shows to decrease upon charging, in agreement with the Gr1 modeling results.

The blue low frequency branch in Fig 17(c, e) is the combined TLM_{comb} impedance. For the Randles circuit, R_{ct} and C_{dl} are a combination of cathode and anode resistances and capacitance. As seen from the fitted values, Table 5(a, b) and Fig. 18, R_{ct} decrease with increasing SOC which is in agreement with the values obtained from the single electrode impedance modelling. Specifically value for R_{ct} obtained from modeling the 26650CC spectrum is approximately the sum of the values obtained for R_{ct} obtained from modeling of the LFP/CB1 and Gr1 spectra.

The value for D obtained from modeling the 26650CC spectrum is around 10^{-13} cm^2s^{-1}, (Fig. 18d). This value is similar to the value obtained from the cathode EIS modelling (Table 3), and does not change drastically with SOC. This shows the value for D obtained from modeling the 26650 spectrum primarily relates to the Li diffusion in the LFP.

$R_{ion,L}$ seems to be fairly constant at different SOCs except at 0% and 100% SOC (Fig.18e). This is possibly related to the full lithiation of $Li_{1-x}FePO4$ and Li_xC_6 at 0% and 100% SOC, respectively. When the battery is discharged, the cathode contribute the most to $R_{ion,L}$, and vice versa.

R_{el} is observed to decrease with SOC (Fig. 18f) and match the values obtained for the cathode (Table 3).

Finally, as for the cathode, when R_{el} is significant relative to $R_{ion,L}$ the generalized TLM_{comb} features a small Ohmic contribution which shift the starting point of the red semi-circle to the left in the Nyquist plot, Fig. 13(a, c).

TABLE 5a Results from EIS fitting of 26650CC (charging mode).

	$R_{Al}Q_{Al}$ element		$R_{SEI}Q_{dl1}$ element		Transmission Line				
					Randles element			Pores	Electrode
	R_{Al} (Ωcm^2)	C_{Al} ($mFcm^{-2}$)	R_{SEI} (Ωcm^2)	C_{dl1} ($mFcm^{-2}$)	R_{ct} (Ωcm^2)	C_{dl2} (Fcm^{-2})	D (cm^2s^{-1})	$R_{ion,L}$ (Ωcm)	R_{el} (Ωcm)
0%	1.81	0.17	7.18	0.54	87.0	0.24	$1.5\cdot10^{-13}$	1929	106
12.5%	1.76	0.17	4.58	0.50	64.0	0.72	$9.0\cdot10^{-14}$	927	79
25%	1.76	0.16	4.51	0.44	40.0	0.65	$8.8\cdot10^{-14}$	1040	92
37.5%	1.80	0.16	4.38	0.44	32.0	0.62	$8.9\cdot10^{-14}$	1025	71
50%	1.86	0.15	4.26	0.48	38.0	0.63	$8.9\cdot10^{-14}$	994	59
62.5%	1.80	0.16	4.27	0.44	42.0	0.58	$1.1\cdot10^{-13}$	997	64
75%	1.84	0.16	3.87	0.48	24.0	0.50	$1.5\cdot10^{-13}$	1144	58
87.5%	1.86	0.16	3.86	0.47	30.0	0.53	$1.3\cdot10^{-13}$	1071	46
100%	1.75	0.16	2.85	0.58	15.4	0.09	$1.4\cdot10^{-13}$	1826	46

TABLE 5b Results from EIS fitting of 26650CC (discharging mode).

	$R_{Al}Q_{Al}$ element		$R_{SEI}Q_{dl1}$ element		Transmission Line				
					Randles element			Pores	Electrode
	R_{Al} (Ωcm^2)	C_{Al} ($mFcm^{-2}$)	R_{SEI} (Ωcm^2)	C_{dl1} ($mFcm^{-2}$)	R_{ct} (Ωcm^2)	C_{dl2} (Fcm^{-2})	D (cm^2s^{-1})	$R_{ion,L}$ (Ωcm)	R_{el} (Ωcm)
100%	1.75	0.16	2.85	0.58	15.4	0.09	$1.4 \cdot 10^{-13}$	1826	46
87.5%	1.82	0.16	4.14	0.43	20.0	0.55	$1.4 \cdot 10^{-13}$	1035	51
75%	1.82	0.16	4.10	0.44	44.0	0.63	$9.4 \cdot 10^{-14}$	1050	73
62.5%	1.84	0.15	4.50	0.44	26.0	0.59	$9.9 \cdot 10^{-14}$	1060	88
50%	1.82	0.16	4.68	0.43	24.0	0.55	$1.6 \cdot 10^{-13}$	1129	81
37.5%	1.80	0.16	4.69	0.44	42.0	0.62	$9.0 \cdot 10^{-14}$	1106	80
25%	1.80	0.17	4.68	0.47	58.0	0.66	$1.0 \cdot 10^{-13}$	1232	84
12.5%	1.78	0.17	4.62	0.53	58.0	0.50	$1.4 \cdot 10^{-13}$	1330	91
0%	1.83	0.17	7.82	0.58	88.7	0.20	$1.3 \cdot 10^{-13}$	2119	102

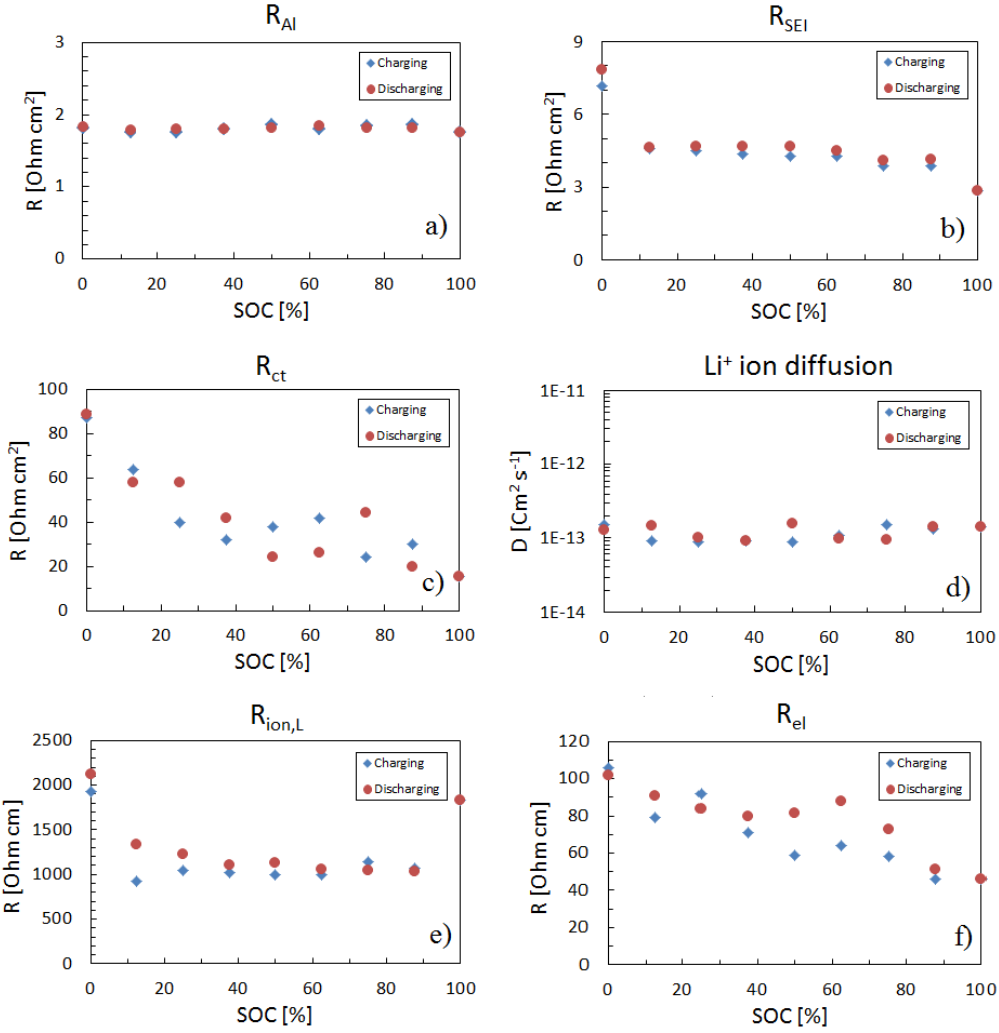

Figure 18. Fitted values as function of SOC.

5. Conclusions

Various circuits have been proposed in literature to model $LiFePO_4$ cathode and Li_xC_6 anode impedance and most of the circuits consist of a transmission line model (TLM) for a porous electrode. The models are often used to distinguish and address the different electrode polarization in impedance spectra.

In this work a commercial 26650 cylindrical $LiFePO_4$/C battery was disassembled and the two electrodes were characterized individually by charge discharge curves and electrochemical

impedance spectroscopy (EIS) in a three-electrode setup, and by FIB/SEM tomography. Two different equivalent circuits were used to model the cathode and anode impedance. The circuits included a TLM for a porous electrode, which involves the parameters pore length L and particle radius r. The values for these parameters were found from the FIB/SEM tomography. A thorough analysis was conducted of the parameter values obtained from fitting the individual electrode impedances. The analysis enabled us to propose a simplified equivalent circuit which also includes a TLM_{comb} to model the full commercial battery impedance. The parameter values obtained from fitting the circuit impedance to the full battery impedance were discussed and validated against the parameter values obtained from fitting the individual electrode impedance spectra.

From fitting the simplified circuit to the commercial battery impedance values were obtained for the ionic resistance $R_{ion,L}$ of Li^+ ions diffusing into the electrode pores, electron resistance R_{el} in the porous electrodes and Lithium diffusivity in the active materials in the electrodes. By comparing the obtained values with the values obtained from single electrode modeling, it was demonstrated that several of these values could be ascribed to either the cathode or the anode.

R_{el} was observed to be negligible for the anode such that R_{el} only depends on the cathode CB network. $R_{ion,L}$ was seen to consist of both cathode and anode contributions and to be dependent on the SOC. Specifically $R_{ion,L}$ was observed to be highest in each of the two electrodes when they were fully lithiated. The lithium diffusion coefficient D was much smaller in $LiFePO_4$ than in C which means D obtained from measurements of the full battery mainly reflects the lithium diffusion in $LiFePO_4$.

Combined with other characterization techniques the simplified equivalent circuit proposed here could be an important tool to study degradation mechanisms in $LiFePO_4$/C batteries when three-electrode impedance analysis in not possible.

To the best of our knowledge this is the first time a TLM_{comb} is used to study the low-frequency branch of commercial cell impedance spectra, taking into account pore resistances from both cathode and anode.

Acknowledgement

The authors gratefully acknowledge financial support from the Danish Strategic Research Council through the project “Advanced Lifetime Predictions of Battery Energy Storage” (contract no. 0603-00589B).

References

[1] "http://batteryuniversity.com/learn/article/types_of_battery_cells." .

[2] S. H. Jensen, J. Hjelm, a Hagen, and M. Mogensen, "Electrochemical impedance spectroscopy as diagnostic tool," *Handb. Fuel Cells*, vol. 6, 2010.

[3] M. D. Levi and D. Aurbach, "Diffusion coefficients of lithium ions during intercalation into graphite derived from the simultaneous measurements and modeling of electrochemical impedance and potentiostatic intermittent titration characteristics of thin graphite electrodes," *J. Phys. Chem. B*, vol. 101, no. 23, pp. 4641–4647, 1997.

[4] J. Thevenin, "Passivating films on lithium electrodes. An approach by means of electrode impedance spectroscopy," *J. Power Sources*, vol. 14, no. 1–3, pp. 45–52, 1985.

[5] N. Mellgren, S. Brown, M. Vynnycky, and G. Lindbergh, "Impedance as a Tool for Investigating Aging in Lithium-Ion Porous Electrodes," *J. Electrochem. Soc.*, vol. 155, no. 4, p. A304, 2008.

[6] J. P. Meyers, M. Doyle, R. M. Darling, and J. Newman, "The Impedance Response of a Porous Electrode Composed of Intercalation Particles," *J. Electrochem. Soc.*, vol. 147, no. 8, p. 2930, 2000.

[7] H. U. a Ju, J. U. N. Wu, and Y. Xu, "Revisiting the electrochemical impedance behaviour of the LiFePO4/C cathode," *J. Chem. Sci*, vol. 125, no. 3, pp. 687–693, 2013.

[8] F. Gao and Z. Tang, "Kinetic behavior of LiFePO4/C cathode material for lithium-ion batteries," *Electrochim. Acta*, vol. 53, no. 15, pp. 5071–5075, 2008.

[9] P. Prosini, M. Lisi, D. Zane, and M. Pasquali, "Determination of the chemical diffusion coefficient of lithium in LiFePO4," *Solid State Ionics*, vol. 148, no. 1–2, pp. 45–51, 2002.

[10] J. P. Schmidt, T. Chrobak, M. Ender, J. Illig, D. Klotz, and E. Ivers-Tiffée, "Studies on LiFePO4 as cathode material using impedance spectroscopy," *J. Power Sources*, vol. 196, no. 12, pp. 5349–5355, 2011.

[11] J. Illig, M. Ender, T. Chrobak, J. P. Schmidt, D. Klotz, and E. Ivers-Tiffee, "Separation of Charge Transfer and Contact Resistance in LiFePO4-Cathodes by Impedance Modeling," *J. Electrochem. Soc.*, vol. 159, no. 7, pp. A952–A960, 2012.

[12] J. Illig, M. Ender, a. Weber, and E. Ivers-Tiffée, "Modeling graphite anodes with serial and transmission line models," *J. Power Sources*, vol. 282, pp. 335–347, 2015.

[13] L. Wang, J. Zhao, X. He, J. Ren, H. Zhao, J. Gao, J. Li, C. Wan, and C. Jiang, "Investigation of modified nature graphite anodes by electrochemical impedance spectroscopy," *Int. J. Electrochem. Sci.*, vol. 7, no. 1, pp. 554–560, 2012.

[14] A. Funabiki, "Impedance Study on the Electrochemical Lithium Intercalation into Natural Graphite Powder," *J. Electrochem. Soc.*, vol. 145, no. 1, p. 172, 1998.

[15] J. Y. Song, H. H. Lee, Y. Y. Wang, and C. C. Wan, "Two- and three-electrode impedance spectroscopy of lithium-ion batteries," vol. 111, pp. 255–267, 2002.

[16] E. Barsoukov, “Kinetics of lithium intercalation into carbon anodes: in situ impedance investigation of thickness and potential dependence,” *Solid State Ionics*, vol. 116, no. 3–4, pp. 249–261, 1999.

[17] N. Ogihara, S. Kawauchi, C. Okuda, Y. Itou, Y. Takeuchi, and Y. Ukyo, “Theoretical and Experimental Analysis of Porous Electrodes for Lithium-Ion Batteries by Electrochemical Impedance Spectroscopy Using a Symmetric Cell,” *J. Electrochem. Soc.*, vol. 159, no. 7, pp. A1034–A1039, 2012.

[18] R. Scipioni, P. S. Jørgensen, D. T. Ngo, S. B. Simonsen, J. Hjelm, P. Norby, and S. H. Jensen, “Low-voltage FIB/SEM Tomography for 3D Microstructure Evolution of LiFePO4/C Electrode,” *ECS Trans.*, vol. 69, no. 18, pp. 71–80, 2015.

[19] H. Nara, D. Mukoyama, T. Yokoshima, T. Momma, and T. Osaka, “Impedance Analysis with Transmission Line Model for Reaction Distribution in a Pouch Type Lithium-Ion Battery by Using Micro Reference Electrode,” *J. Electrochem. Soc.*, vol. 163, no. 3, pp. A434–A441, 2016.

[20] J. Bisquert, G. Garcia-Belmonte, P. Bueno, E. Longo, and L. O. . Bulhões, “Impedance of constant phase element (CPE)-blocked diffusion in film electrodes,” *J. Electroanal. Chem.*, vol. 452, no. 2, pp. 229–234, 1998.

[21] A. K. Padhi, K. S. Nanjundaswamy, and J. B. Goodenough, “Phospho-olivines as Positive-Electrode Materials for Rechargeable Lithium Batteries,” *J. Electrochem. Soc.*, vol. 144, no. 4, pp. 1188–1194, 1997.

[22] Y. Zhang, Q. Huo, P. Du, L. Wang, A. Zhang, Y. Song, Y. Lv, and G. Li, “Advances in new cathode material LiFePO4 for lithium-ion batteries,” *Synth. Met.*, vol. 162, no. 13–14, pp. 1315–1326, 2012.

[23] M. Ender, J. Joos, T. Carraro, and E. Ivers-Tiffee, “Quantitative Characterization of LiFePO4 Cathodes Reconstructed by FIB/SEM Tomography,” *J. Electrochem. Soc.*, vol. 159, no. 7, pp. A972–A980, 2012.

[24] J. Sauvola and M. Pietikäinen, “Adaptive document image binarization,” *Pattern Recognit.*, vol. 33, no. 2, pp. 225–236, 2000.

[25] T. Kryjak and M. Gorgoń, “Parallel implementation of local thresholding in Mitrion-C,” *Int. J. Appl. Math. Comput. Sci.*, vol. 20, no. 3, pp. 571–580, 2010.

[26] B. Münch and L. Holzer, “Contradicting geometrical concepts in pore size analysis attained with electron microscopy and mercury intrusion,” *J. Am. Ceram. Soc.*, vol. 91, no. 12, pp. 4059–4067, 2008.

[27] G. Garcia-Belmonte, F. Fabregat-Santiago, J. Bisquert, M. Yamashita, E. C. Pereira, and S. Castro-Garcia, “Frequency dispersion in electrochromic devices and conducting polymer electrodes: A generalized transmission line approach,” *Ionics (Kiel).*, vol. 5, pp. 44–51, 1999.

[28] R. D. Levie, “On porous electrodes,” *Electrochim. Acta*, vol. 9, no. November 1963, p. 1231, 1964.

[29] N. Ogihara, S. Kawauchi, C. Okuda, Y. Itou, Y. Takeuchi, and Y. Ukyo, “Theoretical and

Experimental Analysis of Porous Electrodes for Lithium-Ion Batteries by Electrochemical Impedance Spectroscopy Using a Symmetric Cell," vol. 159, no. 7, pp. 1034–1039, 2012.

[30] R. Younesi, a. S. Christiansen, R. Scipioni, D.-T. Ngo, S. B. Simonsen, K. Edstrom, J. Hjelm, and P. Norby, "Analysis of the Interphase on Carbon Black Formed in High Voltage Batteries," *J. Electrochem. Soc.*, vol. 162, no. 7, pp. A1289–A1296, 2015.

[31] J. Song and M. Z. Bazant, "Effects of Nanoparticle Geometry and Size Distribution on Diffusion Impedance of Battery Electrodes," *J. Electrochem. Soc.*, vol. 160, no. 1, pp. A15–A24, 2013.

[32] G.J.Brug; A.L.G. Van den Eeden; M. Sluyters-Rehbach; J.H. Sluyters, "The Analysis of Electrode Impedances Complicated by the Presence of a Constant Phase Element," *J. Electroanal. Chem.*, vol. 176, pp. 275–295, 1984.

[33] C. M. Julien, A. Mauger, K. Zaghib, and H. Groult, "Comparative Issues of Cathode Materials for Li-Ion Batteries," pp. 132–154, 2014.

[34] W. C. Chueh, F. El Gabaly, J. D. Sugar, N. C. Bartelt, A. H. McDaniel, K. R. Fenton, K. R. Zavadil, T. Tyliszczak, W. Lai, and K. F. McCarty, "Intercalation pathway in many-particle LiFePO4 electrode revealed by nanoscale state-of-charge mapping," *Nano Lett.*, vol. 13, no. 3, pp. 866–872, 2013.

[35] M. Ender, A. Weber, and E. Ivers-Tiffée, "A novel method for measuring the effective conductivity and the contact resistance of porous electrodes for lithium-ion batteries," *Electrochem. commun.*, vol. 34, pp. 130–133, 2013.

[36] L. Lombardo, S. Brutti, M. A. Navarra, S. Panero, and P. Reale, "Mixtures of ionic liquid-Alkylcarbonates as electrolytes for safe lithium-ion batteries," *J. Power Sources*, vol. 227, pp. 8–14, 2013.

[37] P. Porion, Y. R. Dougassa, C. Tessier, L. El Ouatani, J. Jacquemin, and M. Anouti, "Comparative study on transport properties for LiFAP and LiPF6 in alkyl-carbonates as electrolytes through conductivity, viscosity and NMR self-diffusion measurements," *Electrochim. Acta*, vol. 114, pp. 95–104, 2013.

[38] M. Winter, J. O. Besenhard, M. E. Spahr, and P. Novák, "Insertion Electrode Materials for Rechargeable Lithium Batteries," *Adv. Mater.*, vol. 10, no. 10, pp. 725–763, 1998.

[39] a. Matasso, D. Wetz, and F. Liu, "The Effects of Internal Pressure Evolution on the Aging of Commercial Li-Ion Cells," *J. Electrochem. Soc.*, vol. 162, no. 1, pp. A92–A97, 2014.

[40] H. Lin, Y. Wen, C. Zhang, L. Zhang, Y. Huang, B. Shan, and R. Chen, "A GGAU study of lithium diffusion in vanadium doped LiFePO 4," *Solid State Commun.*, vol. 152, no. 12, pp. 999–1003, 2012.

[41] M. Gaberscek, J. Moskon, B. Erjavec, R. Dominko, J. Jamnik, C. Ho, P. Paolo, M. Lisi, D. Zane, M. Pasquali, M. Park, X. Zhang, M. Chung, G. B. Less, A. M. Sastry, M. Gaberscek, J. Moskon, B. Erjavec, R. Dominko, J. Jamnik, J. H. Sluyters, H. C. Shin, W. Il Cho, H. Jang, P. Paolo, M. Lisi, D. Zane, M. Pasquali, K. Bazzi, B. P. Mandal, M. Nazri, V. M. Naik, V. K. Garg, A. C. Oliveira, P. P. Vaishnava, G. A. Nazri, R. Naik, J. Illig, M. Ender, T. Chrobak, J.

P. Schmidt, D. Klotz, E. Ivers-Tiffee, J. P. Meyers, M. Doyle, R. M. Darling, J. Newman, F. Gao, and Z. Tang, “A review of conduction phenomena in Li-ion batteries,” *J. Power Sources*, vol. 148, no. 24, pp. 7904–7929, 2002.

VI

Analysis of Aging Mechanisms in a Commercial $LiFePO_4$/Graphite 26650 Cylindrical Cell by Low – kV FIB/SEM Tomography

Roberto Scipioni [a,*], Peter S. Jørgensen [a], Daniel I. Stroe [b], Johan Hjelm [a], and Søren H. Jensen [a,**]

[a] DTU Energy, Department of Energy Conversion and Storage, Technical University of Denmark, Frederiksborgvej 399, 4000 Roskilde, Denmark

[b] Department of Energy Technology, Aalborg University, Fredrik Bajers Vej 5, 9100 Aalborg, Denmark

Keyword: Battery, Lithium, Ion, Electrochemical, Impedance, Spectroscopy, Degradation, Mechanisms, Focused, Ion, Beam, Scanning, Electron, Microscopy

Corresponding author: (*) roscip@dtu.dk (Roberto Scipioni), (**) shjj@dtu.dk (Søren Højgaard Jensen)

Abstract

In this work the electrode degradation mechanisms in commercial 2.5 Ah $LiFePO_4$/C 26650 cylindrical cells were examined. Aged and fresh electrode samples were prepared by cycling two cells respectively five and 22k times. Subsequently the cells were disassembled in a glovebox and electrode samples were prepared for electrochemical testing in a 3-electrode setup and for characterization with low-kV FIB/SEM tomography. A thick layer of degradation products was observed at the electrode/electrolyte interface of the aged $LiFePO_4$ electrode. Relative to the fresh $LiFePO_4$ electrode, the aged electrode exhibited a larger polarization resistance which indicates the observed layer increases the ionic resistance. In addition large agglomerates, probably a mixture of carbonaceous material and decomposition products from the electrolyte, were observed at the electrode/electrolyte interface of the aged graphite electrode. Low-voltage FIB/SEM tomography was used to detect charging effects of graphite particles in the carbon electrode. The charging effects were primarily observed in the aged electrode and most of these locally charged particles were found to be close to the electrode/electrolyte interface.

1. Introduction

Lithium ion batteries (LIBs) span a broad range of applications from portable devices to electric vehicles (EVs) [1], [2]. However, limited lifetime is still a challenge for several LIB materials and the relation between degradation mechanisms and loss of performance is still not fully understood.

Despite its poor ionic and electronic conductivity $LiFePO_4$ (LFP) is one of the more interesting cathode material for lithium-ion batteries due to its relatively high cycle-ability and safety [3], [4]. To increase electron percolation in the electrode the LFP is normally mixed with a carbonaceous additive such as carbon black. Graphite (Gr) is one of the early anode materials for commercial LIBs and it is still one of the most used anode materials [5]. Gr have a layered structure and is able to intercalate lithium ions between graphene layers. A solid electrolyte interphase (SEI) layer is always formed on the electrode/electrolyte interface to protect the electrode form solvent intercalation and layer exfoliation.

Several studies examines the degradation mechanisms in laboratory LFP [6]–[8] and Gr electrodes [9]–[11], and various models have been presented to predict performance and lifetime of commercial $LiFePO_4$/graphite cells [12]–[15], however strong links between several of the observed degradation mechanisms and the battery use is still not fully established. It is therefore important to enhance this link by relating the morphological changes in the battery electrodes with the battery use.

Here a commercial $LiFePO_4$/graphite 26650CC cylindrical cell (26650CC) is tested and characterized by low – kV FIB/SEM tomography. The technique was developed to observe the electron percolation in SOFC anode Ni-networks [16] and has later been used to study the electron percolation in a laboratory $LiFePO_4$/CB electrode [8], [17]. Here we use it to examine the electron percolation in the commercial graphite electrodes, in order to identify disconnected particles in the aged anode. Furthermore conventional FIB/SEM tomography is used to study morphological degradation in both the LFP and Gr electrodes.

2. Methods and materials

2.1. Cell testing and disassembling

Two commercial $LiFePO_4$/C 26650 cylindrical cells with a nominal capacity of 2.5 Ah were tested and characterized. The first battery was used as reference and labeled “F26650CC”. It was cycled five times at room temperature at a constant C-rate of 0.1 (250 mA). The second battery labeled “A26650CC”, was cycled 22k times between 25% and 75% state-of-charge (SOC). It was also cycled at room temperature but at a constant C-rate of 4 (10 A). Both cells were characterized by EIS in a two-electrode setup using a Biologic VMP3 with Pstat/Gstat boards (test conditions shown in Table 1).

The two batteries were afterward de-assembled in a glovebox in the discharged state and the positive and negative electrodes were unrolled. The cylindrical cells consist of a 1.5 m $LiFePO_4$/carbonaceous additive positive electrode cast on either sides of an Aluminum foil, a 1.5 m graphite (Gr) negative electrode cast on either sides of a Copper foil and 2 polymeric separators soaked with liquid electrolyte. The battery configuration is schematically presented in Fig. 1a. The carbonaceous additive in the positive electrode is unknown. In order to distinguish the additive from the graphite in the negative electrode we will refer to the additive with "CB" and to the negative electrode with "Gr".

The total area of each of the battery electrodes and separators was 1950 cm^2. The two electrode foils from each cylindrical cell were rinsed with diethyl carbonate and vacuum dried at 120°C in order to remove the liquid electrolyte and subsequently twelve circular electrodes with a diameter of 18 mm (area = 2.55 cm^2) were punched out. From F26650CC four disk electrodes were extracted: two from the cathode foil (LFP1_F and LFP2_F) and two from the anode foil (Gr1_F and Gr2_F). The anode foil was dark grey with no visible difference between the part of the electrode near the core of the battery and the part of the electrode near the skin of the battery.

In contrast to this color difference was found between the skin and the core part of the anode foil from A26650CC. As seen in the photos in Fig. 1(b), the negative graphite foil is characterized by a blue shadowed region in the part of the foil close to the skin of the battery and a red region close to the core. In the presented photos the colors are oversaturated to enhance the visibility of the blue and the red region. The color covers almost completely the anode foil (Fig. 1b,c), with the exception of the sides of the electrode, where the original dark grey color of graphite is observed. Eight circular electrodes have been then punched out from the skin and the core of the electrode foils as shown in Fig. 1(d,e) and listed in Table 1. They were collected from the mid part of the foil, where the colored layer is observed. The electrodes extracted from the skin are then labeled with AB (aged, blue) as suffix, while the ones from the core are labeled with AR (aged, red).

Six out of the twelve electrodes (Table 1) were scratched with a spatula to remove the electrode layer on one side and then tested in EL-CELL® ECC-Combi 3-electrode setups, using lithium metal foil counter electrodes, lithium metal as reference electrode and a glass fiber separator soaked with a standard 1M $LiPF_6$ in 1:1 EC/DMC electrolyte. The electrode samples were fully charged and discharged at a constant C-rate, calculated to be ~0.1 C in order to calculate the remaining capacity (see Table 1 for test conditions). The other identical six electrodes, collected from adjacent region, were instead prepared for microscopy analysis.

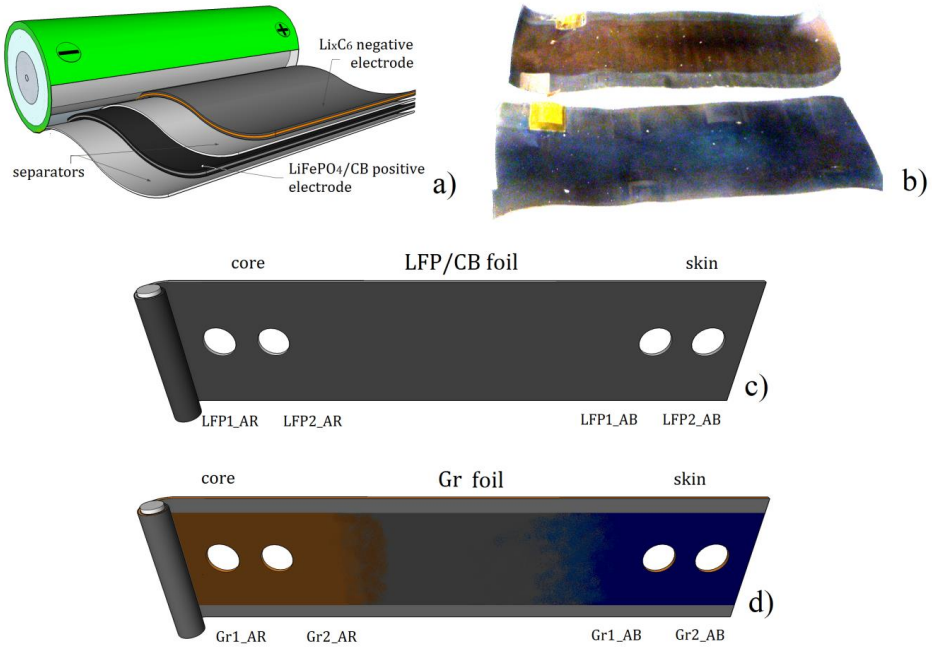

Figure 1. a) Schematic representation of the 26650CC $LiFePO_4$/C battery packaging design. b) Two pieces of the aged Li_xC_6 negative electrode (upper part from the core, lower part from the skin). The image has saturated colors to highlight the color contrast. c) Schematic representation of electrodes punched out from LFP/CB and d) Gr foils.

Table 1. Test conditions for the examined samples

Sample	Current (mA)	Approx. C-rate	SOC range	Total cycle number	Comment
F26650CC	250	0.1	0 – 100 %	5	Cylindrical Cell, 2-electrode setup
A26650CC	10k	4	25 – 75 %	22k	Cylindrical Cell, 2-electrode setup
LFP1_F	0.33	0.1	0 – 100 %	1	Cathode, 3-electrode setup
LFP1_AB	0.33	0.1	0 – 100 %	1	Cathode, 3-electrode setup
LFP1_AR	0.33	0.1	0 – 100 %	1	Cathode, 3-electrode setup
Gr1_F	0.33	0.1	0 – 100 %	1	Anode, 3-electrode setup
Gr1_AB	0.33	0.1	0 – 100 %	1	Anode, 3-electrode setup
Gr1_AR	0.33	0.1	0 – 100 %	1	Anode, 3-electrode setup
LFP2_F	-	-	-	-	Cathode, used for FIB/SEM analysis
LFP2_AB	-	-	-	-	Cathode, used for FIB/SEM analysis
LFP2_AR	-	-	-	-	Cathode, used for FIB/SEM analysis
Gr2_F	-	-	-	-	Anode, used for FIB/SEM analysis
Gr2_AB	-	-	-	-	Anode, used for FIB/SEM analysis
Gr2_AR	-	-	-	-	Anode, used for FIB/SEM analysis

2.2. FIB/SEM tomography

The six electrodes (Table 1) prepared for the FIB/SEM tomography were rinsed with diethyl carbonate and vacuum infiltrated with a silicon resin (Wacker Chemie) for 30 minutes to improve phase contrast between CB particles and pores as described by Ender et al [18]. Subsequently the samples were infiltrated with epoxy resin to enable high-quality grinding and polishing of the sample.

FIB tomography and SEM imaging of the six electrode samples was carried out on a Zeiss 1540XB CrossBeam microscope, using a lateral E-T (Everhart-Thornley) detector and an In-lens detector. A 3D dataset was collected from each of the electrodes with the exclusion of sample Gr2_AB because of failure of the microscope during FIB/SEM image collection. Only 2D SEM images were collected from this sample. Table 2 shows the volume sizes of the five 3D datasets. A Gallium FIB slicing probe of 2nA was used to mill the LFP2 electrodes and the thickness of each slice was estimated to 27, 32 and 14 nm for LFP2_F, LFP2_AB and LFP2_AR respectively. For the Gr2 electrodes the current for the Gallium FIB slicing probe was reduced to 1nA and the thickness of each slice was estimated to be 14 and 23 nm for Gr2_F and Gr2_AR respectively. Since the Gr2 electrodes are softer than the LFP2 ones, the current had to be reduced to enable high-quality imaging for the Gr2 electrodes dataset.

The LFP particles in the positive electrode are much smaller than the Gr particles in the negative one. Thus, in order to perform an accurate image segmentation of LFP particles (to be used for 3D reconstruction and PSD analysis), it was necessary to collect high-resolution images with increased magnification. Specifically, the serial sectioning imaging was performed at 1 kV with a pixel size of 15x15 nm^2 for the three LFP2 electrodes, 49x49 nm^2 and 59x59 nm^2 for the two Gr2 electrodes. The voxel size in the 3D-data sets was then 27x15x15 nm^3, 32x15x15 nm^3 and 14x15x15 nm^3 for LFP2 electrodes (F, AB and AR), 14x49x49 nm^3 and 23x59x59 nm^3 for Gr2 electrodes (F and AR).

Table 2. Volumes of collected datasets.

Dataset	Volume (voxels) X x Y x Z	Volume (μm^3) X x Y x Z
LFP2_F	80 x 850 x 400	2.2 x 12.5 x 5.9
LFP2_AB	81 x 870 x 450	2.6 x 12.7 x 6.6
LFP2_AR	185 x 800 x 360	2.6 x 11.7 x 5.3
Gr2_F	328 x 750 x 150	4.4 x 36.6 x 7.3
Gr2_AR	381 x 920 x 130	8.9 x 53.9 x 7.6

2.3. Low-voltage analysis

The FIB/SEM serial sectioning imaging has been performed and combined with a low-voltage SEM scanning in order to identify the electron percolation in the CB and Gr network. Low-voltage analysis was first described and used by *Thydén et al.* [16] to identify electron percolation in SOFC

anode Ni-network. When the electron beam hits a sample, a variety of elastic and inelastic scattering of the electrons occurs. If the acceleration voltage of the electrons hitting the sample is low (~1 kV) the electron penetration depth is small and the sample interaction volume is small. Secondary electrons (SEs) emitted from the sample have by definition energies <50 eV and at low voltage several materials have an SE yield different than 1 [19], [20], resulting either in positive or negative charge occurring at the sample surface. If the material is insulating or not connected to the ground it will not be able to dissipate this charge (to ground). Instead an equilibrium is rapidly established where the charge (electrons) hitting the sample equals the emitted charge (electrons). As a result the SE yield depends on whether a part of the electrons can be dissipated to ground and this can be detected by the microscope In-lens detector.

The combination of low-voltage SEM and FIB/SEM have been recently been used for 3D electron percolation analysis of a CB additive in a laboratory $LiFePO_4$/CB positive electrode [8], [17].

2.4. Image processing

Segmentation of the 3D FIB/SEM image data was performed with the program ImageJ (NIH). Because of uneven illumination, setting a single threshold for entire micrographs was not feasible. Therefore the Sauvola algorithm [21], [22] was used to perform local thresholds of the data. The Sauvola algorithm works by dividing the input image into square windows (n x n pixel) and setting thresholds for each of them based on the mean and standard deviation of the pixel intensities. Visualizations of the 3D reconstructions of the analyzed data were performed with the program Avizo (FEI).

The particle and void size distributions (PSD) in all electrode samples were analyzed based on the method introduced by Münch et al. [23]: The segmented 3D volumes are filled with spheres of a given radius. By reducing the radius incrementally, more volumes will be filled. The cumulative PSD is then obtained by correlating the incrementally filled volume with corresponding radii.

3. Results

3.1. Galvanostatic Cycling with Potentiostatic Limitation (GCPL)

F26650CC was cycled five times between 2.8 – 3.6 V (the charge and discharge cut-off voltages are specified by the commercial supplier) at room temperature and a nominal C-rate of 0.1 C (250 mA). A26650CC was cycled 22k times at a nominal C-rate of 4 C (10 A) at room temperature, in a SOC range 25-75%. After this A26650CC has been cycled a couple of times at 250 mA, in order to quantify the capacity fade. Fig. 2a shows the charge/discharge curves for F26650CC and A26650CC. The measured charge capacity is scaled to the electrode area (1950 cm^2).

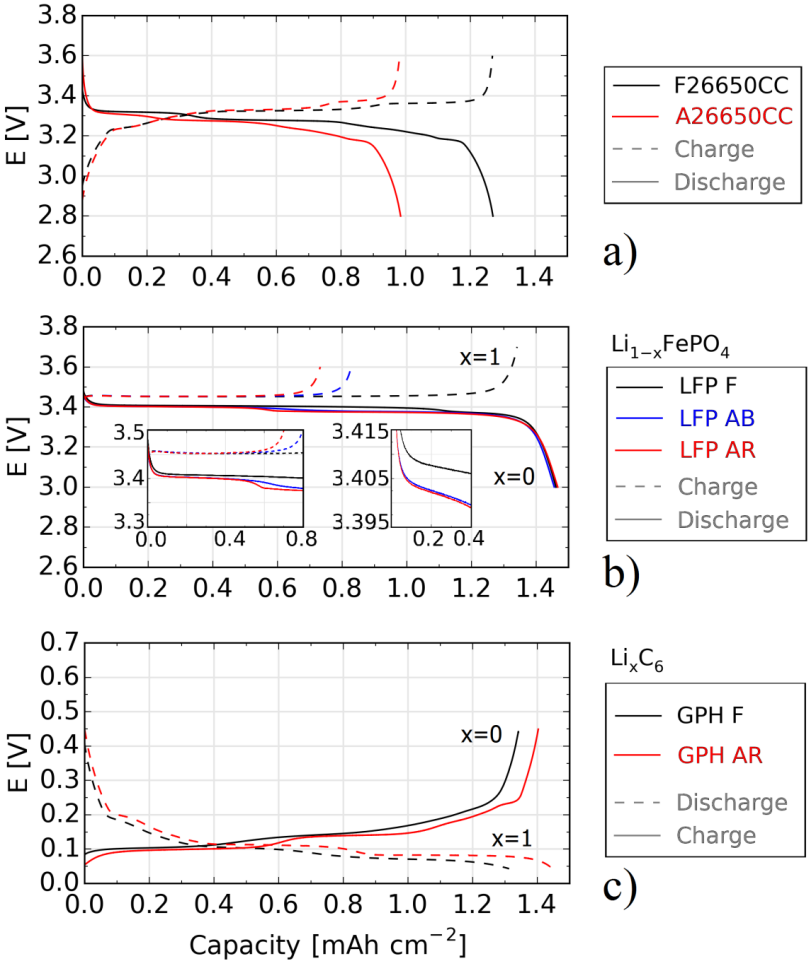

Figure 2. Charge/Discharge curves of a) F26650CC and A26650CC, b) LFP (fresh, aged blue and red) and c) Gr (fresh, aged blue and red)

The total specific discharge capacity in F26650CC is observed equal to 1.27 mAh cm^{-2}, while A26650CC shows a specific discharge capacity of around 0.98 mAh cm^{-2}, indicating a capacity loss equal to 22.5%. To separate the single electrode contributions the two commercial cells have been subsequently de-assembled in the discharged state, fresh and aged LFP/CB1 and fresh and aged Gr1 were extracted and run in three-electrode setup with a lithium metal counter and reference electrode. Fig. 2b and 2c show respectively the charge/discharge curves for the three LFP/CB1 and the three Gr1 electrodes.

The LFP electrodes (Fig. 1b) are cycled between 3.0 – 3.6 V with a constant current of 330 µA, corresponding to a C-rate of 0.1 (calculated for the fresh electrode), considering that its surface area is 2.55 cm^2 and that the unrolled battery electrode was 1950 cm^2. The charge/discharge curves show a flat voltage plateau at around 3.45 V typical for $Li_{1-x}FePO_4$ with $0 \leq x \leq 1$ vs. Li(m) [24], [25]. The charge capacity for LFP1_F is 1.32 mAh cm^{-2} which is comparable to the F266500CC charge capacity (Fig. 1a).

LFP1_AB and LFP1_AR electrodes show a charge capacity of 0.83 and 0.73 mAh cm^{-2} respectively, equal to the 63% and 55% of the charge capacity of LFP1_F. The capacity losses observed in the two different regions are 37% and 45%. From the discharge curves however the aged electrodes are able to completely recover their initial capacity in both regions, showing that there are no electrochemically inactive regions. A little step in lithium intercalation is observed in the discharge curves of LFP1_AB and LFP1_AR, as shown in the left inset in Fig. 1b. The right inset shows that the over polarization for the two aged samples is about 5 mV higher than that for LFP1_F.

The Gr electrodes were cycled between 0.01 V and 0.45 V, also at 330 µA. No big differences are observed between the charge/discharge curves of the Gr1_F and Gr1_AR, the aged sample even show a 4% higher capacity (1.34 and 1.40 mAh cm^{-2} respectively).

3.2. Low – kV FIB/SEM Tomography

Figure 3 shows cross-sectional images recorded with a lateral E-T detector and 1 kV acceleration voltage after FIB milling of the LFP2_F, LFP2_AB, LFP2_AR, Gr2_F, Gr2_AB and Gr2_AR electrodes. The top part of all the images shows a very bright region which is the sample surface after polishing. In Fig. 3(a,b,c) the electrode/electrolyte interface of the three LFP2 electrodes is observed at the right part of the images and three different phases could be distinguished in all the three electrodes: light gray $LiFePO_4$ particles, dark gray pores (infiltrated with silicon resin) and black CB particles. In the right side, where the electrolyte is supposed to be, there is a dark gray bulk of silicon resin and in LFP2_F (Fig. 3a) also few LFP and CB particles probably detached during sample preparation. LFP2_AB and LFP2_AR (Fig. 3b,c) show instead a dark layer of what is supposed to be carbon and decomposition products from the electrolyte at the electrode/electrolyte interface. This layer is thicker and more homogeneous in LFP2_AR.

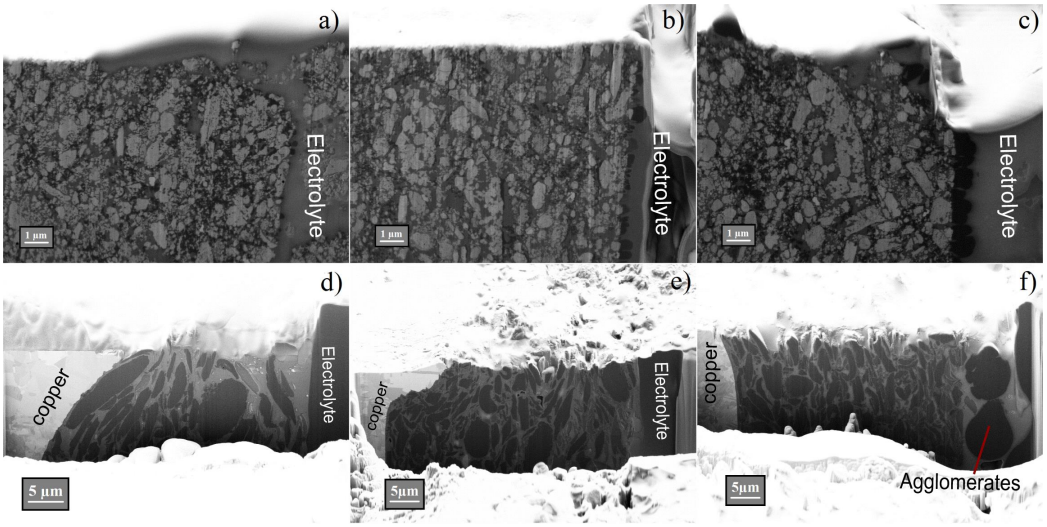

Figure 3. SEM images at 1 kV recorded with Lateral E – T detector of a) LFP2_F, b) LFP2_AB, c) LFP2_AR, d) Gr2_F, e) Gr2_AB and f) Gr2_AR electrodes.

The three Gr2 electrodes are shown in Fig. 3(d,e,f). Only two phases could be distinguished: dark graphite particles and gray pores infiltrated with silicon resin. On the left side the copper/electrode interface is present, while on the right side the electrode/electrolyte interface is found. The darker gray bulk on the right is the epoxy resin, used for sample preparation, which has a different contrast than silicon resin. All the electrodes are characterized by a porous structure of graphite grains. However Gr2_AB and Gr2_AR (Fig. 3e,f) show smaller graphite particles, as later confirmed by PSD. Additionally Gr2_AB have big black agglomerates at the electrode/electrolyte interface.

Figures 4 shows instead cross-sectional In-lens images recorded a 1 kV after FIB milling of all LFP2 and Gr2 electrodes respectively. The low accelerating voltage enables a detection of charging effects on carbonaceous materials [8], [17]. The CB particles in the LFP2 electrodes do not seem to charge, however some of the agglomerates in LFP2_AB are noticed to charge (shown in the red rings, Fig 4b).

A few graphite grains are observed to charge in Gr2_F (shown in the red rings, Fig. 4d), and a higher amount of particles are observed to charge in Gr2_AB and Gr2_AR (Fig. 4e,f), in particular in the part of the electrodes closest to the electrode/electrolyte interface.

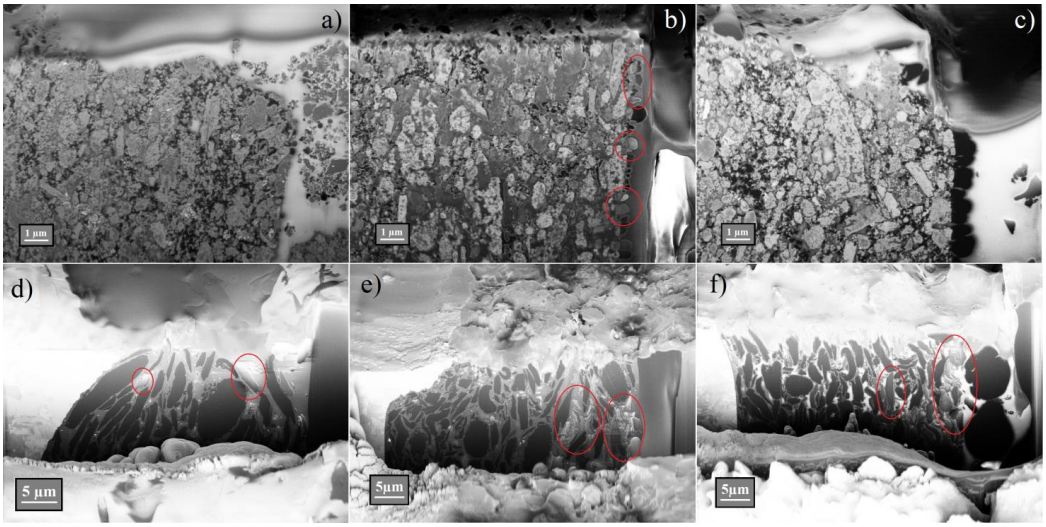

Figure 4. SEM images at 1 kV recorded with In-lens detector of a) LFP2_F, b) LFP2_AB, c) LFP2_AR, d) Gr2_F, e) Gr2_AB and f) Gr2_AR electrodes.

3.3. Three-dimensional reconstruction and data statistical analysis

The three-dimensional reconstructions of the five 3D datasets are shown in Figures 5 and 6 (LFP2 and Gr2 electrodes respectively). Fig. 5 shows the 3D reconstructions of LFP2_F, LFP2_AB and LFP2_AR electrode/electrolyte interfaces. Light gray particles are LFP grains, black particles are CB and pores are transparent blue. At the electrode/electrolyte interface a dark layer is observed. The layer is approximately 0.5 µm and 1 µm thick for LFP2_AB and LFP2_AR respectively.

Particles size distributions (PSD) retrieved from the reconstructions are reported in Fig. 7 and Table 3. The PSD show that relative to the fresh sample, the average LFP particles size decrease respectively ~7 and ~11 % in LFP2_AB and LFP2_AR. A decreased CB particle size and volume fraction is observed. Additionally, the porosity of LFP2_AB and LFP2_AR is which as high as the porosity in the LFP2_F electrode. PSD analysis of the dark agglomerates (Fig. 7f) shows how they increase in size from LFP2_AB to LFP2_AR.

Fig. 6 shows the 3D reconstructions of low-kV In-lens images of Gr2_F and Gr2_AR electrodes. The orange region is the copper current collector. In the electrode three phases can be distinguished. Dark gray particles are graphite grains which are observed to dissipate electron charging to the ground, light gray particles are instead those graphite grains which show some local charging effects during the low-voltage imaging. Finally the pores are again represented as transparent blue. Large agglomerates with a diameter between 5-10 µm in diameter are seen at the Gr2_AR electrode/electrolyte interface. Relative to that of the fresh electrode, the amount of bright graphite particles is observed to be higher in the aged electrode; the bright particles take up 0.8% of the

volume analyzed in Gr2_F, while they occupy 30% of the volume in Gr2_AR. The bright particles are primarily observed in the region close to the electrode/electrolyte interface. The PSD analysis of the dark agglomerates (Fig.7g) only counts a few big particles and is consequently not very accurate.

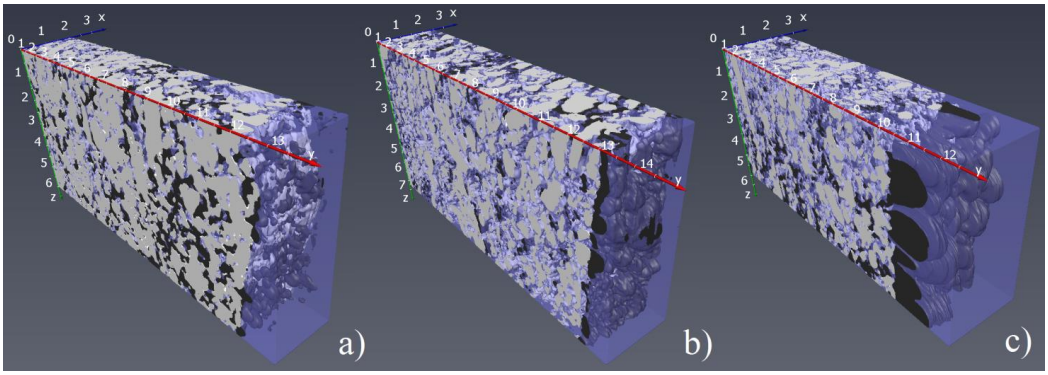

Figure 5. 3D reconstruction of a) LFP2_F, b) LFP2_AB and c) LFP2_AR electrodes. The scale bar units are [µm].

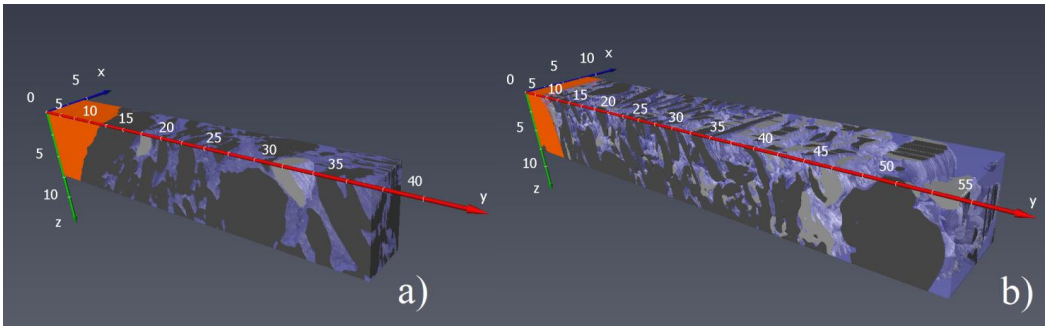

Figure 6. 3D reconstruction of a) Gr2_F and b) Gr2_AR electrodes. The scale bar units are [µm].

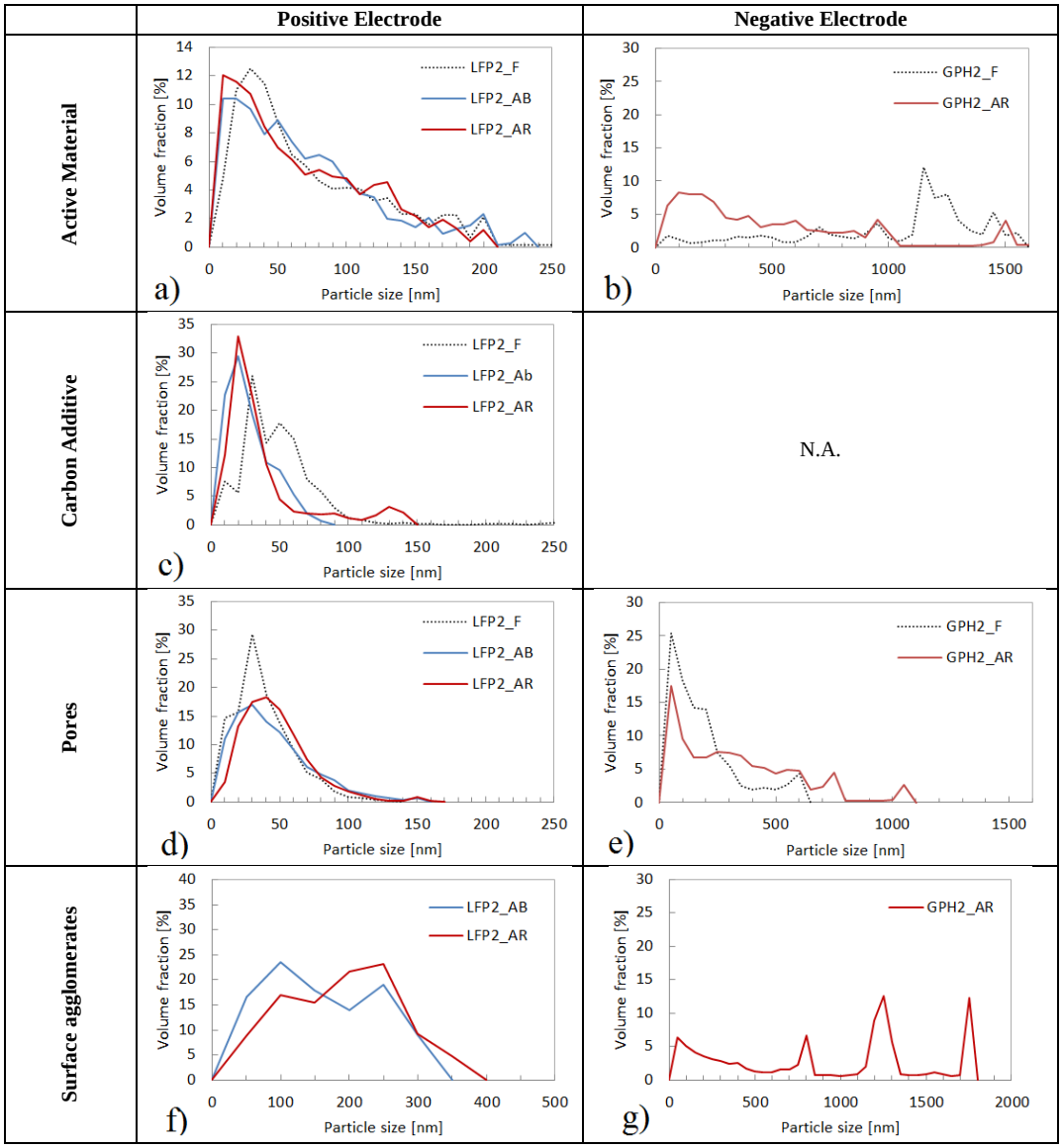

Figure 7. PSD analysis of different phases in a), c), d), f) LFP2 electrodes and b), e), g) Gr2 electrodes.

Table 3. Statistical analysis of LFP2 and Gr2 electrodes.

Phase	LFP2						Gr2					
	Volume Fraction [%]			Avg. particle size [nm]			Volume Fraction [%]			Avg. particle size [nm]		
	F	AB	AR	F	AB	AR	F	AB	AR	F	AB	AR
Active Material	58	44	41	76	71	68	70		70	1096		554
CB Additive	17	7	12	49	28	38	-		-	-		-
Pores	25	49	47	39	45	48	30		30	159		302
Agglomerates	-	-	-	-	141	169	-	-	-	-		875

From the segmented 3D dataset of sample Gr2_AR was also analyzed the graphite connectivity. In this analysis a Gr voxel is considered connected when it has pathway to the left side of the reconstructed data cube (the direction of the copper current collector) through the Gr network. Unknown connectivity is defined as only being connected to one of the other sides of the reconstructed data cube. Fig. 8 shows the electronically connected graphite particles in Gr2_AR without the agglomerates at the electrode/electrolyte interface. Connected particles are highlighted in green, isolated particles are red, while unknown ones are yellow. The amount of connected graphite is found to be higher than 99% for Gr2_AR. This value significantly deviates from the 30% non-electron dissipating particles identified with the low-kV analysis of the same electrode, most likely due to the limited precision of the connectivity analysis which is affected by slicing resolution and segmentation uncertainties.

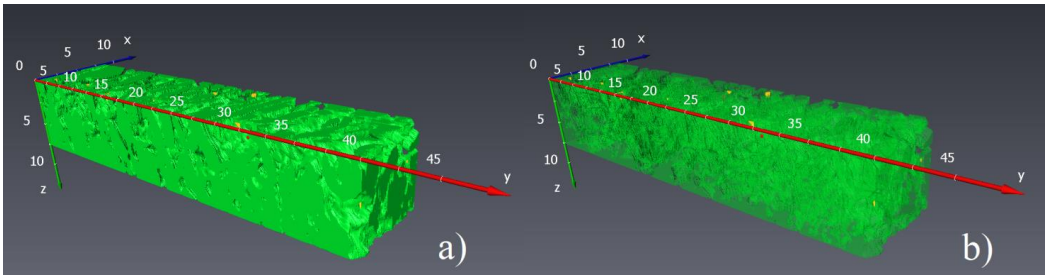

Figure 8. a) Connectivity analysis of Gr2_AR electrode. Green particles are connected with the left side of the segmented volume (closest to the copper current collector). Red particles are unconnected and yellow particles are unknown (could be connected outside the segmented volume). b) Same 3D reconstruction showing the connected particles as transparent green to highlight isolated and unknown particles.

4. Discussion

4.1. Galvanostatic Cycling with Potentiostatic Limitation (GCPL)

As discussed in section 3.1, A26650CC shows a capacity loss of 22.5% after being cycled 22k at 4C between 25% and 75% SOC (Fig.2a). Results of the single electrodes cycling in the electrode

configuration (Fig. 2b,c) are in agreement with the ones observed for the full cylindrical cell (Fig. 2a). The charge/discharge capacities of LFP1_F and Gr1_F match the F26650CC capacity well (Fig. 2). The discharge capacity of LFP1_F is 10% higher than that of F26650CC, which is expected to account for the amount of lithium spent for the initial SEI layer formation at the graphite electrode [26]–[28].

Similar to previous observations [29], [30] LFP1_AB and LFP1_AR show a lower capacity during the first charge (65 and 58% of the fresh electrode capacity, respectively). This means that only a fraction of the LFP was fully lithiated to $LiFePO_4$ during the final discharge and that a substantial part of the LFP remains as $FePO_4$. After the first discharge both LFP1_AB and LFP1_AR are able to recover completely the initial capacity, also in agreement with previous observations [29], [30]. This shows that there are no electrochemically inactive parts of the material, and that all the regions of the electrode are accessible to lithium ions. This suggests that almost no capacity fade occurs to the LFP electrode due to cycling. However, a higher over polarization was observed in the aged electrodes (Fig. 2b, insets). This is possibly related to an increased ionic resistance furnished by the partially blocking layer at the electrode/electrolyte interface on the aged samples (Fig. 7b,c).

Gr1_AR show a capacity slightly larger than that of Gr1_F. Anode capacity fade with cycling was previously observed [29], [30] and the reason for the unexpectedly large capacity of Gr1_AR is not fully understood.

4.2. Morphological changes

The FIB/SEM analysis of the three LFP2 electrodes showed some changes in the morphology of the electrode with cycling. First of all the LFP particle are observed to slightly smaller in the two aged samples. This could probably be an effect of LFP cracking with cycling [6]–[8], [17]. The cracking may also increase the porosity of the aged electrodes, as observed by comparing the pore volumes for the three electrodes (Table 3). The CB black particles are also observed to have a smaller size in the aged samples and their volume fraction is around a half of what is found in LFP2_F. The most important degradation process seems to be the formation of a layer at the electrode/electrolyte interface. The layer is possibly a mixture of carbon and electrolyte decomposition products [8], [17], [29], [30]. The layer is expected to partially block the electrolyte passage thereby increasing the ionic resistance. This increases the over polarization of the aged electrodes during charge/discharge cycling (Fig. 2b, insets).

CB agglomeration is influenced by the CB/LFP ratio in the electrode material [31]. The layer at the electrolyte/electrode interface is probably composed by a mixture of CB and decomposition products from the electrolyte, i.e. Li-organic species, fluorophosphates and LiF [32] and could thus in part explain the loss of lithium inventory (LLI). The layer is found to be thickest in the sample collected from the core of the cylindrical battery, which could be an effect of the accelerated degradation of the electrolyte caused by the higher temperature [33], [34] developed in the core of

the cylindrical cell [35].

FIB/SEM tomography of the Gr2 electrodes also revealed formation of big agglomerates sitting at the electrode/electrolyte interface. The volume fraction between CB and pores (Table 3) is the same for the fresh and the aged sample, however from PSD analysis it is seen that the graphite particles are significantly smaller in Gr2_AR than in Gr2_F. This is probably an effect of cracking of Gr particles with cycling [36], [37].

4.3. Charge contrast and connectivity studies

The low – voltage analysis was previously used to detect charging effect in the CB network of a laboratory LFP electrode to study the changes in the electron dissipation capability in the CB network [8], [17]. The commercial LFP electrode studied here reveal no charging effects due to cycling, however some of the agglomerates in the sample collected from the skin (LFP2_AB) were observed to locally charge, probably due to disconnection of the grain from the CB network.

The low – kV FIB/SEM was useful to detect locally charged particles in Gr2_F and Gr2_AR electrodes. As shown in Fig. 4 and 3D reconstructed in Fig. 6, from identification and quantification of locally charged Gr particles in the negative electrode sample, a distinction between "percolating" and "non-percolating" graphite particles was possible. Non-percolating graphite particles count for 0.8% and 30% in Gr2_F and Gr2_AR respectively. The bright graphite particles are predominantly found in the region of the electrode closest to the electrode/electrolyte interface. This charging effect are not fully understood yet, however they are believed to describe graphite particles that are disconnected from the electron percolating network. Many Gr grains show in fact a flickering intensity between two consecutive images during the milling job. This is probably an effect of connection/disconnection of the same particle from the percolating network concurrently with the ion milling. Furthermore, cracking of graphite particles with cycling, as previously suggested by PSD calculation, would create new carbon/electrolyte interfaces which would be covered by SEI layer after electrolyte decomposition, which is known to be an electron insulator [38]–[40]. This would of course create new secondary smaller graphite grains with an increased electronic resistance.

In contrast to the low – kV FIB/SEM analysis, the connectivity analysis of Gr2_AR electrode (section 3.3) did not show a decreased connectivity. This is probably because of segmentation inaccuracy of low resolution images. For this reason low – kV FIB/SEM analysis seem to be a good complementary technique to the usual connectivity analysis.

5. Conclusions

In this work the electrode degradation mechanisms in commercial 2.5 Ah $LiFePO_4$/C 26650 cylindrical cells were examined. Aged and fresh electrode samples were prepared by cycling two cells respectively five and 22k times. Subsequently the cells were disassembled in a glovebox. Anode and cathode samples were extracted and tested in a 3-electrode setup and characterized with low-kV FIB/SEM tomography.

In agreement with previous studies, galvanostatic cycling with potentiostatic limitation (GCPL) shows that the extracted aged LFP electrodes (cathodes) are not completely lithiated, i.e. that loss of lithium inventory (LLI) contributes to the capacity loss observed in the aged 2.5 Ah cell. After the first charge/discharge cycle both electrodes were able to completely recover the initial capacity showing that there are no electrochemically inactive regions. This is previously observed for the LFP electrodes, but usually aged graphite (Gr) electrodes (anodes) exhibit a significant capacity fade due to loss of active material (LAM). The reason why LAM is not observed for the investigated anode samples is not fully understood.

The electrodes have been analyzed by low – kV FIB/SEM tomography to study changes in morphology. The morphology analysis showed that both the LFP and Gr particle size decrease with cycling. This could be an effect of mechanical stress during lithiation/delithiation process with consequent cracking of particles. CB additive particles in the LFP electrodes are observed to decrease in size and volume fraction and a big layer of what is believed to be electrode/electrolyte decomposition products is observed on the electrode/electrolyte interface of the aged cathode samples. The layers at the anode and cathode electrode/electrolyte interfaces are possibly composed of LiF and Li-organic species, and is believed to be the main degradation mechanism causing loss of lithium inventory (LLI) in the cylindrical cell.

Low – kV FIB/SEM tomography was also used to study the electron percolation in the graphite network in 3D, and several graphite particles in the aged anode were found incapable of dissipating the electric charge induced by the microscope electron beam. This was predominantly observed in the region close to the electrode/electrolyte interface and could be an effect of cracking of Gr particles upon cycling. It is important to note that this contradicts with the GCPL measurement which revealed no LAM. The contradiction can possibly be explained by the difference in volumetric current density; the volumetric current density when the microscope electron beam hits a single Gr particle is several orders of magnitude higher than the volumetric current density during charge/discharging.

Concluding the degradation of a cylindrical cell was studied by electrochemical and physical-chemical characterization. Loss in performances could not be addressed to loss of electrochemically active material (LAM) from either positive or negative electrode, but is most likely due to LLI which occurs in relation to the deposition of a thick layer at the electrode/electrolyte interfaces.

Acknowledgement

The authors gratefully acknowledge financial support from the Danish Strategic Research Council through the project “Advanced Lifetime Predictions of Battery Energy Storage” (contract no. 0603-00589B).

References

[1] M. Armand and J.-M. Tarascon, “Building better batteries.,” *Nature*, vol. 451, no. 7179, pp. 652–657, 2008.

[2] B. Scrosati, J. Hassoun, and Y.-K. Sun, “Lithium-ion batteries. A look into the future,” *Energy Environ. Sci.*, vol. 4, no. 9, p. 3287, 2011.

[3] A. K. Padhi, K. S. Nanjundaswamy, and J. B. Goodenough, “Phospho-olivines as Positive-Electrode Materials for Rechargeable Lithium Batteries,” *J. Electrochem. Soc.*, vol. 144, no. 4, pp. 1188–1194, 1997.

[4] Y. Wang, P. He, and H. Zhou, “Olivine LiFePO4: development and future,” *Energy Environ. Sci.*, vol. 4, no. 3, p. 805, 2011.

[5] Huggins, *Advanced batteries*, vol. 276. 2009.

[6] H. Gabrisch, J. Wilcox, and M. M. Doeff, “TEM Study of Fracturing in Spherical and Plate-like LiFePO[sub 4] Particles,” *Electrochem. Solid-State Lett.*, vol. 11, no. 3, p. A25, 2008.

[7] D. Wang, X. Wu, Z. Wang, and L. Chen, “Cracking causing cyclic instability of LiFePO4 cathode material,” *J. Power Sources*, vol. 140, no. 1, pp. 125–128, 2005.

[8] R. Scipioni, P. S. Jørgensen, D.-T. Ngo, S. B. Simonsen, Z. Liu, K. J. Yakal-kremski, H. Wang, J. Hjelm, P. Norby, S. A. Barnett, and S. H. Jensen, “Electron microscopy investigations of changes in morphology and conductivity of LiFePO4/C electrodes,” *J. Power Sources*, vol. 307, pp. 259–269, 2016.

[9] L. Zou, F. Kang, Y. Zheng, and W. Shen, “Modified natural flake graphite with high cycle performance as anode material in lithium ion batteries,” *Electrochim. Acta*, vol. 54, pp. 3930–3934, 2009.

[10] H. Zheng and M.-S. Kim, “Performance of modified graphite as anode material for lithium-ion secondary battery,” *Carbon Lett.*, vol. 12, no. 4, pp. 243–248, 2011.

[11] R. Dedryvère, H. Martinez, S. Leroy, D. Lemordant, F. Bonhomme, P. Biensan, and D. Gonbeau, “Surface film formation on electrodes in a LiCoO2/graphite cell: A step by step XPS study,” *J. Power Sources*, vol. 174, no. 2, pp. 462–468, 2007.

[12] M. Hellqvist Kjell, S. Malmgren, K. Ciosek, M. Behm, K. Edström, and G. Lindbergh, “Comparing aging of graphite/LiFePO4 cells at 22 C and 55 C - Electrochemical and photoelectron spectroscopy studies,” *J. Power Sources*, vol. 243, pp. 290–298, 2013.

[13] M. Safari and C. Delacourt, “Aging of a Commercial Graphite/LiFePO4 Cell,” *J. Electrochem. Soc.*, vol. 158, no. 10, p. A1123, 2011.

[14] J. Wang, P. Liu, J. Hicks-Garner, E. Sherman, S. Soukiazian, M. Verbrugge, H. Tataria, J. Musser, and P. Finamore, “Cycle-life model for graphite-LiFePO4 cells,” *J. Power Sources*, vol. 196, no. 8, pp. 3942–3948, 2011.

[15] C. Delacourt and M. Safari, “Life Simulation of a Graphite/LiFePO4 Cell under Cycling and Storage,” *J. Electrochem. Soc.*, vol. 159, no. 8, pp. A1283–A1291, 2012.

[16] K. Thydén, Y. L. Liu, and J. B. Bilde-Sørensen, “Microstructural characterization of SOFC Ni-YSZ anode composites by low-voltage scanning electron microscopy,” *Solid State Ionics*, vol. 178, no. 39–40, pp. 1984–1989, 2008.

[17] R. Scipioni, P. S. Jørgensen, D. T. Ngo, S. B. Simonsen, J. Hjelm, P. Norby, and S. H. Jensen, “Low-voltage FIB/SEM Tomography for 3D Microstructure Evolution of LiFePO4/C Electrode,” *ECS Trans.*, vol. 69, no. 18, pp. 71–80, 2015.

[18] M. Ender, J. Joos, T. Carraro, and E. Ivers-Tiffee, “Quantitative Characterization of LiFePO4 Cathodes Reconstructed by FIB/SEM Tomography,” *J. Electrochem. Soc.*, vol. 159, no. 7, pp. A972–A980, 2012.

[19] J. Cazaux, “About the mechanisms of charging in EPMA, SEM, and ESEM with their time evolution.,” *Microsc. Microanal.*, vol. 10, no. 6, pp. 670–684, 2004.

[20] D. J. Stokes, “Recent advances in electron imaging, image interpretation and applications: environmental scanning electron microscopy.,” *Philos. Trans. A. Math. Phys. Eng. Sci.*, vol. 361, no. 1813, pp. 2771–2787, 2003.

[21] J. Sauvola and M. Pietikäinen, “Adaptive document image binarization,” *Pattern Recognit.*, vol. 33, no. 2, pp. 225–236, 2000.

[22] T. Kryjak and M. Gorgoń, “Parallel implementation of local thresholding in Mitrion-C,” *Int. J. Appl. Math. Comput. Sci.*, vol. 20, no. 3, pp. 571–580, 2010.

[23] B. Münch and L. Holzer, “Contradicting geometrical concepts in pore size analysis attained with electron microscopy and mercury intrusion,” *J. Am. Ceram. Soc.*, vol. 91, no. 12, pp. 4059–4067, 2008.

[24] A. Padhi, K. Nanjundaswamy, and J. Goodenough, “Phospho-olivines as positive-electrode materials for rechargeable lithium batteries,” *J. Electrochem. Soc.*, vol. 144, no. 4, 1997.

[25] A. Andersson, “Lithium extraction/insertion in LiFePO4: an X-ray diffraction and Mössbauer spectroscopy study,” *Solid State Ionics*, vol. 130, no. 1–2, pp. 41–52, May 2000.

[26] H. Wang, T. Umeno, K. Mizuma, and M. Yoshio, “Highly conductive bridges between graphite spheres to improve the cycle performance of a graphite anode in lithium-ion batteries,” *J. Power Sources*, vol. 175, no. 2, pp. 886–890, 2008.

[27] A. a Franco, “Multiscale modelling and numerical simulation of rechargeable lithium ion batteries: concepts, methods and challenges,” *Rsc Adv.*, vol. 3, no. 32, pp. 13027–13058, 2013.

[28] J. Yan, J. Zhang, Y. C. Su, X. G. Zhang, and B. J. Xia, “A novel perspective on the formation of the solid electrolyte interphase on the graphite electrode for lithium-ion batteries,” *Electrochim. Acta*, vol. 55, no. 5, pp. 1785–1794, 2010.

[29] M. Klett, R. Eriksson, J. Groot, P. Svens, K. Ciosek Högström, R. W. Lindström, H. Berg, T. Gustafson, G. Lindbergh, and K. Edström, “Non-uniform aging of cycled commercial LiFePO4//graphite cylindrical cells revealed by post-mortem analysis,” *J. Power Sources*, vol. 257, pp. 126–137, 2014.

[30] E. Sarasketa-Zabala, F. Aguesse, I. Villarreal, L. M. Rodriguez-Martinez, C. M. López, and P. Kubiak, “Understanding lithium inventory loss and sudden performance fade in cylindrical cells during cycling with deep-discharge steps,” *J. Phys. Chem. C*, vol. 119, no. 2, pp. 896–906, 2015.

[31] M. Zhu, J. Park, and a. M. Sastry, “Particle Interaction and Aggregation in Cathode Material of Li-Ion Batteries: A Numerical Study,” *J. Electrochem. Soc.*, vol. 158, no. 10, p. A1155, 2011.

[32] M. Cuisinier, N. Dupré, J. F. Martin, R. Kanno, and D. Guyomard, “Evolution of the LiFePO4 positive electrode interface along cycling monitored by MAS NMR,” *J. Power Sources*, vol. 224, pp. 50–58, 2013.

[33] L. Zhao, I. Watanabe, T. Doi, S. Okada, and J. ichi Yamaki, “TG-MS analysis of solid electrolyte interphase (SEI) on graphite negative-electrode in lithium-ion batteries,” *J. Power Sources*, vol. 161, no. 2, pp. 1275–1280, 2006.

[34] M. H. Ryou, J. N. Lee, D. J. Lee, W. K. Kim, Y. K. Jeong, J. W. Choi, J. K. Park, and Y. M. Lee, “Effects of lithium salts on thermal stabilities of lithium alkyl carbonates in SEI layer,” *Electrochim. Acta*, vol. 83, pp. 259–263, 2012.

[35] L. H. Saw, Y. Ye, and A. A. O. Tay, “Electrochemical-thermal analysis of 18650 Lithium Iron Phosphate cell,” *Energy Convers. Manag.*, vol. 75, pp. 162–174, 2013.

[36] D. Liu, Y. Wang, Y. Xie, L. He, J. Chen, K. Wu, R. Xu, and Y. Gao, “On the stress characteristics of graphite anode in commercial pouch lithium-ion battery,” *J. Power Sources*, vol. 232, pp. 29–33, 2013.

[37] S. Bhattacharya, A. R. Riahi, and A. T. Alpas, “A transmission electron microscopy study of crack formation and propagation in electrochemically cycled graphite electrode in lithium-ion cells,” *J. Power Sources*, vol. 196, no. 20, pp. 8719–8727, 2011.

[38] C. Shen, S. Wang, Y. Jin, and W. Q. Han, “In Situ AFM Imaging of Solid Electrolyte Interfaces on HOPG with Ethylene Carbonate and Fluoroethylene Carbonate-Based Electrolytes,” *ACS Appl. Mater. Interfaces*, vol. 7, no. 45, pp. 25441–25447, 2015.

[39] S. C. Nagpure, B. Bhushan, and S. S. Babu, “Multi-Scale Characterization Studies of Aged Li-Ion Large Format Cells for Improved Performance: An Overview,” *J. Electrochem. Soc.*, vol. 160, no. 11, pp. A2111–A2154, 2013.

[40] V. a. Agubra and J. W. Fergus, “The formation and stability of the solid electrolyte interface on the graphite anode,” *J. Power Sources*, vol. 268, pp. 153–162, 2014.